SYNTHESIS, CHARACTERIZATION, AND PROPERTIES OF POLYMER/INORGANIC LAYERED HOST NANOCOMPOSITES

by

Huikang Wu

A thesis

presented to the University of Waterloo

in fulfilment of the

thesis requirement for the degree of

Doctor of Philosophy

in

Chemistry

Waterloo, Ontario, Canada, 1997

The University of Waterloo requires the signature of all persons using or photocopying this thesis. Please sign below, and give address and date.

ABSTRACT

A novel method was found and developed to prepare hybrid polymer/inorganic layered host nanocomposites. The effect of incorporation of polymer on the cation mobility and the performance of some of these novel materials as cathodes in secondary lithium batteries were examined using electrochemical and solid state NMR methods. A mode coupling theory with extension was introduced to explain the spin-lattice relaxation mechanisms of polymer/inorganic nanocomposites, which, the author believes, can be extended to any system containing a submotional phase which may be the source of different relaxation mechanisms.

A $(PPY)_{0.5}MoO_3$ nanocomposite was prepared by a new method, namely, an oxidative polymerization/ion exchange method. The large d-spacing increase (7.0Å) evidenced by XRD was explained by a hydrogen bonding model. FTIR and conductivity data suggested a conductive form of PPY in $(PPY)_{0.5}MoO_3$. The increased conductivity of this nanocomposite, heated at 200°C, was explained as the further polymerization of oligomer within the MoO_3 gallery.

By controlling the degree of swelling of MoO_3^{x-} sheets with various ratios of Li/Na in the molybdenum bronze and by using mixed solvents, both the monolayer $(PEO)_{0.4}NaMoO_3$ and bilayer $(PEO)_{0.9}(Li,Na)MoO_3$ nanocomposites were isolated. A model based on XRD, $^{13}C/^{23}Na$ solid state NMR and FTIR data was proposed for the structure of the monolayer and bilayer nanocomposites. $^{7}Li/^{23}Na$ solid state NMR spin-lattice relaxation and linewidth studies on bilayer $(PEO)_{0.9}(Li,Na)MoO_3$ nanocomposites

show different relaxation mechanisms in different temperature regions; these were explained by a mode coupling theory with extension. A comparative study of the electrochemical insertion of lithium into the two polymer nanocomposites and $NaMoO_3$ by using the materials as cathodes in rechargeable lithium batteries indicates that the kinetics of the electrochemical Li insertion/deinsertion process is improved by incorporation of the polymer.

$(PANI)_{0.4}\alpha$-$Sn(HOPO_3)_2$ and $(PPV)_{1.0}\alpha$-$Sn(HOPO_3)_2$ were prepared either by an acid-base reaction or an ion exchange reaction. $(PPV)_{1.0}\alpha$-$Sn(HOPO_3)_2$ represents the first example of direct insertion of a polymer into a metal phosphate by ion-exchange. While the $(PANI)_{0.4}\alpha$-$Sn(HOPO_3)_2$ exhibit low but measurable conductivity, $(PPV)_{1.0}\alpha$-$Sn(HOPO_3)_2$ behaves as an insulator.

to Yan Li,

Jack and Lisha

for their support and understanding

ACKNOWLEDGEMENTS

I would like to express my appreciation to my thesis supervisor, Professor Linda Nazar, for giving me the opportunity under her direction to work in the fascinating field of chemistry, and especially, for her continual support and encouragement throughout the course of my research.

Special thanks go to also Professor W. Power and Dr. S. Mooibroek, for their assistance with NMR measurements and for the many useful discussions. The technical assistance of Janet Venne with NMR instrumentation is also greatly appreciated. Mr. Henry Tiedje is thanked for his help with conductivity instrumentation.

The professors on my supervisory committee, Dr. D. Irish, Dr. G. Penner, and Dr. M. Pintar are thanked for their time and so much effort in reading through the Thesis. I especially appreciate Dr. Irish's help in many aspects of my life in Waterloo.

The kindness and helpfulness from all my student colleagues in Dr. Nazar's group but, especially, X. T. Yin and T. Kerr are gratefully acknowledged.

TABLE OF CONTENTS

LIST OF FIGURES

LIST OF TABLES

LIST OF ABBREVIATIONS AND TERMINOLOGY

δ	(NMR) chemical shift
θ	(XRD) Bragg angle
τ_c	(NMR) Correlation time of molecular motion
$(Li,Na)MoO_3$	$[Li_x(H_2O)_m Na_y(H_2O)_n]MoO_3$, $x + y = 0.25$
$(PEO)_{0.4}NaMoO_3$	Monolayer PEO/MoO_3 nanocomposite
$(PEO)_{0.9}(Li,Na)MoO_3$	Bilayer PEO/MoO_3 nanocomposite
CP	Cross-polarization
DTA	Differential thermal analysis
EFG	Electric field gradient
FTIR	Fourier transform infrared
MAS	(NMR) Magic angle sample spinning
$NaMoO_3$	$[Na(H_2O)_n]_{0.25}MoO_3$
NMR	Nuclear magnetic resonance
OCV	Open circular voltage
PANI	Polyaniline
PC	Propylene carbonate
PEO	Polyethylene oxide
PPV	Poly(*p*-phenylene vinylene)
PPY	Polypyrrole
T_1	Spin-lattice relaxation time
TGA	Thermal gravimetric analysis

XRD	X-ray diffraction

CHAPTER ONE

GENERAL INTRODUCTION

Traditionally, compounds are divided into two types: inorganic and organic. It was realized by the end of the last century that hybridization of inorganic and organic compounds is possible and coordination chemistry brings inorganic and organic compounds together, thus producing many new properties and materials: e.g. homogeneous catalysts and anti-cancer drugs. During the formation of coordination compounds, there is a strong chemical interaction (coordination bond) between the inorganic and organic components resulting in a change of structure from the parent components. Intercalation chemistry makes it possible to keep the basic structure of the host during the hybridization of organic and inorganic components; this provides versatile methods to produce new materials and modify existing materials. In the last decade, by the extension of the hybridization to organic polymer and layered inorganic compounds or zeolites using intercalation chemistry, new kinds of organic polymer/inorganic host nanocomposite materials have been developed.

Recently, the area of composite organic/inorganic polymeric materials, mixed at the molecular level, has been receiving considerable research interest. The organic polymers can be saturated or conjugated, while the inorganic components can be three-

dimensional (3-D) systems such as zeolites,[1, 2, 3, 4] 2-D layered materials such as clays[5, 6, 7, 8] and metal oxides,[9, 10, 11] and even 1-D materials such as $(Mo_3Se_3^-)_n$ chains.[12, 13]

The introduction of the interaction between polymers and inorganic host is mutually beneficial. Making use of the relative rigidity of inorganic hosts such as layered transition metal oxides, phosphates, clays, and zeolites, the conformation and dimension of the conductive polymer can be controlled and adjusted during the formation of the nanocomposites. On the other hand, by the introduction of the polymer into the host, the properties of the host can be modified or improved. Furthermore unique properties may arise from the interaction of the inorganic host with the polymer on a molecular level. Since the intercalation reaction has been a main method to produce polymer/inorganic host nanocomposite materials, intercalation chemistry will be briefly reviewed first.

1.1 Intercalation Chemistry

Intercalation or insertion into organized two- or three-dimensional structures (layered solids, zeolites) is of increasing importance as a route to the structural control of chemical reactions.[14, 15, 16] The cavities, interlamellar voids, and pores which typify these structures can be considered as micro "reaction chambers" which fulfill, at the same time, a template role; positioning and orientation of the guest molecules can be assisted by exploiting the structural properties of host materials. This approach has been used for the sequential formation of multilayer systems,[17] the synthesis of molecular wires of conducting polymers within channel structures[18] or interleaved with the layers of an

inorganic matrix,[19] for the support of quantum-well particles[20, 21, 22] and, more generally, for the synthesis of microporous pillared layered structures.[23] Several of these materials have been employed in energy storage materials, electrochromic displays, and catalysis.[16, 24, 25, 26, 27]

The general intercalation reaction can be written schematically, following the notation used by Schorn,[28] as

$$xG + M_x[H] \rightleftharpoons G_x[H] \quad (1)$$

One characteristic of intercalation reactions is that no major rearrangements of the solid structure occurs during the intercalation process,[29] so it is known as a soft chemistry method. It consequently requires that during intercalation reactions no extensive bond breaking occurs in the host materials; in turn, this requires special chemical and structural features for the host materials.[14] Despite the structural and chemical restrictions on intercalation reactions, a wide range of different types of compounds satisfy the requirements to serve as the host material. Chain structures, layer lattices, and three-dimensionally connected frameworks containing either tunnels or intersecting channels have all been found suitable as hosts for intercalation reactions. Three-dimensionally connected frameworks containing either tunnels or intersecting channels provide, on one hand, the host lattice that has a strong covalent network of atoms which remains unchanged on reaction and, on other hand, vacant sites in the structure which are interconnected and of suitable size to permit diffusion of the guest species into the solid. The shortcoming of these kinds of hosts is the limitation on the size of guest species. Layered hosts, characterized by strong intralayer bonding and weak interlayer interactions,

however, are adjustable to accommodate different dimensions of guest species by expansion of the lamellar distances and are widely used as hosts to prepare polymer/inorganic layered host nanocomposites.

Layered solids can be conventionally classified into three types according to the charge the layers bear with: (1) neutral layers, such as graphite, TiS_2, FeOCl, V_2O_5, α-MoO_3; (2) positively-charged layers, such as layered double hydroxides; (3) negatively-charged layers, such as smectite clays, ternary alkali metal transition metal oxides.

Compounds with two-dimensional layered structures possess basal planes of atoms that define a "gallery" region between the stacked units.[30] In structures with electrically neutral layers, e.g., graphite, TiS_2, TaS_2 or MoO_3, the galleries are empty with the basal planes of adjacent layers in van der Waals contact. Neutral guest atoms or molecules often can be incorporated between the host layers to form regularly intercalated derivatives. The incorporation of neutral species into the van der Waals gap typically is accompanied by an electron transfer reaction between the molecular guest and the layered host.[31, 32] Figure 1.1 represents the concomitant incorporation and oxidation of Li to form Li/TiS_2 intercalation compounds. The free energy change associated with the electron transfer step provides much of the impetus for the intercalation reaction.

In charged layers, in order to achieve electrical neutrality, counter ions, usually solvated by water or other polar molecules, occupy the gallery region between layers. Thus ionic lamellar compounds qualitatively resemble the conventional intercalation compounds formed by electron transfer reactions between neutral guest and layered host precursors. The ions between the gallery can be ion exchanged with guest ions to form

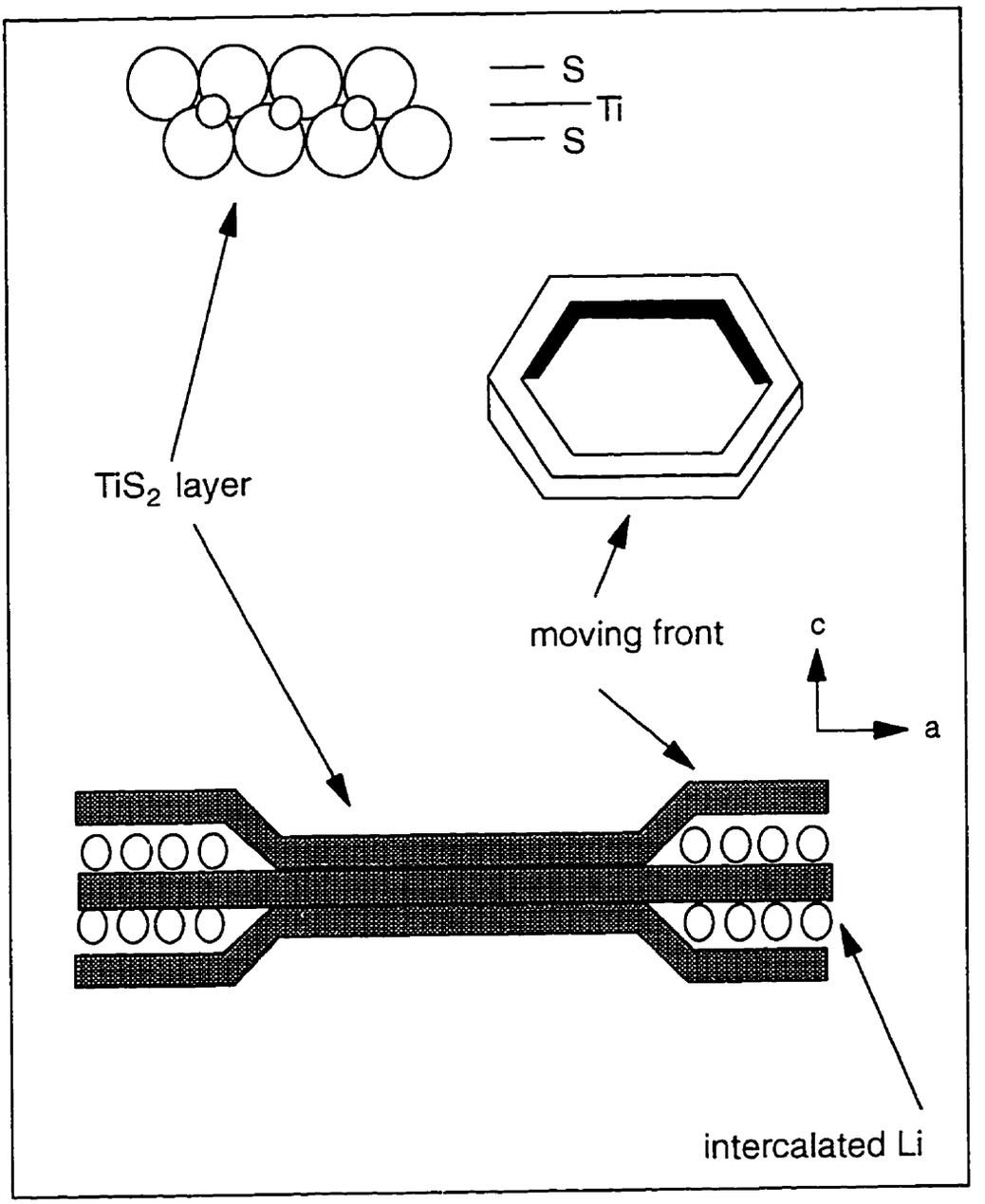

Figure 1.1 **Intercalation of Li into TiS_2**

intercalation materials in which no electron transfer is observed for the intercalation reaction.

The formation of polymer/inorganic host nanocomposite materials is a one step extension of the conventional intercalation reaction. The simultaneous intercalation and oxidative polymerization of some organic compounds such as pyrrole or aniline into a layered host have resulted in the discovery of a wide range of polymer/inorganic host nanocomposite materials. The extension of cations to polyelectrolytes has also resulted in new types of polymer/inorganic host nanocomposite materials, which are discussed below.

1.2 Routes to the Conductive Polymer/Inorganic Layered Host Nanocomposite Materials

Research on conductive polymer/inorganic host nanocomposite materials is still in its infancy. New synthetic methods and better characterization of new materials are urgently needed. Intercalation reactions have played a key role in the preparation of new conductive polymer/inorganic host nanocomposite materials and in control of the conformation of polymers. According to the strategy of formation of polymers in nanocomposite materials, the available preparation methods can be classified as follows.

1.2.1 Method I -- *In situ* intercalative polymerization

It was found that several organic molecules such as pyrrole, aniline, and thiophene will polymerize upon intercalation into layered transition metal oxides such as V_2O_5 (Figure 1.2).[33] The intercalation and polymerization occur simultaneously to form

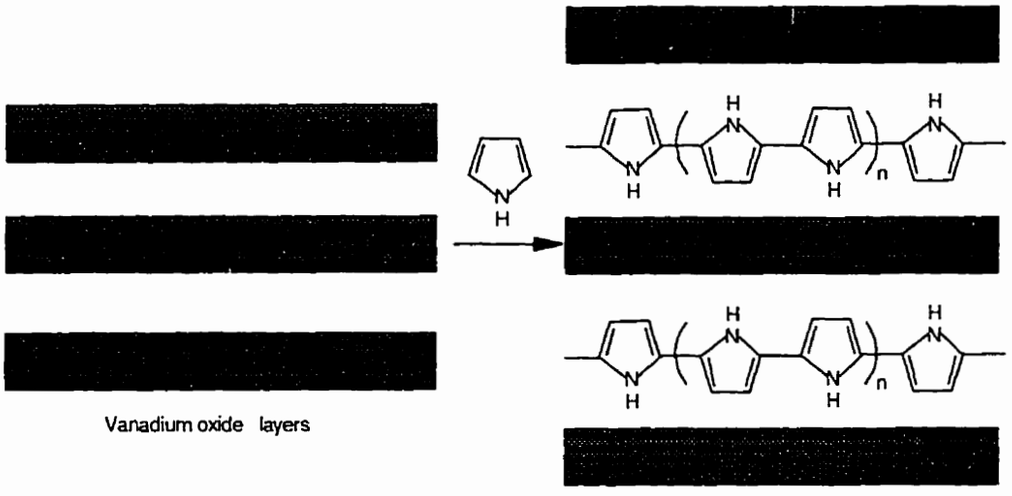

Figure 1.2 Synthetic scheme for PPY/V_2O_5

nanocomposite materials. The products prepared by this method contain the corresponding conjugated polymers (polyaniline, polypyrrole and polythiophene) within an electronically conductive mixed-valence $V^{4+}/^{5+}$ lamellar host. This reaction has been extended to an FeOCl layered host.[34] The host material expands its interlayer distance to accommodate the conductive polymer. In such compounds, the polymeric chains are oriented parallel to the metal-oxide sheets.

1.2.2 Method II --Post-intercalative polymerization

In contrast to the above *in situ* intercalative polymerization, monomers are inserted into the host first and then oxidatively polymerized. This method has the potential to better control the formation process of the conductive polymer. The monomer is first intercalated into the host and so the arrangement of monomers and therefore the polymers are controlled by the host. The change of the properties and the available size of the host can control the arrangement of the monomer and consequently the structure and conformation of the polymers. With the aid of acid-base reactions between the host and aniline, this method has been used to prepare a series of polyaniline/inorganic host nanocomposite materials.[35] Figure 1.3 illustrates one example.

1.2.3 Method III -- Direct insertion of polymers into layered host

Due to the large size of polymer molecules, direct intercalation is most difficult. It is only possible to successfully intercalate polymers into a layered host, as layered hosts can adjust their spacing to accommodate different sizes of guests. It has been shown by this laboratory, for the first time, that a preformed polymer can be inserted into a swollen two-dimensional host, $(Li,Na)MoO_3$ by an ion exchange method (Figure 1.4).[9] This method is interesting in that it provides the opportunity to directly compare the properties between the parent polymer and inserted polymer in layered host and to study the effect of intercalation and host materials on the properties of conductive polymers. The insertion of other preformed polymers into layered hosts has also been reported.[36]

1.3 Survey of Polymer/Inorganic Host Nanocomposite Materials

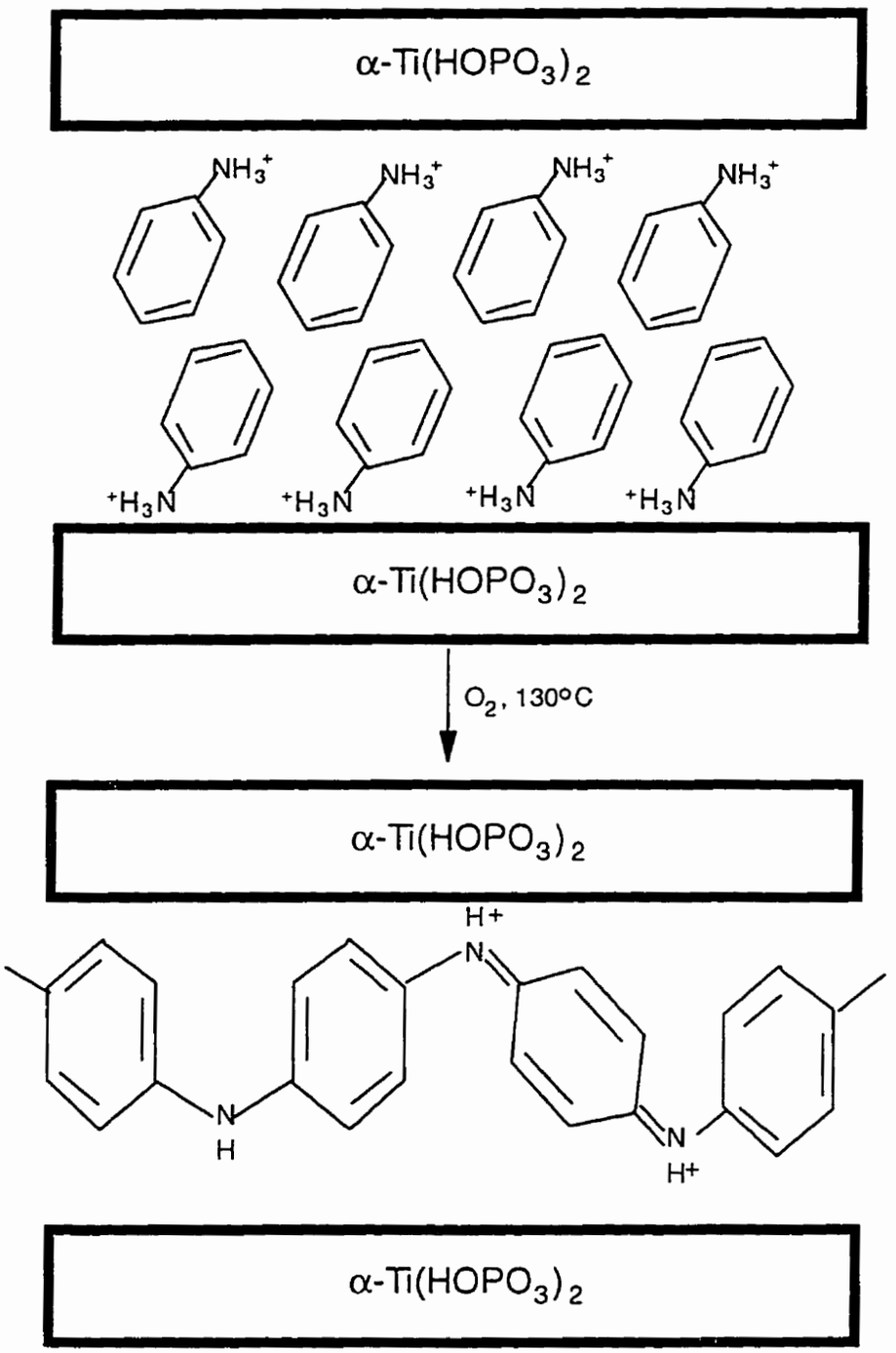

Figure 1.3 **Synthetic scheme for PANI/α-Ti(HOPO$_3$)$_2$**

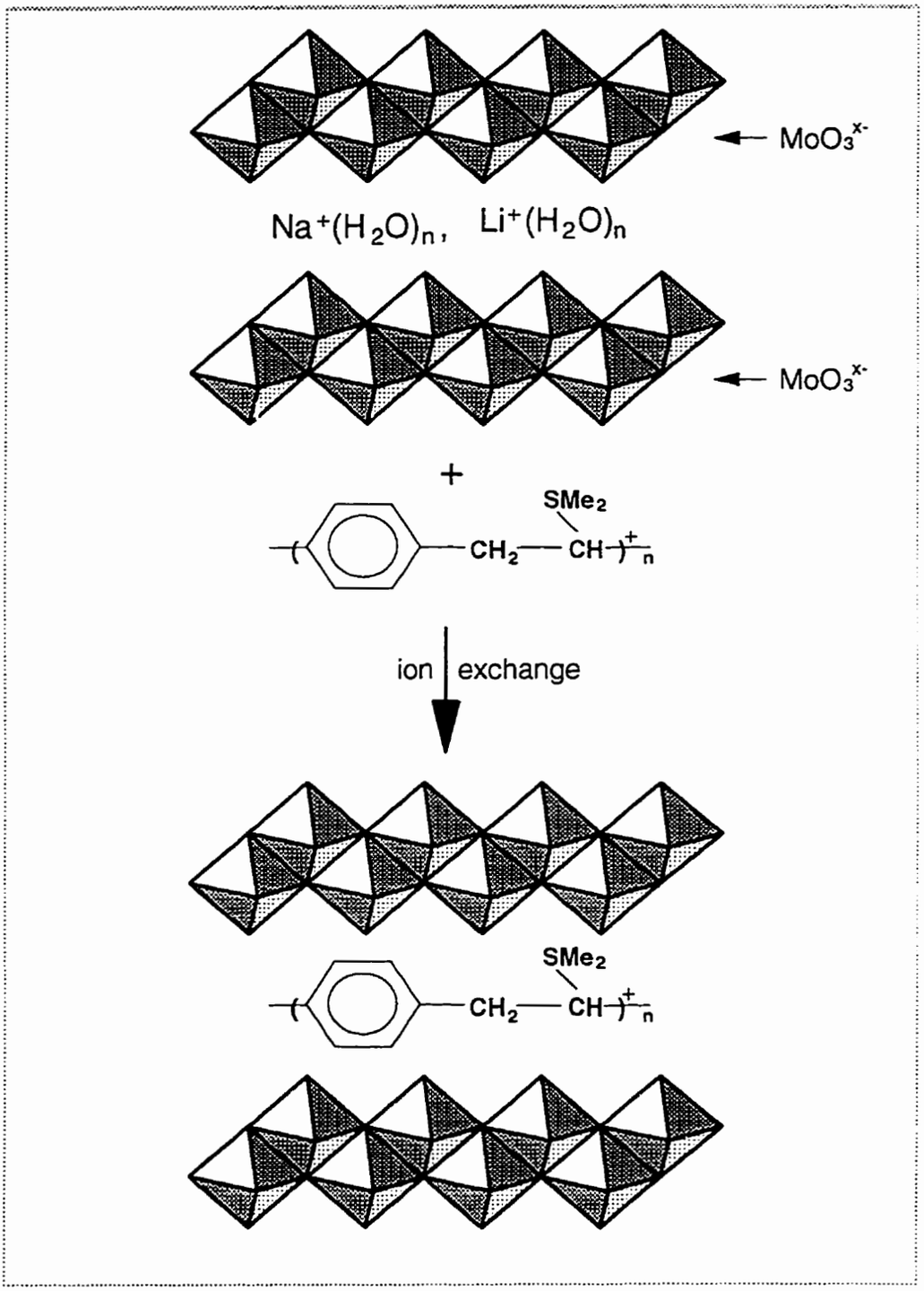

Figure 1.4 **Synthetic scheme for PPV/MoO_3**

There are a few reports of the preparation of the polymer/inorganic layered nanocomposite materials. But it was not until 1987 that the first conductive polymer/inorganic layered materials were reported. Thereafter, there has been a steady increase of interest in this new type of material. The conductivity of the nanocomposite materials is always of main interest. It will be convenient for us to classify the nanocomposite materials according to the conductivity of the guest polymer and the host -- inorganic layered compound.

Table 1.1 Types of Polymer/Inorganic Host Nanocomposite Materials

Polymer/Polymer Salts	Host	Example
Electronically conductive	Electronically conductive	PPV/MoO_3[9]
Electronically conductive	Electronically insulating	PANI/α-HUO_2PO_4[35]
Ionically conductive	Electronically conductive	PEO(Li)/MoO_3[36]
Ionically conductive	Electronically insulating	PEO(Li)/montmorillonite[37]

Table 2 lists the nanocomposite materials which have been prepared up to 1995.

Table 1.2 Survey of Polymer/Inorganic Host Nanocomposite Materials

Host	Guest	Method	Year	Reference
Cu-fluorohectorite	polyaniline	I	1991	38
Cu-fluorohectorite	polypyrrole	I	1992	39
V_2O_5	polythiophene	I	1990	40
V_2O_5	polypyrrole	I	1990	143
Zeolite Y	polypyrrole	I	1989	42
Mordenite	polypyrrole	I	1989	42
FeOCl	polythiophene	I	1989	43
α-$VOPO_4$	polypyrrole	I	1995	53
α-$VOPO_4$	poly(4-anilinoaniline)	I	1995	46
α-$VOPO_4$	poly(4-anilinoanilinum)	I	1995	46
V_2O_5	poly(4-anilinoaniline)	I	1995	46
V_2O_5	poly(4-anilinoanilinum)	I	1995	46

Cu-MCM	polyaniline	I	1994	47
α-$VOPO_4$	polypyrrole	I	1994	48
Layered Double Hydroxides	polyaniline	I	1994	49
FeOCl	PPY	I	1987	50,
H-ZSM-5	polypropene	II	1989	51
α-HUO_2PO_4	polyaniline	II	1993	42
Zeolite Y	polyaniline	II	1989	52
Fluorohectorite	poly(ε-caprolactone)	II	1993	44
Faujasite	polyaniline	II	1989	53
Mordenite	polyaniline	II	1989	53
H-ZSM-5	polyacetylene	II	1991	3
H-ZSM-5	polymethylacetylene	II	1991	3
Mordenite	polymethylacetylene	II	1991	4
Montmorillonite	polyaniline	II	1987	7

α-$VOPO_4$	poly(3-methylpyrrole)	II	1994	48
V_2O_5	poly(vinylpyrrolidone)	III	1993	54
V_2O_5	poly(propylene glycol)	III	1993	54
V_2O_5	methylcellulose	III	1993	54
MoS_2	polystyrene	III	1991	37
Montmorillonite	PEO	III	1990	38, 44
Mo_3Se_3	PEO	III	1990	12
MoO_3	poly(*p*-phenylene vinylene)	III	1992	9
Hectorite	PEO	III	1992	37
Na-montmorillonite	PEO	III	1993	55
MoS_2	poly(vinylpyrolidinone)	III	1993	56
MoS_2	PEO	III	1993	56
MoS_2	poly(propylene glycol)	III	1993	56
MoS_2	methylcellulose	III	1993	56
MoS_2	poly(ethylenimine)	III	1993	56

MoS_2	polyaniline	III	1993	44
Montmorillonite	polystyrene	III	1993	44
V_2O_5	PEO	III	1991	57
MoS_2	PEO	III	1993	58
TiS_2	PEO	III	1993	58

1.4 Objectives and Organization of the Thesis

The past ten years have witnessed rapid growth of the study of polymer/inorganic host nanocomposite materials. Many conductive polymers such as polypyrrole, polyaniline, and polyethylene oxide have been incorporated into rigid inorganic hosts such as V_2O_5 and MoO_3, and transition metal phosphates. Relatively well-ordered materials have been obtained. Interesting properties such as the mutual enhancement of the conductivity have been observed. Promising applications of such materials in high energy-density storage systems have been suggested or explored.

However, the whole status of these kinds of new materials is still in its infancy. New methods of preparation have to be sorted out to extend the nanocomposites to a wide range of polymers and hosts. Better characterization methods are urgently called for to characterize the nanocomposite and to better understand the properties of

nanocomposites. The applications of these materials are waiting to be explored. This thesis, aimed at gaining a better understanding of these nanocomposites, presents a new method of preparation of a series of nanocomposite materials; several modern analytical methods such as powder XRD, solid state NMR, FTIR, thermal analysis, conductivity measurements, and electroanalytical methods have been employed to characterize the new materials; the application of these new materials as cathode materials in secondary lithium batteries has been explored.

The thesis is divided into three parts. In the first part (Chapter 2), a new method to prepare PPY/MoO_3 nanocomposite materials is presented, the interesting phenomenon of enhanced electrical conductivity after annealing the nanocomposites is studied; the nanocomposite is characterized by XRD, FTIR and thermal analysis.

The second part of the thesis is devoted to the new ionic conductive polymer polyethylene oxide/conducting host MoO_3 nanocomposites. Chapter 3 describes the preparation and characterization of both monolayer and bilayer PEO/MoO_3 nanocomposites. In Chapter 4 the cation dynamics of the PEO/MoO_3 nanocomposites are investigated with solid state NMR as a principal method, coupled with XRD and electrical conductivity data. The effect of the structure, and conformation of PEO on the ionic mobility of the cation inside the layer was studied by solid state NMR using linewidth and relaxation data. An extended mode coupling theory was proposed to explain the spin-lattice relaxation mechanisms of polymer/inorganic nanocomposites. In Chapter 5 the effect of the ionic polymer on battery performance of the materials is presented.

The third part of the thesis deals with conducting polymers such as PANI and PPV/transition metal phosphates nanocomposite materials. The preparation of these nanocomposites by either post-intercalation polymerization and direct insertion of preformed PPV precursor is discussed. XRD, ^{13}C, ^{31}P solid state NMR, FTIR, and thermal analysis have been employed to characterize the new materials and to support the monolayer and bilayer models of the intercalation compounds.

1.5 References

1. Enzel, P.; Bein, T. *Chem. Commun.* **1989**, 1326.

2. Enzel, P.; Bein, T. *Chem. Mater.* **1992**, *4*, 819.

3. Pereira, C.; Kokotailo, G. T.; Gorte, R. J. *J. Phys. Chem.* **1991**, *95*, 705.

4. Cox, S. D.; Stucky, G. D. *J. Phys. Chem.* **1991**, *95*, 710.

5. Soma, Y.; Soma, M.; Harada, I. *J. Phys. Chem.* **1984**, *88*, 3034.

6. Soma, Y.; Soma, M.; Harada, I *Chem. Phys. Lett.* **1983**, *99*, 153.

7. Inoue, H.; Yoneyama, H. *J. Electroanal. Chem. Interfacial Electrochem.* **1987**, *233*, 291.

8. Mehrotra, V.; Giannelis, E. P. *Mat. Res. Soc. Symp. Proc.* **1990**, *171*, 39.

9. Nazar, L. F.; Zhang, Z.; Zinkweg, D. *J. Am. Chem. Soc.* **1992**, *114*, 6239.

10. Kanatzidis, M. G.; Wu, C. G.; Marcy, H. O.; Kannewurf, C. R. *J. Am. Chem. Soc.* **1989**, *111*, 4139.

11. Bissessur, R.; DeGroot, D. C.; Schindler, J. L.; Kannewurf, C. R.; Kanatzidis, M. G. *J. Chem. Soc. Chem. Commun.* **1993**, 687.

12. Vassiliou, J. K.; Ziebarth, R. P.; DiSalvo, F. J. *Chem. Mater.* **1990**, *2*, 738.

13. DiSalvo, F. J. *Science* **1990**, *247*, 649.

14. Ozin, G. A.; Kuperman, A.; Stein, A. *Angew. Chem. Int. ed. Engl.* **1989**, *28*, 359.

15. Ozin, G. A. *Adc. Mater.* **1992**, *4*, 612.

16. Ouvrard, G.; Guyomard, D. Current Opinion in Solid State & Materials Science **1996**, *1*, 260.

17. Lee, H.; Kepley, L. J.; Hong, H.; Mallouk, T. E. *J. Am. Chem. Soc.* **1988**, *110*, 618.

18. Bein, T. in *Supramolecular Architecture: Synthetic Control in Thin Films and Solids*, ed. Bein, T., ACS Symp. Ser. **1992**, *499*, 274, and references therein.

19. Ruiz-Hitzky, E. *Adv. Mater.* **1993**, *5*, 334 and references therein.

20. Wang, Y.; Herron, N. *J. Phys. Chem.* **1987**, *91*, 257.

21. Herron, N.; Wang, Y.; Eddy, M. M. Stucky, G. D.; Cox, D. E.; Moller, K.; Bein, T. *J. Am. Chem. Soc.* **1989**, *111*, 530.

22. Moller, K.; Bein, T.; Herron, N.; Mahler, W.; Wang, Y. *Inorg. Chem.* **1989**, *28*, 2914.

23. Mitchell, I.V., ed., *Pillared Layered Structures: Current Trends and Applications*, Elsevier, London, **1990**.

24. Harris, S.; Chianelli, R. R. *Chem. Phys. Lett.* **1983**, *101*, 603.

25. Weisser, O.; Landa, S. *Sulfide Catalysts: Their Properties and Applications;* Pergamon Press: Oxford, U.K., **1973**.

26. Whittingham, M. S.; Ebert, L. B. in *Intercalated Layered Materials*; Levy, F. A., Ed.; D. Riedel: Dordrecht, Holland, **1979**; Vol. 6, pp 533-562.

27. Smith, J. J. *Naval Res. Rev.* **1985**, *2*, 3.

28. , Schollhorn, D. D. *Inclusion Compounds*, Atwood, J.L.; Davies, J. E. D.; MacNicol, D. D. Eds., Academic Press, New York (**1984**): (1) Intercalation compoumds. Chapter 7, pp. 249-349; (2) The Hoffmann-type and related inclusion compounds, Chapter 2, pp. 29-57.

29. Jacobson, A. J. in *Solid State Chemistry, Compounds*; Cheetham, A. K.; Day, P. Eds.; Oxford University Press: New York. **1992**.

30. Pinnavaia, T. J.; Kim, H. in *Zeolite Microporous Solids: Synthesis, Structure, and Reactivity*, Derouane, E. G. Ed.; Kluwer Academic Publishers, Netherlands, **1992**; pp. 79-90.

31. *Intercalation Chemistry*, Whittingham, M. S.; Hacobson, A. J. Eds. Academic Press, New York, **1982**.

32. Eckert, H.; Herber, R. H. *J. Chem. Phys.* **1984**, *80*, 4526.

33. Kanatzidis, M. G. *C&EN* December 3, **1990**, pp. 36.

34. Wu, C.-G.; DeGroot, D. C.; Marcy, H. O.; Schindler, J. L.; Kannewurf, C. R.; Bakas, T.; Papaefthymiou, V.; Hirpo, W.; Yesinowski, J. P.; Liu, Y.-J.; Kanatzidis, M.G.; *J. Am. Chem. Soc.* **1995**, *117*, 9229.

35. Liu, Y.-J.; Kanatzidis, M. G. *Chem. Mater.* **1995**, *7*, 1525.

36. Nazar, L. F.; Wu, H.; Power, W. P. J. *Mater. Chem.* **1995.**

37. Aranda, P.; Ruiz-Hitzky, E. *Chem. Mater.* **1992**, *4*, 1395.

38. Mehrotra, V.; Giannelis, E.P. *Solid State Commun.* **1991**, *77*, 155.

39. Mehrotra, V.; Giannelis, E.P. *Solid State Ionics* **1992**, *51*, 115.

40. Kanatzidis, M.G.; Wu, C.-G.; Marcy, H. O.; DeGroot, D. C.; Kannewurf, C. R.; *Chem. Mater.* **1990**, *2*, 222.

41. Giannelis, E.P. *JOM* **1993**, *3*, 28.

42. Bein, T.; Enzel, P. *Angew. Chem. Int. Ed. Engl.* **1989**, *28*, 1692.

43. Kanatzidis, M.G.; Hubbard, M.; Tonge, L. M.; Marks, T. J.; Marcy, H. O.; Kannewurf, C. R. *Synth. Met.* **1989**, *28*, C89.

44. Kanatzidis, M.G.; Bissessur, R.; DeGroot, D. C.; Schindler, J. L.; Kannewurf, C. R *Chem. Mater.* **1993**, *5*, 595.

45. Stefanis, A. D.; Foglia, S.; Tomlinson, A. A. G. *J. Mater. Chem.* **1995**, *5*, 475.

46. Nakajima, H.; Matsubayashi, G. *J. Mater. Chem.* **1995**, *5*, 105.

47. Wu, C.-G.; Bein, T. *Chem. Mater.* **1994**, *6*, 1109.

48. Nakajima, H.; Matsubayashi, G. *J. Mater. Chem.* **1994**, *4*, 1325.

49. Challier, T.; Slade, R. C. T. *J. Mater. Chem.* **1994**, *4*, 367.

50. Kanatzidis, M.G.; Tonge, L.M.; Marks, T. J.; Marcy, H. O.; Kannewurf, C. R *J. Am. Chem. Soc.* **1987**, *109*, 3797.

51. Kofke, T. J.; Gorte, R. J. *J. Catal.* **1989**, *115*, 233.

52. Bein, T. *J. Phys. Chem.* **1989**, *93*, 6270.

53. Bein, T.; Enzel, P. *Synth. Mat.* **1989**, *29*, E163.

54. Liu, Y.-J.; DeGroot, D. C.; Schindler, J. L.; Kannewurf, C. R.; Kanatzidis, M. G. *Adv. Mater.* **1993**, *5*, 369.

55. Vaia, R. A.; Ishii, H.; Giannelis, E. P. *Chem. Mater.* **1993**, *5*, 1694.

56. Bissessur, R.; Kanatzidis, M.G; Schindler, J. L.; Kannewurf, C. R *Chem. Commun.* **1993**, 1582.

57. Kanatzidis, M.G; Wu, C.-G.; Liu, Y.-J.; DeGroot, D. C.; Schindler, J. L.; Marcy, H. O.; Kannewurf, C. R *Mat. Res. Soc. Symp. Proc.* **1991**, *233*, 183.

58. Ruiz-Hitzky, E.; Jimenze, R.; Casal, B.; Manriquez, V.; Ana, A. S.; Gonzalez, G. *Adv. Mater.* **1993**, *5*, 738.

59. Aranda, P.; Ruiz-Hitzky, E. *Chem. Mater.* **1992**, *4*, 1395.

60. Kanatzidis, M. G. *C & EN* **1994**, *6*, 20.

61. Butterworth, M. D.; Armes, S. P.; Simpson, A. W. *Chem. Commun.* **1994**, 2129.

CHAPTER TWO

CONDUCTIVE POLYMER/CONDUCTIVE HOST NANOCOMPOSITES

-- Preparation and Characterization of $(PPY)_{0.5}MoO_3$ Nanocomposite

2.1 Introduction

The electronic conduction properties of inorganic polymers have been known for a long time.[1] It was not until the late 70's that researchers at the University of Pennsylvania reported that it was possible to transform films of organic polyacetylene into conducting by reacting (doping) nonconductive polyacetylene with a suitable electron-withdrawing group or electron donating group.[2, 3, 4, 5] Since that time, a large number of conducting polymers have been discovered. One class of these conducting polymers is the polyheterocycles, such as polypyrrole, polyaniline and its chalcogen analogues. Polymers based on heterocyclic monomers (e.g. pyrrole) offer a number of important advantages.[6] These polymers are more stable than, for example, polyacetylene; they can be highly conducting, and they can be conveniently synthesized by either chemical or electrochemical methods.

Conductivity as high as 10^5 S/cm has been reported for conducting polymers, a value comparable to the conductivity of metallic copper, $\sigma = 6 \times 10^5$ S/cm. The high

polymers. Many applications of conducting polymers in lithium batteries, smart windows and various sensors have been explored. However, despite the large body of data from both practical and theoretical work -- due to the amorphous morphology of most conducting polymers -- their microstructures, such as chain conformation, packing, and crosslinking have not been well characterized and remain uncontrolled. [1, 7, 8]

Encapsulation of conducting polymers such as polypyrrole or polyaniline in a rigid inorganic lattice such as layered FeOCl, V_2O_5, α-$M(HOPO_3)_2$ (M = Ti, Zr, Hf) has been reported. In these so-called conductive polymer/inorganic layered nanocomposite materials, there are interleaved stacks of polymer chains and inorganic layered sheets. The polymers are usually lined up in these nanocomposite materials.[8, 9, 10, 11, 12] That is, the 2D host can control and affect the conformation of intercalated polymer chains; this property may provide the opportunity to study the conduction mechanism of the conductive polymer in the restricted matrix. More interestingly, the possibility of interactions of the organic and inorganic components at the molecular level suggests that new or enhanced properties may result from their combination.

Up till now, only a few polypyrrole nanocomposite materials have been reported. Table 2.1 lists the conductive polymer/inorganic host nanocomposite materials that have been prepared. While Bein[13] was able to encapsulate polypyrrole in zeolite (three dimensional structure), Kanatzidis[8, 9, 10] and Giannelis[11] both used 2-dimensional layered materials, clay and transition metal oxide chlorides. In this chapter, we will report on the use of MoO_3 as an inorganic matrix to encapsulate polypyrrole by an unprecedented method.

Table 2.1 PPY/Inorganic Host Nanocomposites

Host	Nanocomposite	Conductivity $(\Omega\ cm)^{-1}$	Reference
FeOCl	$(C_4H_3N)_{0.34}FeOCl$	~1	8
Fluorohectorite	$(C_4H_3N)_{2.3}Cu_{0.8}(Mg_{4.4}Li_{1.6})[Si]_8)_{20}2.5H_2O$	0.01	11
Zeolite (Y)	$Cu_{15}Na_{26}Y(PPY)_{50}$	$< 10^{-9}$	13
Mordenite (M)	$Cu_{2.5}Na_3\ M(PPY)_{0.75}$	$< 10^{-9}$	13

The use of MoO_3 as a host is suggested for the following two reasons. First, the versatility of MoO_3 as a host for intercalation chemistry is well known. MoO_3 has an extended layered structure. The anisotropic bonding in different directions makes it an ideal candidate for intercalation chemistry.[14, 15, 16, 17, 18, 19] Second, many transition metal oxides are of great interest for electrochemical and catalytic applications.[20, 21, 22] Since high energy density is of primary importance for the practical application of materials as cathodes in secondary lithium batteries, the transition metal oxides are attracting more attention.[21, 22, 23] Molybdenum oxides, with molybdenum in its +6 oxidation state, are expected to be ideal candidates for cathodes in high energy density secondary lithium batteries.[24, 25] The low conductivity of molybdenum oxide and its non- conducting property in its highest oxidation state, however, restricts its application as the cathode

material in secondary lithium batteries. The conductive property of MoO_3 can be modified and greatly enhanced by inserting or intercalating species to form the layered molybdenum oxide bronzes. These bronzes can be classified into two groups: a group of hydrogen insertion compounds H_xMoO_3, $0.23 < x < 0.20$ (hydrogen bronzes) and another group of hydrated-ion intercalation compounds $A_x(H_2O)_yMoO_3$. A = H^+, Li^+, Na^+, K^+, Rb^+, Cs^+, Mg^{2+}, Ca^{2+}, Sr^{2+}, Ba^{2+} (hydrated bronzes).[26] Generally, they all have good electronic conductivity. However, some of them (hydrogen bronzes) are difficult to topotactic intercalate wwith lithium ion in applications such as rechargeable secondary lithium batteries due to the layered sheets being held strongly by the interaction of the sheets with hydrogen or hydrated cations. Some of them may also have a very low ionic conductivity due to the strong interaction between layered molybdenum oxide and intercalated hydrated cations, which limits their use as cathode materials in secondary lithium batteries.[22]

We tried to insert electronically-conductive polymers and ionically-conductive polymers into molybdenum oxides using the intercalation method to prepare the polymer/MoO_3 nanocomposites. By incorporating the electronically-conductive polymer into molybdenum oxide, we expected to improve and enhance the electronic conductivity of molybdenum oxide by mutual interaction and also to improve the ionic conductivity due to the pillar effect of the polymer. We expected, therefore, to improve the performance of molybdenum oxide as cathode material in secondary lithium batteries. Since the structure of polypyrrole would be modified by the inorganic lattice, different interactions between polymer and host/donor may result in mutually enhanced conducting properties.

In the following sections, we will report on the preparation of PPY/MoO_3 nanocomposite material using an unprecedented method, its characterization with powder XRD, FTIR, and thermal analysis, and studies of its electrical conductivity.

2.2 Experimental

2.2.1 Synthesis

Materials: Pyrrole (A.R.) MoO_3, $Na_2S_2O_4$ and were supplied by Aldrich. Na_2MoO_4 was supplied by Alfa Ventron. $[Na^+(H_2O)_n]_{0.25}MoO_3^{-0.25}$ (n = 4,5) ("$NaMoO_3$") was prepared according to the method described by Thomas and McCarron.[16]

Preparation of $(PPY)_{0.5}MoO_3$ nanocomposite: 100 mg $NaMoO_3$ suspended in 100 mL H_2O in a 500 mL Erlenmeyer flasks was sonicated in an ultrasonic bath for 30 minutes to promote swelling of the oxide layers and to decrease the particle size of $NaMoO_3$. 2 mL pyrrole and 80 mL butanol were added into the suspension. The mixture was stirred vigorously. 25 mg $FeCl_3$ in 15 mL H_2O were added to the above solution. The solution was stirred vigorously at room temperature for 1 hour. The solution was filtered and thoroughly washed with water and butanol. The black product was dried in the air. Chemical and thermogravimetric analysis resulted the following formula of $(PPY)_{0.5}MoO_3$ for the product (Chemical analysis: Found (%), C, 13.86; H, 1.03; N, 4.06. Calculated (%), C, 13.55; H, 1.71; N, 3.95). Iron was found to be 0.53% from elemental analysis, and sodium was not analyzed.

2.2.2 Instrumentation

Powder x-ray diffraction patterns were measured on a Siemens D 500 diffractometer using CuK_α radiation. Infrared spectra were recorded on a Nicolet 520 Fourier transform infrared spectrometer from KBr pellets. Differential thermal analysis (DTA) and thermal gravimetric analysis (TGA) were run in an atmosphere of flowing air with a heating rate of 5°C/min on a PL thermal Science STA 1500 thermal analysis system. Conductivity was measured by the two-probe method in a vacuum chamber with a pressure lower than 10^{-4} Torr. Thin films of the sample $(PPY)_{0.5}MoO_3$ were prepared by casting the suspension on Corning 7059 glass substrates. Electrodes were affixed to the film using silver paint. The sample was then mounted in the vacuum chamber, and conductivity was measured under a voltage of 1 V.

2.3 Results and Discussion

2.3.1 Preparation of $(PPY)_{0.5}MoO_3$ nanocomposite

The methods of preparing the conductive polymer/inorganic layered host nanocomposite materials were discussed in Chapter one. We will first discuss the conditions for using these methods to prepare nanocomposites and then describe the new method to prepare the $(PPY)_{0.5}MoO_3$ nanocomposite.

Method I, as originally reported by Kanatzidis et al.,[8, 9, 10] is the *in situ* intercalative polymerization, in which monomers such as pyrrole, aniline and thiophene are concomitantly intercalated and oxidatively polymerized by host materials. In this so-called

intercalative oxidation polymerization reaction, the host acts as an oxidizing agent. Therefore the host material, in addition to being able to accommodate the guest polymer, should have a high enough oxidizing power to topotactiely polymerize the monomer. The method is limited to only certain types of host materials possessing moderate oxidizing power. FeOCl and V_2O_5 have been used successfully for this application. The method has been modified recently and has been extended to include zeolites and clay materials[1] by Bein and Enzyl[13, 28, 29] and Mehrotra and Giannelis.[11, 27] Cations such as Fe^{3+} and Cu^{2+} were introduced into the nonoxidative zeolite and clay materials as oxidants by ion exchange. Pyrrole and aniline can be polymerized by these ion-exchanged zeolites and clays to form conducting polymer/inorganic host nanocomposite materials. In this modified method I, the oxidant is not the rigid host itself but is rather the mobile guest cations.

Method II involves step intercalation and polymerization of monomers in the host materials illustrated below for the preparation of polyaniline/α-HUO_2PO_4:[30]

aniline + α-HUO_2PO_4 → aniline/α-HUO_2PO_4 → polyaniline/α-HUO_2PO_4

The intermediate product -- monomer intercalated compound (e.g., aniline/α-HUO_2PO_4) -- is stable and can be isolated. To convert the monomer located between the inorganic lattice to polymer, an external oxidant such as oxygen or $FeCl_3$ is required. In this method, the host does not act as an oxidant. The host helps to bring together and arrange the monomers to be polymerized within the layers. So far, this method has only been successful in preparing polyaniline nanocomposite materials.

In Method III. polymers are inserted directly into the host by ion exchange or a coordination reaction. It usually requires the polymers to be water soluble and the host materials to have exchangeable ion species.

Since polypyrrole does not dissolve well in water, we cannot use Method III to prepare the PPY/MoO_3 nanocomposite material. For Method I to be successful, as indicated above, the inorganic host should possess a high enough potential to oxidatively polymerize pyrrole. MoO_3 is not a good oxidant and therefore Method I cannot be used. Method II requires intercalating pyrrole in MoO_3 before the monomer is polymerized. However the intercalation of non-donor organics into MoO_3 is very difficult. Schollhorn reported that the kinetics of the intercalation process of MoO_3 with an organic base depends upon the basicity of the Lewis base. By thermal reaction of the organics with MoO_3, low pK_b compounds such as tetradecylamine (pK_b = 3.13) were intercalated relatively easily, however, the reaction of pyridine (pK_b = 8.75) with MoO_3 was fairly slow (reported conditions were 180^{o}C for 30 days). Since pyrrole is a much weaker base (pK_b = 13.61),[31] it is difficult to intercalate it into MoO_3 and then to polymerize it as in Method II.

A new method was sought to prepare the PPY/MoO_3 nanocomposite: the Na^+ /Li^+ intercalation compound of MoO_3 was employed as the starting material. The major feature of this new route is the use of the hydrated sodium cation intercalation compound of MoO_3, which can be easily swelled in solvents, and the use of an external oxidant, $FeCl_3$. The introduction of the hydrated sodium cation as the intercalate in MoO_3 facilitates the swelling of MoO_3 host sheets such that they can host the polymer; the use of an external

oxidant, in this case, resulted in a novel route for preparing electronically conductive polymer/inorganic layered host nanocomposite materials; this extends the range of usable inorganic hosts.

$NaMoO_3$ was prepared according to the method described by Thomas and McCarron[16]. It is known that there are two phases for the bronzes. One is the fully hydrated phase and the other is the partially dehydrated phase. They have the d-spacings of 11.4 and 9.7 Å corresponding to bilayer-water and monolayer-water hydrated cations respectively between the layers. The swelling of the MoO_3 sheets is dependent on the degree of hydration of the cation. The degree of this kind of swelling affects the encapsulation of polymer by the host. We used wet $NaMoO_3$ which was kept under a nitrogen atmosphere of 90% moisture. Under this condition, the $NaMoO_3$ contains bilayer-water phases and expands much more easily than the monolayer-water $NaMoO_3$ phase.

It should be pointed out that we cannot introduce oxidants such as Fe^{3+} and Cu^{2+} as pseudo internal oxidants into the sodium molybdenum bronze by ion exchange to intercalatively polymerize pyrrole because the sodium molybdenum bronze is unstable towards these oxidants. Although $NaMoO_3$ is a good ion exchanger, and can be exchanged with many ions such as H^+, Li^+, Na^+, K^+, Rb^+, Cs^+, Mg^{2+}, Ca^{2+}, Sr^{2+}, Ba^{2+}, Co^{2+}, Ni^{2+}, and La^{3+}, etc., it is not stable in the Fe^{3+} and Cu^{2+} solution. Upon adding the Fe^{3+} or Cu^{2+} solution into the $NaMoO_3$ suspension, the suspension is bleached. The dark blue color is rendered colorless, due to the sodium molybdenum bronzes being oxidatively converted into MoO_3. Therefore the following experiment was conducted. Before adding

Fe^{3+} solution, we added the pyrrole into the $NaMoO_3$ suspension; the product will be the compatible reaction of $NaMoO_3$ and pyrrole with Fe^{3+}. The solution was bleached again, and there was no reaction between Fe^{3+} and pyrrole. We rationalized it as a result of the poor contact between inorganic Fe^{3+} and organic pyrrole in water. To enhance the reaction between Fe^{3+} and pyrrole over $NaMoO_3$, a polar organic solvent was introduced into the reaction system. Butanol was added into the solution before the addition of the oxidant $FeCl_3$. The butanol acted as a phase transfer catalyst. It is not clear what function the $NaMoO_3$ had in this reaction, besides acting as a host. Many other organic solvents such as methanol, ethanol, propanol, tetrahydrofuran and chloroform were tried. The reaction occurred in the presence of all the above solvents except chloroform, suggesting that the degree of miscibility of the solvents with water plays a key role in the reaction.

This reaction represents a new method of preparing electronically conductive polymer/inorganic layered host nanocomposite materials. Intercalation and polymerization occur simultaneously. But it differs from Method I where the oxidant is the host itself or a pseudo internal oxidant is used. In our case an external oxidant was used and the host $NaMoO_3$ is not an oxidant at all. Using this method, polyaniline/MoO_3 nanocomposite was also prepared and characterized with XRD, FTIR, and thermal analysis. The mechanism of the reaction will be discussed later.

2.3.2 XRD

The layered structure of MoO_3 is shown in Figure 2.1. The overall structure of MoO_3 is a stack of two-dimensional infinite $(MoO_3)_\infty$ sheets with the terminal oxygen atoms of the MoO_6 octahedra pointing towards the space between the MoO_6 octahedra of

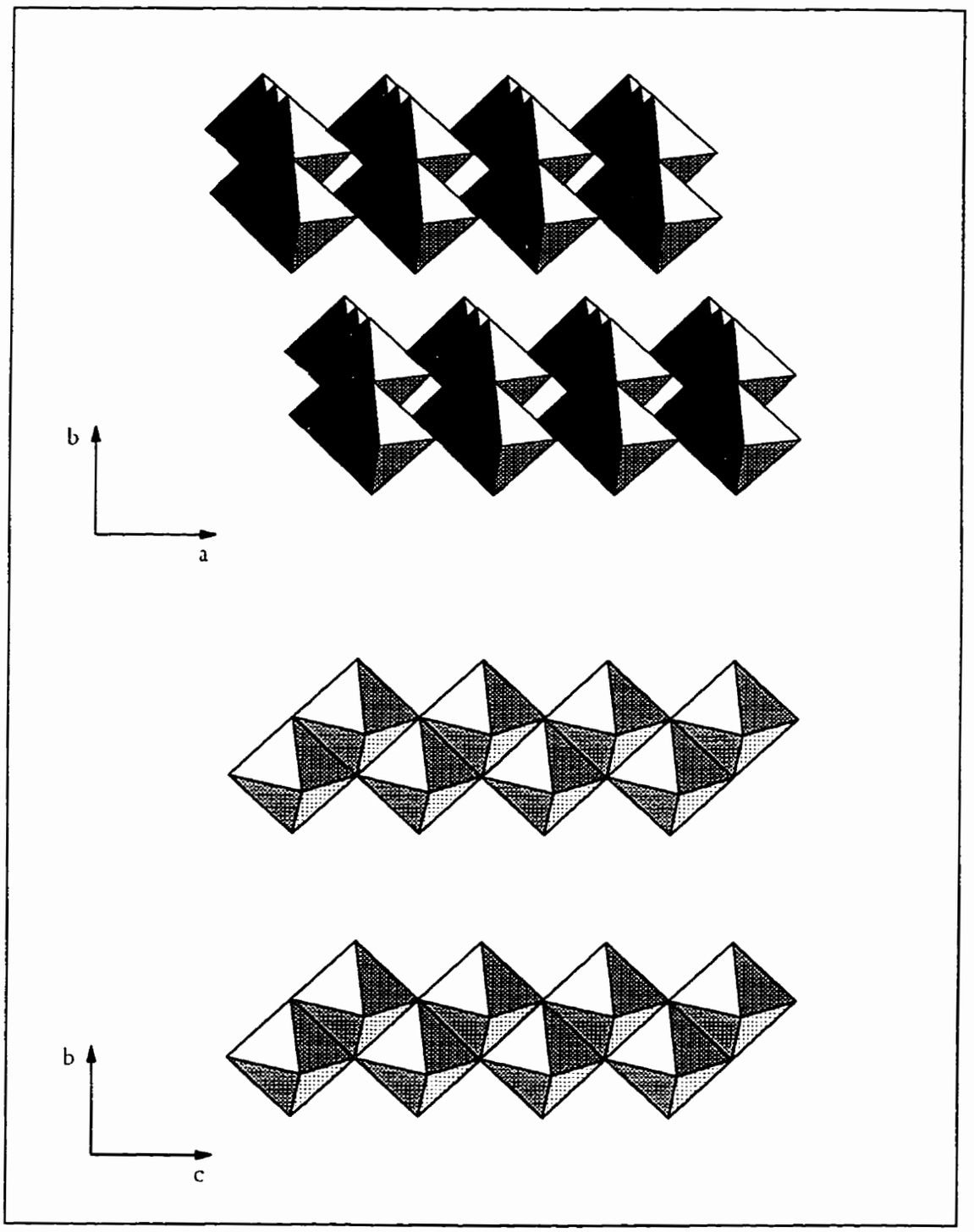

Figure 2.1 Overview of layered structure of MoO_3

the neighboring layers.[19, 32] Since there are different terminal and bridging oxygen atoms in each octahedra, the MoO_6 octahedra is far from ideal. Within the layers, molybdenum is connected by strong chemical bonding. Along the c axis, neighbouring molybdenum atoms are linked with two bridging oxygen atoms (edge sharing) while along the a axis, neighbouring molybdenum atoms are linked by one bridging oxygen atom (corner sharing). Between layers, there exists only weak van der Waals interactions. The anisotropic interaction within MoO_3 makes it an ideal host for intercalation reactions.

To prepare the $(PPY)_{0.5}MoO_3$ nanocomposite, we first converted MoO_3 into hydrated sodium cation molybdenum bronze by an intercalation reaction. Upon intercalation of MoO_3 with the hydrated sodium cation, there was little change within the individual sheet while the d-spacing between layers (along the b axis)increased.[15, 16, 33, 34] For the fully hydrated sodium cation intercalated molybdenum oxide bronze, the d-spacing increased from 6.9 Å in MoO_3 to 11.2 Å in the bronze. The 4.3 Å expansion is consistent with the Stoke's radius of the hydrated sodium cation. Therefore the change of the d-spacing of layered compounds provides solid evidence of the intercalation and the measurement of the dimension of the guest species.

Figure 2.2 shows the XRD patterns of $(PPY)_{0.5}MoO_3$ and $NaMoO_3$. Upon encapsulation of PPY in MoO_3, the d-spacing increased to 13.9 Å. The observed 13.9-11.2 = 2.7 Å new layer expansion represents the removal of the hydrated sodium layer from the interlamellar space followed by the insertion of a monolayer of polypyrrole. Therefore the actual gallery height is 7 Å in $(PPY)_{0.5}MoO_3$. The increase in d-spacing depends mainly on the dimension and the orientation of the guest species and also on the site of the guest species in the interlamellar gap and the interaction forces between the

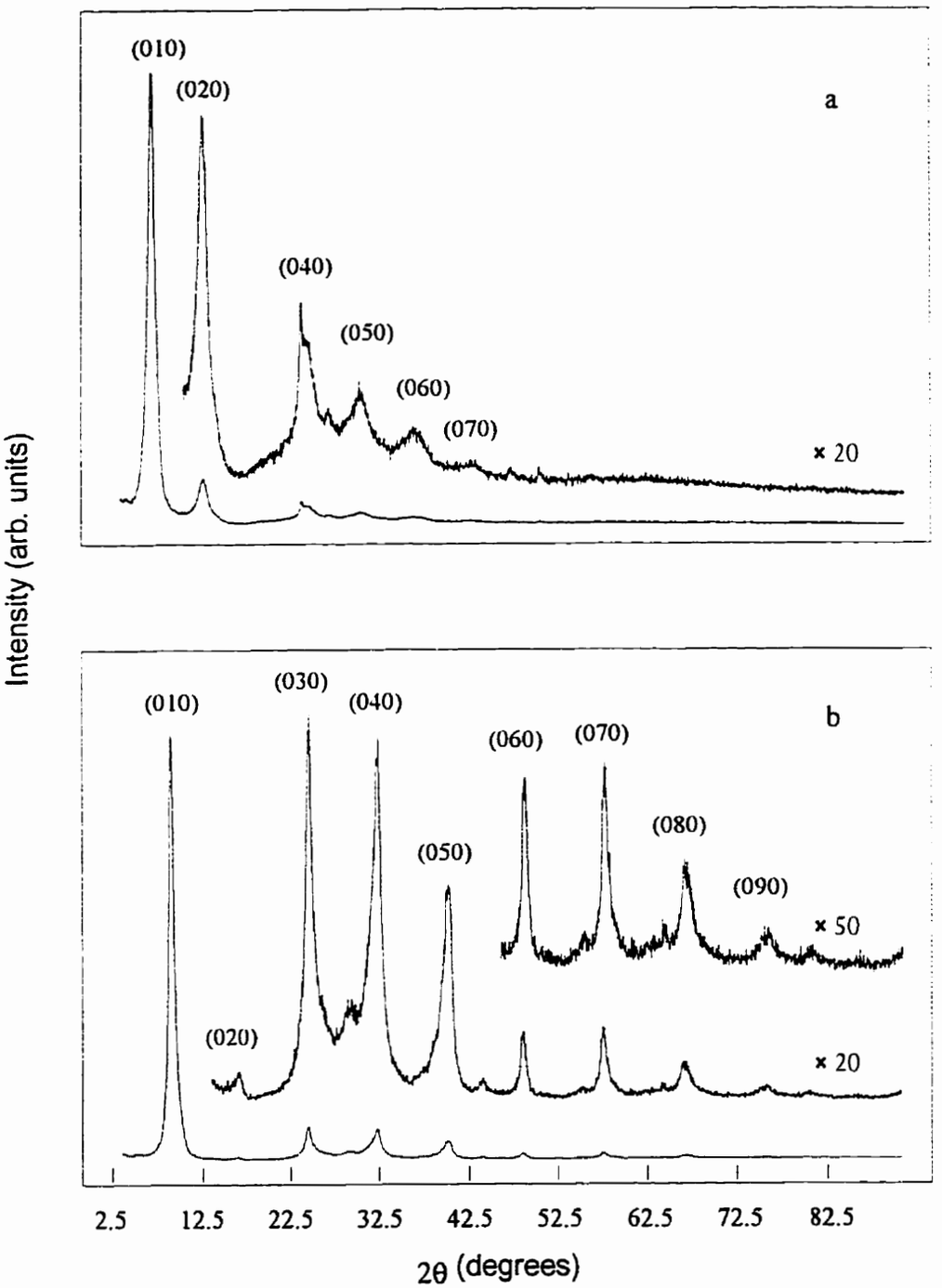

Figure 2.2 **Powder XRD pattern of oriented films of (a) $(PPY)_{0.5}MoO_3$ and (b) $[Na(H_2O)_2]_{0.25}MoO_3$**

host layer and the guest species. For the nanocomposite formed by the intercalation of a monolayer polypyrrole with the aromatic ring perpendicular to the layers, the d-spacings of 4.55 Å to 5.23 Å have been reported.[8, 9, 10, 11] Our value, 7 Å, is larger than the reported value. It supports the encapsulation of polypyrrole in MoO_3. In the XRD pattern, up to 7 harmonics of diffraction from the orientated film can be determined, which suggests that the nanocomposite material retains the crystalline structure of the starting material MoO_3. The larger gallery height could be due in part to the shift of the MoO_3 layer so that the terminal oxygen atoms of the MoO_6 octahedra of adjacent layers point towards each other, as opposed to the MoO_3 where they point towards the space between the MoO_6 octahedra of the neighbouring layers.[18] The shift is possible as it better accommodates the polymer chains in the valley of the layers.

The larger d-spacing of $(PPY)_{0.5}MoO_3$ can be more clearly understood by observing the spatial relationship between the host and guest. It is generally accepted that the polypyrrole is $\alpha\alpha'$ bond-linked. Upon formation of the dimer or trimer, there is a small change in the bond length and bond angle in the pyrrole unit. We take the dimension of the central pyrrole ring of the trimer as the best model for the polypyrrole, and assume that the polypyrrole chain is more linear in the $(PPY)_{0.5}MoO_3$ nanocomposite than in the free polypyrrole. Thus the dimension for the polypyrrole in the nanocomposites is shown in Figure 2.3

The repeat unit length of polypyrrole is 3.73 Å. This value is very close to that of the c axis of MoO_3 (c = 3.696 Å). This leads us to suggest that the polypyrrole in the nanocomposites lines up in the c-direction in the following model (Figure 2.4).

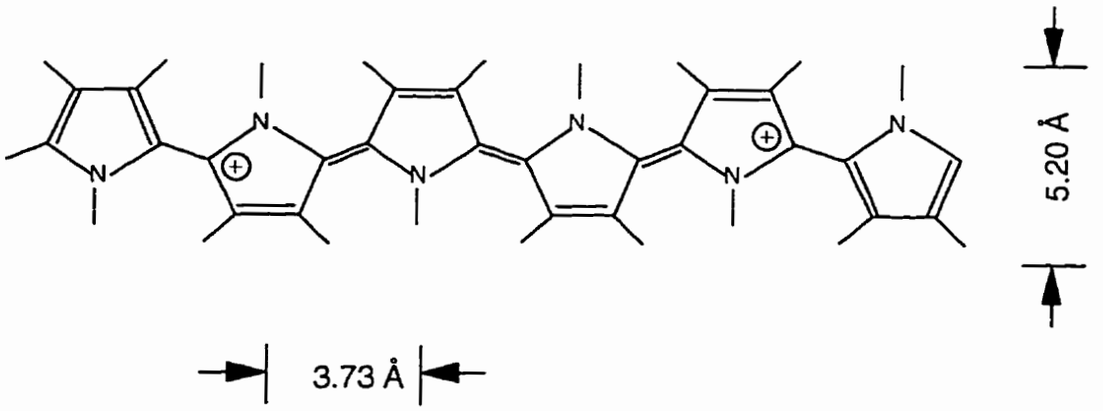

Figure 2.3 Structure of PPY

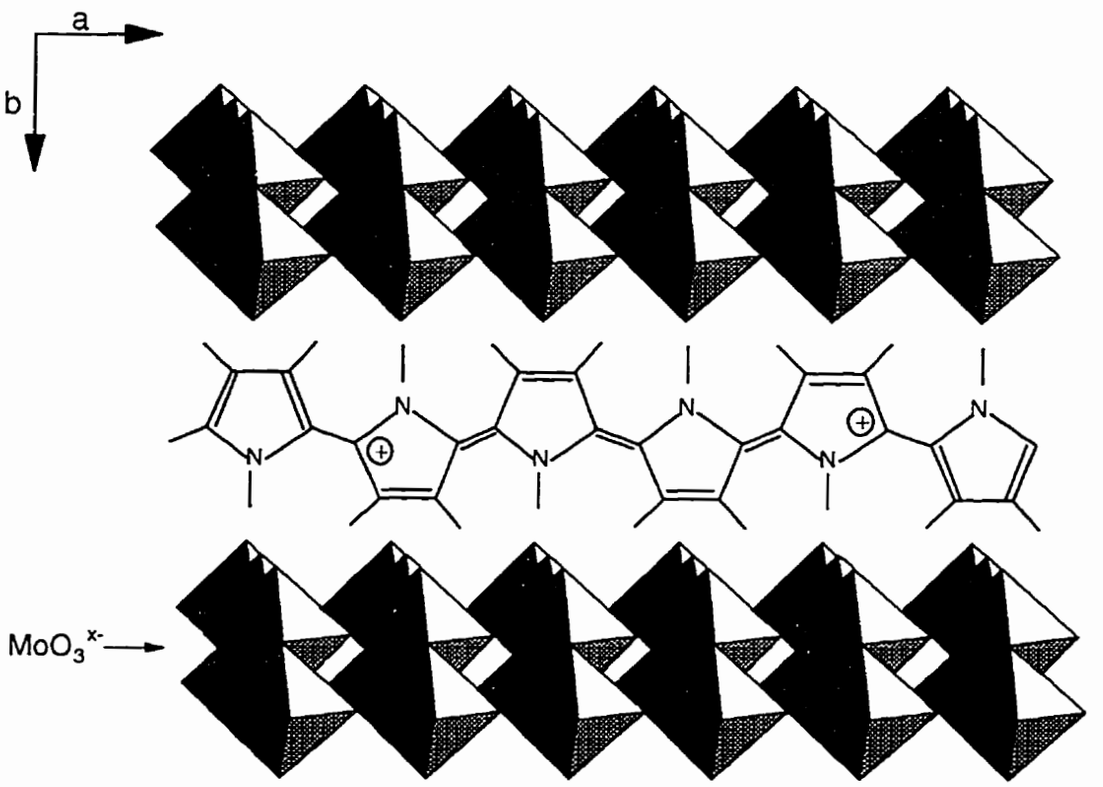

Figure 2.4 Conformation of $(PPY)_{0.5}MoO_3$

In this model, every molybdenum unit in the c-direction can accommodate one pyrrole unit. Since every unit of MoO_3 along the c axis in each layer contains two molybdenum atoms and if we suggest the polypyrrole chain lines up in c direction in every a unit distance (3.96 Å), then the theoretical formula for the nanocomposite will be pyrrole: MoO_3 = 1:2. It is very close to the stoichiometric amount obtained from elemental analysis and thermal gravimetric analysis. The above model is plausible it maximizes hydrogen bonding between the guest polypyrrole and the layered host. The oxygen atom in MoO_3 which is pointing directly towards the layer involes a terminal double bond and so is electron-rich. It would be reasonable to assume that hydrogen bonding occurs between the terminal oxygen and N--H of pyrrole. To form the hydrogen bonds between every pyrrole unit and the molybdenum terminal oxygen, the only modification required for the prinstal MoO_3 structure is the shift of the neighbouring MoO_3 sheet every c/2 along the c direction. This kind of shift has been reported for the formation of $Al_{13}MoO_3$, and PPY/FeOCl nanocomposite materials.[8, 9, 10, 18] To minimize the electrical repulsion between the chains of polypyrrole and to maximize the formation of hydrogen bonding between polypyrrole and MoO_3, the polypyrrole chain sits apart every a units along the a direction. The model structure, emphasizing the hydrogen bonding interaction is shown below (Figure 2.5).

From this model, we can further look at the d-spacing of $(PPY)_{0.5}MoO_3$. The repeat distance between layers in MoO_3 is 13.855/2 = 6.927 Å., which consists of both the double octahedral layer thickness of the MoO_3 sheet and the van der Waals gap between the layers. In the $(PPY)_{0.5}MoO_3$ nanocomposite, the d-spacing represents the thickness of

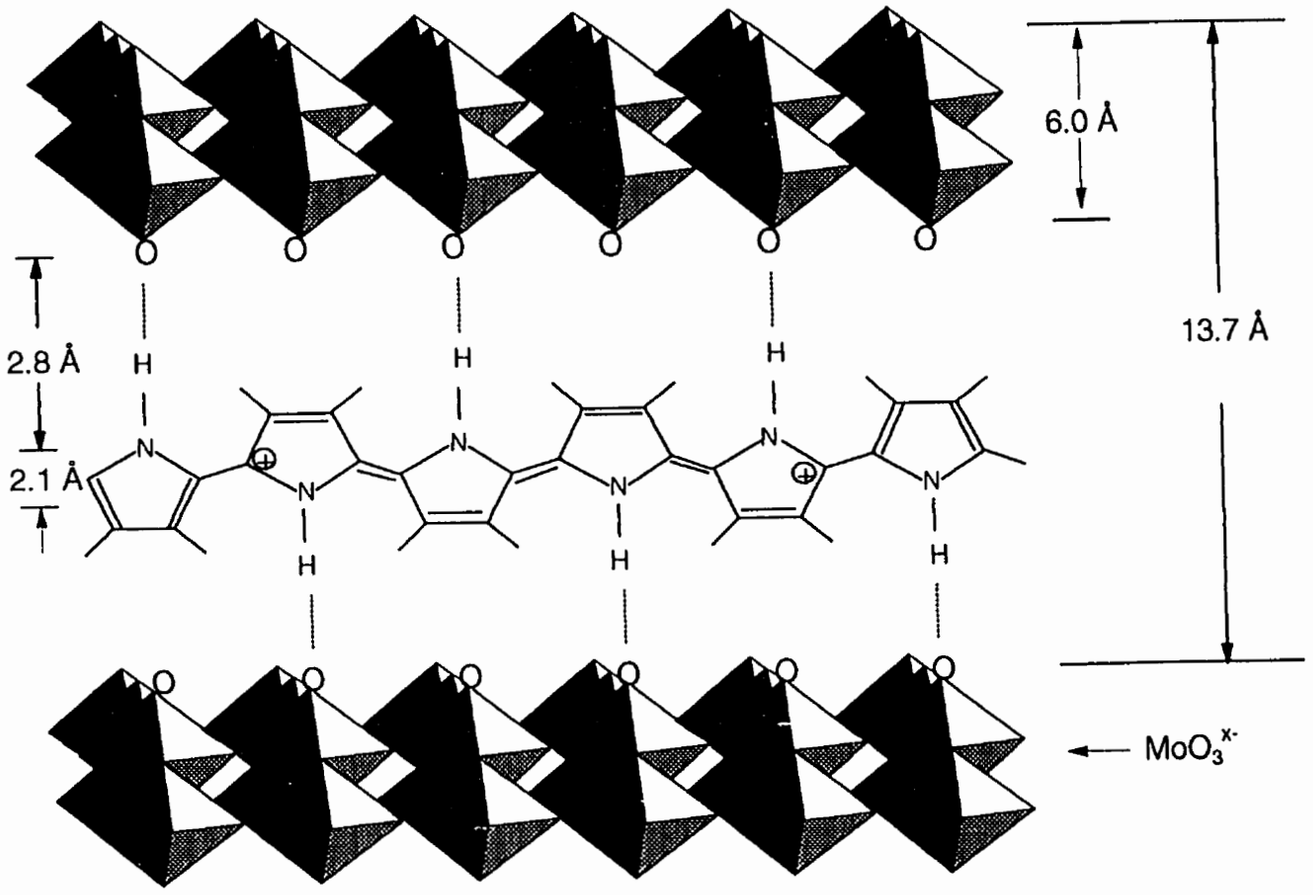

Figure 2.5 **Model for $(PPY)_{0.5}MoO_3$ emphasizing the hydrogen bonding and the calculated d-spacing**

the double octahedral MoO_3 sheet, the dimension of the polypyrrole and the replacement of the van der Waals gap by two hydrogen bonds between the pyrrole nitrogen hydrogen and the terminal oxygen of the MoO_3 sheet. By simple calculation from the crystal structure of MoO_3,[32] the real double octahedral layer thickness between two opposite terminal oxygens of the same layer is 6.03 Å; the height of the pyrrole ring is 2.1 Å; [1, 35] and the N--H--O is taken as 2.8 Å (Figure 2.5).[36] The d-spacing of the nanocomposite therefore equals the thickness of double chain molybdenum oxide + height of polypyrrole ring + 2 × (N -- H -- O) = 6.0 + 2.1 + 2 × 2.8 = 13.7 Å. The d-spacing found by XRD is 13.9 Å. It is obvious there is a reasonable match between the experimental data and our suggested model. It also explains the larger expansion between the layers than that of PPY/FeOCl. Among others, it is the replacement of the van der Waals gap (0.9 Å) by two hydrogen bonds (2 × 1.5 = 3.0 Å) which contributes largely to the larger d expansion in $(PPY)_{0.5}MoO_3$ than the summation of the dimension of PPY and MoO_3 sheet.

2.3.3 FTIR spectroscopy

Figure 2.6 shows the IR spectra of $NaMoO_3$, polypyrrole, and $(PPY)_{0.5}MoO_3$. The corresponding peaks are listed in Table 2.2. All main peaks for the chemically prepared polypyrrole were observed in the $(PPY)_{0.5}MoO_3$ nanocomposite. The spectra of polypyrrole and $(PPY)_{0.5}MoO_3$ both show a featureless increase in transmission from 4000 to 1700 cm^{-1}, which is generally suggested as the tail of the – 1 ev peak for conductive polypyrrole.[1] The ν(NH) and ν(CH) stretch bands are therefore not observable in the conducting polypyrrole, because they are masked by the tail of the – 1 ev peak.[37] This suggests that the polypyrrole formed in the nanocomposite material is in its conducting

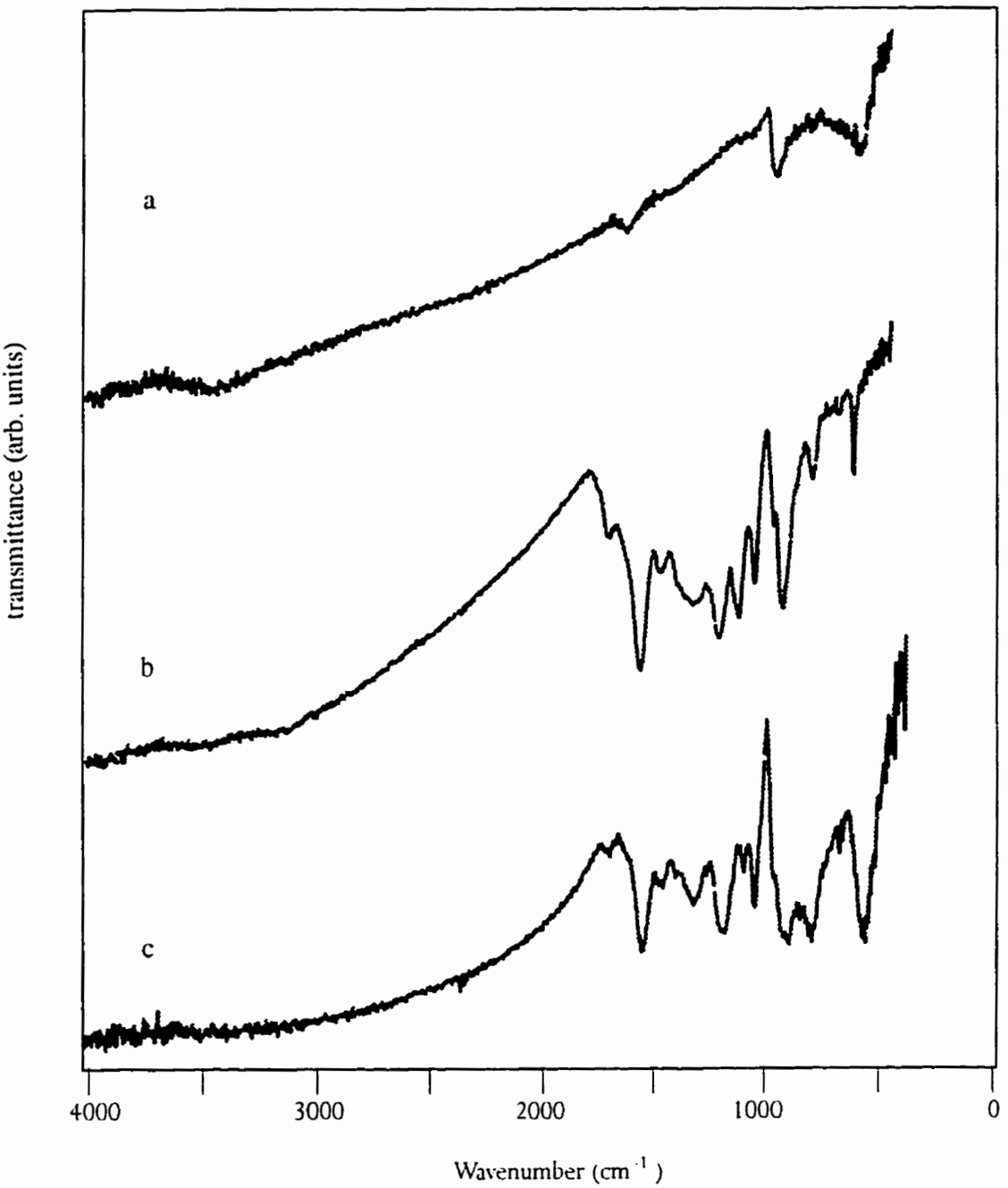

Figure 2.6 **FTIR spectra of (a) $[Na(H_2O)_2]_{0.25}MoO_3$; (b) PPY and (c) $(PPY)_{0.5}MoO_3$**

Table 2.2 FTIR data for $(PPY)_{0.5}MoO_3$, PPY, MoO_3, and $NaMoO_3$

$(PPY)_{0.5}MoO_3$	PPY	MoO_3	$NaMoO_3$
1700 (vw)	1706 (w)		
1551(s)	1565(s)		
1465(w)	1473(w)		
1320(m)	1321(m)		
1189(s)	1207(s)		
	1124(s)		
1098(s)			
1049(s)	1054(s)		
		990(s)	
969(s)			960(s)
920(s)	926(s)		
		851(s)	
800(s)	798(m)		
	682(w)		
	619(s)		
585(s)		548(s)	560(s)

form. The region from 1600 to 400 cm^{-1} contains the pyrrole ring vibrations. The IR patterns in this region are very similar in the chemically prepared polypyrrole and $(PPY)_{0.5}MoO_3$, however the positions of the peaks are not identical. This has also been

observed for other polypyrrole nanocomposites by Bein and Kanatzidis.[8, 9, 10, 13, 38] The information hinted at by these kinds of peak shifts in polypyrrole has not been fully interpreted for polypyrrole. This represents one of the difficulties in studying the structure and property relationships for conducting polymers. Further theoretical studies in better ordered polymers obtained in nanocomposite materials are highly desired. In the region from 1000 cm^{-1} to 400 cm^{-1}, two strong bands at 960 cm^{-1} and 583 cm^{-1} in the $(PPY)_{0.5}MoO_3$ nanocomposite were observed; these are the characteristic bands of the sodium molybdenum bronze. This suggests that the structure of the molybdenum oxide sheet in the sodium molybdenum bronze is mainly retained. The broad peak around 850 cm^{-1} of MoO_3 is not observed. This is the critical difference between the sodium molybdenum bronze and MoO_3 and suggests that the oxidation of $NaMoO_3$ by Fe^{3+} during the formation of PPY/MoO_3 nanocomposite material is negligible. On the other hand, the broad peak around 800 cm^{-1} of the nanocomposite material may be partially due to the partial oxidation of the bronze.

It is worthwhile to note here that the IR peak of polypyrrole and $(PPY)_{0.5}MoO_3$ nanocomposite are relatively sharp, compared to those of many other conducting polymers. This is believed to be due to the non-degenerate ground state of polypyrrole, which prevents polypyrrole from ever becoming metallic, even at the highest achievable doping levels.

2.3.4 Thermal Analysis

The TGA and DTA traces for $NaMoO_3$, PPY, and PPY/MoO_3 in Figure 2.7 show two major weight losses for $NaMoO_3$. The first weight loss ends at a temperature of about

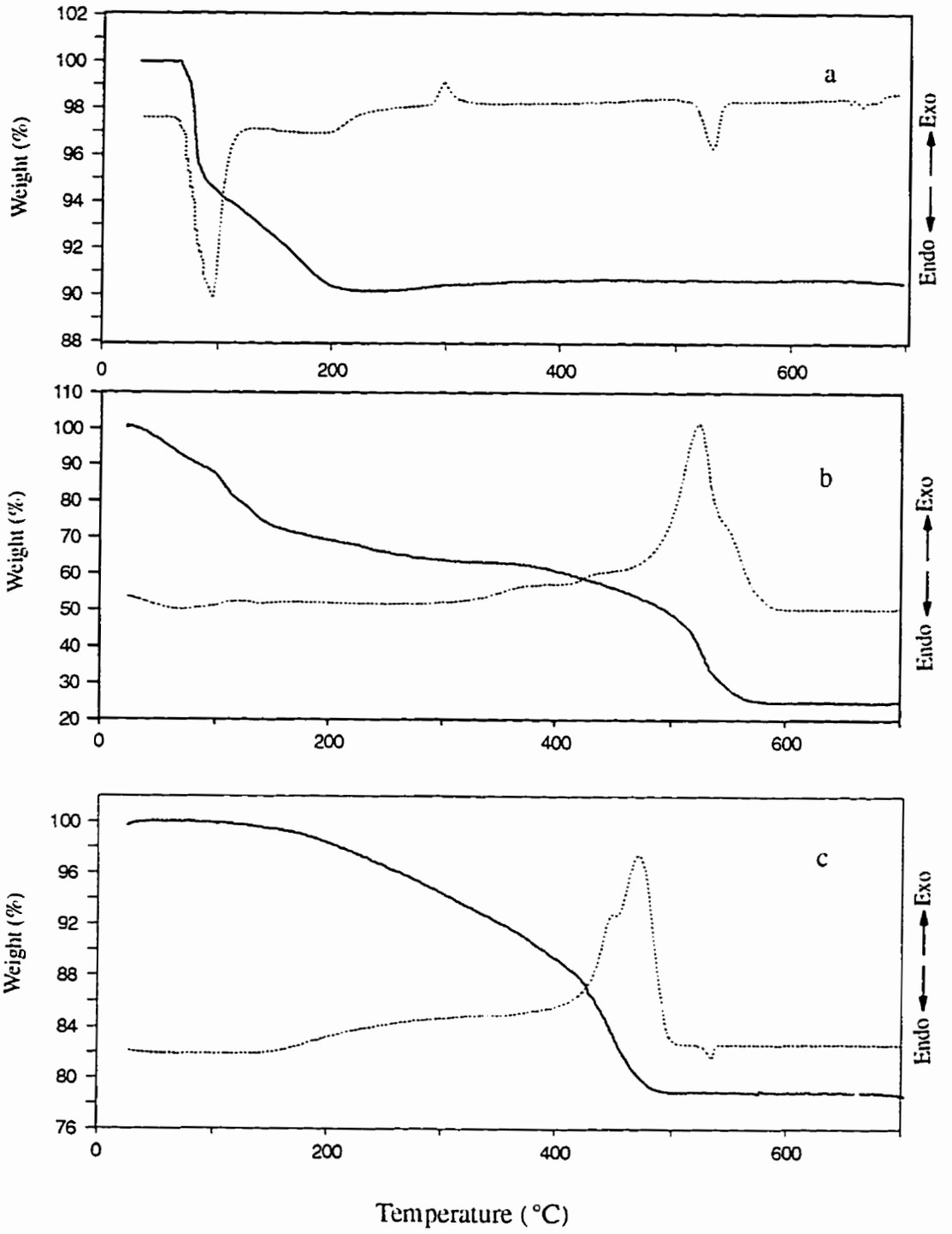

Figure 2.7 Simultaneous TG-DTA traces for (a) $[Na(H_2O)_2]_{0.25}MoO_3$; (b) PPY and (c) $(PPY)_{0.5}MoO_3$

80°C. The second weight loss ends before 200°C. These weight loss levels are consistent with the two layer water model for the sodium molybdenum bronze. The weight percent is similar for both weight losses, which suggests that one layer of water was lost before the second layer. The difference in the temperature for the weight loss, however, does not mean the interactions for the two water layers with the sodium cation in the bilayer phase of the bronze are different. Conversely, it means that the difference lies in the stability of the bilayer water phase vs. the monolayer water phase, as is evidenced by the fact that the bilayer water phase easily loses water when placed under vacuum or even when standing in the air for a couple of days.

There is hardly any weight loss before 200°C for the $(PPY)_{0.5}MoO_3$ nanocomposite material. Comparison of the TGA and DTA curves of $(PPY)_{0.5}MoO_3$ with those of $NaMoO_3$ suggests that there are no hydrated sodium cations in the nanocomposite material. The major weight loss was observed at about 450°C for the nanocomposite material, which corresponds with the loss of polypyrrole. The gradual weight loss between 200°C and 400°C suggests that low molecular weight pyrrole oligomer was also formed during the reaction. This weight loss is also observable in the chemically prepared free polypyrrole.[39] The weight loss corresponding to PPY found from TGA (Figure 2.7 c) between 200°C and 500°C is about 19%, corresponds well with 18.4% required for $(PPY)_{0.5}MoO_3$. Careful comparison of the TGA and DTA curves of PPY and $(PPY)_{0.5}MoO_3$ indicates that there is a temperature shift (ΔT = 50°C) for the major weight loss of two samples in the temperature range of 450°C and 550°C. The polypyrrole in the nanocomposite is thermally not as stable as that of free polymer, in

contrast to that observed for the polypyrrole/silicate nanocomposite. This difference reflects the effect of MoO_3 on the thermal stability of polypyrrole. The thermal destabilization of polypyrrole is not due to the incorporation of the polypyrrole into the rigid inorganic lattice, but probably to the catalytic properties of MoO_3. It may also reflect the lack of cross linkage between polypyrrole chains in the nanocomposite material, due to the restricted space between MoO_3 sheets..

2.3.5 Conductivity

The temperature dependence of conductivity of the $(PPY)_{0.5}MoO_3$ nanocomposite as prepared and after being treated at 200°C and 250°C for 3 hours under nitrogen are presented in Figure 2.8. The conductivity data were plotted against $1/T$, $1/T^{(1/2)}$, $1/T^{(1/3)}$, and $1/T^{(1/4)}$, respectively. The shape of the line is similar to that of conductive polypyrrole,[8, 9, 10] which suggests that the polypyrrole formed in the $(PPY)_{0.5}MoO_3$ nanocomposite material is in its conductive form. Upon heating the nanocomposite material at 200°C under nitrogen for 3 hours, a great increase in the conductivity of the nanocomposite material was observed. However the conductivity of that heated at 250°C under nitrogen for three hours is slightly lower than that heated at 200°C. Although in most cases annealing of conductive polymers in the air, especially in wet air, results in the loss of conductivity of the polymer, there are several examples where conductivity is stable or is increased upon annealing up to a temperature of 200°C for polypyrrole.[2, 40, 41, 42, 43, 44] If annealing takes place in an inert atmosphere such as argon and nitrogen, in most cases the conductivity increases or remains unchanged. It is also worth noting that even for annealing conducted in wet air, a notable conductivity loss was only observed after several

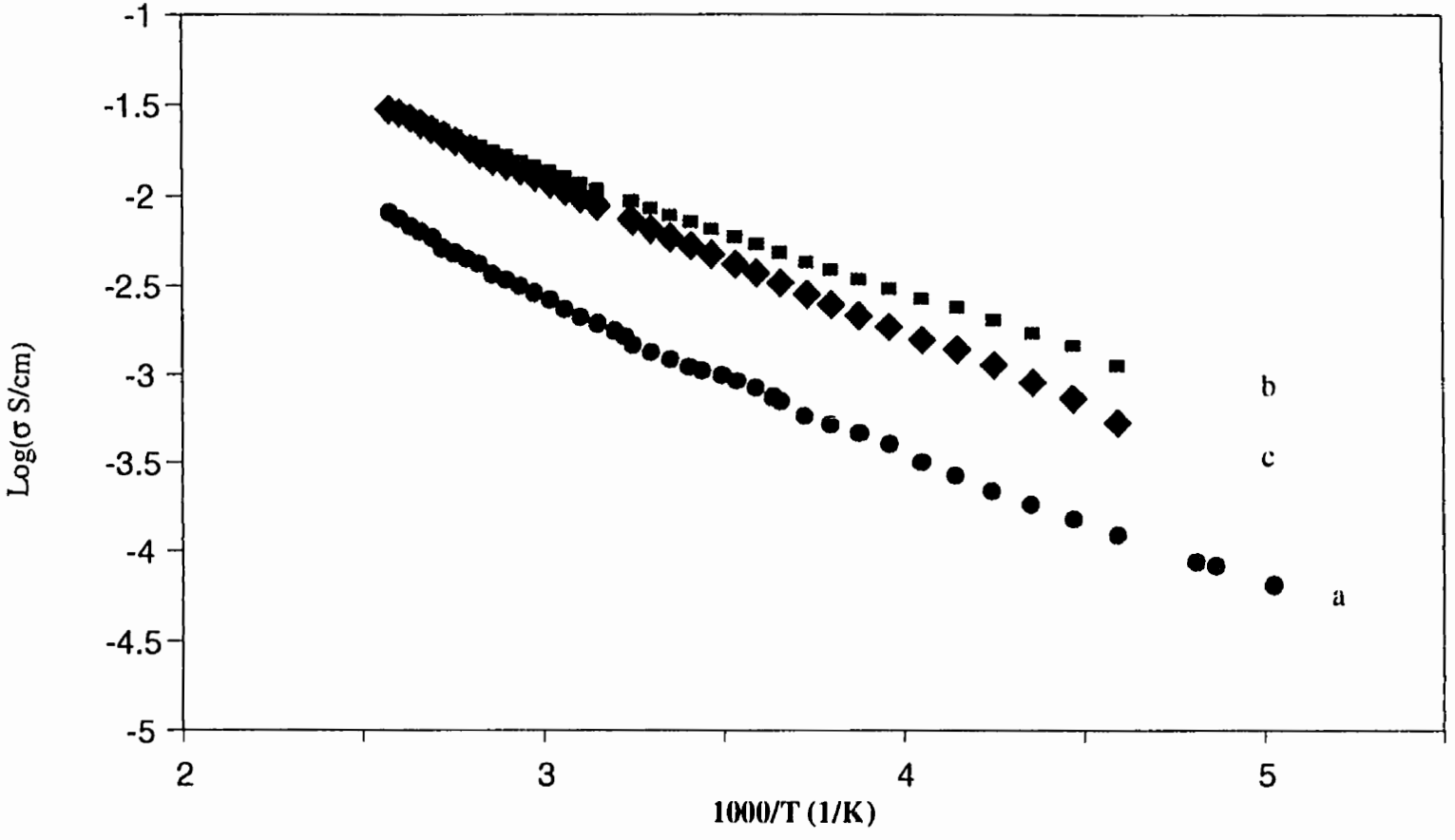

Figure 2.8 Two-probe variable temperature electrical conductivity data for thin films (glass substrate) of $(PPY)_{0.5}MoO_3$. (a) as prepared; (b) heated under N_2 at 200°C for 3 hours; (c) heated under N_2 at 250°C for 3 hours (continued)

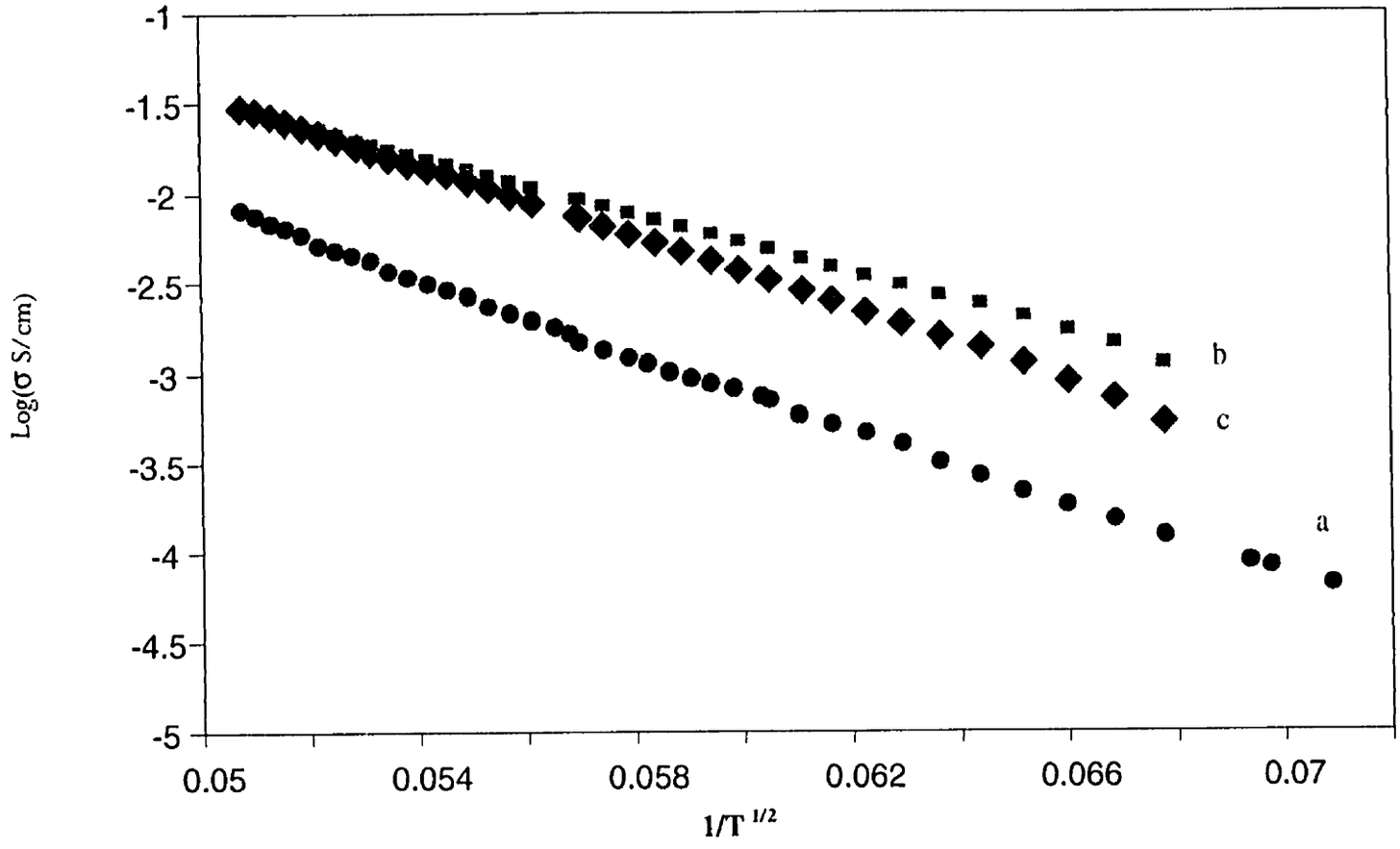

Figure 2.8 (continued) Two-probe variable temperature electrical conductivity data for thin films (glass substrate) of $(PPY)_{0.5}MoO_3$. (a) as prepared; (b) heated under N_2 at 200°C for 3 hours; (c) heated under N_2 at 250°C for 3 hours

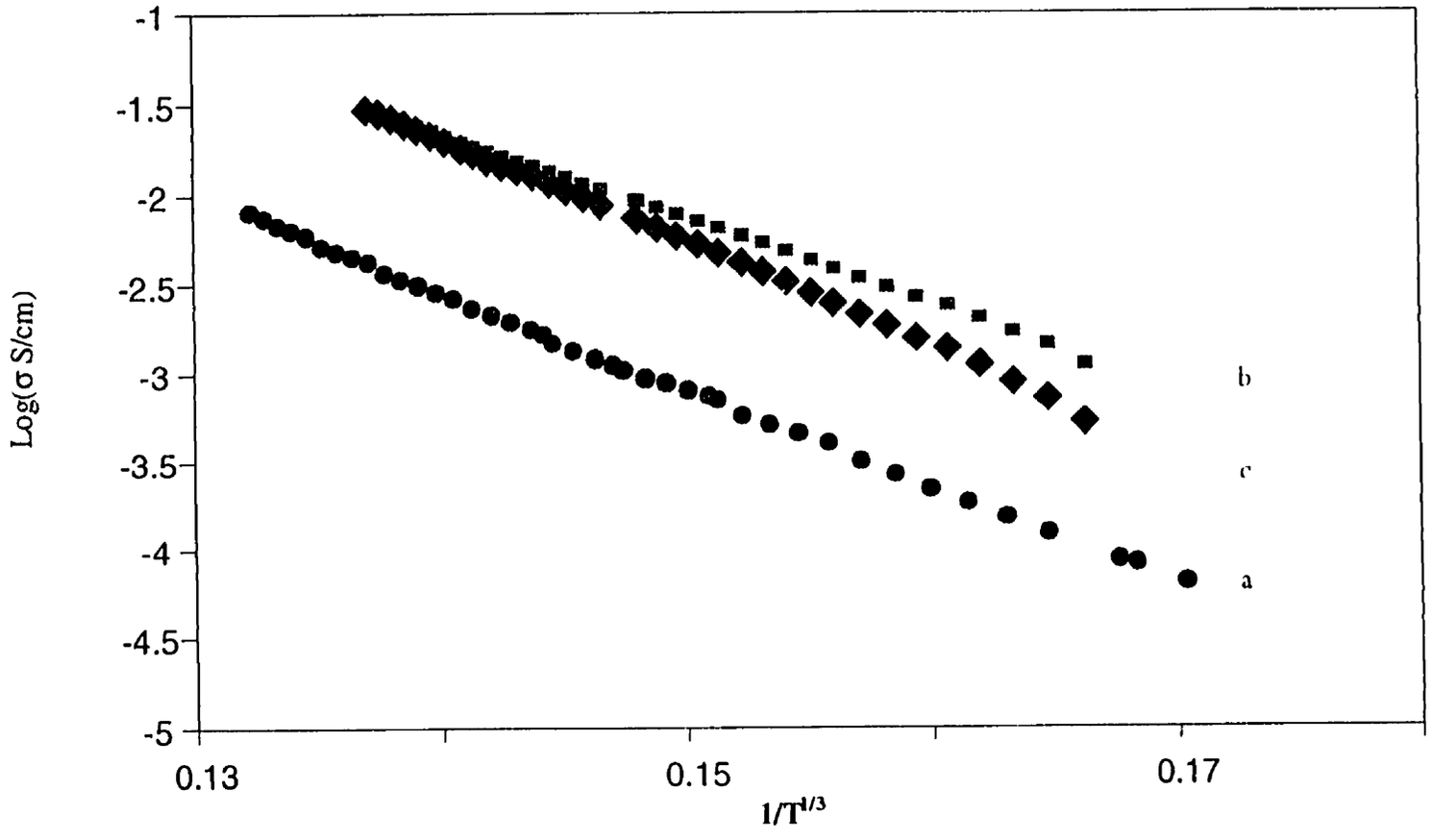

Figure 2.8 (continued) Two-probe variable temperature electrical conductivity data for thin films (glass substrate) of $(PPY)_{0.5}MoO_3$. (a) as prepared; (b) heated under N_2 at 200°C for 3 hours; (c) heated under N_2 at 250°C for 3 hours

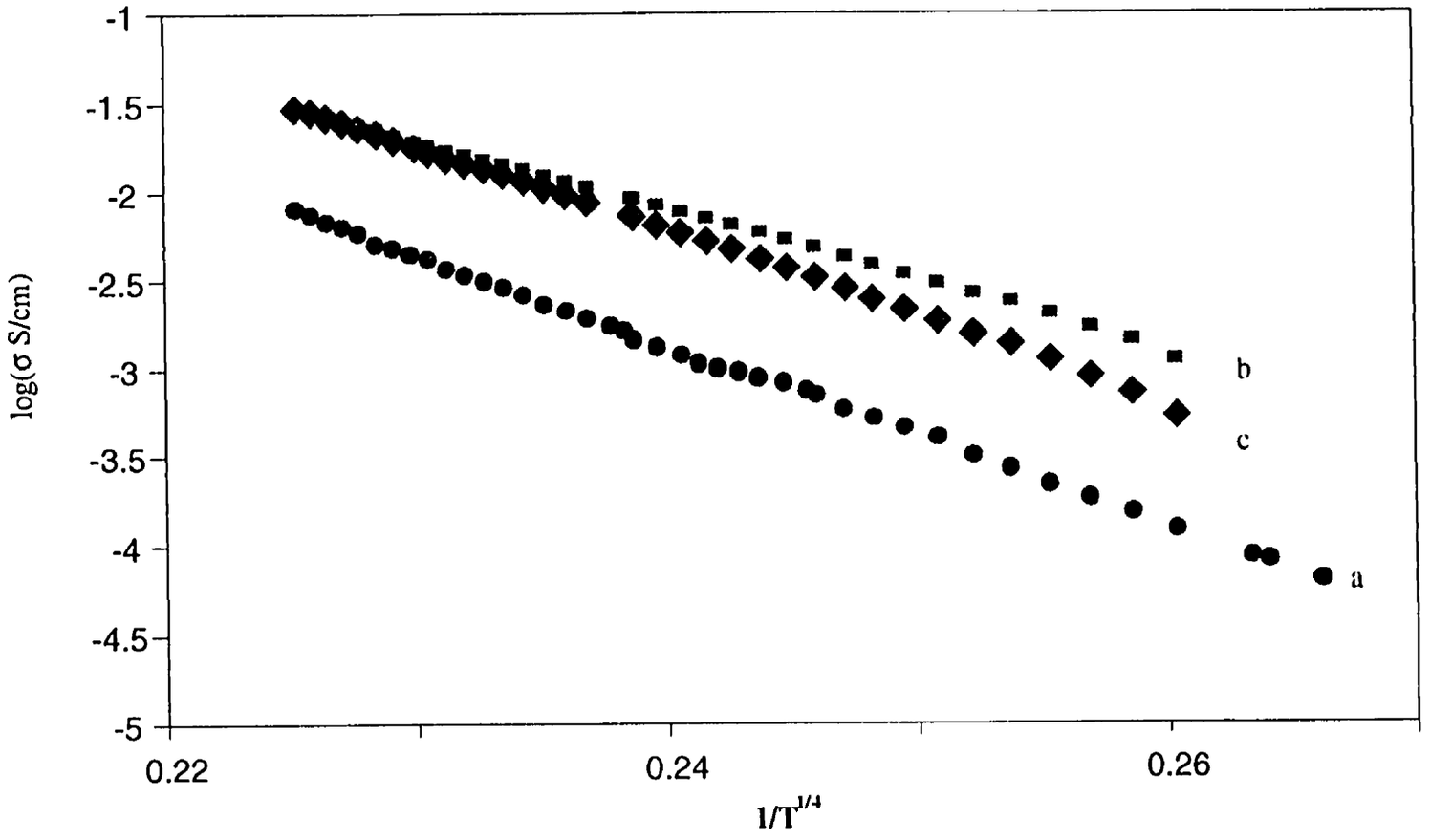

Figure 2.8 (continued) Two-probe variable temperature electrical conductivity data for thin films (glass substrate) of $(PPY)_{0.5}MoO_3$. (a) as prepared; (b) heated under N_2 at 200°C for 3 hours; (c) heated under N_2 at 250°C for 3 hours

hours. The above discussion means that the heating process itself did not destroy the conductivity of polypyrrole, however, the reaction of polypyrrole with oxygen, water will become more favorable at high temperatures. It is this reaction which most likely destroys the conductivity of the polypyrrole. Therefore, the brief annealing of the $(PPY)_{0.5}MoO_3$ nanocomposite material at 200°C under nitrogen would not destroy the conductivity of the nanocomposite in this respect. On the other hand, the large increase in conductivity can be the result of the more homogeneous distribution of conducting carriers and, more importantly for the nanocomposite material, is perhaps from the increased conjugated length of polypyrrole, due to the increased length of the polymer chain upon heating. It may be reasonable to suggest that the oligomer of pyrrole cointercalated in MoO_3 with polypyrrole is brought together by the host and is in the spatial position ready to be further polymerized by the accessible oxidant. Upon heating, the layered MoO_3 may act as a catalyst to facilitate the polymerization of these oligomers, resulting in higher conductivity. At 250°C, $(PPY)_{0.5}MoO_3$ starts to decompose, resulting in lower conductivity. It should be pointed out, however, that even for the heat-treated nanocomposite material, the conductivity is only slightly higher than that of the host material $NaMoO_3$. The reason may be that the communication between the two conducting components -- polypyrrole and $NaMoO_3$ -- is not very good, i.e., they do not match very well. The conduction is not mutually reinforced but may just be "diluted". Exploring the conductivity of matched host and guest materials for the nanocomposite, therefore, is needed, and matched host and guest should be expected to reinforce the conductivity and provide new and higher conductivity materials.

The conductivity data plotted according to the Arrhenius relationship ($\log(\sigma) \sim 1/T$), and metallic islands ($\log(\sigma) \sim 1/T^{1/2}$), and for the variable hopping model ($\log(\sigma) \sim 1/T^{1/4}$), and as for the two dimensional conduction model ($\log(\sigma) \sim 1/T^{1/3}$) are all shown in Figure 2.8. Basically, within experimental errors, they all give a straight line. Thus the analysis of the temperature dependence of conductivity for this nanocomposite material did not shed any light on the mechanism of conduction. It is also difficult to distinguish if conduction occurs by a two dimensional or three dimensional mechanism. [45, 46, 47, 48, 49]

2.3.6 The reaction mechanism for the synthesis of $(PPY)_{0.5}MoO_3$ nanocomposite material

Three possible mechanisms can be suggested for the formation of the $(PPY)_{0.5}MoO_3$ nanocomposite material (mechanisms A, B, and C, Figure 2.9).

Mechanism B can be rejected. Since the pyrrole cation is not stable, as soon as the pyrrole is oxidized, it will be polymerized. Furthermore, the oxidative polymerization of pyrrole inside the lattice of MoO_3 will require the oxidant Fe^{3+} to be accessible in the layer. However we know that under this condition, the host layer would be oxidized first. In Mechanisms A and C, $NaMoO_3$ and pyrrole will compete with each other to react with Fe^{3+}. In mechanism A, it is suggested that the first redox reaction happens between $NaMoO_3$ and Fe^{3+}, and then the instantly formed MoO_3 will oxidatively intercalatively polymerize pyrrole as was observed for host material V_2O_5 and FeOCl. However, the direct reaction of MoO_3 with pyrrole did not result in the redox intercalative polymerization. This mechanism is also unlikely to be true, although one may suggest that the instantly-formed MoO_3 would react with pyrrole much faster than MoO_3 powder.

Mechanism C which involves first oxidative polymerization of pyrrole to form a cationic polypyrrole chain, then ion exchange of hydrated sodium cations with this multi-charged polymer chain to form $(PPY)_{0.5}MoO_3$ is therefore more reasonable. First, it is well

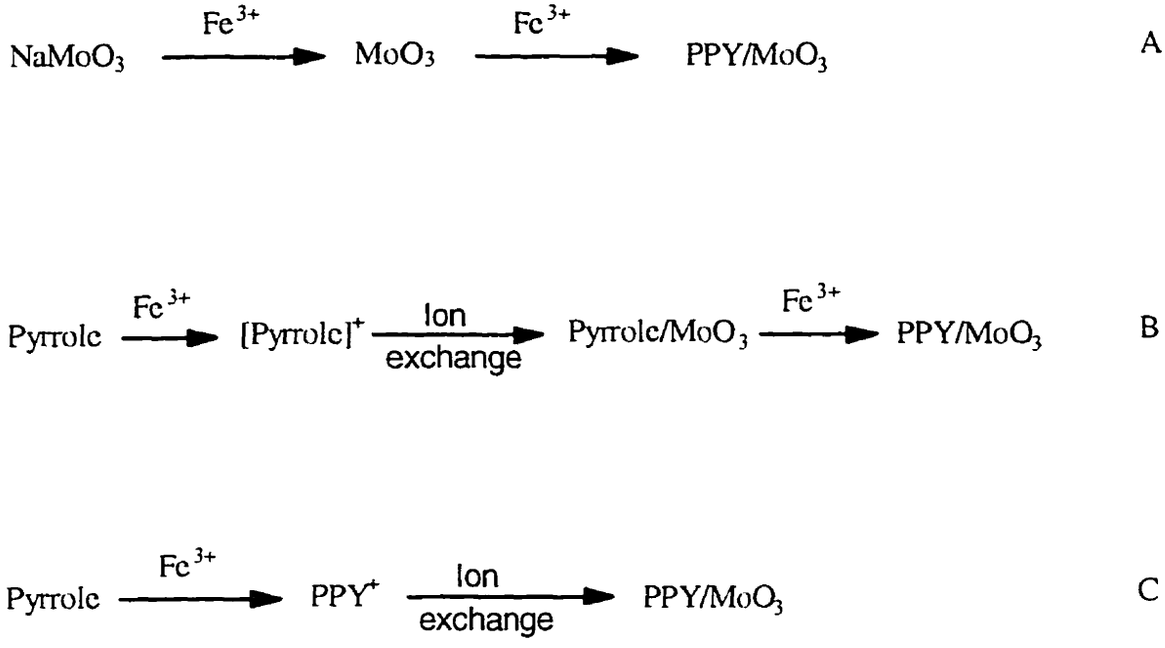

Figure 2.9 Supposed mechanism of (A) in situ intercalative polymerization, (B) oxidation/ionic exchange/polymerization and (C) oxidative polymerization/ionic exchange for synthesis of $(PPY)_{0.5}MoO_3$ nanocomposite

known that the oxidation of pyrrole with $FeCl_3$ in water solution will result in the conductive polypyrrole possessing multipositive charges. Second, it has been shown in this laboratory that $NaMoO_3$ is ready to be ion exchanged with multipositive charged inorganic clusters and organic cationic polymers such as the precursor of PPV to form the pillared

material or electronic conductive polymer/MoO_3 nanocomposite material.[12, 14] However, there are also other questions associated with Mechanism C. How does the propagation of the polypyrrole chain compete with the ion exchange process, i.e., does the ion exchange process exchange the wide range of oligomer cations and polymer cations? Due to the restriction of the rigid layered lattice of $NaMoO_3$, the propagation process may be terminated by an ion exchange process. The wide temperature range observed for thermal analysis suggests that there is a wide molecular weight distribution for this nanocomposite material. It is also consistent with the conductivity increase of this nanocomposite upon annealing.

2.4 Conclusion

A new conductive polymer/inorganic layered host nanocomposite material, namely $(PPY)_{0.5}MoO_3$, was prepared by an unprecedented method. This method extends the range of inorganic layered compounds useful as host materials for preparation of polymer/inorganic layered nanocomposite materials. $(PPY)_{0.5}MoO_3$ was characterized by powder XRD, FTIR, and thermal analysis. A structural model for $(PPY)_{0.5}MoO_3$ was suggested featuring hydrogen bond formation between polymer and $(MoO_3)_\infty$ sheets and the shift of $(MoO_3)_\infty$ sheet by c/2 along the c crystal axis, which accounts for the larger d-spacing observed for this nanocomposite material. Electronic conductivity studies show that polypyrrole sitting between $(MoO_3)_\infty$ sheets is in its conductive form; however, the variable temperature conductivity studies cannot distinguish different conduction mechanisms. An oxidative polymerization/ion exchange mechanism was proposed for this new method of preparation of hybrid polymer/inorganic nanocomposites.

2.5 References

1. "Handbook of conducting polymers"; Skotheim, T. A., Ed; Marcel Dekker: New York, **1986.**

2. Samuelson, L. A.; Druy, M. A. *Macromolecules*, **1986**, *19*, 284.

3. Shirakawa, H.; Louis, E. J.; MacDiarmid, A. G.; Chiang, C. K.; Heeger, A. J. *J. Chem. Soc. Chem. Commun.* **1977**, 578.

4. Chiang, C. K.; Fincher, C. R.; Park, Y. W.; Heeger, A. J.; Shirakawa, H.; Louis, E. J.; Gau, S. C.; MacDiarmid, A. G. *Phys. Rev. Lett.* **1977**, *39*, 1098.

5. Chiang, C. K.; Druy, M. A.; Gau, S. C.; Heeger, A. J.; Louis, E. J.; MacDiarmid, A. G.; Park, Y. W.; Shirakawa, H. *J. Am. Chem. Soc.* **1978**, *100*, 1013.

6. Penner, R. M.; Martin, C. R. *J. Electrochem. Soc.* **1986**, *133*, 310.

7. Matsubayashi, G.; Nakajima, H. *Chem. Lett.* **1993**, 31.

8. Kanatzidis, M. G.; Tonge, L. M.; Marks, T. J.; Marcy, H. O.; Kannewurf, C. R. *J. Am. Chem. Soc.* **1987**, *109*, 3797.

9. Kanatzidis, M. G.; Marcy, H. O.; McCarthy, W. J.; Kannewurf, C. R.; Marks, T. J. *Solid State Ionics* **1989**, *32-33*, 594.

10. Kanatzidis, M. G.; Hubbard, M.; Tonge, L. M.; Marks, T. J.; Marcy, H. O.; Kannewurf, C. R. *Synth. Metals* **1989**, *28*, C89.

11. Mehrotra, V.; Giannelis, E. P. *Solid State Ionics* **1992**, *51*, 115.

12. Nazar, L. F.; Zhang, Z.; Zinkweg, D. *J. Am. Chem. Soc.* **1992**, *114*, 6239.

13. Bein, T.; Enzel, P. *Angew. Chem. Int. Ed. Engl.* **1989**, *28*, 1692.

14. Nazar, L. F.; Liblong, S. W.; Yin, X. *J. Am. Chem. Soc.* **1991**, *113*, 5889.

15. Schollhorn, R.; Kuhlmann, R.; Besenhard, J. O. *Mat. Res. Bull.* **1976**, *11*, 83.

16. Thomas, D. M.; McCarron, E. M. *Mat. Res. Bull.*, *21*, **1986**, 945.

17. Kolodiejski, W.; Lalik, E.; Lerf, A.; Klinowski, *J. Chem. Phys. Lett.* **1992**, *194*, 429.

18. Lerf, A.; Lalik, E.; Kolodiejski, W.; Klinowski, J. *J. Phys. Chem.* **1992**, *96*, 7389.

19. *Solid State Chemistry, Compounds*, Cheetham, A. K.; Day, P. Eds.; Oxford Science Publications, **1992.** pp 212.

20. Hu, Y.; Davies, P. K.; Feist, T. P. *Solid State Ionics* **1992**, *53-56*, 539.

21. West, K.; Skaarup, S.; Jacobsen, T. *Solid State Ionics* **1992**, *53-56*, 356.

22. Desilvestro, J.; Haas, O. *J. Electrochem. Soc.* **1990**, *137*, 5c.

23. Dampier, F. W. *J. Electrochem. Soc.* **1974**, *121*, 656.

24. Kumagai, N.; Tanno, K. *J. Appl. Electrochem.* **1988**, *18*, 57.

25. Julien, C.; Hussain, O. M.; El-Frah, L.; Balkanski, M. *Solid State Ionics* **1992**, *53-56*, 400.

26. Eda, K.; Hatayama, F.; Kunitomo, M.; Kohmoto, T.; Sotani, N. *J. Mater. Chem.* **1994**, *4*, 205.

27. Mehrotra, V.; Giannelis, E. P. *Solid State Commun.* **1991**, *77*, 155.

28. Enzel, P.; Bein, T. *J. Chem. Soc. Chem. Commun.* **1989**, 1326.

29. Enzel, P.; Bein, T. *J. Phys. Chem.* **1989**, *93*, 6270.

30. Liu, Y.; Kanatzidis, M. G. *Inorg. Chem.* **1993**, *32*, 2989.

31. Morrison, R. T.; Boyd, R. N. "Organic Chemistry", 4th ed. Allyn & Bacon Inc. Boston **1983**.

32. Kihlborg, L. *Arkiv Kemi* **1963**, *21*, 443.

33. Sotani, N.; Eda, K.; Sadamatu, M.; Takagi, S. *Bull. Chem. Soc. Jpn.* **1989**, *62*, 903.

34. Sotani, N.; Eda, K.; Kunitomo, M. *J. Solid State Chem.* **1990**, *89*, 123.

35. Harmony, M. D.; Laurie, V. W.; Kuczkowski, R. L.; Schwendeman, R. H.; Ramsay, D. A.; Lovas, F. J.; Lafferty, W. J.; Maki, H. G. *J. Phys. Chem. Ref. Data* **1978**, *8*, 619.

36. Wells, A. F. *Structural Inorganic Chemistry*, 5th ed. Clarendon Press, Oxford, **1984**.

37. Lei, J.; Liang, W.; Martin, C. R. *Synth. Met.* **1992**, *48*, 301.

38. Brandt, P.; Fischer, R. D.; Martinez, E. S.; Calleja, R. D. *Angew. Chem. Int. Ed. Engl.* **1989**, *28*, 1265.

39. Thieblemont, J. C.; Brun, A.; Marty, J.; Planche, M. F.; Calo, P. *Polymer* **1995**, *36*, 1605.

40. Skakalova, V.; Kosina, S.; Koren, B.; Annus, J.; Omastova, M. *Synth. Met.* **1990**, *36*, 253.

41. Munstedt, H. *Polymer* **1988**, *29*, 296.

42. Truong, V. T. *Synth. Met.* **1992**, *52*, 33.

43. Turcu, R.; Neamtu, C.; Brie, M. *Synth. Met.* **1993**, *53*, 325.

44. Machida, S.; Miyata, S. Techagumpuch, A. *Synth. Met.* **1989**, *31*, 311.

45. Mott, N. *Conduction in Non-crystalline Materials*, 2nd ed., Oxford Science Publications, New york, **1993**.

46. Chien, J. C. W. *Polyacetylene, Chemistry, Physics, and Material Science*, Academic Press, New York, **1984**.

47. Mott, N.; Davis, E. A. *Electronic Processes in Non-crystalline Materials*, Clarendon Press, Oxford, England, **1971**.

48. *The Physics and Chemistry of Low Dimensional Solids*, Alcacer, L. Ed., D. Reidel Publishing Company, London, England, **1980**.

49. Mott, N. F. *Metal-insulator Transitions*, 2nd ed., Taylor & Francis, London, England, **1990**.

CHAPTER THREE

PEO LITHIUM (SODIUM) COMPLEXES/ELECTRONIC CONDUCTIVE HOST NANOCOMPOSITES (I)

-- SYNTHESIS, CHARACTERIZATION AND PROPERTIES OF PEO/MoO_3 NANOCOMPOSITES

3.1 Introduction

Many transition metal oxides and sulfides with a 3D open-framework or 2D layered structures are attractive as potential cathode materials in secondary lithium batteries or electrochromic devices. Their inherent structural characteristics give rise to sites for lithium intercalation, and allow diffusion of lithium cations during the charge and discharge process.[1,2] Oxides are strongly preferred because of their higher operating voltage.[3] Although these are primary considerations, it is desirable that the material be an electronic conductor as well. Materials such as vanadium oxides (e.g., V_6O_{13}),[4, 5] $M_yV_2O_5$ phases (where M is an alkali or transition metal),[6,7] MoO_3,[8] vanadium-molybdenum oxides,[9] Li_xCoO_2,[10] and $LiMn_2O_4$[11] have all been found to be promising materials for such applications, amongst others.

MoO_3 is an example of a material with a layered structure that has been examined as a potentially useful cathode.[8] As is the case with many metal oxides, diffusion of the lithium cations is hindered primarily due to strong electrostatic interaction with the oxygen

atoms of the molybdenum oxide sheets. We are interested in improving the lithium mobility in layered oxides in general, and in MoO_3 in this case, by introducing an ionically conductive polymer, such as poly(ethylene oxide) between the layers. The intercalation of poly (ethylene oxide) ["PEO"] into MoO_3 is expected to enhance the mobility of lithium ions between the layers through a combination of effects: by "solubilizing" the ions since PEO is a good solvent for alkali metal salts, by decreasing the interaction of the cations with oxygen of the MoO_3 lattice, and by propping open the layered structure thus providing more spacious environments for the cations.

Numerous examples of PEO intercalation into layered oxides have been reported. Aranda and Ruiz-Huitzky[12] and later others[14] reported the insertion of PEO into aluminosilicate clays. Liu *et al.* reported the intercalation of PEO into V_2O_5,[15] and West and co-workers have examined the effects of PEO in the reversible insertion of Li in the V_2O_5 structure. [16] There are, however, few studies of the effect of the polymer on ion mobility in the inorganic lattice, although indirect evidence is encouraging. In all cases, it has been suggested that Li ion diffusion may be enhanced due to the polymer. Quantitative estimates of the effect on ion mobility, and the mechanism by which the polymer influences conductivity have not yet been addressed. Ruiz-Huitzky has pointed out that it should be possible to focus on the issue of cation mobility in these systems since the inorganic host lattice acts as an immobilized charge balancing anion.[17]

To introduce PEO between the layers of MoO_3, we first intercalated sodium ions between the layers of MoO_3. This was followed by the insertion of PEO into the metal bronze. The driving force for the insertion reaction arises from the solvation of the cations

by the PEO, together with the increase in entropy resulting from displacement of water molecules from the interlamellar region. We find that both mono and bi-layers of PEO can be incorporated between the oxide sheets. Here, we report the synthesis and characterization of the $(PEO)_X[Na(H_2O)_n]_{0.25}MoO_3$ nanocomposite (x = 0.40; or 0.90) using x-ray diffraction and solid state MAS NMR as the primary characterization tools. We have also carried out a preliminary comparative study of the electrochemical insertion of lithium into the two polymer nanocomposites (NC), by using the materials as cathodes in rechargeable lithium batteries.

3.2 Experimental

3.2.1 Synthesis

Materials: MoO_3, $Na_2S_2O_4$, and PEO (average molecular weight of 100,000 Daltons) were supplied by Aldrich. Na_2MoO_4 was supplied by Alfa Ventron. $[Na(H_2O)_n]_{0.25}MoO_3$ (n = 4, 5), ("$NaMoO_3$") was prepared according to the method described by Thomas and McCarron. [18]

The PEO single layer composite: $(PEO)_{0.4}[Na(H_2O)]_{0.25}MoO_3$, or the monolayer composite, was prepared by suspending 100 mg of $NaMoO_3$ in 100 mL of H_2O. The dispersion was sonicated in an ultrasonic bath for 30 minutes to promote swelling of the oxide layers and to decrease the particle size of $NaMoO_3$. The suspension was mixed with 50 mL of an aqueous PEO solution (13.2 g/L, i.e., 0.3 M expressed in terms of oxyethylene units), stirred for 3 hours at room temperature, filtered and thoroughly

washed with water and air dried. Chemical and thermogravimetric analysis gave the formulation; $(PEO)_{0.4}[Na(H_2O)]_{0.25}MoO_3$ (Galbraith - C: 5.70%; H: 1.25%; Mo: 45.18%)

The PEO Bilayer composite: A nanocomposite that contains a bilayer of PEO chains was prepared most readily from $NaMoO_3$ that was ion exchanged with Li. $[Li,Na]_{0.25}MoO_3$ was prepared as above, but using Li_2MoO_4 as the buffer in place of Na_2MoO_4. 2.0 g of this material was then ion-exchanged with LiCl twice for 2 days. The material was collected after centrifugation. The precipitate, "$LiMoO_3$", was washed with water and dried in air. 250 mg of the precipitate was then stirred in 500 mL of a 50/50 H_2O/methanol PEO solution at room temperature under nitrogen for 10 hours. We found this mixture provided greater control over the intercalation reaction than the use of a single aqueous solvent. The colloid was centrifuged, the precipitate was washed with H_2O, and dried in air. Chemical and thermogravimetric analysis indicated a PEO/MoO_3 ratio of 0.9:1, i.e., the formulation $(PEO)_{0.9}[Na(H_2O)_{0.5}]_{0.25}MoO_3$

3.2.2 Instrumentation

Powder x-ray diffraction (XRD) patterns were carried out in a Siemens D500 diffractometer equipped with a graphite monochromator using Cu-Kα radiation, and a step scan of $2\theta = 0.2°$/second. Infrared spectra were recorded on a Nicolet 520 FTIR as KBr pellets. Differential thermal analysis and thermal gravimetric analysis (DTA/TGA) were run in air with a heating rate of 5°C/min and a flow rate of 20 mL/min on a PL Thermal Science STA 1500 thermal analysis system. The NMR experiments were performed at 125.8 MHz and 132.3 MHz for ^{13}C and ^{23}Na, respectively, on a Bruker

AMX-500 spectrometer equipped with a solids accessory rack and a Bruker MAS (magic angle spinning) multinuclear probe. ^{13}C spectra were collected using a cross polarization pulse sequence with a 3.3 μs 90° pulse, a relaxation delay of 4 seconds, contact times ranging from 100 μs to 3 ms, and high power proton decoupling. The MAS rate was varied between 8 and 12 kHz. ^{23}Na chemical shift was referenced to solid state NaCl as external standard.

Two-probe conductivity measurements were performed in a vacuum chamber with a pressure below 10^{-4} Torr. A thin film of the material was prepared by casting the oxide bronze or polymer NC suspension on Corning 7059 glass substrates. Electrodes were affixed to the film using silver epoxy, and cured at 150°C. The conductivity was measured using a voltage of 1.0 V.

3.3 Results and Discussion

3.3.1 Intercalation of PEO

The proposed structure of $[Na(H_2O)_2]_{0.25}MoO_3$ (vacuum dried) and $[Na(H_2O)_n]_{0.25}MoO_3$ ($n > 4$) (air dried), based on previous studies [18, 20] is shown in Figure 3.1. In the former, the sodium ion is coordinated by two water molecules and 4 terminal oxygen's (Mo=O) of the molybdenum oxide layers. On the other hand, in the air dried sample, the sodium ion is octahedrally coordinated by six water molecules. These water

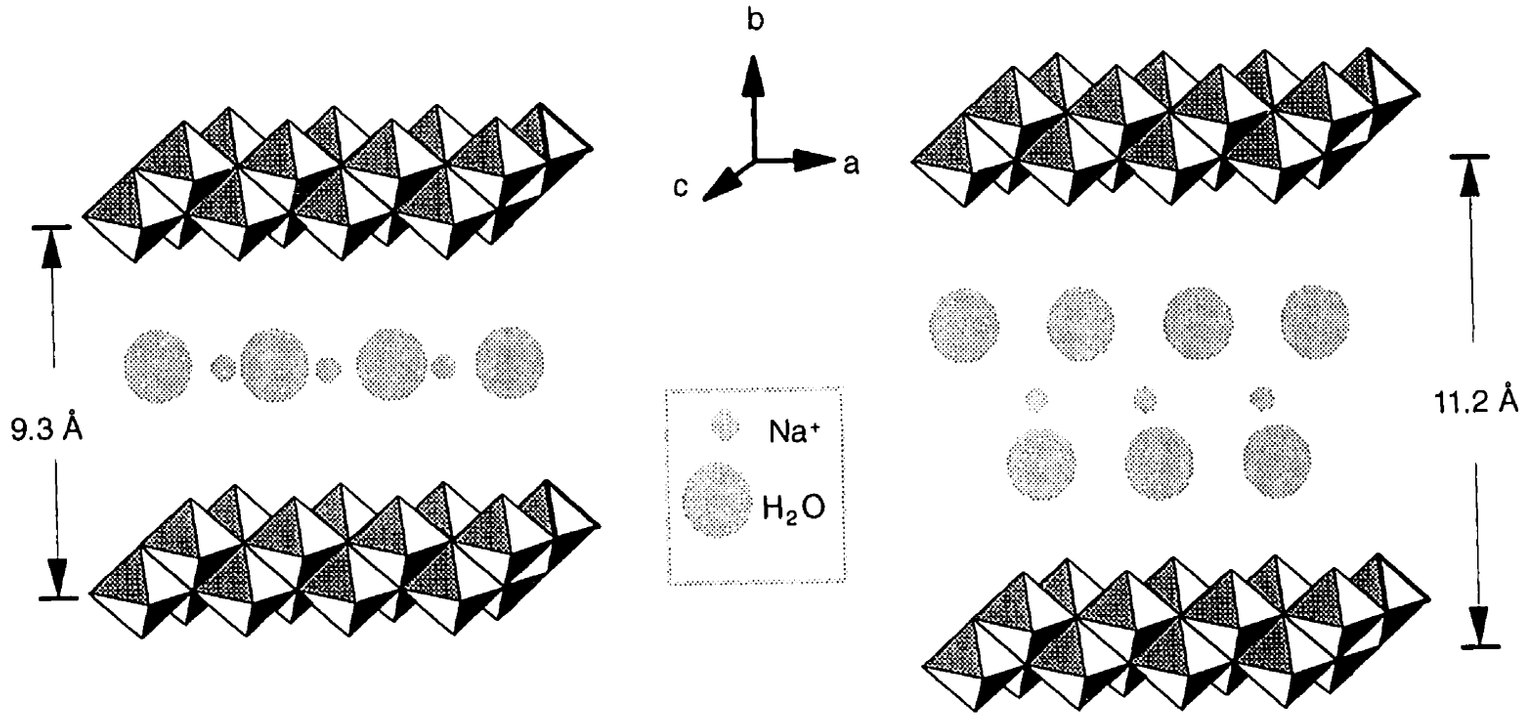

$[Na(H_2O)_n]_{0.25}\ MoO_3$ (n = 2)
monolayer hydrate

$[Na(H_2O)_n]_{0.25}\ MoO_3$ (n = 4, 5)
bilayer hydrate

Figure 3.1 **Proposed schematic structure of $[Na(H_2O)_2]_{0.25}MoO_3$ (vacuum dried) and $[Na(H_2O)_n]_{0.25}MoO_3$ (n > 4) (air dried)**

molecules sit between the sodium cation and the Mo=O oxygen atoms in the layers. This phase is much more easily swelled in water than the vacuum dried material. Due to the relatively large solvation energy of the sodium cation, extensive hydration results in an influx of water molecules that expands the coordination shell of the ion, and hence results in interlayer swelling. To intercalate the PEO, $NaMoO_3$ was first swelled in water. A concentrated PEO/water solution was then introduced.

Figure 3.2 shows the XRD pattern of the $[Na(H_2O)_n]_{0.25}MoO_3$ (n>4) ($NaMoO_3$) and its PEO intercalation compounds. The use of an excess amount of PEO (a molar ratio of PEO/$NaMoO_3 \geq 7$) ensured that one phase was obtained (Figure 3.2b). At lower molar ratios, a second phase was observed in the diffraction pattern corresponding to unaltered $NaMoO_3$. The increase in the d-spacing from 11.1 Å to 12.9 Å (1.8 Å) upon intercalation of PEO is the combined result of polymer intercalation and the loss of some of the water of hydration in $[Na(H_2O)_n]_{0.25}MoO_3$; i.e., water molecules are replaced by the polymer. From this, we infer that the strong interaction between the sodium cations and PEO is the main driving force for intercalation, in addition to the increase in entropy associated with release of the sodium cations. Heat treatment of (PEO)$NaMoO_3$ at 130°C for 1 hour results in a slight decrease of the d-spacing, whereas corresponding treatment of $[Na(H_2O)_n]_{0.25}MoO_3$ results in conversion to $[Na(H_2O)_2]_{0.25}MoO_3$, and a dramatic decrease in the interlayer distance to 9.4 Å.[20] Therefore, the interlayer gap resulting from polymer incorporation is 3.5 Å, comparable to that arising from PEO intercalation in V_2O_5.[12, 13, 14] This corresponds to a monolayer of PEO in the zig-zag conformation (proposed for PEO-V_2O_5) or in the planar type-I conformation (zig-zag like) adopted by $HgCl_2$ complexes. [21, 22] It is clear that the PEO does not adopt a helical conformation in

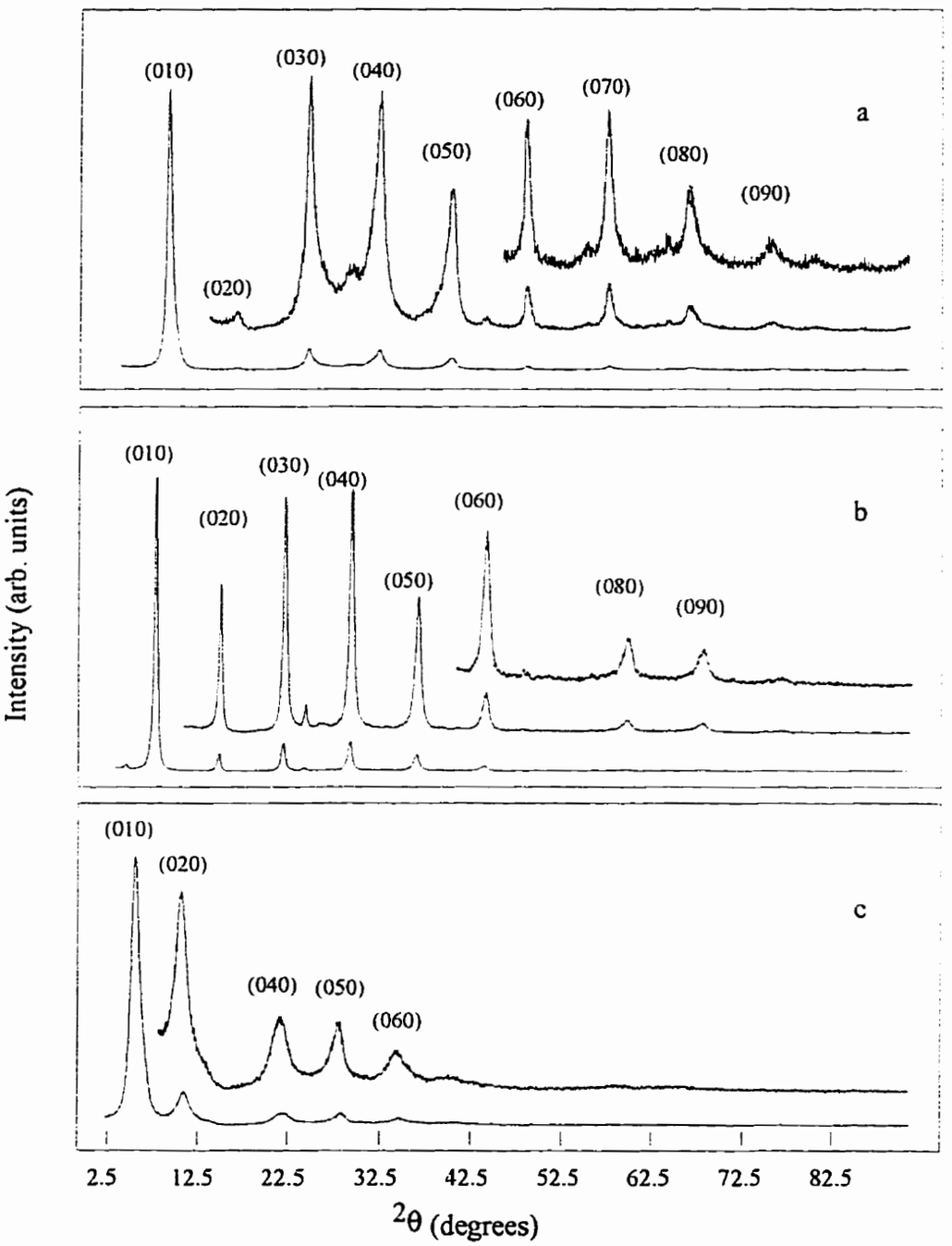

Figure 3.2 **Powder XRD pattern of oriented films of (a) $[Na(H_2O)_n]_{0.25}$ MoO_3 (n = 4, 5); (b) the single PEO-layer nanocomposite, $(PEO)_{0.4}[Na(H_2O)]_{0.25}MoO_3$; and (c) the double PEO-layer nanocomposite, $(PEO)_{0.9}[Na(H_2O)_n]_{0.25}MoO_3$**

the intercalation compound, such as that observed in crystalline $[(PEO)_nM^+]X^-$ salts, or that proposed for PEO/clay composites[15] which would give rise to an 8-9 Å *increase* in the interlayer distance.

3.3.2 Preparation of Multilayers of PEO in $(Li,Na)_{0.25}MoO_3$

The exfoliation of the MoO_3^{x-} layers can be controlled by varying the interlayer cation. The tendency of the MoO_3 layers to swell is maximized when lithium resides between the layers since its solvation energy exceeds that of sodium. For example, we have shown that a fairly high Li/Na ratio is needed to intercalate a long chain, high molecular weight ($>10^5$ Da) polyelectrolyte into MoO_3, such as the precursor to poly(p-phenylene vinylene).[23] Likewise, by changing the dielectric constant of the solvent, we can control the degree of exfoliation. Increasing the lithium content of [Na, Li]MoO_3 gives rise to enhanced tumescence and permits the introduction of more than one layer of polymer between the layers. It also, however, results in a somewhat more disordered polymer intercalation compound. In order to prepare "$LiMoO_3$", the $(Li,Na)MoO_3$ was exchanged twice with LiCl under nitrogen for 2 days. The resulting $LiMoO_3$ was reacted with PEO in H_2O using the same procedure as that used to prepare the $(PEO)_xNaMoO_3$. This method usually produced a phase with an interlayer d-spacing of 15 Å resulting from two layers of PEO between the sheets. This interlayer spacing is observed in PEO intercalation compounds of clays,[12, 13, 14] MPS_3,[24] and MS_2[25] compounds. On occasion, however, the MoO_3 layers remained dispersed on addition of PEO and no solid could be isolated. If electrolytes were added to these dispersions, the $[Na^+]_xMoO_3^{x-}$ layers were reassembled, and the starting material was precipitated from the dispersion.

More reproducible results were obtained using a solvent mixture of 50/50 H_2O/methanol. This produced a pure 15 Å phase (Figure 3.2c); at short reaction times, a mixture of the 12 and the 15 Å phase was obtained. A phase with an interlayer d-spacing of 17 Å that may represent a hydrated form of the 15 Å phase was also observed at very long reaction times, although it could not be isolated.

3.3.3 Thermal analysis

Thermal analysis of the monolayer $(PEO)_{0.4}[Na(H_2O)]_{0.25}MoO_3$ nanocomposite (Figure 3.3a) reveals a 3-5% weight loss up to 200°C accompanied by a broad endotherm that can be ascribed to the loss of water. Comparison with $[Na(H_2O)_2]_{0.25}MoO_3$, which exhibits a 10% weight loss in this temperature range (Figure 3.3b), suggests that some of the coordinated water molecules around the sodium cation have been replaced by PEO. The bilayer nanocomposite exhibits very similar thermal behaviour, albeit with a negligible weight loss in this region (not shown). The absence of a distinct endotherm at 65°C in the DTA data corresponding to the melting point transition of PEO shows that crystalline PEO is not present on the surface of the nanocomposites. At about 280°C, the intercalated PEO begins to decompose, followed by a second decomposition step at about 400°C. The reason for the two step decomposition is not clear, since only one layer of PEO is contained within the layers. It may be the result of dissimilar PEO environments in the MoO_3 lattice; alternatively, the two step process may correspond to aerobic oxidation and oxidation by the MoO_3 lattice oxygen. A two-step weight loss was also observed for (PEO)-intercalated-barium montmorillonites in N_2 for which no interpretation was offered.[13] Bulk PEO, however, also decomposes in two steps

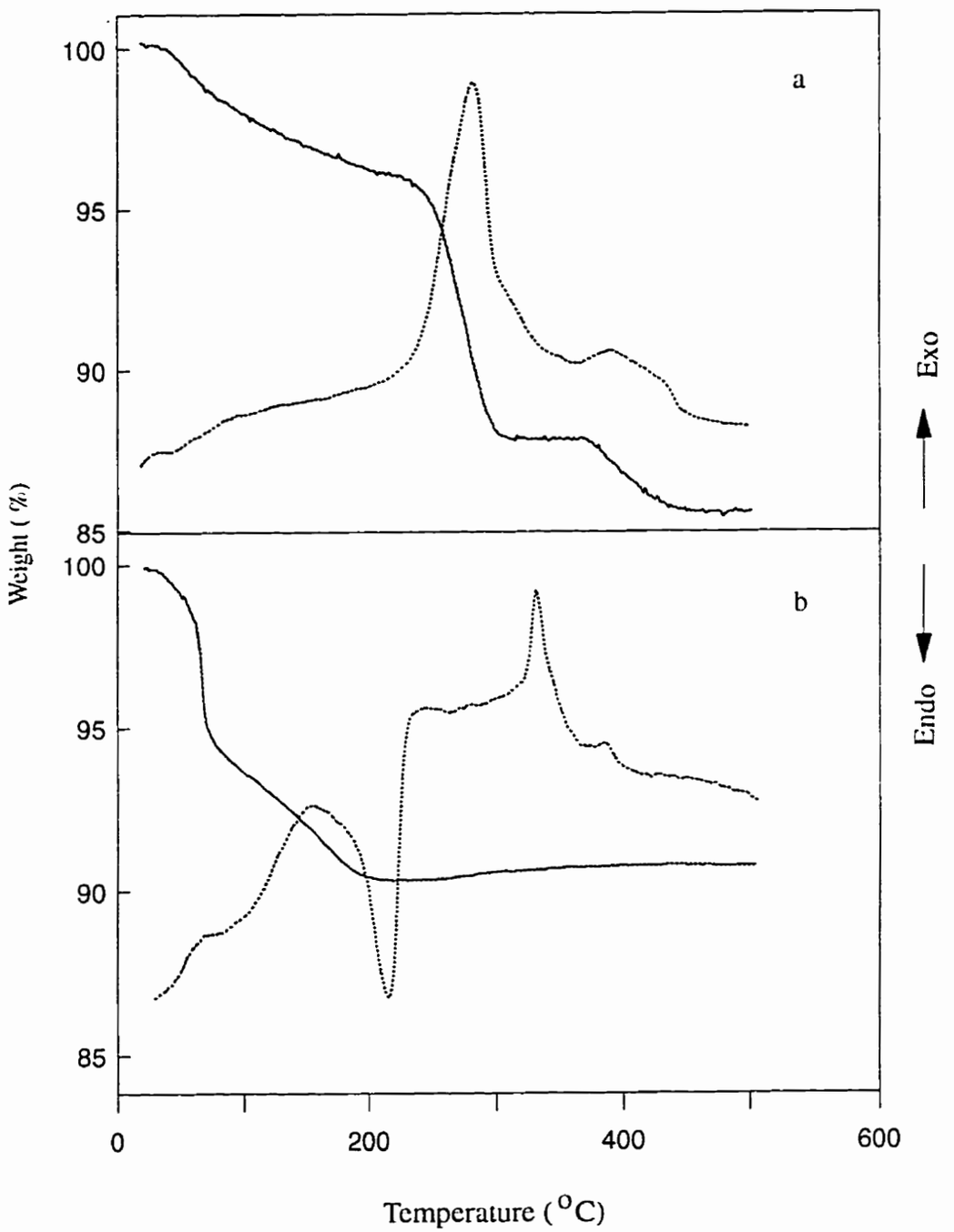

Figure 3.3 **Simultaneous TG-DTA traces for (a) the single PEO-layer nanocomposite, $(PEO)_{0.4}[Na(H_2O)]_{0.25}MoO_3$ and (b) $[Na(H_2O)_n]_{0.25}\ MoO_3$ (n = 4, 5)**

on pyrolysis in air, at about 350°C and 450°C, although in this case the second decomposition step corresponds to only 10% of the total weight loss. It is interesting to note that the decomposition of PEO in the MoO_3 nanocomposite occurs at a lower temperature than in the bulk, and at a somewhat lower temperature than in montmorillonites (ca. 330°C), [12, 13, 14] which is clearly an effect of the transition metal oxide lattice. The same effect was observed for $(PPY)_{0.5}MoO_3$ nanocomposite.

3.3.4 Infrared Spectroscopy

The host MoO_3^{x-} lattice displays a very strong absorption band in the near IR region which extends into the visible, and gives rise to the intense blue-black metallic appearance of this material. Unfortunately, this band also tails to the mid IR, resulting in very low transmission in the spectra, especially between 3000 - 10000 cm^{-1}. Nevertheless, numerous well-defined bands resulting from both absorption of the host lattice and the intercalated PEO are visible in the IR spectrum of the bilayer PEO/MoO_3 nanocomposite (Figure 3.4; the monolayer nanocomposite gave a very similar, but poorer quality spectrum). Spectral information is tabulated and assigned in Table 3.1. The broad and intense $\nu_{CH}(\text{--}CH_2\text{--})$ band centered at 2890 cm^{-1} in pure PEO is resolved into two distinct bands in the nonocomposite at 2840 and 2920 cm^{-1}, similar to that observed for other PEO nanocomposites.[12, 13, 14] This has been ascribed to strong interactions between the oxygen atoms of the PEO chain and the interlayer cations. The CH_2 deformations in the region between 1500 and 500 cm^{-1} are sensitive to the PEO chain structure, and can, in principle, be used to help distinguish between a PEO conformation in the helical, zig zag and type I and II PEO-$HgCl_2$ complexes (vide infra). Some of these bands, diagnostic of trans and

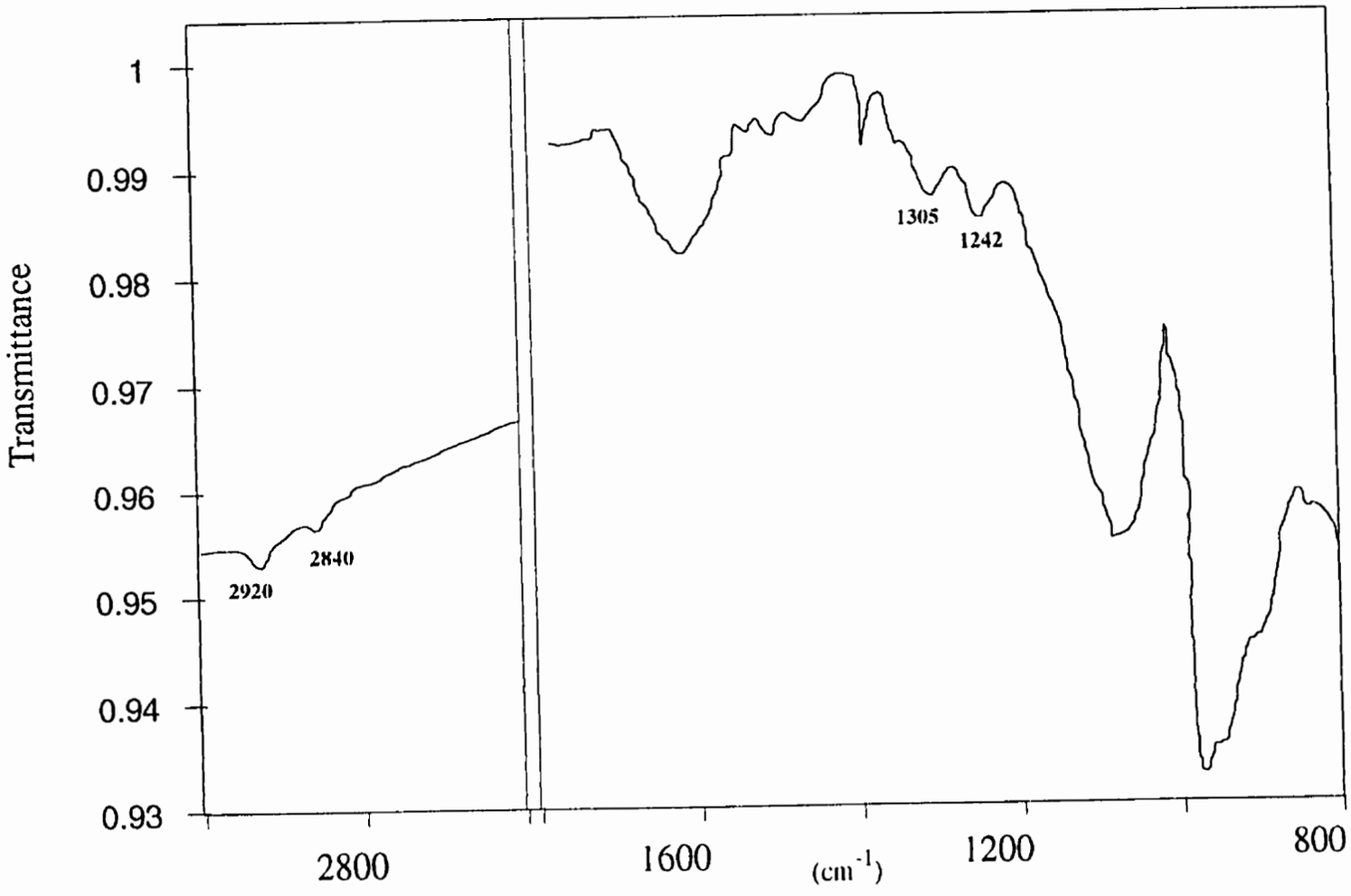

Figure 3.4 **FTIR spectrum of the bilayer $(PEO)_{0.9}(Li,Na)MoO_3$ nanocomposite**

Table 3.1 FTIR data for $(PEO)_{0.9}$(Li, Na)MoO_3, PEO and the type I PEO-$HgCl_2$ complex and the assignments

PEO/Li(Na)MoO_3[a]	PEO[b,c]	PEO-$HgCl_2$ Type I[c]	Assignment[b,c]
2930 (m)	2940-2800e	2930 (ms)	υ_{CH}(--CH_2--)
2856 (m)		2880 (sh)	υ_{CH}(--CH_2--)
1465 (w)	1470 (m)	1466 (m)	δ_{CH_2}
1450 (w)	1453 (m)	1442 (m)	δ_{CH_2}
-f	1358 (mw)	1354 (w)	$\upsilon_{(C-C)}$, δ_{CH_2} (w)
1344 (m)	1342 (m)	1346 (mw)	δ_{CH_2}
1305 (m)		1309(mw)/1324(w)	trans O--[CH_2CH_2]--O
-f	1283 (m)	1284 (vw)	t_{CH_2}
1243 (m)	1240 (m)	1243 (m)	t_{CH_2}
1155 (m)	1147 (s)	1154 (sh)	$\upsilon_{(C-C)}$, $\upsilon_{(COC)}$
ca. 1072-1082 (br. sh)	1103 (s)	1081-1104 (br. s)	$\upsilon_{(COC)}$
-f	1062 (m)g	1046 (m, sh)	-
-f		1029/1014 (m, sh)	*-h*
ca. 980 (vs)			υ_{MoO}[MoO_3^{x-}]
951 (s)	949 (sh)/964 (m)	942 (m)	$\delta_{CH_2(r)}$
910 (s)	937 (sh)	924 (m)/890 (mw)	δ_{CH_2} + $\upsilon_{(COC)}$
-f	*-f*	872 (mw)	$\delta_{CH_2(r)}$
-f	*-f*	856 (mw)	$\delta_{CH_2(r)}$
835 (m)	844 (m)	832 (m)	$\delta_{CH_2(r)}$
577 (vs)			υ_{MoO}[MoO_3^{x-}]

[a] All frequency values are expressed in cm^{-1}: v = very strong, m = medium, w = weak, sh = shoulder. [b]From reference 23. [c]From reference 22. [e]A very broad and strong band centred at 2890 cm^{-1}. [d]w = wagging, r = rocking, t - twisting mode. [g]From reverence 22(b). [h]Assigned in reference 23 as being possibly due to a combination of CH_2 rocking and ν(COC) modes characteristic of the trans-conformation: the band appears on the side of the strong band at 1100 cm^{-1} and may be obscured in the oxide nanocomposite. [f]Not observed; may be obscured.

gauche x-$(CH_2)_2$-x conformations (i.e., CH_2 rocking modes), are obscured in the nanocomposite by the extremely intense $\nu_{Mo=O}$ stretching vibration bands (MoO_3 lattice) which appear in the 1000-500 cm^{-1} region at 977 and 588 cm^{-1}. Comparison of the IR spectra of PEO, PEO/metal salt complexes reported in the literature, and of the bilayer (or monolayer) nanocomposites suggests that the helical structure adopted by crystalline PEO is lost upon intercalation. In particular, we base this on the appearance of a strong band at 1305 cm^{-1}. This band is characteristic of vibrations of O-$(CH_2)_2$-O groups in type-I-PEO/$HgCl_2$ complexes, where it is observed at 1309/1324 cm^{-1},[26, 27] but is completely absent in the helical conformation of PEO.[28] For the monolayer, this is consistent with the results from x-ray diffraction, which show a 4 Å expansion of the layers after incorporation of the polymer chains, which could only arise from PEO in a zig-zag-like or planar conformation. In the case of the bilayer, the data suggest that two planar PEO layers are contained between the MoO_3 sheets. We assign the strong, relatively broad band at 1071 cm^{-1} to a combination of symmetric and asymmetric C-O-C stretching modes of the intercalated polymer. This band occurs at about 1103 cm^{-1} in pure PEO, although it is shifted to lower frequency on complexation to alkali cations (i.e., to 1090 cm^{-1} or 1085 cm^{-1} in the case of the PEO·NaSCN complex).[28] The significant low-frequency shift that we observe is again an indication of very strong interaction of the ether oxygen of the PEO chain with either the alkali cations, the host MoO_3^{x-} lattice, or both.

3.3.5 Solid State NMR Spectroscopy

Extensive ^{13}C solid state NMR studies of bulk PEO and PEO/alkali metal salt complexes have shown that the information on polymer conformation, complexation and chain mobility can be derived from the analysis of chemical shift and relaxation data. Previous work has shown that in pure PEO, for example, two components with different chain mobilities are visible in the ^{13}C CPMAS NMR spectrum at approximately the same chemical shift.[29] A narrow peak ($\Delta\nu < 50$ Hz) with an extremely short ^{13}C T_1 observable at long contact times, has been unequivocally assigned to an amorphous component that corresponds to highly mobile chains. The other component, characterized by a broad resonance line (750 - 1000 Hz wide) with a longer T_1 observable at shorter contact times, arises from the highly ordered portion of the PEO chains. Based on the relaxation data, these segments are thought to be substantially less mobile,.

Figure 3.5 shows the ^{13}C CPMAS NMR spectra of the monolayer nanocomposite. Two ^{13}C resonances at δ=71 ppm and 66 ppm, both possessing a line width of approximately 600 Hz are resolved, and can be clearly distinguished on the basis of contact time variation experiments and by application of a Bloch decay pulse sequence (HPDEC). The Bloch decay or single-pulse experiment provides a quantitative estimate of the proportion of the ^{13}C nuclei in each of the sites, when long relaxation delay times are used. At short relaxation delay times, it provides an indirect estimate of the relative spin-lattice relaxation times of the nuclei if changes are observed compared to the cross-polarized spectrum. The peak at 71 ppm dominates the Bloch decay spectrum (Figure 3.5), when very short relaxation delay times are used (< 1 sec), indicating that the ^{13}C

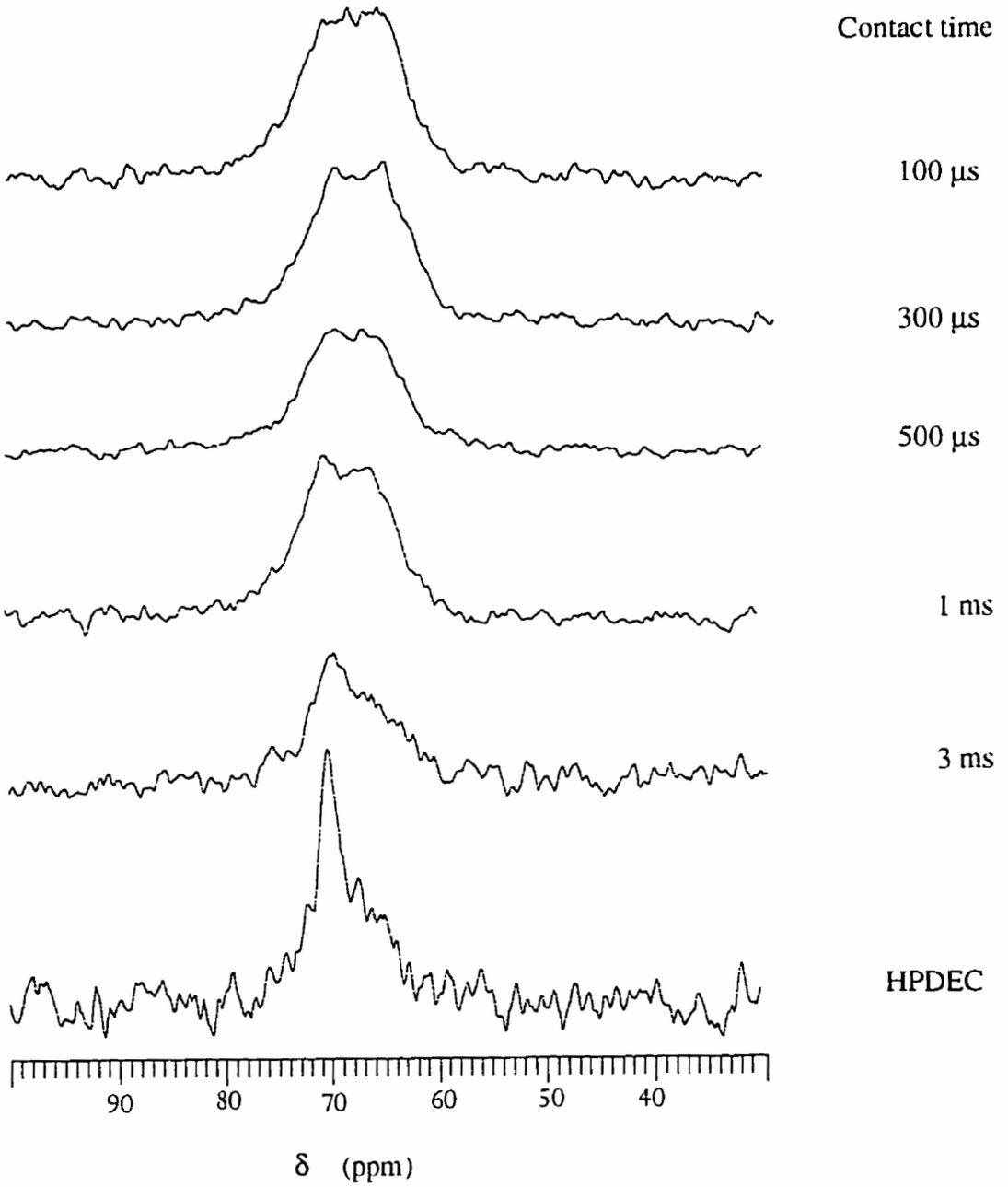

Figure 3.5 **^{13}C CPMAS NMR spectra of $(PEO)_{0.4}[Na(H_2O)]_{0.25}MoO_3$ taken at various contact times; the lower spectrum corresponds to the single pulse Bloch decay experiment (HPDEC)**

nuclei responsible for this signal have a very short spin-lattice relaxation time (T_1). These nuclei cross-polarize well at long contact times ranging up to 3 ms. Conversely, the peak at 66 ppm is greatly reduced in intensity in the Bloch decay spectrum (HPDEC, lower trace), suggesting that these ^{13}C nuclei have substantially longer T_1's, and are thus suppressed as a result of spin saturation. These nuclei cross-polarize well at shorter contact times from 100 μs to 1 ms. At longer contact times (> 1 ms), their signal is no longer observable.

Both peaks have fairly broad line widths, which indicates that no part of the chain is extremely mobile. Therefore, although the chains cannot be said to be either strictly crystalline or amorphous, the interaction with the cations and/or the MoO_3 lattice appears to constrain the polymer motion to some degree. The breadth of the peaks is probably due to chemical shift dispersion and/or inefficient decoupling due to the rate of molecular motion being comparable to the decoupling frequency. These two peaks have two distinct chemical shifts that are in excellent agreement with values obtained for complexed and uncomplexed PEO segments (or complexed/uncomplexed crown ethers).[30] The upfield shift (66 ppm) has been assigned to units that on complexation acquire a gauche configuration, and become constrained and less mobile.[31, 32, 33] The gauche conformation is thought to interact more strongly with polar or cationic groups. The downfield shift (71 ppm) has been assigned to uncomplexed units (perhaps in trans conformation) that interact less efficiently; hence these are not constrained and may undergo less restricted motion.[34, 35] The relaxation data support the above interpretation. The signal at 71 ppm has a shorter T_1 and $T_1\rho$ (^1H) (i.e., it cross polarizes at longer contact time) which are indications of

greater chain motion, consistent with an unconstrained environment (no complexation). Conversely, the signal at 66 ppm has a longer T_1 and shorter $T_1\rho$ (since it cross polarizes only at short contact times) suggesting that these carbon nuclei are pinned due to sodium complexation of the adjacent oxygen atoms of the PEO chain.

^{23}Na MAS NMR can also be used to indirectly probe the interaction between the cation and the PEO chains, since it is sensitive to the coordination sphere around the sodium cation. The ^{23}Na NMR spectrum of air-dried $[Na(H_2O)_{4\text{-}5}]_{0.25}MoO_3$ (Figure 3.6a) shows an asymmetric resonance at δ = -16.5 ppm with a broad shoulder centered at about ~30 ppm. An upfield shift of the ^{23}Na NMR resonance corresponds to decreasing degrees of solvation of the sodium cation.[36] The asymmetry of the peak is the result of multiple sodium coordination environments arising from slightly different degrees of hydration of the sodium cations in the lattice; i.e., in the air-dried sample, some of the sodium cations are partially dehydrated.[37] Acquisition of the spectrum at a lower field strength (4.7T, 52.9 MHz), revealed a narrower lineshape, thus ruling out the contribution of quadrupolar effects to the lineshape asymmetry. The effect of dehydration can also be seen in Figure 3.6b and 3.6c, which correspond to $[Na(H_2O)_2]_{0.25}MoO_3$ vacuum dried at 130°C for 1 and 12 hours respectively. The latter shows a single, symmetric peak shifted upfield to δ = -27 ppm.[41, 42, 43, 44, 44] The ^{23}Na MAS NMR spectrum of $(PEO)_{0.40}[Na(H_2O)_n]_{0.25}MoO_3$($n < 1$) dried at 130°C for 12 hours (Figure 3.6d), on the other hand, contains a single relatively symmetric peak at δ = -16.1 ppm, similar to that observed in PEO/Na-hectorite (-10.8 ppm), or Na^+ in PPO.[12, 13, 14, 38] Hence, the sodium cations in the nanocomposite are in relatively homogeneous environments, and are highly solvated, probably by a combination

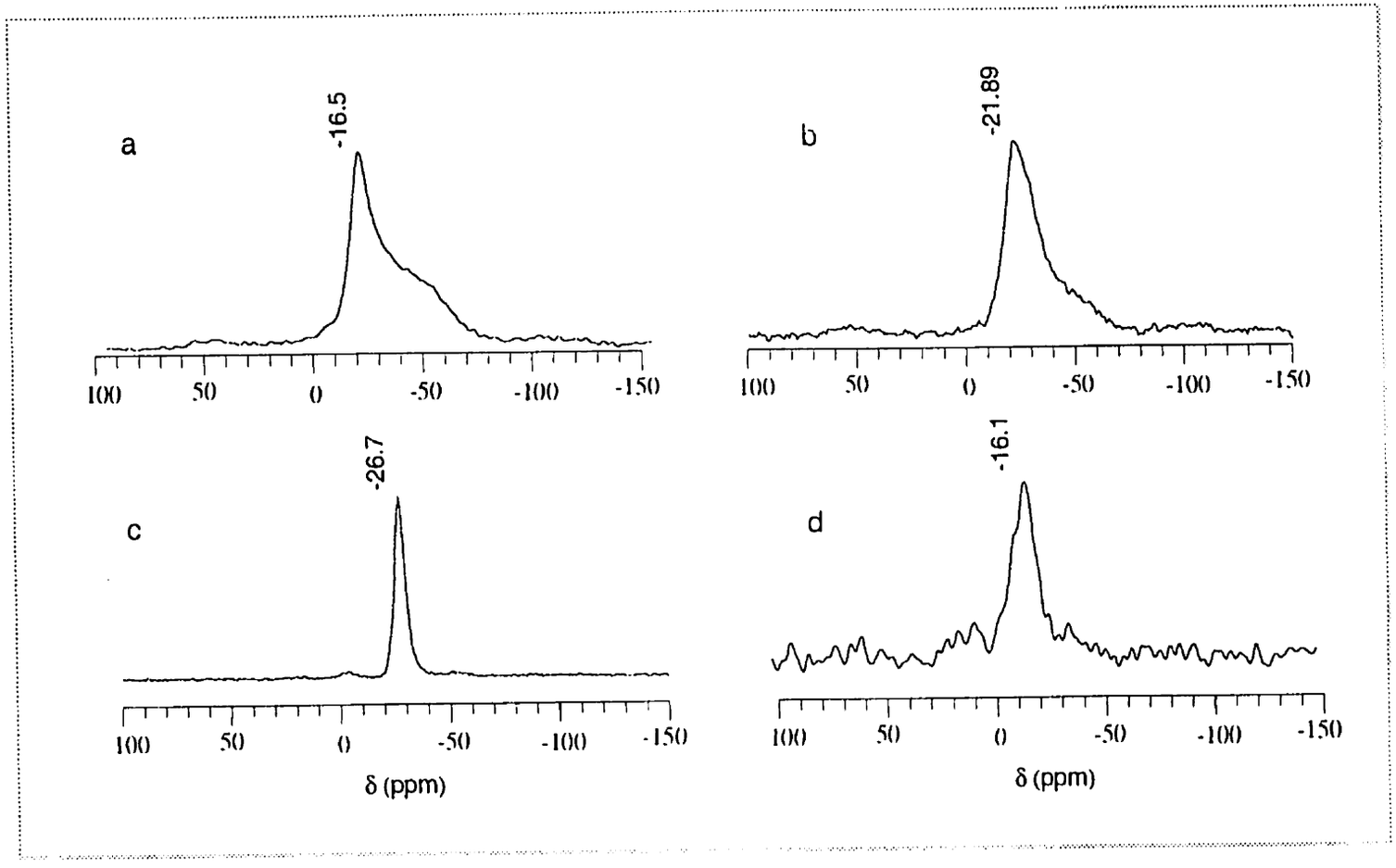

Figure 3.6 ^{23}Na MAS NMR spectra of (a) $[Na(H_2O)_n]_{0.25}MoO_3$ (n > 4) (air dried); (b) $[Na(H_2O)_n]_{0.25}MoO_3$ (n > 4) dried under vacuum at 130°C for 1 hr; (c) $[Na(H_2O)_n]_{0.25}MoO_3$ (n> 4) dried under vacuum at 130°C for 12 hr; (d) $(PEO)_{0.4}[Na(H_2O)_n]_{0.25}MoO_3$ dried under vacuum at 130°C for 12 hr

of the PEO oxygen atom and residual water molecules.

3.3.6 Proposed structural models for PEO between the MoO_3 sheets

PEO occurs in several conformations, the most stable being the helical configuration. The zigzag structure is observed only in stretched PEO.[21] Formation of a PEO/metal salt complex, however, can alter the conformation due to the interaction of the EO segments with the metal cation. When PEO is complexed to the mercury cation, for example, two types of structures have been identified, designated as type I and type II.[22, 26, 27] Formation of an alkali metal salt complex such as $LiBF_4$ or $LiClO_4$/PEO, however, results in a conformation comprised of helical turns.[39, 40] The PEO conformation is thought to be important to the ionic conductivity of the PEO/salt complex, although it should be noted that the highest conductivity occurs in the amorphous polymer state. Motion of the EO segments in the chain in particular conformations can enhance mobility of the cations or anions by a cooperative process.

On the basis of the XRD, IR and NMR data, we conclude that PEO does not adopt a helical conformation in the monolayer nanocomposite (12.9 Å phase). The strong IR band at 1305 cm^{-1} suggests the existence of trans O-$(CH_2)_2$-O units,[28] which are present only in the type I or zig-zag conformations; the fact that the strictly zig-zag conformation is only observed in stretched PEO films, and not in any metal salt complexe suggests that it is not a likely conformation in this case. In addition, the NMR data indicate that the polymer contains both complexed and uncomplexed units. The requirement based on the above formula (approximately 2:1 EO/Na) has led us to propose the following tentative model for the structure, shown in Figure 3.7.

In this model, the PEO chains adopt a type I -like conformation, with a Na cation residing in each pocket, probably alternately slightly above and below the plane of the polymer. This would give rise to a Na/PEO stoichiometry close to that observed. The shortest repeat distance between the sodium cations in $[Na(H_2O)_5]_{0.25}MoO_3$ is 5.48 Å along the 101 direction[20] which is similar to the repeat distance of 5.87 Å in the type I conformation.[22] We propose that the Na cation completes its coordination sphere through solvation by some additional water molecules. Such a "trilayer" of water-polymer/cation water is consistent with the observed interlayer distance of 12.9 Å, which is 1.7 Å larger than the interlayer spacing in $[Na(H_2O)_5]_{0.25}MoO_3$. It is also in good agreement with the thermal analysis results for the monolayer, which show that the incorporation of the PEO chains displace some, but not all, of the water molecules. The site for the Na cation is formed by a pocket of gauche PEO units. These segments would be constrained by complexation and hence could correspond to the upfield signal in the ^{13}C NMR spectrum at 66 ppm. Conversely, trans segments linking these pockets would not be complexed directly to the Na cation, and hence may undergo a higher degree of motion; these would give rise to the 71 ppm signal. We note that these arguments could probably be extended to the type II conformation, since both are similar and effectively planar structures in which complexes and uncomplexed segments could be envisaged. It is rather difficult to distinguish between them in this case; our NMR and IR data, however, are most consistent with a type I-like conformation. This model is easily extended to account for the

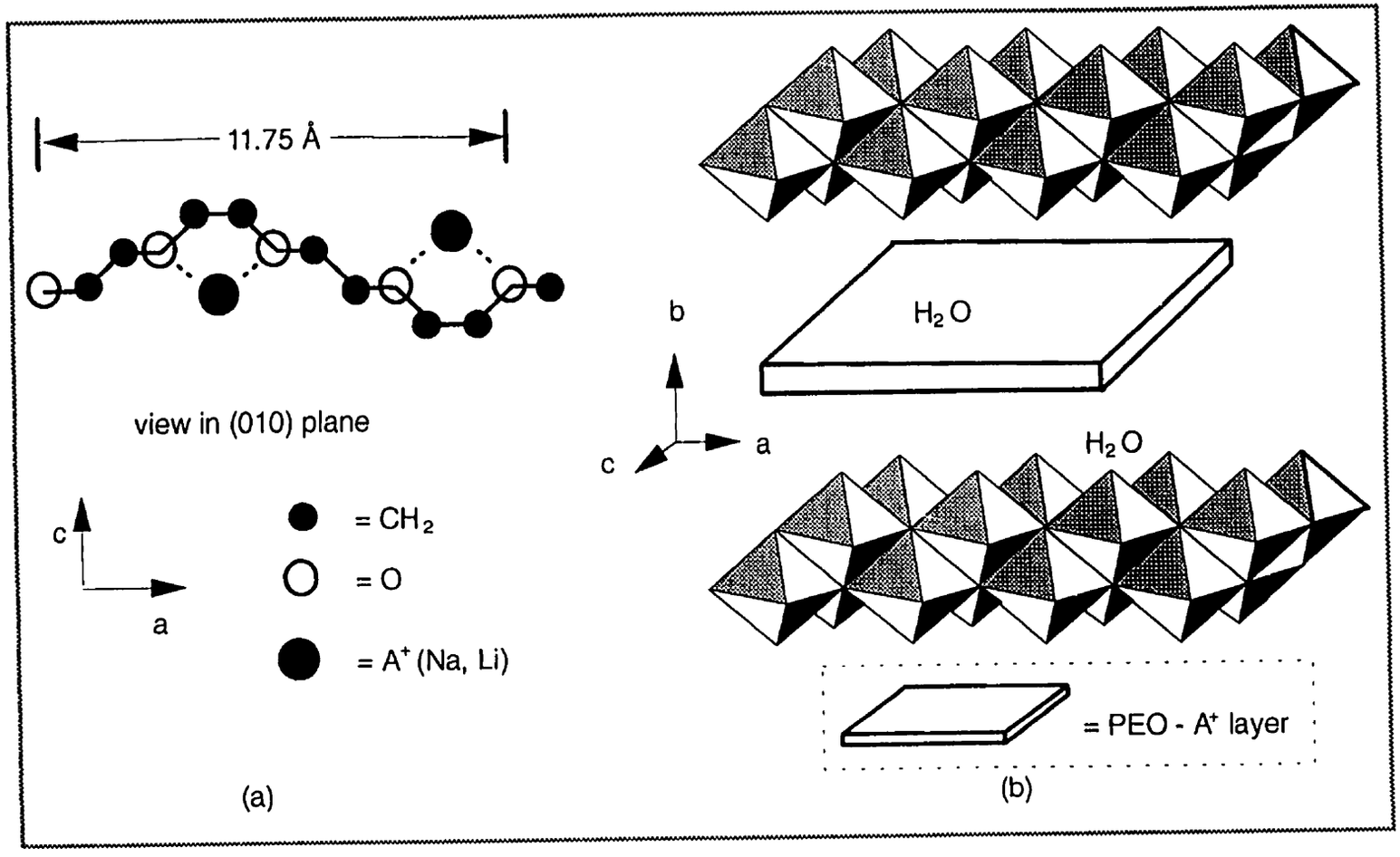

Figure 3.7 Schematic diagrams of the proposed structure of the monolayer $(PEO)_{0.4}[Na(H_2O)_n]_{0.25}MoO_3$ nanocomposite showing views of (a) the plane parallel to and midway between the MoO_3 sheets and (b) the view of the plane perpendicular to the MoO_3 sheets (*100*)

incorporation of a second layer of PEO between the MoO_3 sheets, aligned parallel to the first. In this case, the most likely site for the sodium cations would be sandwiched within the polymer bilayer, thus displacing additional water molecules from the sodium coordination sphere. Again, this is supported by the thermal analysis data, which indicates a very low water content for this material.

3.3.7 Conductivity

The charge transport characteristics of the nanocomposite were examined by two probe electrical conductivity measurements on thin films of the material. Variable temperature conductivity curves from 450K to 200K for $NaMoO_3$, the monolayer NC $(PEO)_{0.4}[Na(H_2O)]_{0.25}MoO_3$ and the bilayer NC $(PEO)_{0.9}[Na(H_2O)]_{0.25}MoO_3$ are shown in Figure 3.8. Conductivity data exhibit non-linear behavior with reciprocal temperature, probably as a result of both electronic and ionic contributions to the conductivity that cannot be resolved using these methods. The conductivity of the monolayer NC at low temperature is one order of magnitude lower than that of $NaMoO_3$, and at all temperatures, is higher than that of the bilayer NC. If we assume that the intercalation of the PEO does not affect the relative electronic energy levels of the MoO_3^{x-} layers, and that at low temperature the total conductivity is dominated by the electronic conductivity, the reduced conductivity of the nanocomosites at low temperature is primarily due to the dilution of the host by the electronically insulating polymer. This effect is clearly most evident for the bilayer nanocomposite that contains the largest amount of polymer. At high temperatures, however (>140°C), the conductivity of the monolayer reaches and surpasses that of $NaMoO_3$. Within the same temperature regime, the bilayer material exhibits a

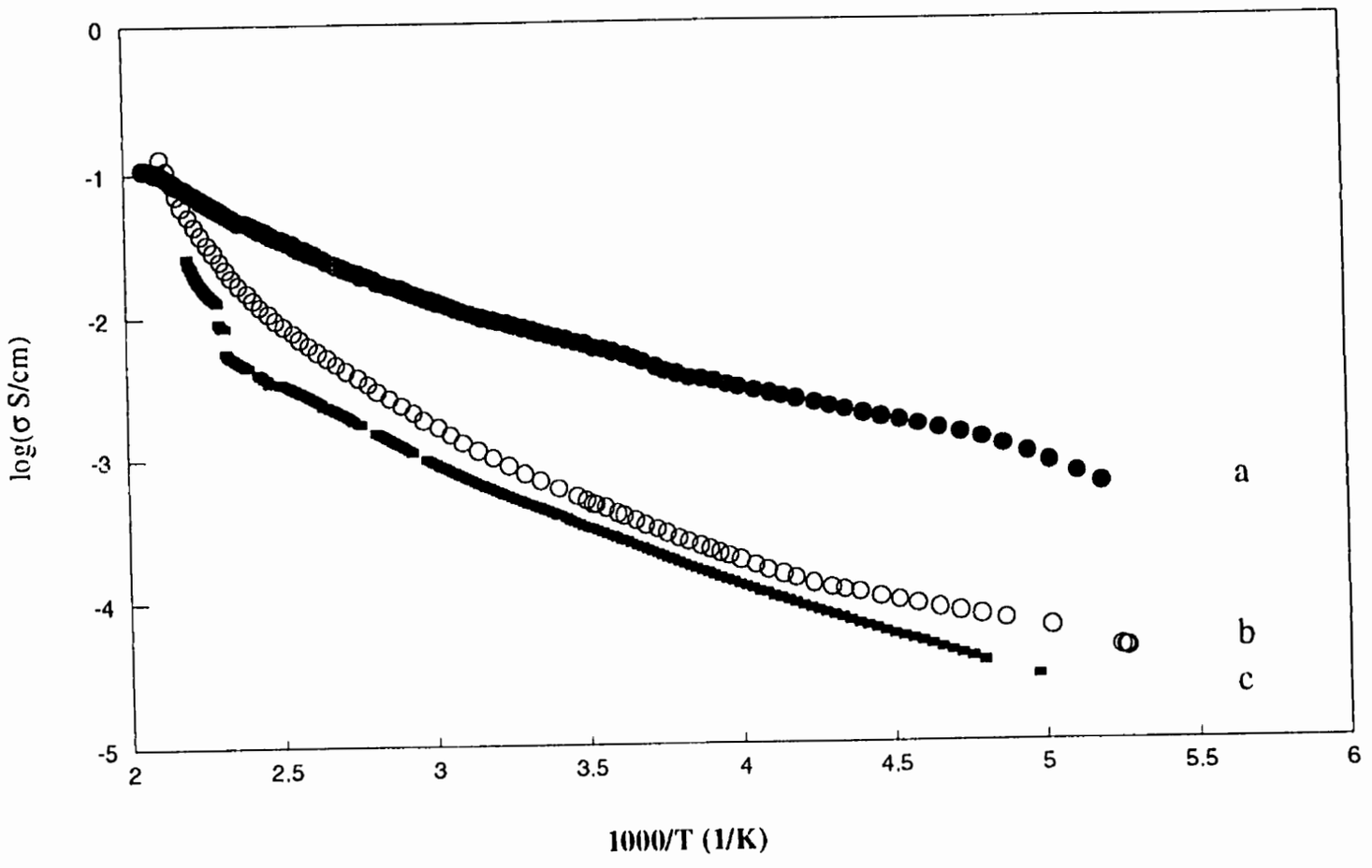

Figure 3.8 Two-probe variable temperature electrical conductivity data for thin films (glass substrate) of (a) $NaMoO_3$; (b) $(PEO)_{0.4}[Na(H_2O)_n]_{0.25}MoO_3$ and (c) $(PEO)_{0.9}[Na(H_2O)_n]_{0.25}MoO_3$

sharp, rather than a gradual increase in conductivity. We attribute this reversible process to a phase change. Although the details of the conductivity behavior cannot be unravelled at this point, it is clear that there is an increased contribution of the ionic conductivity component at higher temperature in both nanocomposites. It furthermore suggests that the ionic mobility is increased by intercalation of PEO, as a result of a weakened interaction of the Na^+ ions with the MoO_3^{x-} layers (as suggested by ^{23}Na MAS NMR), arising from Na^+ coordination to the PEO chains.

Extensive electrochemical measurements as well as solid state ^7Li NMR measurements of the lithium ion dynamics in these nanocomposites will be discussed in subsequent chapters.

3.4 Conclusion

By controlling the degree of swelling of MoO_3 sheets with mixed solvents, different molar ratio of Li/Na in (Li, Na)MoO_3, both monolayer and bilayer PEO/MoO_3 nanocomposites were prepared. A structural model for the nanocomposites were proposed based on powder XRD, solid state ^{13}C, ^{23}Na NMR, and FTIR data.

3.5 References

1. Whittingham, M. S. *Prog. Solid State Chem.* **1978**, *12*, 41.

2. Walk, C. R. *Lithium Batteries*, Gabano, J. P. Editor, Academic Press, Inc., New York (1993)

3. Delmas, C. *Lithium Batteries*, Editor G. Pistoia, Elsevier, Industry Chemistry Library, **vol. 5, 1994.**

4. Murphy, D. W.; Christain, P. A.; DiSalvo, F. J.; Carides, J. N. *J. Electrochem. Soc.* **1979**, *126*, 497.

5. West, K.; Zachau-Christiansen, B.; Jacobsen, T. *J. Electrochem. Soc.* **1983**, *28*, 1829.

6. Garcia-Alvarado, F.; Tarascon, J. M.; Wilkens, B. *J. Electrochem. Soc.* **1992**, *139*, 3206.

7. Maingot, S.; Baddour, R.; Pereira-Ramos, J. P.; Baffier, N.; Willimann, P. *J. Electrochem. Soc.* **1993**, *140*, L158.

8. Julien, C.; Nazri, G.A.; Guesdon, J.P.; Gorenstein, A.; Khelfa, A.; Hussain, O.M. *Solid State Ionics* **1994**, *73*, 319.

9. West, K.; Zachau-Christiansen, B.; Skaarup, S.; Jacobsen, T. *Solid State Ionics* **1992**, *53*, 356.

10. Mizushima, K.; Jones, P. C.; Wiseman, P. J.; Goodenough, J. B. *Mater. Res. Bull.* **1980**, *15*, 783.

11. Guyomard, D.; Tarascon, J. M. *J. Electrochem. Soc.* **1992**, *139*, 937, and references therein.

12. Aranda, P.; Ruiz-Hitzky, E. *Adv. Mater.* **1990**, *2*, 545.

13. Aranda, P.; Ruiz-Hitzky, E. *Chem. Mater.* **1992**, *4*, 1395.

14. Giannelis, E. P.; Mehrotra, V.; Tse, O. K.; Vaia, R. A.; Sung, T. C. in *Synthesis and processing of ceramics; Scientific Issues*, Rhine, W. E. et al., eds., MRS Symp. Proceedings, **1992**, *249*, 547.

15. Liu, Y. J.; Degroot, D. C.; Schindler, J. L.; Kannewurf, C. R.; Kanatzidis, M. G. Chem. Mater. 1991, 3. 992.

16. West, K.; Zachau-Christiansen,B.; Jacobsen, T. Skaarup, S. *Electrochim. Acta* **1993**, *38*, 1215.

17. Ruiz-Hitzky, E. *Adv. Mater.* **1993**, *5*, 334.

18. Thomas, D. M.; McCarron, E. M. *Mat. Res. Bull.* **1986**, *21*, 945.

19. BIO-LOGIC, Ave. de l'Europe, F-38640 Claix, France.

20. Sotani, N.; Eda, K.; Kunitomo, M. *J. Solid State Chem.* **1990**, *89*, 123.

21. Takahashi, Y.; Sumita, I.; Tadokoro, H. *J. Poly Sci. Polymer Physics* **1973**, *11*, 2113.

22. Yokoyama, M.; Ishihara, H.; Iwamoto, R.; Tadokoro, H. *Macromolecules* **1969**, *2*, 184.

23. Nazar, L. F.; Zhang, Z.; Zinkweg, D. *J. Am. Chem. Soc.* **1992**, *114*, 6239.

24. Lagadic, I.; Leaustic, A.; Clement, R. J. *J. Chem. Soc., Chem. Commun.* **1992**, 1396.

25. Lemmon, J. P.; Lerner, M. M. *Chem. Mater.* **1994**, *6*, 207.

26. Iwamoto, R.; Saito, Y.; Ishihara, H.; Tadokoro, H. *J. Poly. Sci.* **1968**, *6*, 1509.

27. Blumberg, A. A.; Pollack, S. S.; Hoeve, C. A. J. *J. Poly. Sci.* **1964**, *2*, 2499.

28. Papke, B. L.; Ratner, M. A.; Shriver, D. F. *J. Phys. Chem. Solids* **1981**, *42*, 493.

29. Johannson, A.; Tegenfeldt, J. *Macromolecules* **1992**, *25*, 4712.

30. Krane, J.; Amble, E.; Dale, K.; Daasvatn, K. *Acta Chem. Scand.* B. **1980**, *34*, 255.

31. Bjorling, M.; Karlstrom, G.; Linse, P. *J. Phys. Chem.* **1991**, *95*, 6706.

32. Ibemesi, J. A.; Kinsinger, J. B. J. *Poly. Sci. Poly. Chem. Ed.* **1980**, *18*, 1123.

33. Stark, R. E.; Greenbaum, S. G.; Pak, Y. S. *Solid State Ionics* **1989**, *34*, 275.

34. Dechter, J. J. *J. Poly. Sci. Poly Lett. Ed.* **1985**, *23*, 261.

35. Komoroski, R. A.ed.; *High Resolution NMR Spectroscopy of Synthetic Polymers in Bulk*, VCH Publishers, **1987**.

36. Akitt, J. W. in "*Multinuclear NMR*", Mason, J. ed., Plenum Press, N. Y., N. Y. **1987**, page 206.

37. Behrens, H. J.; Schnabel, B.; *Physica* **1982**, *114b*, 185.

38. Greenbaum, S. G.; Pak, Y. S.; Adamic, K. J.; Wintersgill, M.C.; Fontinella, J. J. *Solid State Ionics* **1988**, *31*, 241.

39. Zahurak, S. M.; Kaplan, M. L.; Rietman, E. A.; Murphy, D. W.; Cava, R. J. *Macromolecules* **1988**, *21*, 654.

40. Gorecki, W.; Belorizky, E.; Berthier, C.; Donoso, P.; Armand, M. *Electrochem. Acta* **1992**, *37*, 1685.

41. Laperche, V.; Lambert, J. F.; Prost, R.; Fripiat, J. J. *J. Phys. Chem.* **1990**, *94*, 8821.

42. Colson, S.; Szu, S.-P.; Klein, L. C. *Solid State Ionics* **1991**, *46*, 283.

43. Kline, D.; Story, H. S. J. Chem. Phys. 1972, 57, 5180.

44. Schcherbakov, V. N.; Gabuda, S. P.; Seryshev, S. A. *Sov. Phys. Solid State* **1971**, *12*, 2477.

45. Gabuda, S. P.; Grinchenko, I. V.; Schcherbakov, V. N. *Sov. Phys. Solid State* **1969**, *11*, 663.

CHAPTER FOUR

PEO LITHIUM (SODIUM) COMPLEXES/ELECTRONIC CONDUCTIVE HOST NANOCOMPOSITES (II)

-- Solid State NMR Spin-lattice Relaxation and Linewidth Studies of PEO/MoO_3 Nanocomposites

4.1 Introduction

Wright's first disclosure of the conductivity of the polyethylene oxide (PEO)-NaI complexes twenty four years ago have stimulated a widespread and sustained interest within the scientific community for solid polymer electrolytes, i.e., the ionic conductors resulting from the complexation of low lattice-energy salts with solvating polymers. So far, PEO, which has extremely strong solvation properties for a wide variety of salts through interaction of the ether oxygen with cations, is still the most widely studied polymer matrix for solid polymer electrolytes. Combining the achievements from the last decade of insertion of polymer into layered metal oxides and the high ionic conductivity of PEO-alkali cation complexes, we have successfully inserted the ionic conductive PEO-alkali cation complexes into MoO_3 to improve the ionic conductivity of metal oxides which are potentially useful candidates as cathode materials in secondary lithium batteries.[1] Improved ionic conductivity is a requisite for many potential cathode materials such as metal oxides in secondary lithium batteries. For example, MoO_3 is a potentially useful cathode in secondary lithium batteries; however, its use is hindered by its low ionic

ionic conductivity of metal oxides such as MoO_3, and V_2O_5 by intercalating polyoxymetal cations or electronically conductive polymers such as polypyrrole or polyaniline into the host materials.[1,2] In some cases, both the energy density and cyclability of secondary lithium batteries have been improved. The synthesis and characterization of PEO/MoO_3 have been described in the previous chapter. In this chapter, we will report the mobility of lithium/sodium cations in PEO/MoO_3 nanocomposites probed by ^{7}Li, ^{23}Na NMR T_1 and linewidth measurements.

Much effort has been applied to probe the cation mobility of the PEO/Li(Na) complexes by NMR methods.[3, 4] ^{7}Li, and ^{23}Na NMR have been shown to be effective methods for probing the dynamic behavior of ions in solid electrolytes in general[5] and polymer electrolytes in particular.[6, 7] NMR studies have, in general, contributed to the advancement of solid polymer electrolytes. PEO is semicrystalline under ambient temperature conditions and forms crystalline complexes with most of the salts used as ionic dopants. These complexes are well defined materials that do not contribute to the ionic conductivity, which, as shown by their recently determined structure, are quite satisfactorily explained by the total occupancy of the solvation sites.[8, 9] With the aid of NMR studies, it has been recognized that in such electrolytes ionic transfer occurs in the amorphous polymer regions and is very often governed by the segmental motions of polymer chain.[6, 10] Many different methods have been proposed to inhibit the crystallization of PEO based electrolytes: decreasing the molecular weight, increasing the length of the carbon units and using branched polymers which resulted in the studies of poly(propene oxide) (PPO)$_n$ adding inorganic fillers.[11, 12, 13] By the use of ^{23}Na NMR the

presence of both bound and mobile sodium in polymer electrolytes has been demonstrated.[22] The two ^{23}Na resonances are characterized by vastly different spin-lattice relaxation times (T_1). The short T_1 (~0.2-30 ms) component is slightly narrower than the long T_1 (~1 s) component at low temperature, and undergoes substantial motional narrowing above T_g. The linewidth of the long T_1 resonance, on the other hand, does not appear to have a pronounced temperature dependence. The short T_1 narrow line is therefore attributed to mobile Na^+ ions, while a bound Na configuration gives rise to the broad line.

Recent advances in polymer electrolyte NMR studies have helped elucidate the detailed understanding of ionic transport mechanisms and relaxation mechanisms of solid polymer electrolytes. Particularly, the relationship between structural relaxation and the glass transition temperature has been studied. A change of relaxation behavior around a critical temperature (T_c) at about 1.2 T_g was observed by ^{23}Na, and ^7Li NMR T_1 and linewidth studies for poly(propylene oxide)-$NaClO_4$ and poly(propylene-glycol)-$LiCF_3SO_3$.[14, 15] This anomalous behavior, showing the crossover in dynamics around the glass transition temperature, [16, 17] has been observed for various organic and inorganic compounds from viscosity measurements,[18] dielectric relaxation studies,[19] light scattering experiments,[20, 21] neutron scattering experiments,[23, 24] and NMR measurements.[25, 26, 27, 28] Several theories to describe this change in relaxation behavior have been proposed to explain the phenomena. In the fluid regime, an Arrhenius law is well-established for higher temperatures,[29] but it fails to describe the relaxation data around the glass transition temperature region. The equation most used to extend the fit is

the Vogel-Fulcher equation $\eta=\eta_o \exp[C/(T-T_\infty)]$.[30, 31] The reference temperature T_∞ lies in most cases well above the transition temperature T_g, thus, this formula cannot describe the systems with a viscosity above 10^4 Poise.[32] In the frame of the free-volume theory, namely the Williams-Landel-Ferry approach, and the excess entropy theory of the glass transition, a equation similar to the Vogel-Fulcher equation is derived, but in this case T_∞ is well below the glass transition point T_g.[33] This formula fails to describe the data at higher temperatures in the fluid regime. Recently, the mode coupling theory attracted a lot of attention to explain the phenomena. According to mode coupling theory (MCT), the mechanism of dynamic relaxation changes from "liquid-like" to "glass-like" at some critical temperature $T_c>T_g$. In its idealized form, the MCT envisages the particles of the fluid below T_c as being permanently trapped in cages formed by their neighbors. And above T_c, the particle can escape out of the cage due to the softening of the cage. That is, ionic transport in alkali metal-doped polymer electrolytes results from a coupling of the ions to polymer segmental relaxation above T_c and from thermally activated hopping below T_c. Within this theoretical approach, the singularity at a transition temperature T_c governs the dynamics of the liquid at high temperatures and a power law, i.e., $\eta \propto (T-T_c)^{-\gamma}$ is predicted. For temperatures below T_c, a thermally activated "hopping" mechanism is assumed which leads to a smearing out of the ideal glass transition and an Arrhenius behavior is anticipated near T_g. Hence, two different dynamic regimes emerge from this theory for the glass transition. For the mobility of cations in a PEO complex, the cation is expected have a different motion scale than the polymer. At low temperatures, even when the polymer is totally rigid, the cations still can move in the restricted environment. This

motion is expected to affect the relaxation process until the motions of the polymer play a major role. In this sense, the critical temperature is expected to be better defined in solid polymer electrolytes than in organic polymers.

Problems have been, in general, encountered in relating NMR linewidth and spin-lattice relaxation times in polyether electrolytes with ionic conductivity for most materials studied with these methods. Particular problems for NMR studies in solid polymer electrolytes are the complexity of the morphology of polymer, and the absence of a minimum in the observed spin lattice relaxation time, T_1, data. The principal difficulty, however, is connected with relating NMR T_1 and linewidth parameters to long range diffusion of cations. Because the dominant relaxation mechanisms, such as dipole-dipole and quadrupolar interactions are short range, NMR may be sensitive only to localized motion. Generally, caution must be exercised in using ^{7}Li, ^{23}Na T_1 and linewidth measurements to probe ionic mobility as the existence of a crystalline phase, aggregation of cations, and/or different relaxation mechanisms at different temperatures may be involved.

In PEO/MoO_3 systems, PEO/Li(Na) is in a restricted environment defined by MoO_3 sheets. Also due to the confined space for cations within MoO_3 sheets, the aggregation of cations is unlikely, which simplifies the situation and allows us to have a deeper look at the relaxation mechanisms.

4.2 Experimental

The NMR experiments were performed at 194.0 MHz and 132.3 MHz for ^{7}Li and ^{23}Na, respectively, on a Bruker AMX-500 spectrometer equipped with a solids accessory

rack and Bruker MAS (magic angle spinning) multinuclear probe. Standard inversion-recovery pulses were used for the T_1 experiment and a single one pulse for line width measurements. Full widths at half-maximum (FWHM) were then determined from expanded plots. All linewidths reported in this study are FWHM.

4.3 Results and Discussion

4.3.1 ^{7}Li NMR spin-lattice relaxation studies of bilayer nanocomposite $(PEO)_{0.9}(Li,Na)MoO_3$

Spin-lattice relaxation of a system of nuclei with spin number I > 1/2 occurs via a magnetic interaction between the nuclear magnetic moments and fluctuating local magnetic fields, and via a quadrupolar interaction between the nuclear electric quadrupolar moments and fluctuating local electric field gradients. Both relaxation processes can produce a non-exponential magnetization recovery. Under the experimental conditions of our study, i.e., the initial condition of the spin system is taken to be the result of the application to the system in the thermal equilibrium of a "θ - degree radio frequency pulse", , a biexponential magnetization recovery is expected for magnetic relaxation:[34]

$$M(t)/M_0 = 1 - 0.1\exp(-2wt) - 0.9\exp(-12wt)$$

For a quadrupolar relaxation mechanism, the spin-lattice relaxation is also biexponential:

$$M(t) - M_o = M_o(\cos\theta - 1)[\tfrac{4}{5}\exp(-a_1 t) + \tfrac{1}{5}\exp(-a_2 t)$$

where

$$a_1 = 2(eQ/\eta)^2 J(2\omega_{\eta})$$

$$a_2 = 2(eQ/\eta)^2 J(\omega_\eta)$$

For the inversion-recovery experiment, $\theta = 180°$, letting T_{1f} stand for the fast relaxation time and T_{1s} for the slow relaxation time, we obtain

$$\frac{M(t)}{M_o} = 1 - 2 \times 0.8 \exp(-t / T_{1s}) - 2 \times 0.2 \exp(-t / T_{1f})$$

Therefore, generally, for quadrupolar nuclei, a biexponential magnetization recovery is expected except for an extremely narrow region. Two T_1 values can be obtained by fitting the magnetization recovery data. From the above equations, we know that

$$1/T_{1s} = 2(eQ/\eta)^2 J(2\omega_0)$$

$$1/T_{1f} = 2(eQ/\eta)^2 J(\omega_\eta)$$

Therefore the BPP model still holds for two separate T_1s. At high temperature these T_1s become equal.

In the inversion-recovery method which we used to measure the T_1, the following pulse sequence was employed:

$(\pi - \tau - \pi/2 - A_t - D)_n$ with $A_t + D \geq 5T_1$

The equilibrium magnetization is first inverted by a π pulse and is then allowed to recover during a time delay τ. The following pulse $\pi/2$ projects the recovered magnetization into the xy plane. The signal intensity is a function of the recovery time τ. The intensity of the recorded signals follows a simple exponential accumulation function:

$$I_\tau = I_o[1 - 2A \exp(-\tau / T_1)]$$

where I_τ is the intensity of a signal after delay τ, I_o is the intensity of the signal when the spins have fully recovered, and A is a fitting parameter which is close to unity. The relaxation time T_1 is then obtained by a semilogarithmic or an exponential fitting of the data. For a multiexponential system, the following equation can be written for the signal intensity:

$$I_\tau = \sum I_{o,i}[1 - 2A_i \exp(-\tau / T_{1,j})]$$

Relaxation times T_1 are obtained by multiexponential fitting.

However, deviations from a single exponential are often hard to detect for ^{7}Li, because ^{7}Li has a relatively small quadrupolar moment and strong dipole-dipole interactions. Figure 4.1 shows the plot of the ^{7}Li magnetization of a bilayer $(PEO)_{0.9}(Li,Na)MoO_3$ nanocomposite and the fitted curve to a single exponential decay. We also tried to fit the Li magnetization recovery function of the bilayer $(PEO)_{0.9}(Li,Na)MoO_3$ nanocomposite with two T_1's; however, this did not improve the fitting in comparison to the one T_1 fitting. This can be due to the inhomogeneous character of the bilayer $(PEO)_{0.9}(Li,Na)MoO_3$ nanocomposites. It requires a distribution of correlation times leading to a different form of $G(t) = \exp[-(t/\tau_c)]$. Strictely, therefore the BPP model is not suitable to this kind of materials, because the BPP model spontaneously suggested the single exponential correlation function. Therefore we could be using an apparent single correlation time to represent the distribution of correlation times, which is

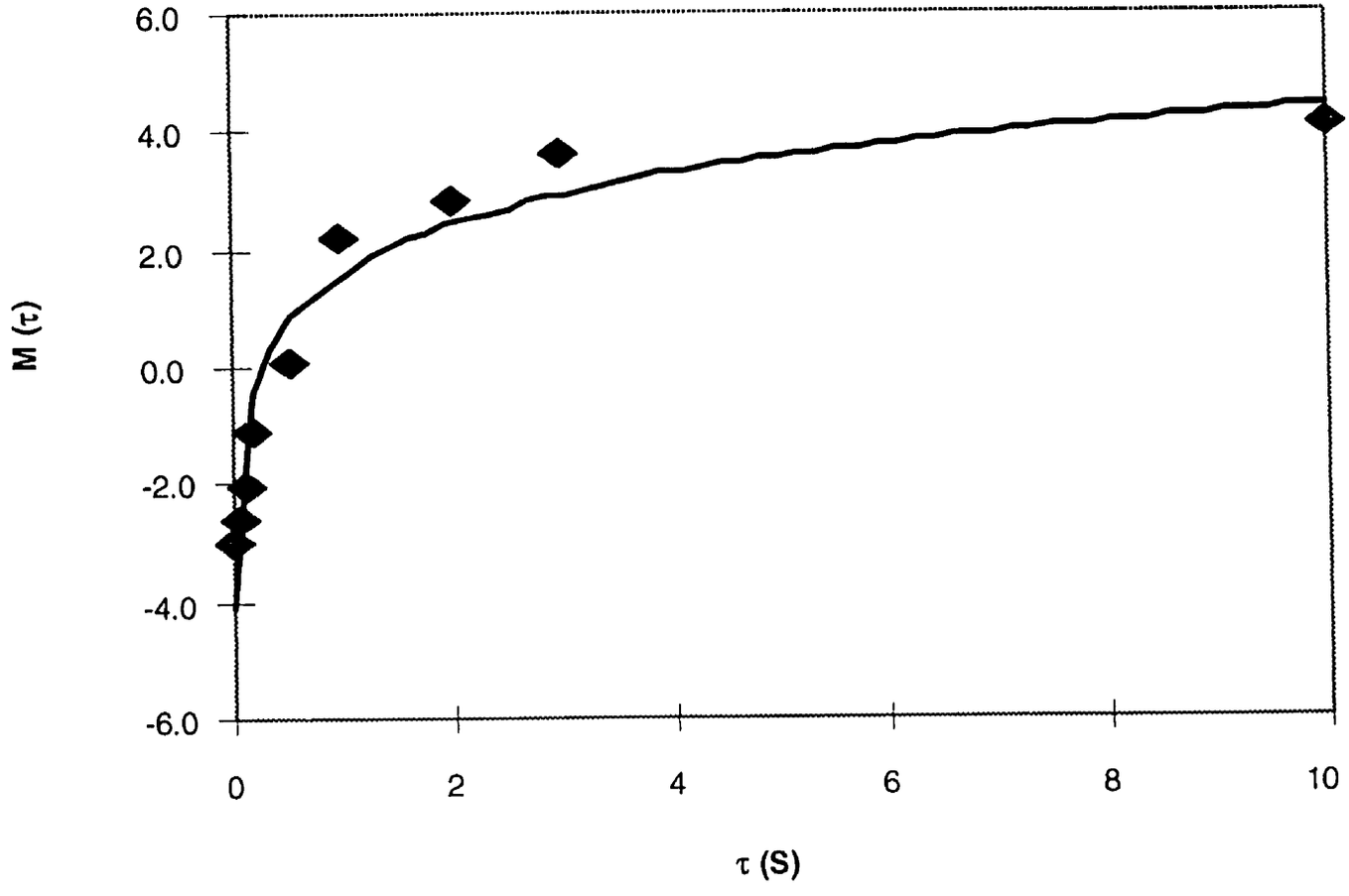

Figure 4.1 Plot of intensity of ^{7}Li NMR magnetization vs. pules time delay τ in π-τ-$\pi/2$ pulse and the fitted curve with single exponential decay for bilayer nanocomposite $(PEO)_{0.9}(Li,Na)MoO_3$

a reasonable approximation for this kind of material. This kind of single exponential approximation has been used to account for ^{7}Li NMR spin-lattice relaxation in other polyether complexes.[36, 15, 38, 39, 39] In the discussion which follows, the ^{7}Li magnetization was determined to relax with a single time constant T_1 at all temperatures studied.

Spin-lattice relaxation times were measured over the temperature range between 230 to 410K. The T_1 measured at 194.0 MHz are shown in Figure 4.2 as a function of reciprocal temperature. In solid superionic conductors, NMR measurements have been used to probe the dynamic processes through their contribution to the spin-lattice relaxation times, T_1. With the NMR one can, with the same instrument, examine both the static structural features of solid polymer electrolytes as well as the dynamics of the ionic conduction process.

Bloembergen, Purcell, and Pound were the first to relate the spin-lattice relaxation to ionic motions and described in terms of a correlation function G(t). By assuming that the magnetization decays exponentially and that the nuclei are interacting with a randomly distributed (amorphous) lattice, they arrived at the general expression for spin-lattice relaxation rate:

$$1/T_1 = \tfrac{3}{2}\gamma^4 h^2 I(I+1)[J_1(\omega_0) + \tfrac{1}{2}J_2(2\omega_0)$$

$1/T_1$ depends on the spectral densities, $J_i(\omega)$, which in turn implies usage of different time correlation functions $G(\tau)$ as shown by the following equation:

$$J_o(\nu) = \int_{-\infty}^{+\infty} G(\tau) e^{i2\pi\nu\tau} d\tau$$

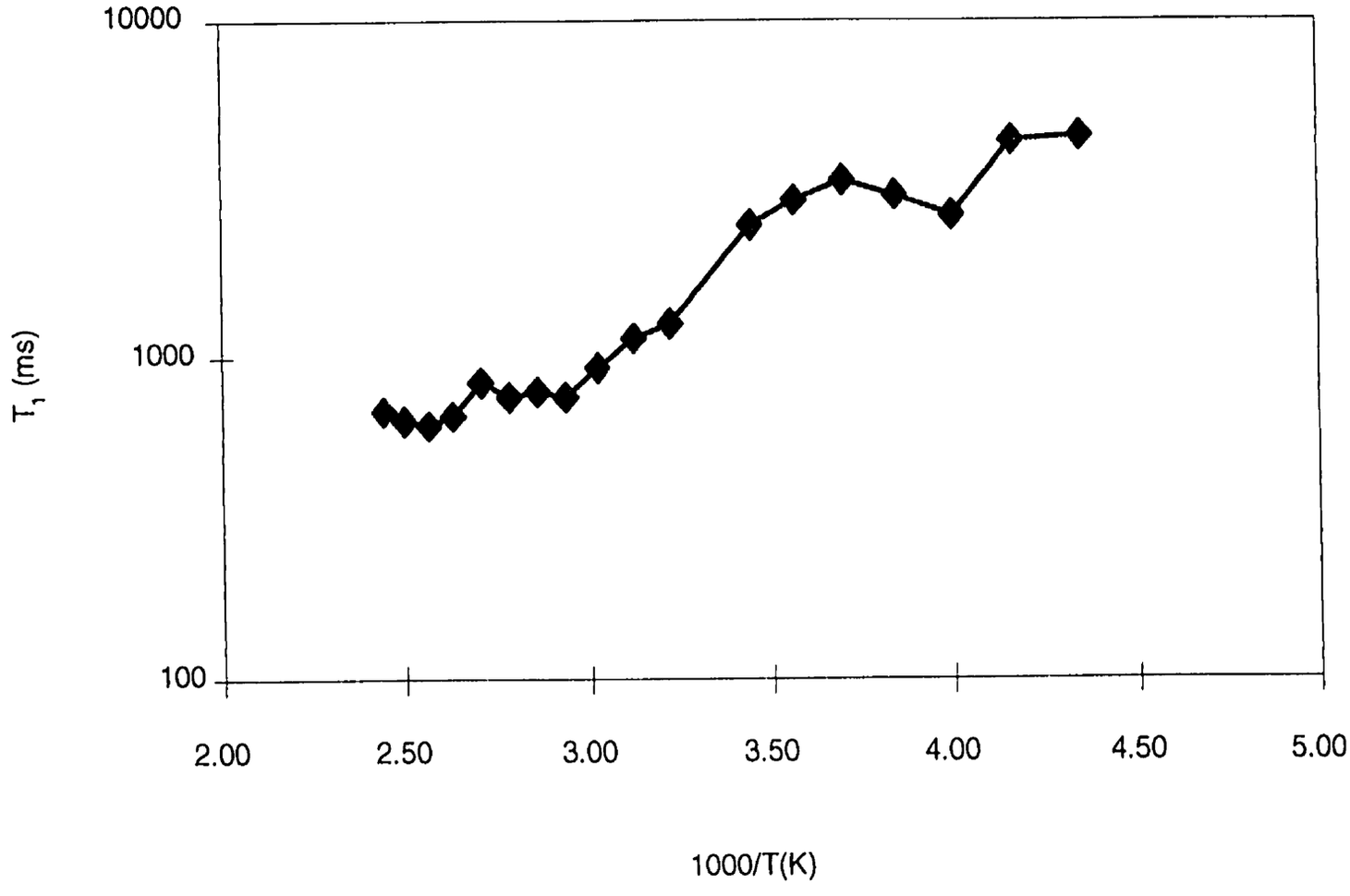

Figure 4.2 ^{7}Li nuclear spin-lattice relaxation times as a function of inverse temperature for bilayer nanocomposite $(PEO)_{0.9}(Li,Na)MoO_3$

The BPP model uses the (Debye) exponential correlation function:

$$G(\tau) = \exp(-\tau / \tau_c)$$

the relaxation rate $1/T_1$, becomes a simple function of the correlation time τ_c:

$$\frac{1}{T_1} = C\left(\frac{\tau_c}{1+\omega_0^2\tau_c^2} + \frac{4\tau_c}{1+4\omega_0^2\tau_c^2}\right) \qquad (4.1)$$

where ω_0 is the Larmor frequency of the observation, and the prefactor C depends on the spin interaction responsible for the relaxation. For ^{7}Li, C can be dominated either by the local electric field gradient (EFG) or by the magnetic dipolar field. The interpretation of the resulting correlation time τ_c depends on the form of the correlation function. Where the BPP theory applies, and the temperature dependence of the correlation time is given by the Arrhenius Law

$$\tau_c = \tau_{c0} \exp^{E_A/RT}$$

plots of $\ln(1/T_1)$ vs. $1/T$ are linear with a low temperature slope of $-E_a/R$. BPP expressions were fitted to our data, and the resulting E_a and τ_0 are summarized in Table 4.1. The simple BPP model has been shown to describe well the ^{7}Li NMR spin-lattice relaxation for the confined polymer electrolyte, which is the only study that has been performed on materials such as these PEO/MoO_3 nanocomposites.[38] Chung *e. al.*[15] have also used the BPP model to explain their ^{7}Li spin-lattice relaxation data for polyether electrolytes and indicated that their effort to use the Vogel-Tamman-Fulcher (VTF) form:

$$\tau_c = \tau_o \exp[B / K(T - T_o)]$$

Table 4.1 Dynamic Parameters from T_1 and Linewidth Analysis

Nuclei	Sample	E_a (kJ/mol)	τ_0 (10^{-13} s)	reference
		T_1 analysis		
^{7}Li	Bilayer PEO/MoO_3	16.6 ± 0.3	32.95 ± 1.0	this work
^{23}Na	Bilayer PEO/MoO_3	19.6 ± 0.4[1]		this work
^{23}Na	Bilayer PEO/MoO_3	26.3[2] ±0.5	311.3 ± 9.0	this work
^{7}Li	PEO:Li-fluorohectorite	22.1 ± 0.5	5.3 ± 0.9	38
^{7}Li	PEO:$LiClO_4$	27.7 ± 0.1	1.9 ± 0.1	42
^{7}Li	PEO:$LiCF_3SO_3$	24.1 ± 5.8	14.2 ± 1.6	15
		Linewidth Analysis		
^{7}Li	Bilayer PEO/MoO_3	19.6 ± 1.0	124000 ± 6200	this work
^{7}Li	PEO:Li-montmorillonite	26.7 ± 1.8	5700± 4600	38
^{7}Li	PPG:$LiCF_3SO_3$	32.8 ± 10.0	8.0 ± 5.0	15

[1] Determined from the temperature range of 290-340K

[2] Determined from temperature range of 350-420K

to fit T_1 data was unsuccessful. However, they pointed out that a distribution of τ_c's may be more appropriate, as was found to be the case in ^{109}Ag NMR studies of silver borate superionic conductors.[40] To verify this, measurements at higher temperatures are needed as well. Later, reexamining the data, they[14] pointed out that the turning point in their ^7Li T_1 data using the BPP model was significant and can be explained with mode coupling theory, which we will discuss later in some detail.

The activation energy, thus obtained for bilayer $(PEO)_{0.9}(Li,Na)MoO_3$ nanocomposite from ^7Li T_1 data in the temperature range of 280K to 360K is 16.6 kJ/mol, about one third lower than the corresponding data in the literature listed in Table 4.1, which suggests that the relaxation process does not correspond to the cation mobility. The activation energy probed by T_1 in this temperature range for the confined PEO complexes is different from the bulk solid polymer electrolytes, while Wong *et al.*[37] have found that they are similar for PEO:Li-montmorillonite and deuterated PEO:Li-fluorohectorite confined PEO electrolytes and general PEO electrolytes. The τ_o values however are consistent with most T_1 analyses of SPEs, which find $\tau_0 \approx 10^{-12} \sim 10^{-13}$ s. This indicates that the dynamic process probed by T_1 is the same for these materials. It has been pointed out that the dynamic process in this frequency region is very different from that corresponding to the bulk conductivity and that the dynamic processes in this region are very frequency-dependent. Through the ^7Li NMR linewidth experiments, we will show later that a much slower dynamic process than a spin-lattice relaxation process can be detected.

Careful inspection of the ln (T_1) vs. 1000/T(K) plot for ^{7}Li NMR of the bilayer $(PEO)_{0.9}(Li,Na)MoO_3$ nanocomposite shows "turning points" on the plot, which is significant for the nanocomposite as can be seen from the following discussion.

It has been argued in other studies of ^{7}Li spin-lattice relaxation in aqueous systems that both the dipolar and the nuclear quadrupolar interactions are important.[41] Unfortunately, it is difficult to distinguish the two modes of relaxation because both interactions have the same frequency dependence. However, experimental data for solid polymer electrolytes suggested that the ^{7}Li relaxation process is dominated by the molecular reorientation through the modulation of the quadrupolar interaction by the fluctuations of the electric field gradient at the nuclei sites for these materials. Chung *et al.* [15] have indicated that the spin-lattice relaxation is governed by quadrupolar coupling between Li^+ nuclear moments and the polymer lattice for the poly(propylene glycol)-$LiCF_3SO_3$ complex by comparing the experimental $T_{1,min}$ with that calculated by using the second moments of the static linewidth as a measure of the strength of the interaction. This has also been demonstrated by complete deuterated $(PEO)_8LiClO_4$, which produces no measurable effects on the T_1 relaxation times of the ^{7}Li nuclei.[42] Further agreement in ^{7}Li spin-lattice relaxation studies of solid polymer electrolytes is that the fluctuating fields responsible for ^{7}Li spin lattice relaxation are the same for both the cation and the polymer. It is attributed to the dynamics of the polymer. This is reiterated in the recent confined polymer electrolyte studies. EXAFS studies of PEO-based SPEs confirm the solvation of cations by the oxygen as are found in Li^+-crown ether complexes.[43] Therefore the local environment contributing to the EFG arises from interactions with the lone pair electrons

of oxygen in the PEO backbone. Motion of either Li or the polymer will relax the ^{7}Li nuclei equivalently whether the relaxation mechanisms dominate by the dipolar interaction or by the quadrupolar interaction. Using deuterated PEO, Wong *et al.*[37] found that the values for E_a and τ_o are sufficiently similar for ^{2}D and ^{7}Li NMR spin-lattice relaxation that a single process causes the fluctuating fields at both nuclei; because the lone pair electrons from oxygen in the PEO backbone contribute to the EFG at the Li sites, motion of either the Li or the polymer will relax the ^{7}Li nuclei equivalently.[37]

The cause of the fluctuation of the local magnetic field which induces the spin-lattice relaxation would not be the same over the large temperature window. This is documented with many studies performed on glass-forming materials, including inorganic solid superionic conductors, solid polymer electrolytes, and organic polymers with various methods of physical measurement such as viscosity studies, neutron-scattering experiments, dielectric constant studies and NMR relaxation studies. An anomalous behavior of the crossover dynamics was observed at a certain temperature, namely, T_c which is about 1.2 T_g. These observations have catalyzed the development of mode coupling theory, which states that there is a critical temperature at which the mechanism of a dynamic process changes. In its idealized form, the MCT envisages the particles of the fluid below T_c as being permanently trapped in cages formed by their neighbors. Because particles have no chance to escape, density fluctuations no longer totally decay. Above T_c the density fluctuations always decay to zero because the cages only succeed in localizing the particles for a finite time.

If the change of mechanism ascribed to a critical temperature is somewhat more artificial for polymers, this could be more true for alkali metal-doped polymer electrolytes. Although, either the motion of cations or of the constituent atoms changing the EFG would induce spin-lattice relaxation, depending on the temperature, the motion of cationic species or the polymer may dominate in certain temperature ranges. In general for the polyether - Li (Na) complex, motion of the polymer means motion of all environments for cations; therefore it is equivalent to consider it as cation motion, or at least no distinction can be made by NMR. However with the MCT model, we are able to say that motions from different species are responsible for the spin-lattice relaxation process. It is reasonable to separate these mechanisms into the restricted motion of cations and the motion of the polymer. Below T_c, ionic motion is decoupled from the polymer segmental relaxation rate, as the motion of polymer has become considerably slower than the hopping rate of the ion. In other words, below a certain temperature, e.g., 1.2 T_g, the motion of the polymer, which is a macromolecule, is frozen from the NMR viewpoint. Therefore, if any relaxation does occur, it is reasonable to assume that it is due to the motion of the cations. However, due to the confining polymer matrix, motions of the cations are restricted. At this temperature, the relaxation time is usually long, the relaxation process is slow, and this relaxation should not be related to the conductivity at all. Many studies for both solid polymer electrolytes and other solid ionic conductors suggested that above T_c (1.2 T_g), there is a change in relaxation mechanism. For solid polymer electrolytes, above T_c the polymer started to be rubberized. At 1.2 T_g , the motion of the polymer became the dominant factor causing spin-lattice relaxation. Above

T_c, motions of the cations are also enhanced, both by the higher temperature and the rubberized environment compared to the rigid matrix at temperatures under T_g. The turning point in a plot of T_1 vs. temperature is expected at this temperature. From the plot of T_1 vs. 1000/T (K) for ^{7}Li for the bilayer PEO/MoO_3 nanocomposite, we see the turning points at 280K and 340K. This means that the turning point on the plot reflects intrinsic properties of solid polymer electrolytes. Since this usually happens at temperatures above T_g, the T_1 has been assigned to the motion of the polymer backbone. But as pointed out above, while the polymer is tumbling, the motion of the cations is enhanced. As these processes happen at the same time, it is difficult to separate them by NMR techniques. With the aid of the MCT model, we are able to assign these processes to the motions of different species for solid polymer electrolytes in different temperature regions.

The more interesting point in our data set is that the occurrence of another turning point around 370K, which has not been observed for general solid polymer electrolytes and nor in the only other confined polyether electrolyte studied.[38] It is at this temperature that we observed a dramatic change in the conductivity of the bilayer $(PEO)_{0.9}$(Li,Na)MoO_3 nanocomposite. It implies that the cation does not move efficiently enough to conduct electricity until this temperature.

This is the result of the restricted motion of PEO between the MoO_3 sheets. In analogy to the MCT model, in which different motions have been assumed below and above T_g of the polymer, we propose three regions of motion corresponding to the relaxation in bilayer $(PEO)_{0.9}$(Li,Na)MoO_3 nanocomposite. The motions in different temperature regions are illustrated by the following diagram (Figure 4.3). At a low

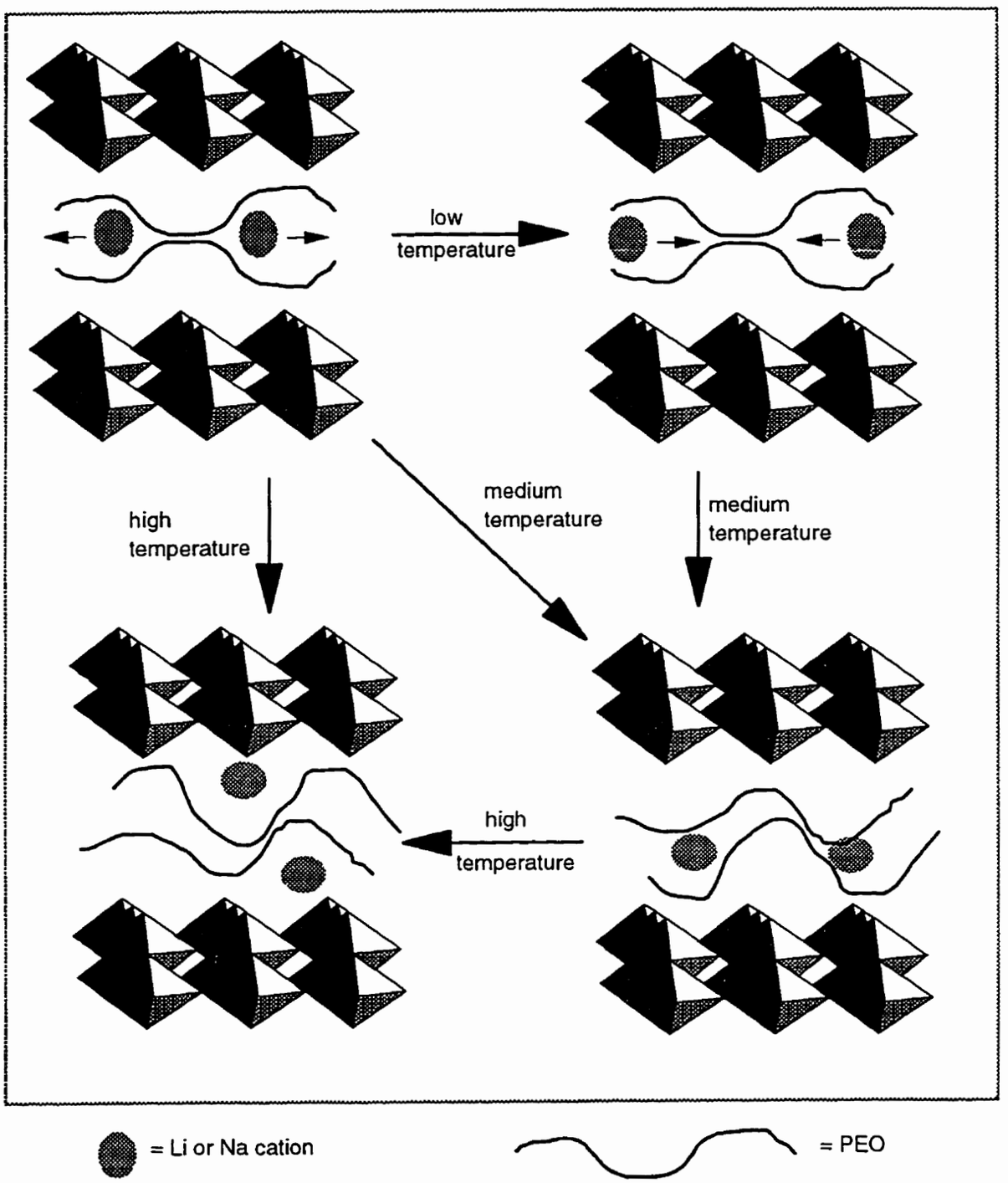

Figure 4.3 Schematic diagrams of the proposed motional species in the different temperature regions for bilayer nanocomposite $(PEO)_{0.9}(Li,Na)MoO_3$

temperature (for example, below T_g), the restricted cation motion in the frozen polymer causes the spin-lattice relaxation; at a medium temperature, the restricted motion of the polymer in the rigid MoO_3 sheets is the origin of spin-lattice relaxation; while at a high temperature, the fast cation motion in the rubberized polymer matrix responds, which will not only averages the interaction between cation and polymer but also the interaction between cation and MoO_3 sheets.

Therefore, whenever the preceding motional process is not enough to induce the full decay of density fluctuations, the next slower motion will operate at an elevated temperature to induce the spin-lattice relaxation. For the nanocomposite, depending on the temperature, three different relaxation processes are involved (figure 4.3). At low temperatures, the cations move in the frozen polymer matrix. In the medium temperature region, the polymer matrix is able to move but is restricted in the MoO_3 sheets; this induces the spin relaxation and enhances the motion of the cations. At 370K, the cation is able to move over longer distances and thus to induce the faster density fluctuation decay above this temperature, although the motion of the polymer is still restricted by the available space between the MoO_3 sheets. At this temperature, the cations reach the useful point for effective to conducting of electricity; this is consistent with our conductivity measurements, that the conductivity of bilayer nanocomposites rises dramatically above 370K.[1] Therefore T_1 studies can be used to study the establishment of cation mobility, as soon as we know which processes induce the spin-lattice relaxation. However, it should be pointed out that many motion processes can induce the full T_1 relaxation. It is a question of finding the right relaxation process related to conductivity, but very often, different

relaxation processes overlap, and before the cations moves fast enough to conduct electricity the relaxation is already too fast to measure with NMR.

The above extended MCT model for relaxation of polymer/metal oxide nanocomposites should be able to be extended, in general, to other systems containing submotional phases which may possess to different relaxation mechanisms.

4.3.2 ^{23}Na NMR spin-lattice relaxation studies of bilayer nanocomposites $(PEO)_{0.9}(Li,Na)MoO_3$

Quadrupolar perturbed ^{23}Na NMR is a very sensitive and accurate tool for investigating ionic motions in disordered rigid media when it is the dynamics of the diffusing ions which cause fluctuations in the local electric field gradient (EFG) or magnetic dipolar fields. ^{23}Na (I=3/2) has larger quadrupolar interactions compared to ^{7}Li nuclei otherwise in the same constituent EFG. As discussed in the previous section for ^{7}Li, biexponential decay of ^{23}Na magnetization is expected similar to the poly(propylene oxide)-$NaClO_4$ electrolytes using the inversion recovery pulse sequence.[114] However, a single exponential decay of ^{23}Na magnetization was observed for bilayer $(PEO)_{0.9}(Li/Na)MoO_3$ nanocomposites using an inversion recovery pulse. We tried to fit the data with two T_1 time constants, but it didn't improve the fitting. For all temperatures, the ^{23}Na magnetization was determined to relax with a single time constant T_1. The reason why only one spin-lattice relaxation constant was observed for ^{23}Na is the same as was discussed for ^{7}Li; it is most probably due to the inhomogenity of the material; in addition,

it may also be due to the inability to resolve two T_1s by our current NMR settings because two T_1s that differs by only a factor of 3 are difficult to measure and resolve.

Figure 4.4 is a plot of ^{23}Na T_1 vs. 1000/T(K) for the bilayer $(PEO)_{0.9}(Li,Na)MoO_3$ nanocomposite. Similar to the ^7Li T_1 data, turning points occur at 280K and 340K. The one at 280K is a little higher than that observed for ^7Li T_1 in the same material, and the one at 340K is very close to the one for ^7Li T_1 for the same material. This observation is a good test for the original MCT model. At low temperatures, the spin-lattice relaxation is due to the motion of sodium cations, while at or above T_c, the spin-lattice relaxation is due to the motion of the polymer backbone; it is more affected by the softening of the polymer matrix. Another change corresponding to the cation mobility (in accordance with our extended MCT model) is seen at 380K (which is a bit higher than in ^7Li T_1 data). The big difference between ^7Li and ^{23}Na is in the two T_1 minima. ^7Li reaches the T_1 minimum at 390K. However, ^{23}Na does not reach the T_1 minimum even at 420K, the highest temperature accessible with our instrument. While the value of T_1 minimum is related to the strength of the interaction between the nuclei spins and the lattice, the temperature at which the T_1 minimum occurs is more relevant to the mobility of cations or surrounding atoms. According to our extended MCT model, in this temperature range, it is related to the mobility of the cations. A clear trend for the T_1 minimum to move to higher temperature with increasing poly(propylene oxide) molecular weight and salt concentration for poly(propylene oxide)-$NaClO_4$ complexes has been observed, as the salt is expected to increase the number and extent of transient crosslinks between polymer chains which constrain the segmental motion of the polymer backbone. Hence the time scale of the motion is shifted to higher temperatures. In bilayer $(PEO)_{0.9}(Li,Na)MoO_3$

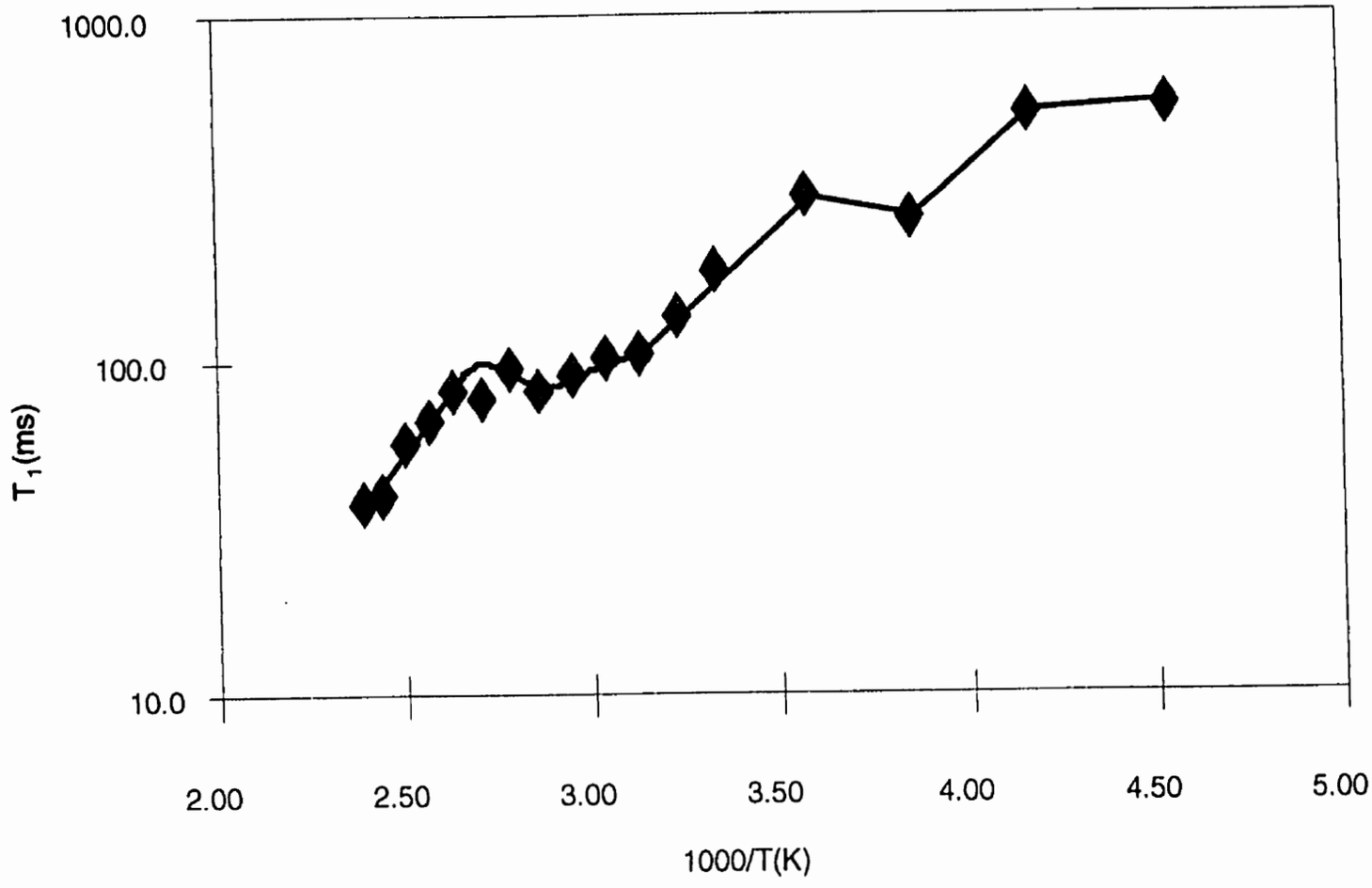

Figure 4.4 **^{23}Na nuclear spin-lattice relaxation times as a function of inverse temperature for bilayer nanocomposite $(PEO)_{0.9}(Li,Na)MoO_3$**

nanocomposites, due to the larger size of sodium cations than lithium cations, it is expected that the T_1 minima of sodium will appear at a higher temperature than that of lithium if the relaxation process is due to the motion of cations. Therefore, our data further supports that the relaxation mechanism at high temperatures (>370K) is more directly related to the motion of cation in the bilayer $(PEO)_{0.9}(Li,Na)MoO_3$ nanocomposite. At about 400K, motion of sodium is much slower than that of ^7Li (consider that ω_0 of ^{23}Na is much smaller than that of ^7Li), i.e., the correlation time is much longer for sodium than that of ^7Li at this temperature.

It should be pointed out that the T_1 value of ^{23}Na close to the minimum and its neighboring temperatures is about one order of magnitude smaller than that of ^7Li NMR T_1 for the same material, similar to the ratio of $Q(^7Li)$ to $Q(^{23}Na)$. Since it is reasonable to suggest that lithium and sodium have similar environments in the nanocomposite, this smaller T_1 value for ^{23}Na NMR implies that at least for ^{23}Na, the relaxation mechanism is dominated by quadrupolar interactions at these temperatures.

The activation energy determined from the BPP plot is included in Table 4.1. The two processes are also distinguished by the activation energy data. The activation energy of the relaxation process corresponding to the polymer backbone motion is 19.6 kJ/mol. The activation energy of processes corresponding to the cation motion at higher temperatures is 26.3 kJ/mol. These values again support the change of the relaxation mechanism at about 370K. The dynamic process having an activation energy of 26.3 kJ/mol has routinely been quoted as the effective cation motion for solid polymer electrolytes.

4.3.3 Temperature variation studies of the ^{7}Li NMR linewidth for bilayer $(PEO)_{0.9}(Li,Na)MoO_3$ nanocomposite

Useful information about cation mobility and its microscopic environment may be obtained from temperature-dependent studies of the linewidth of transitions between nuclear spin energy states of $|1/2>$ and $|-1/2>$. In inhomogeneous environments, found in solid polymer electrolytes, local variations in environment are substantial and broaden out those nuclear spin transitions which depend upon the quadrupolar energy. Only transitions between the spin eigenstates $|1/2>$ and $|-1/2>$ contribute to the observed spectrum. The spectral breadth is dominated by couplings to nearby magnetic fields associated with other spins (Figure 4.5).[38] Narrowing of the NMR line commences when the rate of the local field fluctuations is comparable to the rigid lattice linewidth. Linewidth changes reflect averaging over these local fields due to dynamics, which should have a better relationship with cation mobility than T_1 relaxation data, as they probe the slower motion of cations.

^{7}Li NMR linewidths of a bilayer $(PEO)_{0.9}(Li,Na)MoO_3$ nanocomposite vs. 1000/T is plotted in Figure 4.6. As can be seen from the plot, ^{7}Li linewidths are sensitive to temperature. In the high temperature region, the NMR linewidth was motionally narrowed. It is of interest to note that, similar to that observed for the T_1 studies, the turning point from linewidth changing with temperature at 260K was observed. In the low temperature region (<250K), there is a motional narrowing of linewidth most probably due to the cation motions in the rigid polymer chain cage. From 260K, there is a

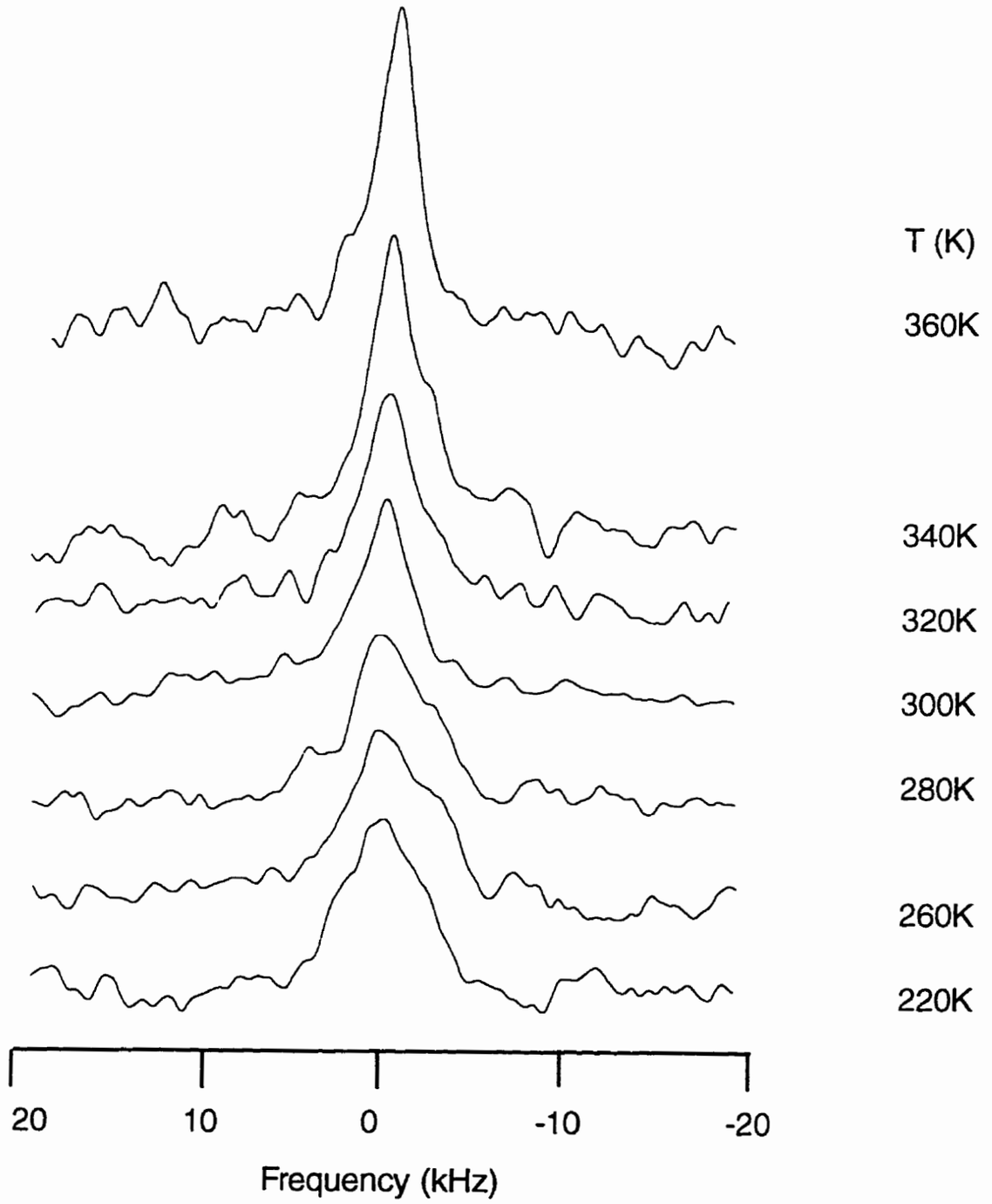

Figure 4.5 **Temperature dependence of the ^{7}Li spectra for a sample of bilayer nanocomposite $(PEO)_{0.9}(Li,Na)MoO_3$**

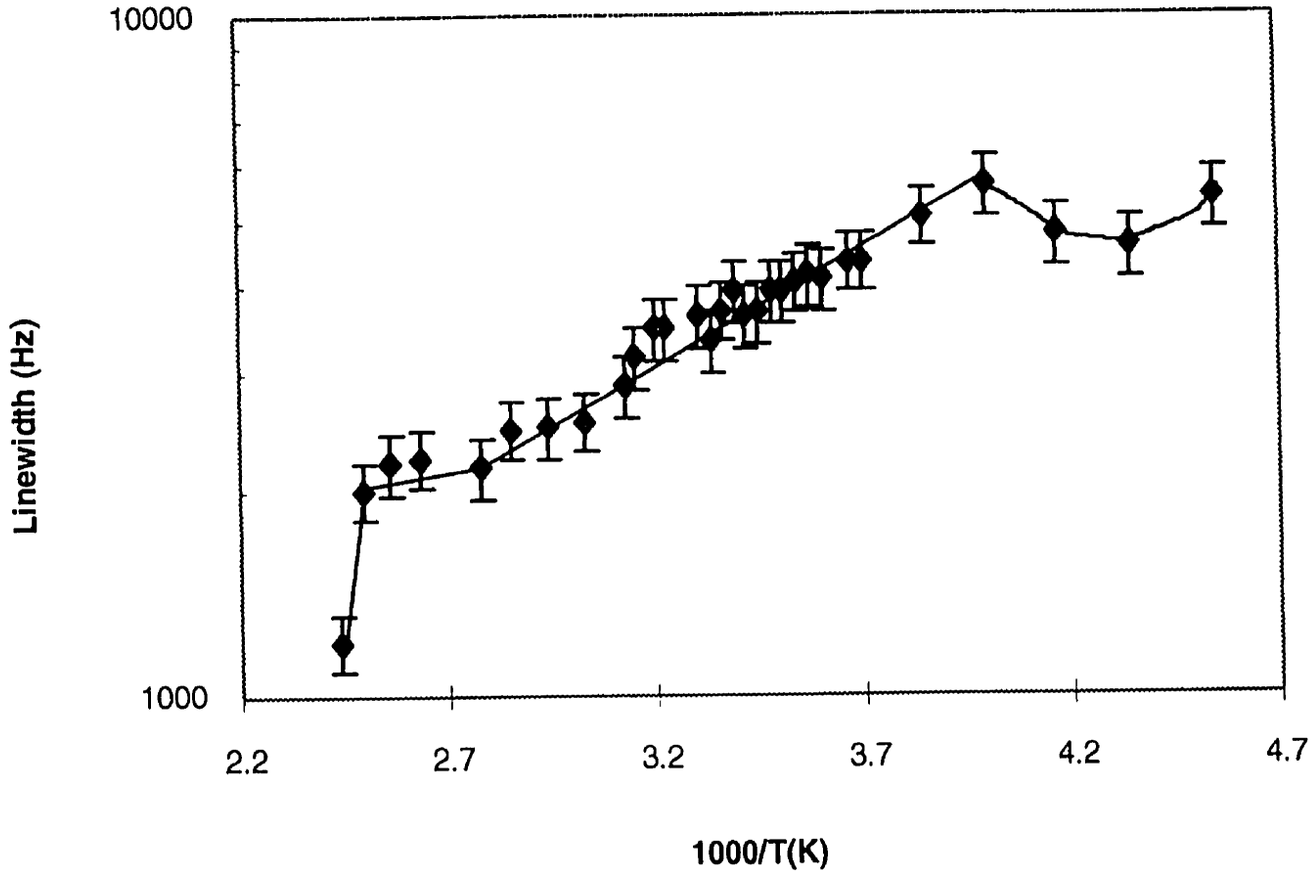

Figure 4.6 ^{7}Li NMR temperature-dependent linewidth for bilayer nanocomposite $(PEO)_{0.9}(Li,Na)MoO_3$

continuous narrowing of linewidth, which from the analysis of T_1 data, we know, is due to the rubberization of PEO and involves the motion of polymer and the enhanced motion of the cation. The relatively drastic narrowing, occurring at about 260K for bilayer $(PEO)_{0.9}(Li,Na)MoO_3$ nanocomposite, is the same as what found for most PEO-Li complexes. This linewidth change has been correlated by others to the onset of cation diffusion by averaging the inhomogeneous distribution of local fields for solid polymer electrolytes.[38, 14, 39]

The motional narrowing is limited at 350K for bilayer $(PEO)_{0.9}(Li,Na)MoO_3$ nanocomposite, resulting in a residual linewidth of about 2000Hz, which is still quite broad (Gupta *et al.* observed the residual linewidth of 300Hz for $(PEG)_xLiCl$ after the first motional narrowing[39]). In many cases, such averaging reduces the interactions to zero and is manifested in wideline NMR as a narrowing of the resonance line. This narrowing between temperatures of 260K and 350K is the result of the averaging of the dipole-dipole interactions between lithium cations and protons of the polymer backbone. The residual linewidth is most probably due to the restricted motion of PEO in MoO_3 sheets, which means that the dipole-dipole interactions are not removed completely. It also could be the result of an EFG induced by the MoO_3 sheets, which has not been averaged at this temperature, because the lithium cations can only move freely in a fixed unit of PEO, and are not able to jump between different MoO_3 units (Figure 4.3). The paramagnetic effect by $MoO_3^{-0.25}$ may also induced the life broadening for ^7Li spectra.

We analyzed the data in this narrowing temperature range (260-350K) with the BPP model. At intermediate temperatures, when $1/\tau$ is comparable to the square root of

the Van Vleck second moment, the linewidth $\Delta\omega$ varies continuously from the low-temperature value $\Delta\omega_l$ in a way described to a good approximation by the BPP model[38, 39, 45, 46, 47]

$$\frac{1}{\tau} = \frac{\alpha(\Delta\omega)}{2\pi \tan((\pi/2)(\Delta\omega/(\Delta\omega_l)^2)}$$

where α is a constant whose value depends on the line shape and falls in the range 1 - 10. This analysis can be refined to account for the residual linewidth, $\Delta\omega_r$, typically observed at high temperatures due to the inhomogenity of the magnetic field, and thus the empirical modification[47, 48]

$$\frac{1}{\tau} = \frac{\alpha(\Delta\omega - \Delta\omega_r)}{2\pi \tan((\pi/2)((\Delta\omega - \Delta\omega_r)/(\Delta\omega_l - \Delta\omega_r))^2)}$$

provides a more precise determination of $1/\tau$.

Using this equation, and the Arrhenius activation process for tumbling, we have calculated the activation energy and τ_0, listed in Table 4.1. The activation energy found from linewidth measurements is comparable to that obtained from the T_1 analyses and to the literature data. However, the τ_0 is much larger than that found from T_1 analysis and is one order of magnitude larger than those for the PEO/montmorillonite nanocomposite found from linewidth analyses. The smaller τ_0 is quite significant for solid polymer electrolyte studies; it is closer to the dynamic process effective in conductivity measurements. However, in bilayer $(PEO)_{0.9}(Li,Na)MoO_3$ nanocomposite, in this temperature region, the conductivity has not been enhanced significantly due to the

restricted motion of PEO. This is further supported by the activation energy of 19.6 kJ/mol. Most reported data for cation motion give an activation energy of 25 kJ/mol for solid polymer electrolytes.

It has been observed for PEO-alkali cation complexes, the linewidth is further broadened upon increasing temperature after it reaches the minimum at ~320K. There has been controversy in the literature about such temperature minima. Greenbaum *et al.*[49] have attributed this linewidth minimum to the minimum of the central transition predicted by Baram, Luz, and Alexander[50] when $\omega_Q\tau_c \sim 1$. The increased linewidth after the minimum is due to the collapse of quadrupolar interactions into the central line. Through calculations, Jeffrey *et al.*[15] have shown that the minima observed in the ^{23}Na linewidth measurements are probably due to changes in the dynamics of the mobile Na ions which are expected to be reflected in the temperature dependence of τ_c. But they did not point out what dynamics are responsible for these changes. There is no reasonable explanation why the dynamics should be different above this temperature. Very close to this situation are the studies of Gupta *et al.*[39] They did not see the minimum in their studies; instead, they observed two well-separated narrowing processes for the $(PEG)_xLiCl$ system.

In the $(PEO)_{0.9}(Li,Na)MoO_3$, the residual linewidth of 2 kHz at temperature between 350 - 400K was seen a dramatic narrowing started at temperature ~ 410K. This was consistent with the T_1 analysis. At this temperature region, the Na^+ started to jump between different MoO_3 sites, averaging further the residual dipole-dipole interaction between Li^+ and PEO and also any interaction composed by MoO_3. This jump of Li^+ over long distance is supported by electricity conductivity data for bilayer nanocomposite,

which exhibits a dramatic change of electricity conductivity at ~400K (Figure 3.8). The resulted linewidth of ~1 kHz at ~410K also suggests that the paramagnetic effect of $MoO_3^{-0.25}$ on the linewidth of ^7Li spectra of $(PEO)_{0.9}(Li,Na)MoO_3$ is not significant, contrast to that observed for PEO/Montmorillonite nanocomposite.[38]

The studies tell us that, although the intercalation of PEO/(Li/Na) complexes into MoO_3 may improve the ionic conductivity of MoO_3 by screening the interaction between lithium/sodium cation and MoO_3 sheets, it is unable to improve the ionic conductivity significantly, since the motion of PEO is restricted in the nanocomposites, and ion dynamics are needed to conduct electricity effectively. Also, the motion of the cation is affected by the MoO_3 sheets, which results in much higher temperatures for cation motion than is usual for solid polymer electrolytes.

4.4 Conclusion

^7Li, and ^{23}Na NMR T_1 relaxation and linewidth measurements were performed on the bilayer $(PEO)_{0.9}(Li/Na)MoO_3$ nanocomposite. All the data suggest that different relaxation mechanisms dominate in different temperature regions. Based on these measurements, an extended MCT model was proposed, and the author believes that this extended MCT model can be applied to any system which has different submotional phases that may induce relaxation of the species of interest.

4.5 References

1. Nazar, L. F.; Wu, H.; Power, W. P. *J. Mater. Chem.* **1995**, 5, 1985-93.

2. Leroux, F.; Koene, B. E.; Nazar, L. F. *J. Electrochem.* Soc. **1996**, *143*, 1181.

3. Donoso, P.; Gorecki, W.; Berthier, C.; Defendini, F.; Poinsignon, C.; Armand, M. B. *Solid State Ionics*, **1988**, *28-30*, 969.

4. Wintersgill, M. C.; Fontanella, J. J.; Pak, Y. S.; Greenbaum, S. G.; Al-Mudaris, A.; Chadwick, A. V. *Polymer*, **1989**, *30*, 1123.

5. Brinkmann, D. *Solid State Ionics* **1981**, *5*, 53.

6. Berthier, C.; Gorecki, W.; Minier, M.; Armand, M.; Rigaud, Ph; Chabagno, J. M. *Solid State Ionics* **1983**, *11*, 91.

7. Greenbaum, S. G.; Pak, Y. S.; Adamic, K. J.; Wintersgill, M.C.; Fontinella, J. J. *Solid State Ionics* **1988**, *31*, 241.

8. Chatani, Y.; Okamura, S. *Polymer* **1987**, *28*, 1815.

9. Lightfoot, P.; Mehta, M. A.; Bruce, P. G. *J. Mater. Chem.* **1992**, *2*, 379.

10. Minier, M.; Berthier, C.; Gorecki, W. *J. Phys. (Paris)* **1984**, *45*, 739.

11. Cameron, G. C.; Ingram, M. D. in *Polymer Electrolyte Reviews*, MacCallum, J. R., Vincent, C. A., Eds.; Elsevier: London, **1989**; Vol. 2.

12. Vincent, C. A. *Prog. Solid State Chem.* **1987**, *17*, 145.

13. Wieczorek, W.; Such, K.; Chung, S. H.; Stevens, J. R. *J. Phys. Chem.* **1994**, *98*, 9407.

14. Chung, S. H.; Jeffrey, K. R.; Stevens, J. R. *Phys. Rev. B.* **1995**, *51*, 2826.

15. Chung, S. H.; Jeffrey, K. R.; Stevens, J. R. *J. Chem. Phys.* **1991**, *94*, 1803.

16. *The Physics of Glassy Polymers*, Haward, R. N. Ed., Applied Science, **1973**.

17. *Structure and Mobility in Molecular and Atomic Glasses*, O'Reilly, I. M.; Goldstein, M. Eds., New York Academy of Science, New York, **1981**, vol. 371.

18. Rossler, E.; Eiermann, P. *J. Phys. Chem.* **1990**, *92*, 3725.

19. McCrum, N. G.; Read, B. E.; Williams, G. *Anelastic and Dielectric Effects in Polymeric Solids*, Wiley, New York, **1967**.

20. Li, G.; Du, W. M.; Chen, X. K.; Cummins, H. Z.; Tao, N. J. *Phys. Rev. A* **1992**, *45*, 3867.

21. Li, G.; Du, W. M.; Chen, X. K.; Cummins, H. Z.; Tao, N. J. *Phys. Rev. A* **1992**, *46*, 3343.

22. Greenbaum, S. G.; Pak, Y. S.; Adamic, K. J.; Wintersgill, M.C.; Fontinella, J. J.; Schultz, J. W.; Andeen, C. G. *J. Electrochem. Soc.* **1988**, *135*, 235.

23. Frick, B.; Fargo, B.; Richter, D. *Phys. Rev. Lett.* **1990**, *64*, 2921.

24. Petry, W. Z. *Phys. B* **1991**, *83*, 175.

25. Wong, J.; Angell, C. A. *Glass-Structure by Spectroscopy*, Marcel Dekker, New York, **1976**.

26. Dries, Th.; Fujara, F.; Kiebel, M.; Rossler, E.; Sillescu, H. *J. Chem. Phys.* **1988**, *88*, 2139.

27. Rossler, E.; Eiermann, P. *J. Phys. Chem.* **1994**, *100*, 5237.

28. Schnauss, F.; Fujara, F.; Sillescu, H. *J. Chem. Phys.* **1992**, *97*, 1378.

29. Andrade, E. N. da C. *Nature* **1930**, *125*, 309.

30. Vogel, H. *Phys. Z.* **1925**, *22*, 625.

31. Fulcher, G. S. *J. Am. Ceramic Soc.* **1925**, *6*, 339.

32. Laughlin, W. T.; Uhlmann, D. R. *J. Phys. Chem.* **1972**, *76*, 2317.

33. Fox, T. G.; Flory, P. J. *J. Appl. Phys.* **1950**, *21*, 581.

34. McDowell A. F. *J. Magnetic Resn. A* **1995**, *113*, 242.

35. Andrew, E. R.; Tunstall, D. P. *Proc. Phys. Soc.* **1961**, *78*, 1.

36. Gorecki, W.; Jeannin, M.; Belorizky, E.; Roux, C.; Armand, M. *J. Phys. Condens. Matter* **1995**, *7*, 6823.

37. Wong, S.; Vasudevan, S.; Vaia, R. A.; Giannelis, E. P.; Zax, D. B. J. *Am. Chem. Soc.* **1995**, *117*, 7568.

38. Brown, S. D.; Greenbaum, S. G.; McLin, M. G.; Wintersgill, M. C.; Fontanella, J. J. *Solid State Ionics* **1994**, *67*, 257.

39. Gupta, S.; Shahi, K.; Binesh, N.; Bhat, S. V. *Solid State Ionics* **1993**, *67*, 97.

40. Sandahl, J.; Schantz, S.; Borjesson, L.; Torell, L. M.; Stevens, J. R. *J. Chem. Phys.* **1989**, *91*, 655.

41. Geiger, A.; Hertz, H. G. *Adv. Mol. Relaxation Process* **1976**, *9*, 293.

42. Gorecki, W.; Donoso, P.; Armand, M. *Brazilian J. Phys.* **1992**, *22*, 194.

43. Catlow, C. R. A.; Chadwick, A. V.; Greaves, G. N.; Moroney, L. M.; Worboys, M. R. *Solid State Ionics* **1983**, *9/10*, 1107.

44. Panero, S.; Scrosati, B.; Greenbaum, S. G. *Electrochem. Acta.* **1991**, *94*, 1803.

45. Bloembergen, N.; Purcell, E. M.; Pound, R. V. *Phys. Rev.* **1948**, *73*, 679.

46. Abragam, A. *The Principles of Nuclear Magnetism*, Clarendon Press: Oxford, **1961**: pp 196-199.

47. Whittingham, M. S.; Sibernagel, B. G. in *Solid Electrolytes*: Hagenmuller, P., van Gool. W., Eds., Academic Press: **1978,** pp 93-108.

48. Richards, P. M. in *Physics of Superionic Conductors, Topics in Current Physics*, M. B. Salamon, Ed., *vol. 15*, Springer, Berlin, **1979**.

49. Greenbaum, S. G. in *Solid State Ionics II*, Huggins, R. A. and Balkanski, M., Eds., MRS Symposia Proceedings No. 210 (Materials Research Society, Pittsburgh, **1991**), p237.

50. Baram, A.; Luz, Z.; Alexander, S. *J. Chem. Phys.* **1973**, *584*, 558.

CHAPTER FIVE

PEO LITHIUM (SODIUM) COMPLEXES/ELECTRONIC CONDUCTIVE HOST NANOCOMPOSITES (III)

-- ELECTROCHEMICAL BEHAVIOR OF PEO/MoO_3 NANOCOMPOSITES

5.1 Introduction

Research into lithium batteries began in the 1950s when it was noticed that Li-metal was stable in a number of nonaqueous electrolytes such as fused salts, liquid SO_2 or organic electrolytes such as $LiClO_4$ in propylene carbonate.[1] This stability was attributed to the formation of a passivating layer that prevents the direct chemical reaction between lithium metal and the electrolyte but still allows for lithium to go into solution during cell discharge.[4] In the early 1970s the idea of using materials that undergo intercalation reactions as the electrochemically active components of batteries began to be explored and accepted. Very rapidly a series of compounds, mostly transition metal chalcogenides, were found to have many of the desired properties for a high energy density cathode. Titanium disulfide was the most studied because of its rapid kinetics of reaction, easy reversibility, and electronic conductivity. Although the transition metal chalcogenides have many of the properties desired for a reversible cathode, their electrode potentials are too low when

capacity. Much effort has therefore been directed towards oxides that show the same basic behavior, have a higher electrode potential, and moreover are easier to handle. Lithium-ion batteries are the state-of-the-art rechargeable power sources for consumer electronics and are candidates for eventual use in electric vehicles. They store about twice the energy per unit mass of any competing rechargeable battery technology.[4, 3] They are currently of great interest and some are being commercialized by Moli Energy Ltd. and Sonny Energy Inc.[5, 7, 8] The cathode materials used in these batteries are $LiNiO_2$ or $LiCoO_2$. Accordingly, other first transition metal series oxides such as vanadium oxides, and manganese oxides have been extensively studied as candidate cathode materials.

For a material to be an efficient cathode for a lithium battery, it must: (a) possess high working voltage as the energy density is a primary consideration, (b) intercalate Li^+ efficiently and provide high Li^+ mobility; and (c) accept electrons and provide high electronic conductivity. Transition metal oxides are favored over sulfides as cathode material due to their high energy density, even though there are sulfides known to intercalate/deintercalate lithium more efficiently and reversibly than oxides.[9] Intercalation electrodes have been intensively studied as they are expected to intercalate /deintercalate Li^+ efficiently and reversibly due to their topotactical properties.[10] Therefore, layered transition metal oxides are very attractive materials for cathodes. They have high working voltages[11] and undergo topotactical chemical reactions. That is, during charge and discharge, no chemical bonds are broken and the layers remain intact, which is expected to improve the reversibility of the lithium battery.

Several molybdenum oxides have been studied as electrodes in non-aqueous lithium batteries.[12, 13, 14, 15, 16, 17] They offer high energy density and wide composition intervals for lithium intercalation. MoO_3 is particularly interesting, because (i) the orthorhombic phase (α-MoO_3) has a two-dimensional layered structure favorable for Li^+ intercalation, [18] and (ii) it is exceptionally stable.[19]

The usefulness of MoO_3 as a reversible cathode was first discovered by Campanella and Pistoia (1971).[20] They studied cells of the type $Li/LiAlCl_4$·BL/MoO_3,C, where BL = butyrolacetone, which had an OCV of 2.8V. They reported a single step redox reaction for MoO_3. Their battery was influenced by the participation of Cl^- ions (from the dissociation of electrolyte) in the electrode discharge reaction, probably through the formation of molybdenum oxychlorides.[22]

Dampier (1974) studied the effect of the current density and the storage period on the efficiency of the MoO_3 battery.[23] Due to the low conductivity of MoO_3, the discharge behavior was affected by the current density and the discharge efficiency of a battery stored for 6 months showed a 50% loss of capacity.

Margalit (1974) studied the discharge process of MoO_3 and pointed out that there was a dispersion on the discharge curve at x(Li) of 0.5 mole per mole of MoO_3, suggesting the formation of a new phase during lithium intercalation.[14] The formation of a new cathode material in Li/MoO_3 cells after the apparent n = 0.5 reduction is also confirmed by a 2.4-2.5 V open circuit voltage observed for a partially discharged cell.

There is one study of the effect of the electrochemical insertion of lithium on the structure of MoO_3 (1982).[16] It was found that the d-spacing of Li_xMoO_3 varies with the

Li composition and reaches a maximum at x(Li) = 0.5. They pointed out that highly expanded Li_nMoO_3 intermediates might be suitable starting materials. In the end product of lithium intercalation studied by XRD, one new compound, Li_2MoO_4, was found in addition to the starting material.

Bonino et al. (1985) studied the battery performance of amorphous MoO_3.[24] The working voltage of the amorphous MoO_3 is slightly lower than that of crystalline MoO_3. 1.5 lithium equivalents per mole of cathode material can be inserted for the cut-off voltage of 1V vs. Li.

A thin film MoO_3 battery has been studied by Bohnke and Robert (1982).[25] Recently, Julien et al. (1992, 1994) studied the influence of the growth conditions on the electrochemical features of a MoO_3 film battery.[15,26] No dispersion in the charge and discharge curve was observed, suggesting that clustering is unlikely and the discharge product would be a homogeneous compound of the formula Li_xMoO_3. The starting OCV of the battery is 3.15V. Due to the method used to prepare the MoO_3 film, many oxygen vacancies existed in their MoO_3. They pointed out that the oxygen vacancies control the electrochemical characteristics of the galvanic film cell. This probably explains why the film battery has different electrochemical processes than bulk molybdenum oxide batteries.

Since MoO_3 has high electrochemical equivalence (greater than 1.3 Ah cm^{-3}) and high theoretical specific energy (670 Wh kg^{-1}), it will continue to be studied as a candidate for cathode materials in lithium batteries. However, as is the case with many metal oxides, diffusion of the lithium cations is hindered primarily due to strong electrostatic interactions with the oxygen atoms of the molybdenum oxide sheets. In our efforts to improve the

ionic and electronic conductivity of MoO_3, we intercalated electronically-conducting polymers such as PPV, PPY, and PANI and/or polymer such as PEO that can conduct cation to form the polymer/MoO_3 nanocomposite materials.

The use of polymer/MoO_3 nanocomposites as a cathode material in secondary lithium batteries was encouraged by: (i) the development of the chemistry of polymer/inorganic layered host nanocomposite materials during the last decade,[28, 29, 30] and, (ii) the knowledge that these polymers are known to be stable under conditions suitable for lithium batteries, since some such as PPY and PANI have been extensively studied as cathode materials in lithium batteries. Some such as PEO are well known polymers used for the lithium ion electrolyte in lithium batteries to conduct Li ion. With the introduction of these polymers into MoO_3 on a nanoscale by intercalation chemistry it is expected that both the electronic and ionic conductivity will be improved. The polymer in the layers can also be viewed as a "pillar". It will improve the dimensional stability of the host during the lithium intercalation/deintercalation process. The lack of stability of layered compounds has been accused as being the main problem associated with the use of layered compounds as cathode materials. As has been pointed out,[16] the cycling stability is regarded to be higher for the "dimensionally stable" intercalation electrode, i.e., for rigid framework host matrices, than for simple layered structures. Similarly, single phase solid solutions are more stable than two-phase systems. In addition to the above, the favorable processing of these polymers may improve the manufacturing of lithium batteries.

In this chapter, we will focus on the electrochemical behavior of polymer-intercalated MoO_3 in secondary lithium batteries and the effect of polymer on the discharge and recharge of batteries.

5.2 Experimental

Electrochemical cycling of lithium battery was carried out using a multichannel galvanostat /potentiostat (MACPILE[21]) system. The cells were cycled galvanostatically between preset voltage limits, or between set values of lithium insertion/deinsertion. The cathode was prepared from 15-20 mg of vacuum-dried (80°C) $(PEO)_xA_{.25}MoO_3$ (A = Na, Li) that was mixed with graphite (30% by weight), and pressed to form a pellet of 13 mm diameter under a pressure of 105 kPa. The pellets were dried again at 80°C under vacuum (10^{-4} Torr) for 48 hours. The cell was assembled in an argon dry box using a lithium metal disk as the anode. The electrodes were separated by porous glass paper soaked in 1 M $LiClO_4$ in propylene carbonate (PC) as the electrolyte. The assembled cells were then charged at a very slow constant current rate while the potential was monitored as a function of time. By numerical differentiation the corresponding "differential capacity", dx/dE, curves were obtained. For convenience the differential capacity during recharge is plotted as positive values; i.e., the capacity plots follow the convention: sign $(dx/dE)_{anodic} \equiv +$, sign $(dx/dE)_{cathodic} \equiv -$, albeit dx/dE is always negative. In this way, curves similar to cyclic voltammograms are obtained.[31, 32]

5.3 Results

5.3.1 The current density and the discharge capacity

Figure 5.1 shows the effect of current density on the discharge ability of the lithium battery with monolayer nanocomposite $(PEO)_{0.4}NaMoO_3$ (30% carbon as conductive additives) as cathode. As the current density increased from 20 $\mu A/cm^2$ to 100 $\mu A/cm^2$, the discharge capacity of the battery dropped from 0.95 Li to 0.5 Li per formula weight voltage cut-off of 2.0 V. If we consider the capacity 0.95 Li per formula weight at current density of 20 $\mu A/cm^2$ and at the voltage cut-off of 2.0 V as the 100% discharge capacity, only 55% of the discharge efficiency was realized when the current density increased to 100 $\mu A/cm^2$ (Figure 5.2). This probably indicates slow kinetics for Li transport inside the monolayer nanocomposite $(PEO)_{0.4}NaMoO_3$.[133] The current density for the following experiments for the battery with 30% carbon as conductive additive was chosen as 30 μA, to ensure the battery could be cycled several times before it dies.

5.3.2 Cycling behavior of a lithium battery with $NaMoO_3$ as cathode (x(Li) = 0.8)

Figure 5.3a shows voltage curves for cycling of $NaMoO_3$ down to 2.0V versus Li, corresponding to a capacity of 0.80 Li per formula weight after the initial discharge and charge cycle of the battery. The smooth continuous potential decrease observed on the discharge cycle, together with the absence of a well-defined plateau region, suggests a

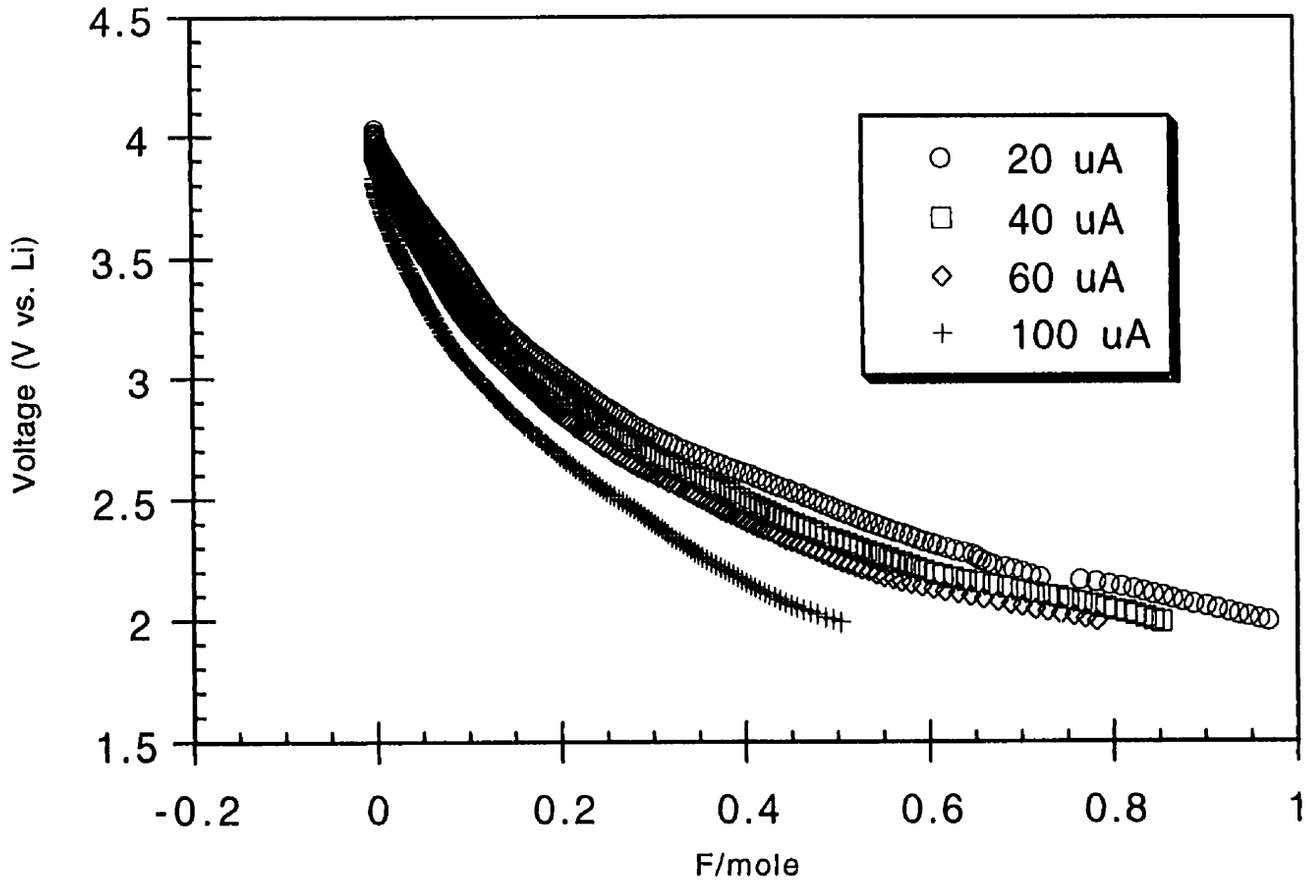

Figure 5.1 **Influence of the current density on the discharge curves of monolayer nanocomposite $(PEO)_{0.4}NaMoO_3$ electrodes (30% weight graphite) in a 1M $LiClO_4$ solution in PC**

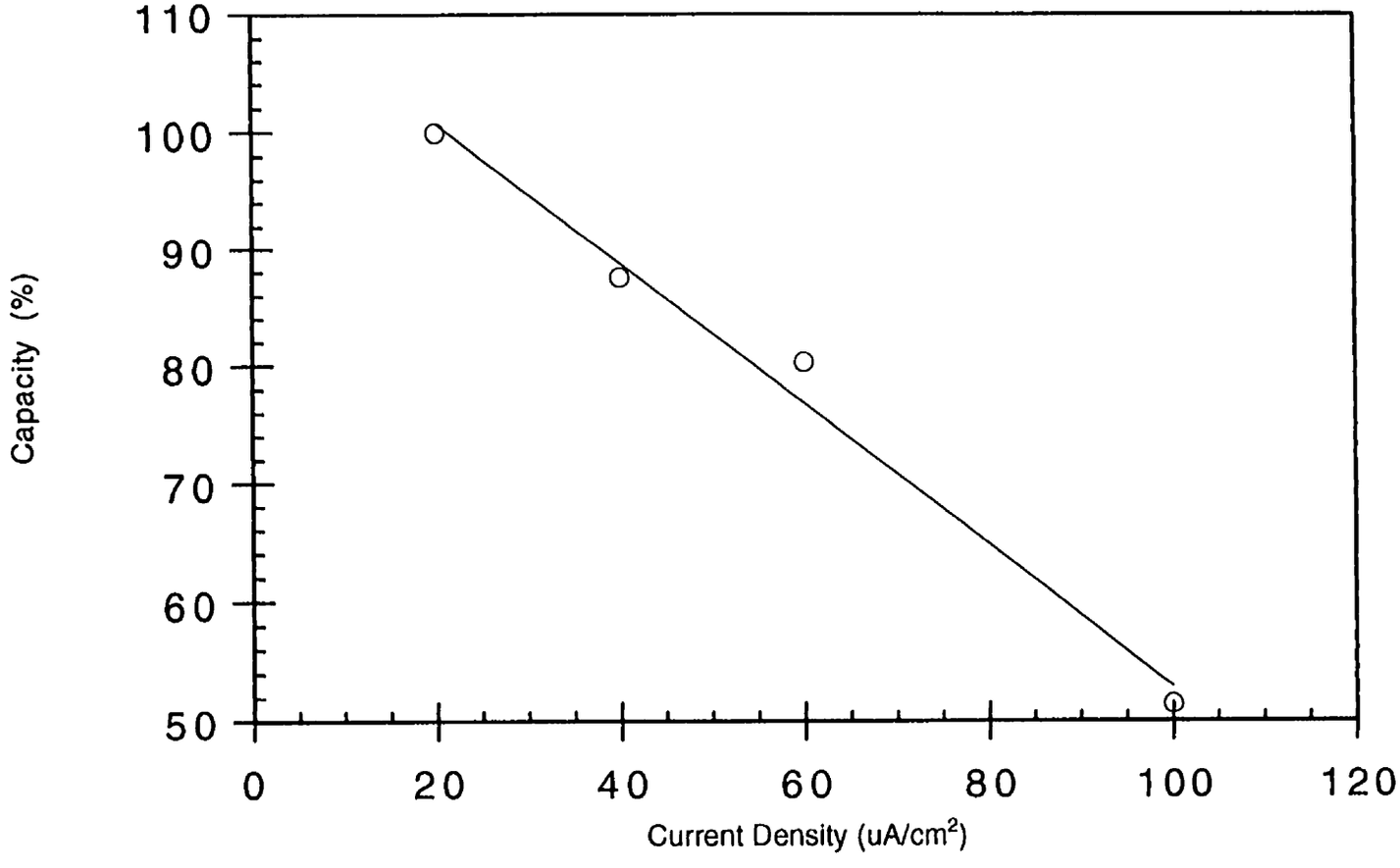

Figure 5.2 Capacity vs. current density for monolayer nanocomposite $(PEO)_{0.4}NaMoO_3$/Li cells in a 1M $LiClO_4$ solution in PC as electrolyte cycled between 4.2 and 2.0V

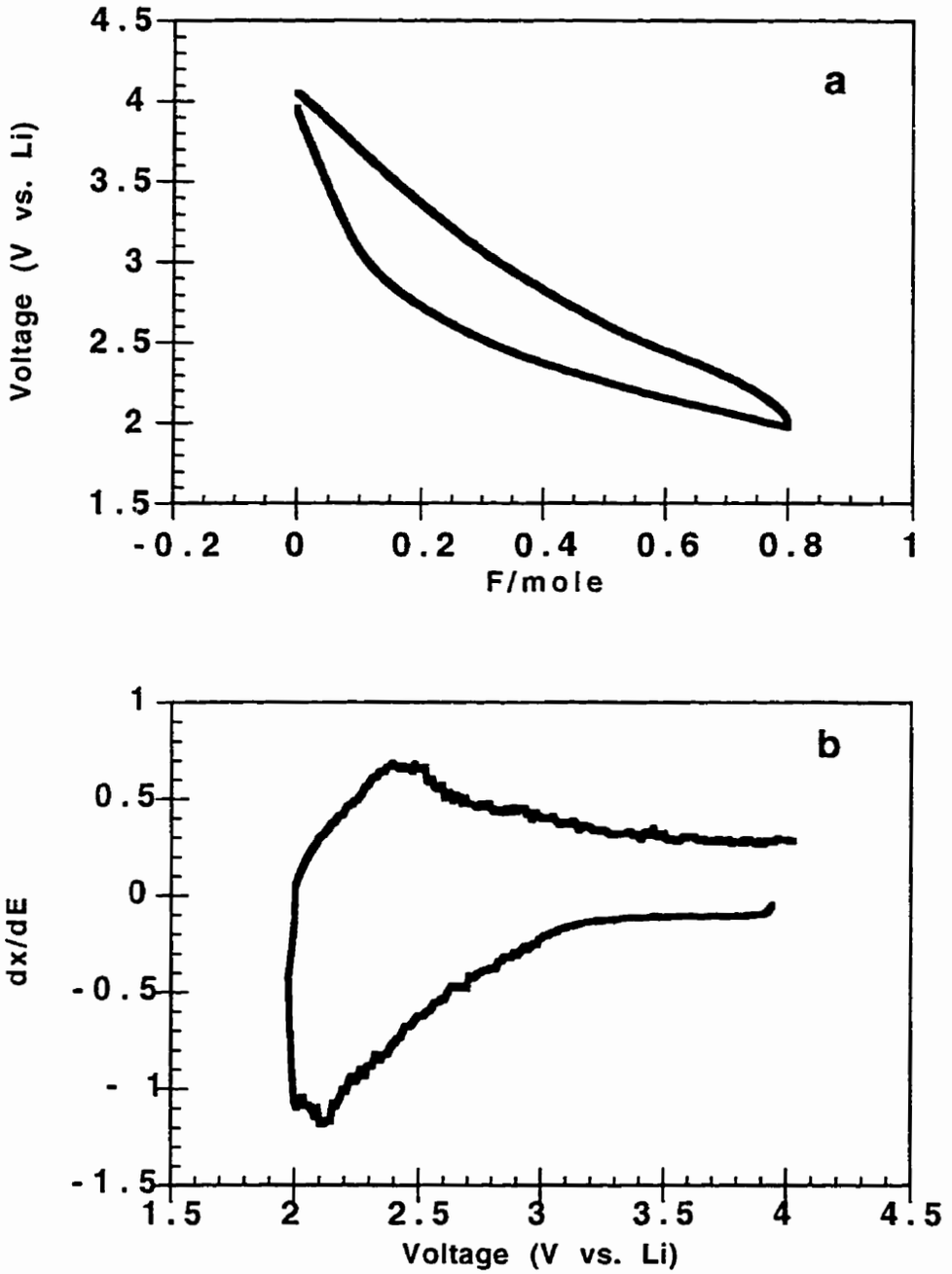

Figure 5.3 (a) Voltage vs. composition for Li insertion into $NaMoO_3$ and (b) differential capacity (dx/dE) vs. voltage corresponding to (a)

topotactic single phase Li^+ insertion process. Thus, limited structural rearrangement appears in this region. The small change between the first and the second cycle confirms that the original structure is recovered during charging (Figure 5.4). If we plot the data as differential capacity, the CV-like curve can be obtained (Figure 5.3 b).[32] In this case, very broad peaks appear during both on charging and discharging which are centered at 2.5 and 2.1V, respectively. The broad line shape confirms the continuous one phase Li insertion in this battery.[32] The separation between two peaks is 400mV, indicating there is a large polarization for the lithium intercalation/deintercalation. Figure 5.5 shows the extended cycling curves for the battery and their corresponding differential capacity plots.

5.3.3 Cycling behavior of a lithium battery with monolayer nanocomposite $(PEO)_{0.4}NaMoO_3$ as cathode (x(Li) = 0.8)

Figure 5.6 shows voltage curves for cycling of monolayer nanocomposite $(PEO)_{0.4}NaMoO_3$ down to 2.2V versus Li, corresponding to a take of 0.80 lithium per formula weight after the initial cycling. Similar to that of $NaMoO_3$, the smooth continuous potential decrease was observed on the first discharge cycle for monolayer nanocomposite, suggesting a topotactic single phase Li^+ insertion process. The differential capacity plot differs substantially from that of $NaMoO_3$. While there was still one symmetric and broad peak on both discharge and charge processes, (characteristic of one phase lithium insertion reactions), a much smaller separation of 50 mV between peaks of discharge and charge was observed. This implies that the reversibility of $NaMoO_3$ was greatly improved upon intercalation of PEO. The absence of a sharp voltage decrease at the termination of the reduction cycle (x=0.80) indicates that the intercalation step in this

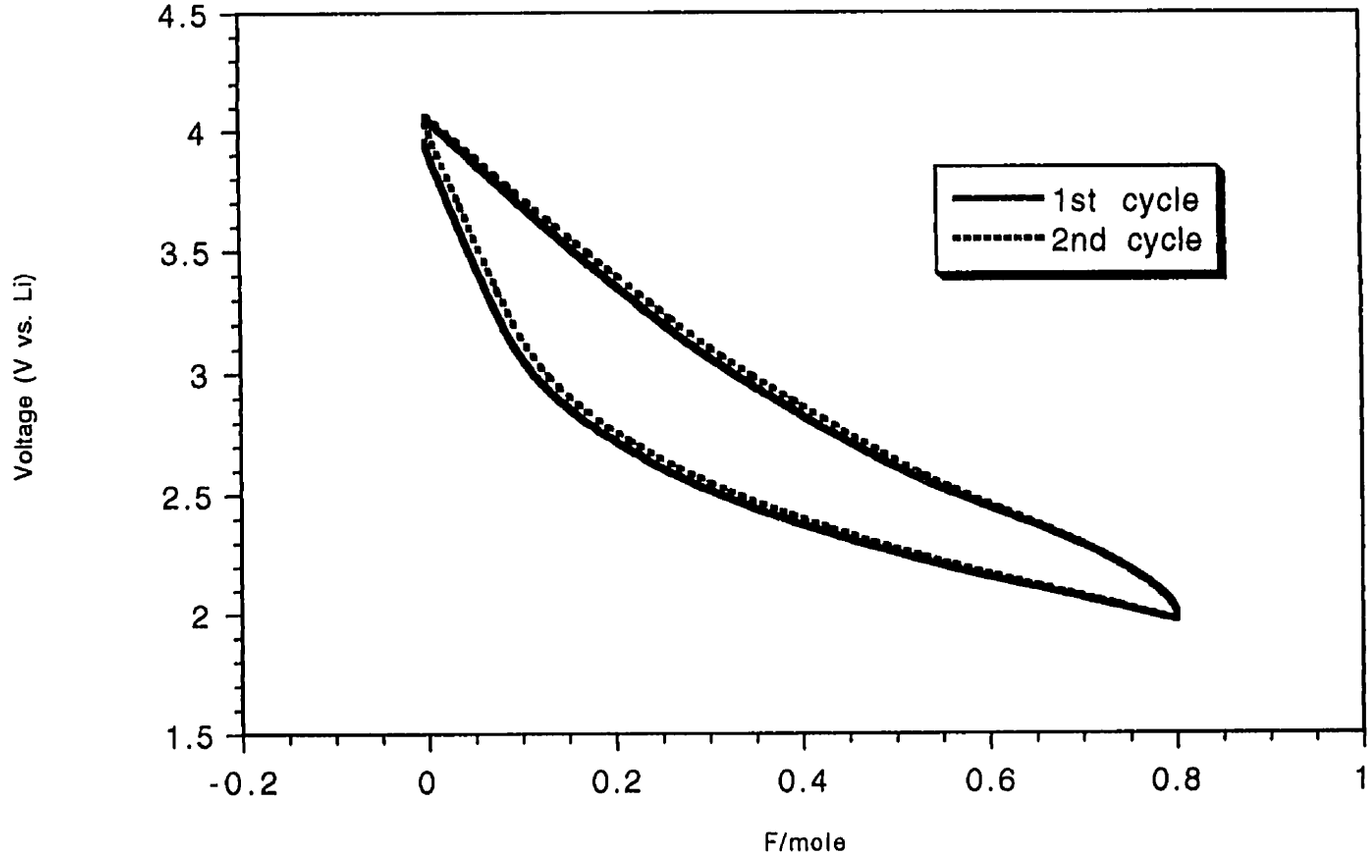

Figure 5.4 **Voltage vs. composition for Li insertion into $NaMoO_3$ for the first and second cycling after the initial cycling**

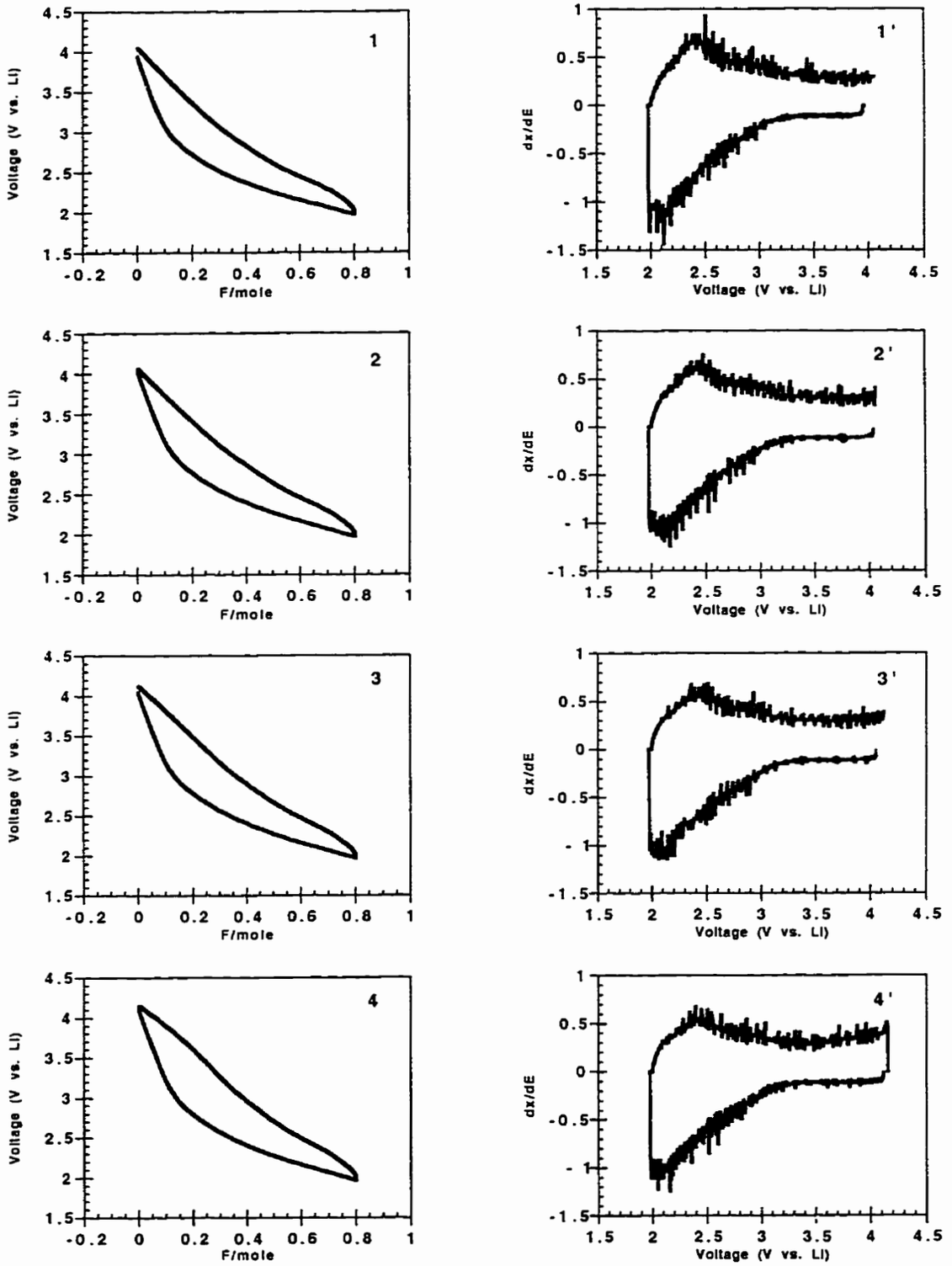

Figure 5.5 Voltage vs. composition, and differential capacity (dx/dE) vs. voltage for Li insertion into $NaMoO_3$. The number indicates the cycling number. (continued)

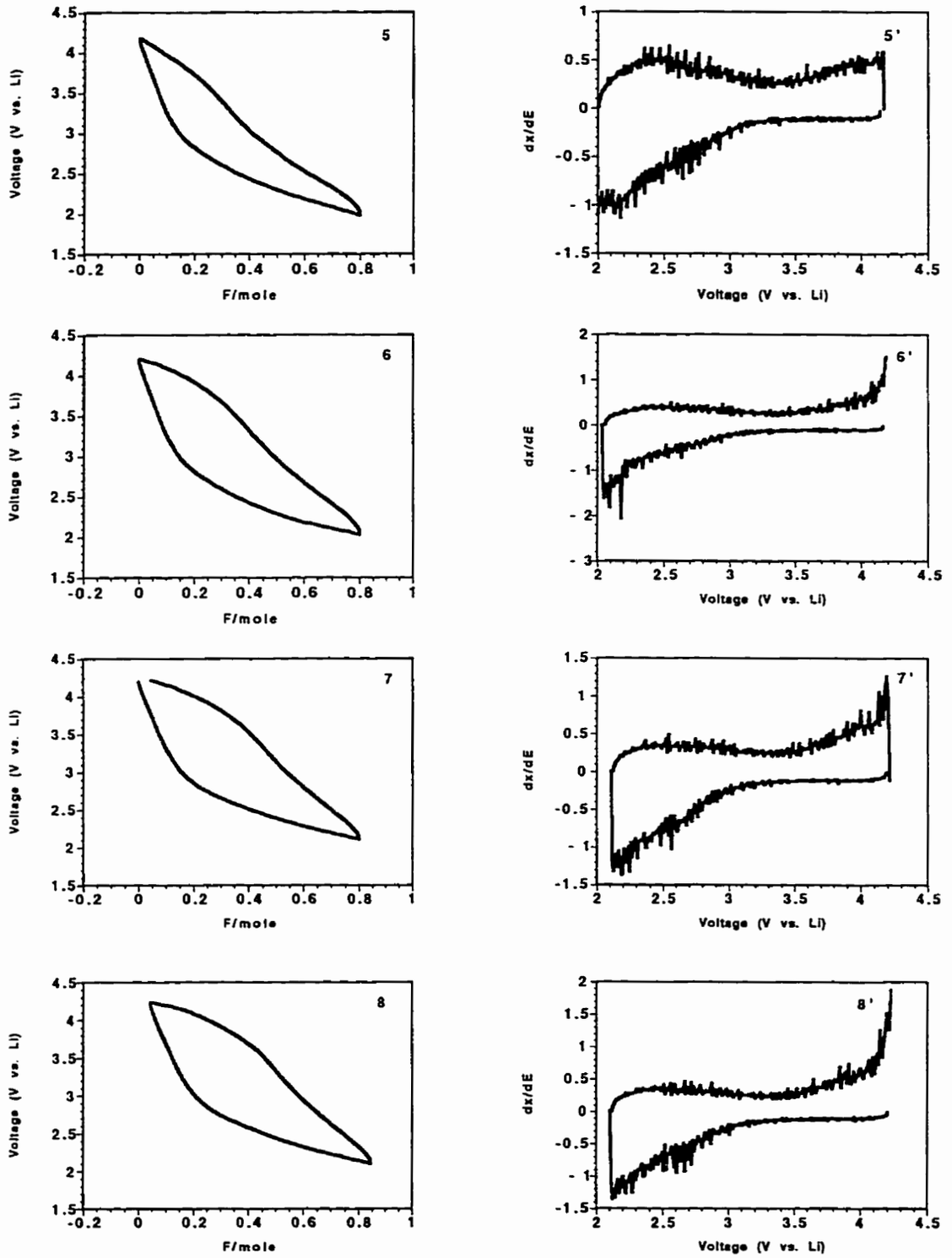

Figure 5.5 (continued) Voltage vs. composition, and differential capacity (dx/dE) vs. voltage for Li insertion into $NaMoO_3$. The number indicates the cycling number.

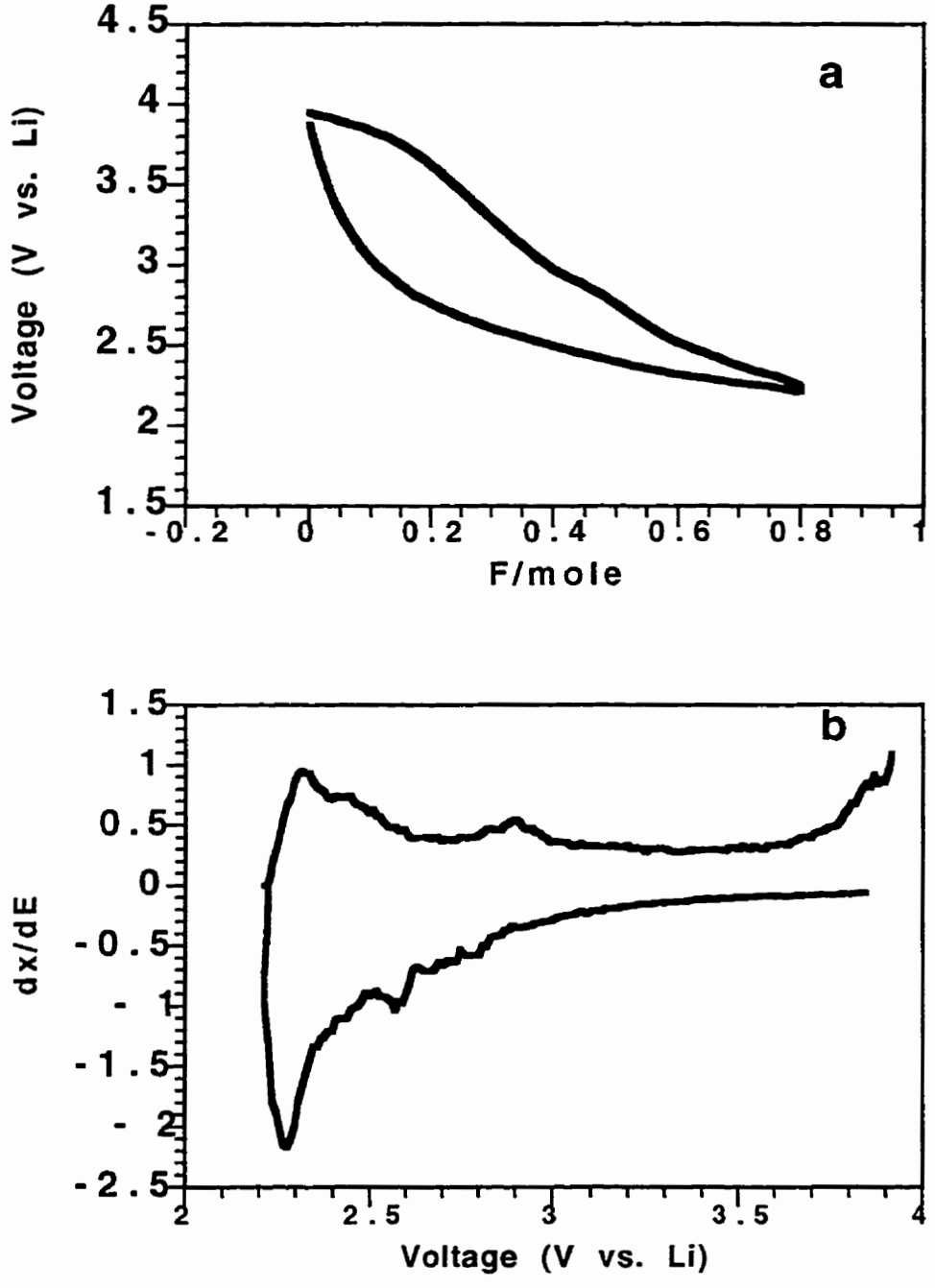

Figure 5.6 (a) Voltage vs. composition for Li insertion into monolayer nanocomposite $(PEO)_{0.4}NaMoO_3$ and (b) differential capacity (dx/dE) vs. voltage corresponding to (a)

phase is not limited (structurally or electronically) to the degree of Li insertion into the nanocomposite.

From the cycling curves of extended charge and discharge of the battery (Figure 5.7), we see that for the first three cycles (1, 2, 3), there is a noticeable decrease of the cell polarization at x(Li) between 0.1 and 0.2. This is in contrast to the $NaMoO_3$ (Figure 5.5), for which the polarization increases upon cycling. This should make the discharge and charge processes more favorable. However, this is soon surpassed by the gradual development of a plateau at x(Li) between 0.3 and 0.4 (at the working voltage of 3.0V), as can be seen from the charge curve of the fourth cycling. The plateau is obviously not well developed at the discharge curve. This can be more clearly shown by the differential capacity plot (Figure 5.7). In addition to the main broad peak at 2.3 V which corresponds to a topotactic lithium insertion process, there is a gradual increase in intensity of the peak at 3.0V on recharge. On the fourth charge process the peak of 3.0V is already well developed but this is not the case for the discharge process. The peak on charge grows sharper upon further cycling suggesting the formation of a new phase.[32] Upon further cycling, the sharp peak at 3.0V continuously grows and the broad peak of 2.3 V fades. In contrast to the broad peak at 2.3V, there is no peak on discharge corresponding to the sharp peak of 3.0V on charge. The lack of the corresponding peak on discharge to the sharp peak of 3.0V on charge indicates that the newly formed phase on charge is difficult to discharge; this would be mostly responsible for the decay of the battery. The working voltage drops continuously upon further cycling, accompanied by the gradual growth of the new phase of 3.0V on charge. It drops below the cut-off value of 1.6V after only 6 cycles (Figure 5.8). This is also in contrast to the $NaMoO_3$, for which

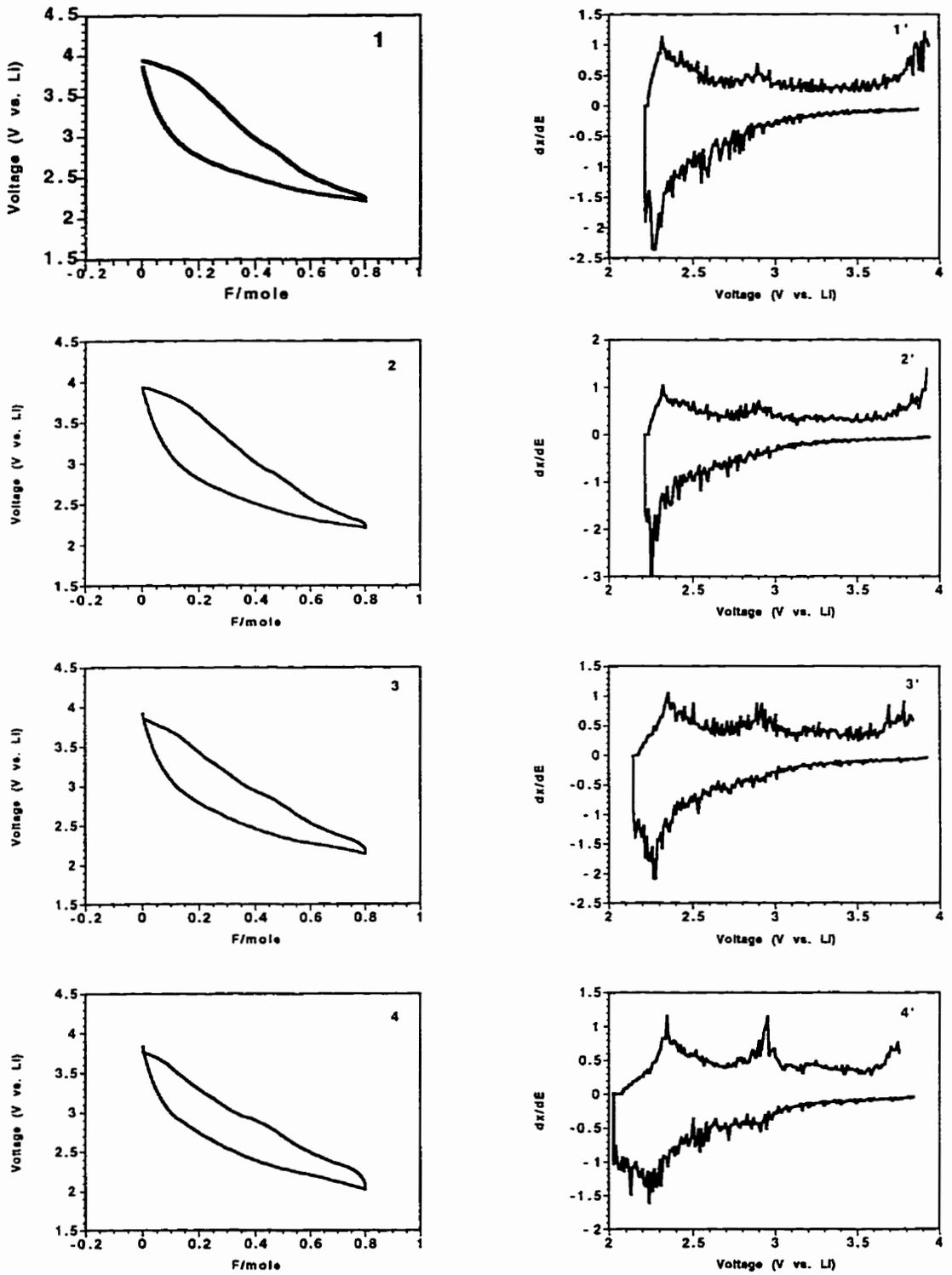

Figure 5.7 **Voltage vs. composition, and differential capacity (dx/dE) vs. voltage for Li insertion into monolayer nanocomposite $(PEO)_{0.4}NaMoO_3$. The number indicates the cycling number. (continued)**

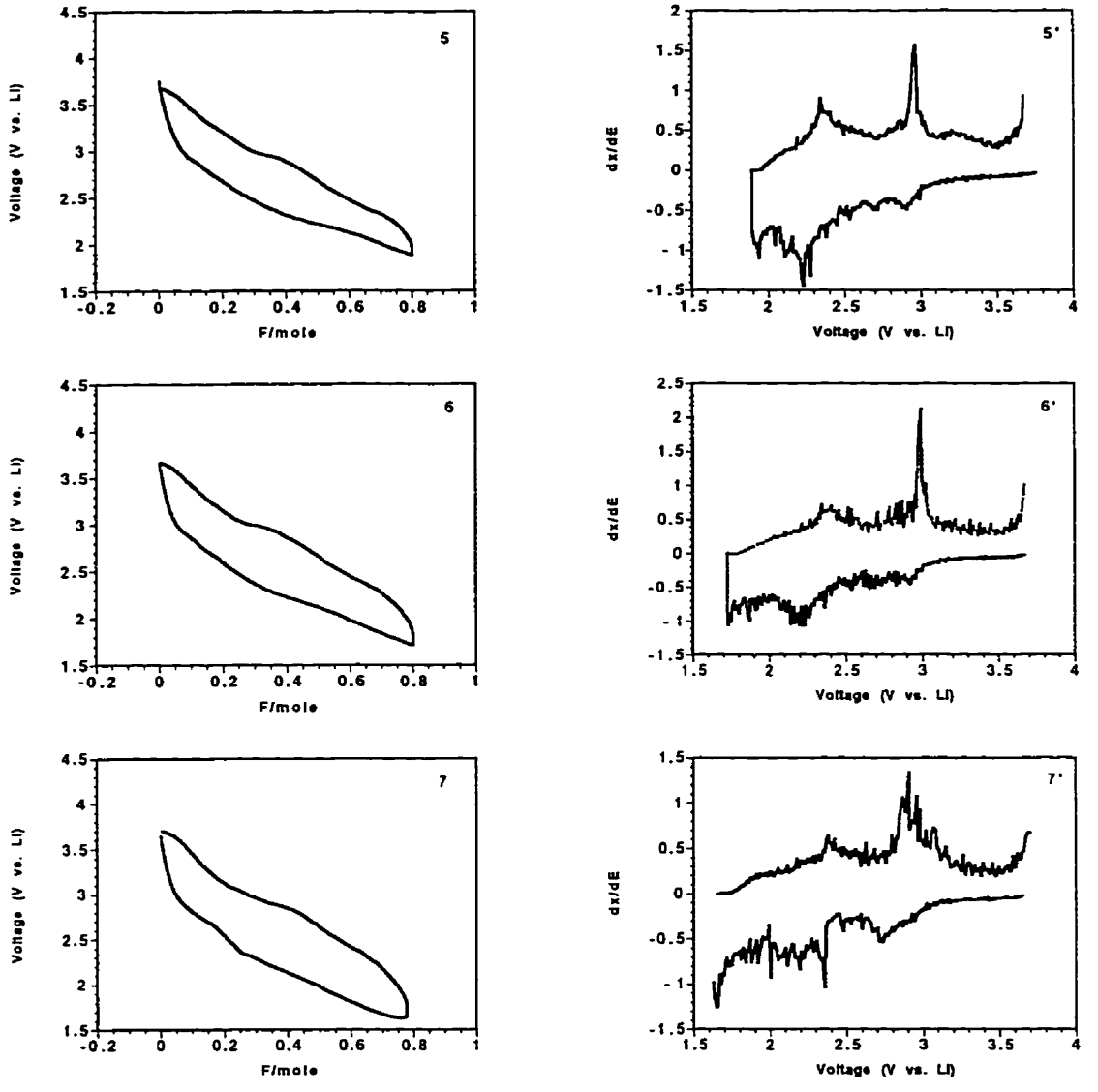

Figure 5.7 (continued) Voltage vs. composition, and differential capacity (dx/dE) vs. voltage for Li insertion into monolayer nanocomposite $(PEO)_{0.4}NaMoO_3$. The number indicates the cycling number.

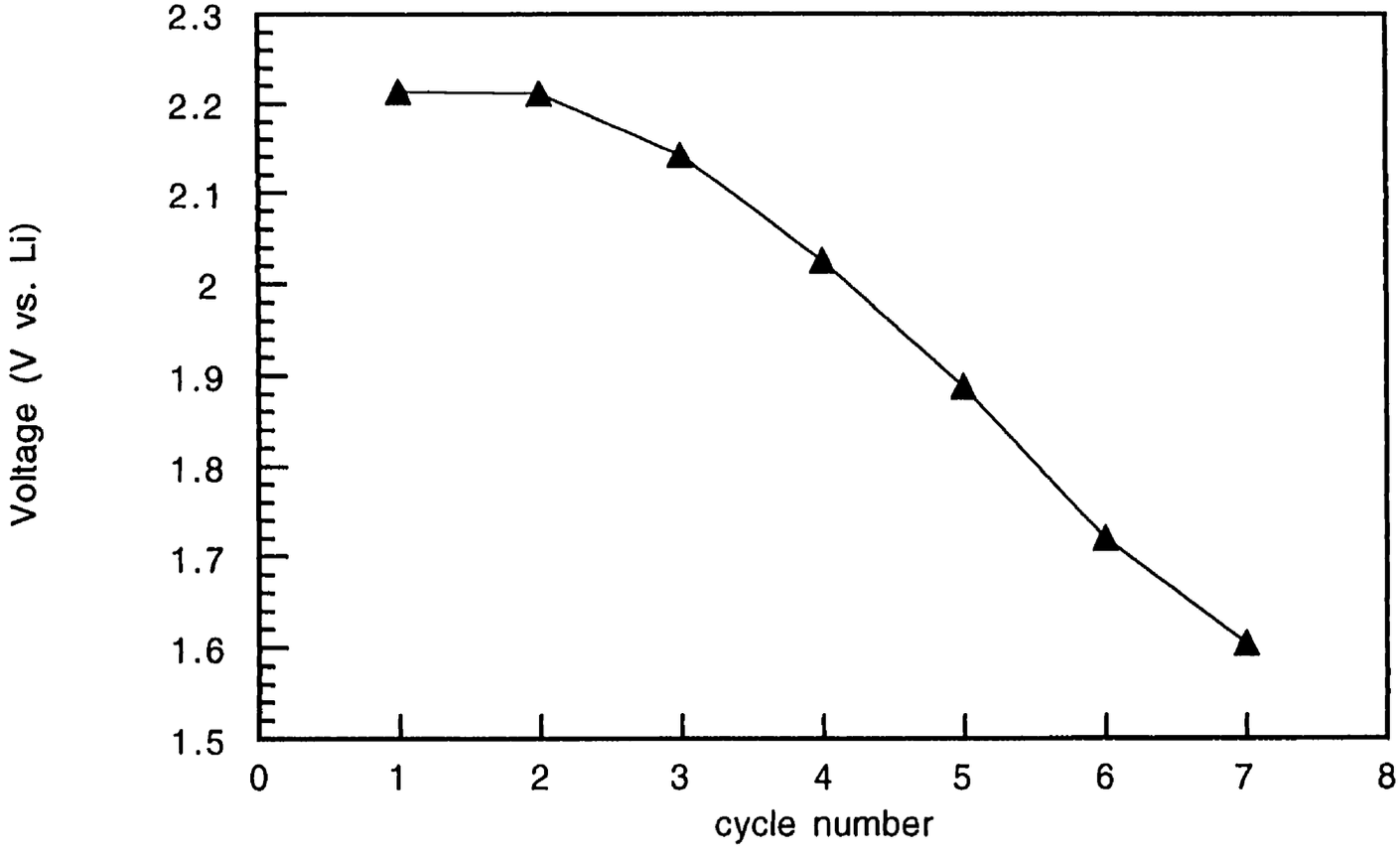

Figure 5.8 **Voltage at x(Li) = 0.8 (end of discharge) vs. cycle number for monolayer nanocomposite $(PEO)_{0.4}NaMoO_3$/Li cell using 1M $LiClO_4$ solution in PC as electrolyte**

no new phase at 3.0V was detected and the cell failed due to the high polarization of the charging process. This behavior is similar to that found for monolayer PEO/V_2O_5 nanocomposites, where polymer incorporation led to a significant drop in cell capacity, even after the first cycle.[32] The new phase formed in this process requires further exploration. It shows that the differential capacity plot is a very useful tool for identification of the redox process, otherwise not well presented in discharge and charge cycling curves.

5.3.4 Cycling behavior of lithium battery with bilayer nanocomposite $(PEO)_{0.9}(Li,Na)MoO_3$ as cathode (x(Li) = 0.8)

Figure 5.9 shows voltage curves for cycling of the lithium battery with bilayer nanocomposite $(PEO)_{0.9}(Li,Na)MoO_3$ as the cathode material after the initial cycling. The voltage of discharge goes down to 2.1V, corresponding to a take of 0.80 lithium per formula weight. As for the monolayer nanocomposite $(PEO)_{0.4}NaMoO_3$ battery, the smooth continuous decrease observed on the first discharge cycle for bilayer nanocomposites, together with the absence of a well-defined plateau region, suggests a topotactic single phase Li^+ insertion process. The hysteresis between the discharge and charge curves is much smaller than that of monolayer nanocomposite, suggesting better reversibility. The differential capacity plot is quite similar to that of monolayer nanocomposites in the first three cycles. There is a broad symmetrical peak at 2.3V for both charge and discharge processes, suggesting a one phase lithium insertion. The small peak separation (< 50 mV) shows the lithium insertion is quite reversible. Further it is

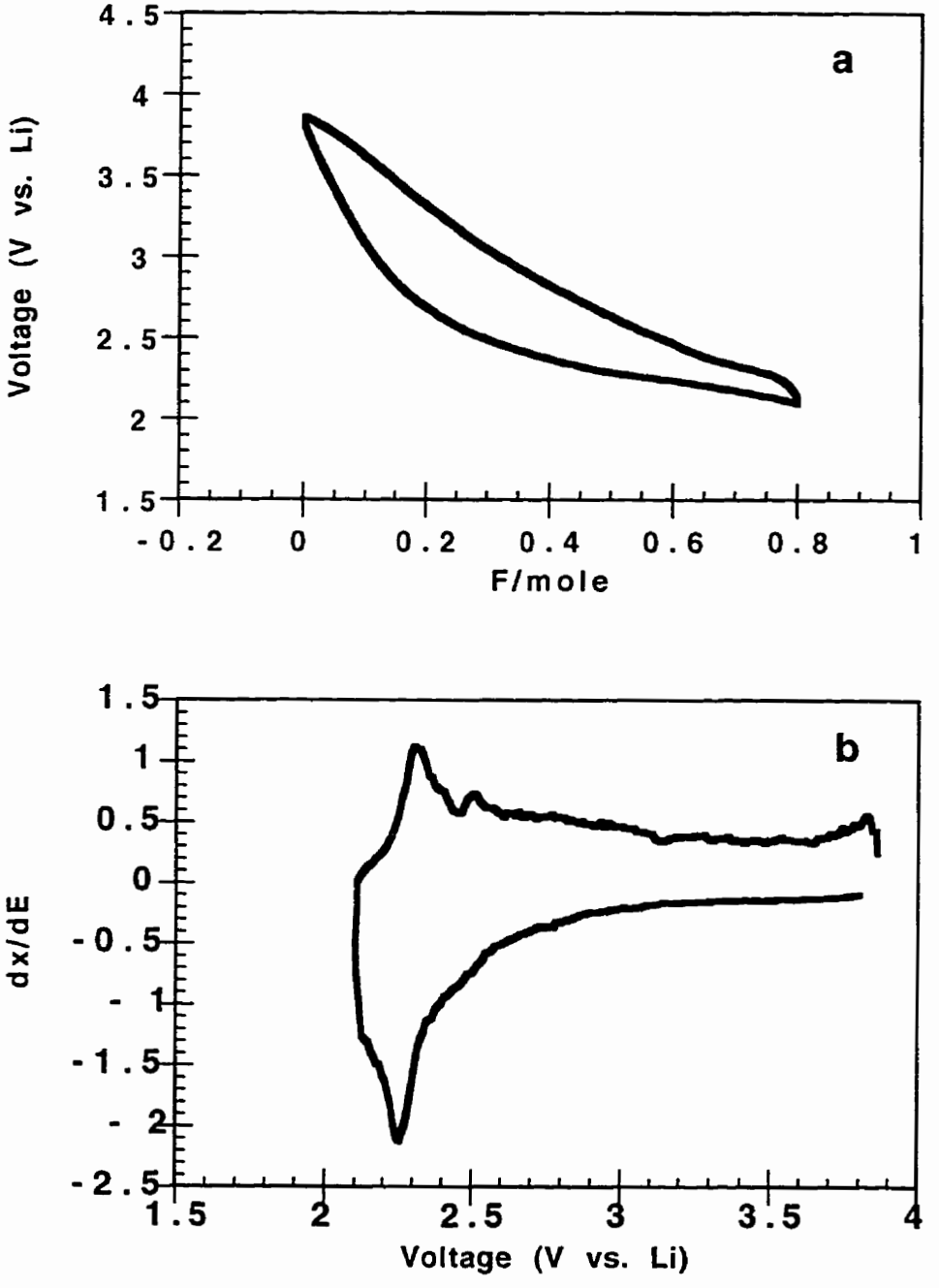

Figure 5.9 (a) Voltage vs. composition for Li insertion into bilayer nanocomposite $(PEO)_{0.9}(Li,Na)MoO_3$ and (b) differential capacity (dx/dE) vs. voltage corresponding to (a)

noticed that the peak separation is slightly smaller than that for the monolayer nanocomposite.

The end charge voltage of the bilayer $(PEO)_{0.9}(Li,Na)MoO_3$ is lower than that of the monolayer $(PEO)_{0.4}NaMoO_3$ nanocomposite (Figure 5.10), suggesting a lower cell polarization. As was observed for the monolayer nanocomposite battery, there is a decrease of hysteresis on the charge and discharge curve upon cycling. The plateau at 3.0V on the charge process also developed on further cycling (Figure 5.11), but at a lower rate than that of monolayer nanocomposite. The phase transition can be seen more clearly on the differential capacity plot. The peak of 3.0V similar to that monolayer began to be visible on the fifth cycle, which can be compared with the monolayer nanocomposite $(PEO)_{0.4}NaMoO_3$, where the 3.0V peak was observed from the third cycle. This is the same phase which makes the monolayer battery fail after only six cycles. The evolution of the new phase is very complicated upon further charge and discharge. The intensity of the charge peak at 3.0V continuously increases and that of 2.3V decreases. On the 14^{th} charge, the peak at 2.3V almost disappears and that of 3.0V grows and becomes very sharp. At the same time there is a growing intensity at about 2.8V on the charge curve. Meanwhile, on the discharge curve, the peak at 2.3V did not disappear completely and a broad peak was also seen at 2.8V. This indicates that another new phase (2.8V) is being formed upon extended charge. It is a reversible process as it has a broad peak and a very small peak separation on charge and discharge which is comparable with the single phase Li insertion of 2.3V. From the cycles 15 to 20, the peak at 3.0V of the charge process gradually disappears and merges with that of 2.8V. Meanwhile, on discharge, the intensity

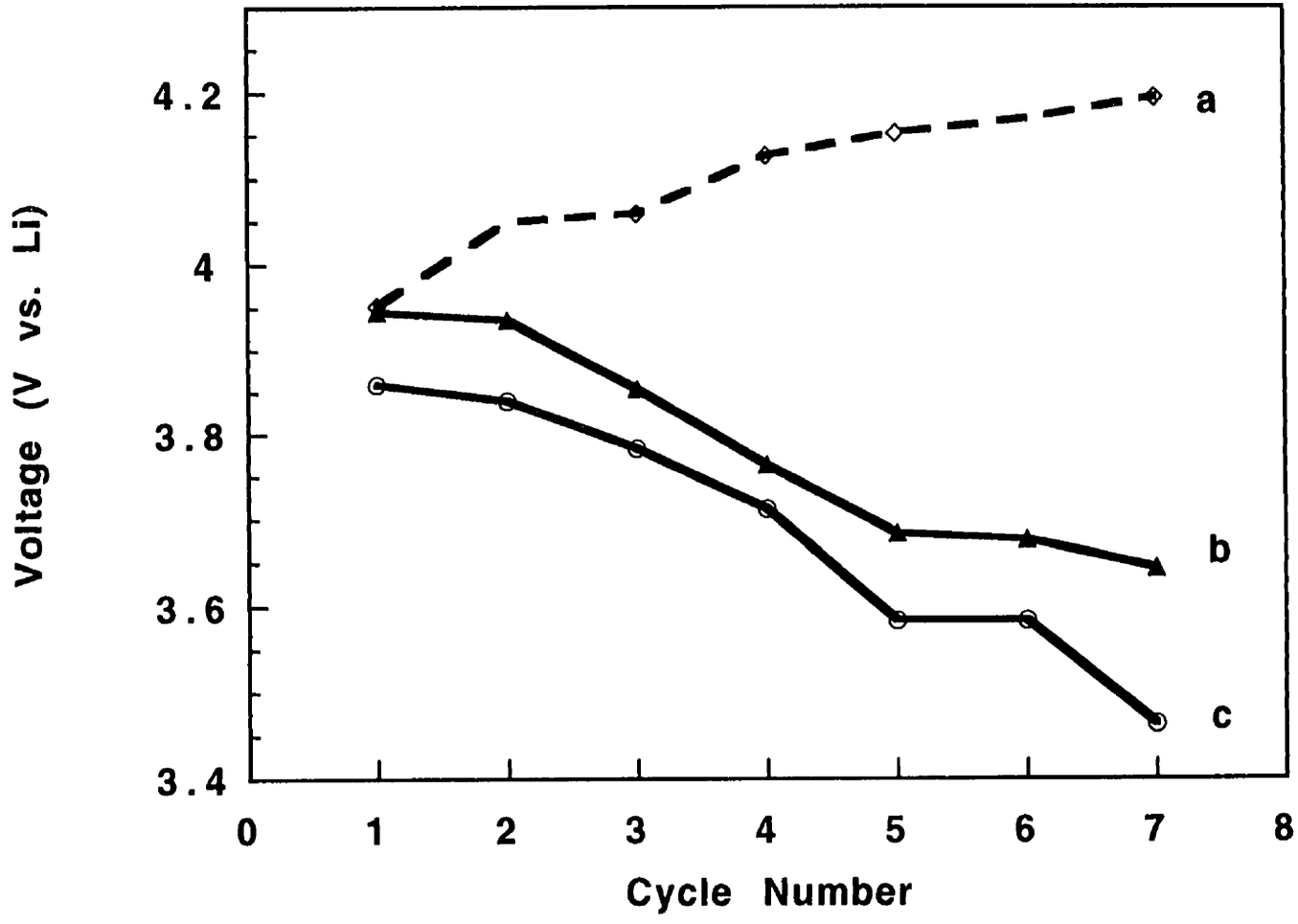

Figure 5.10 Voltage at x(Li) = 0 (end of charge) vs. cycle number for (a) $NaMoO_3$, (b) monolayer nanocomposite $(PEO)_{0.4}NaMoO_3$ and (c) bilayer nanocomposite $(PEO)_{0.9}(Li/Na)MoO_3$

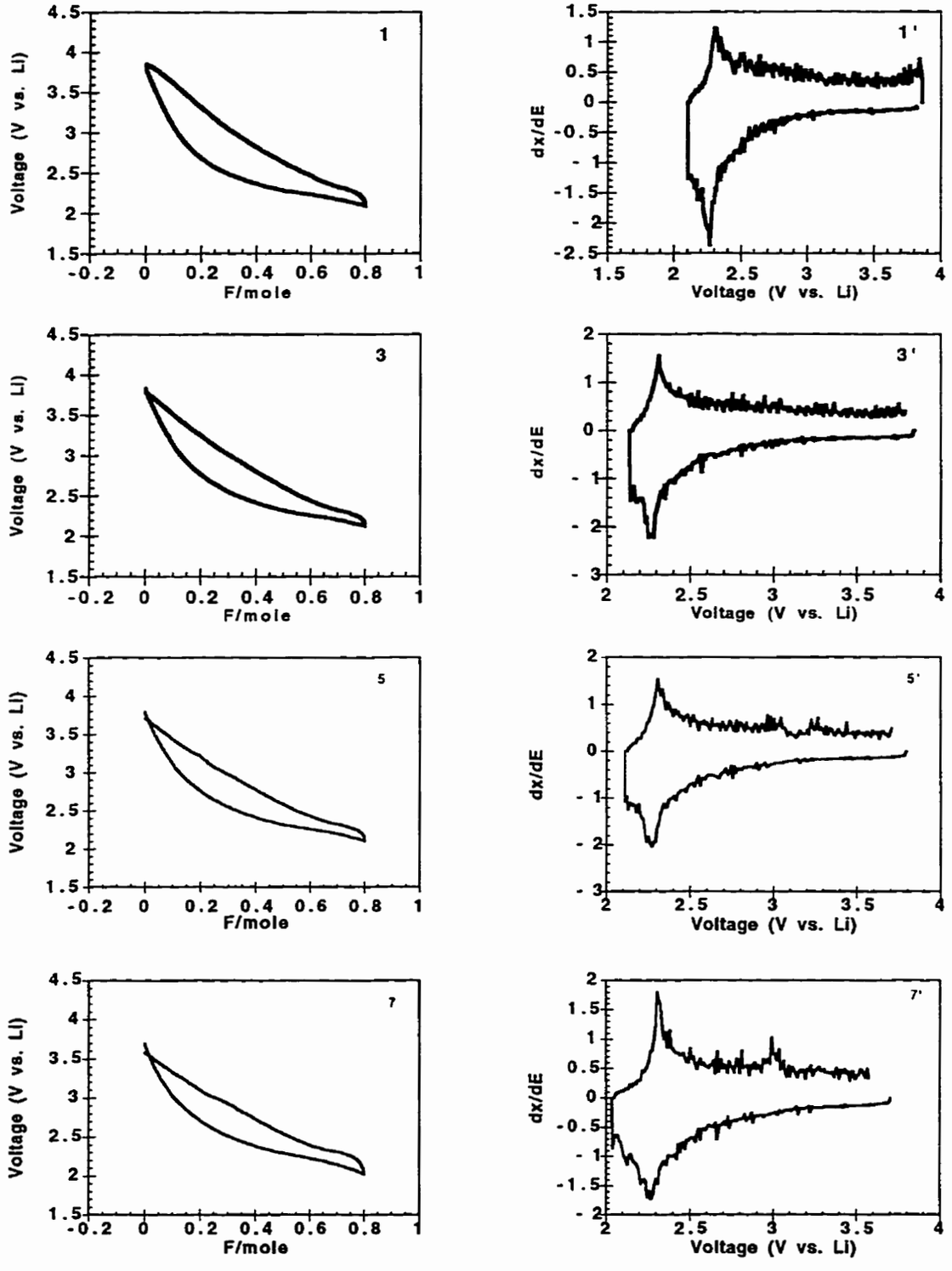

Figure 5.11 Voltage vs. composition, and differential capacity (dx/dE) vs. voltage for Li insertion into bilayer nanocomposite $(PEO)_{0.9}(Li,Na)MoO_3$. The number indicates the cycling number. (continued)

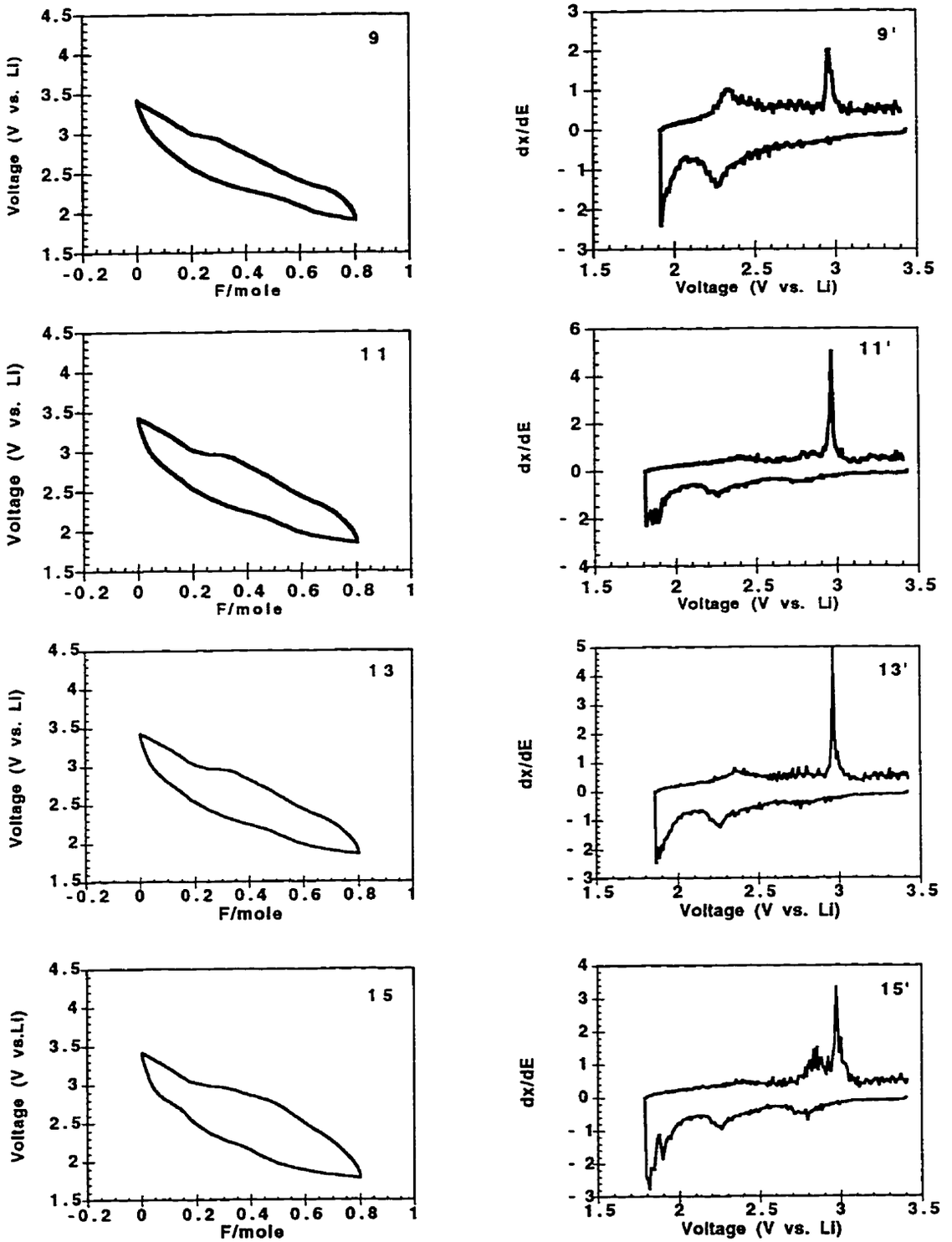

Figure 5.11 (continued) Voltage vs. composition, and differential capacity (dx/dE) vs. voltage for Li insertion into bilayer nanocomposite $(PEO)_{0.9}(Li,Na)MoO_3$. The number indicates the cycling number.

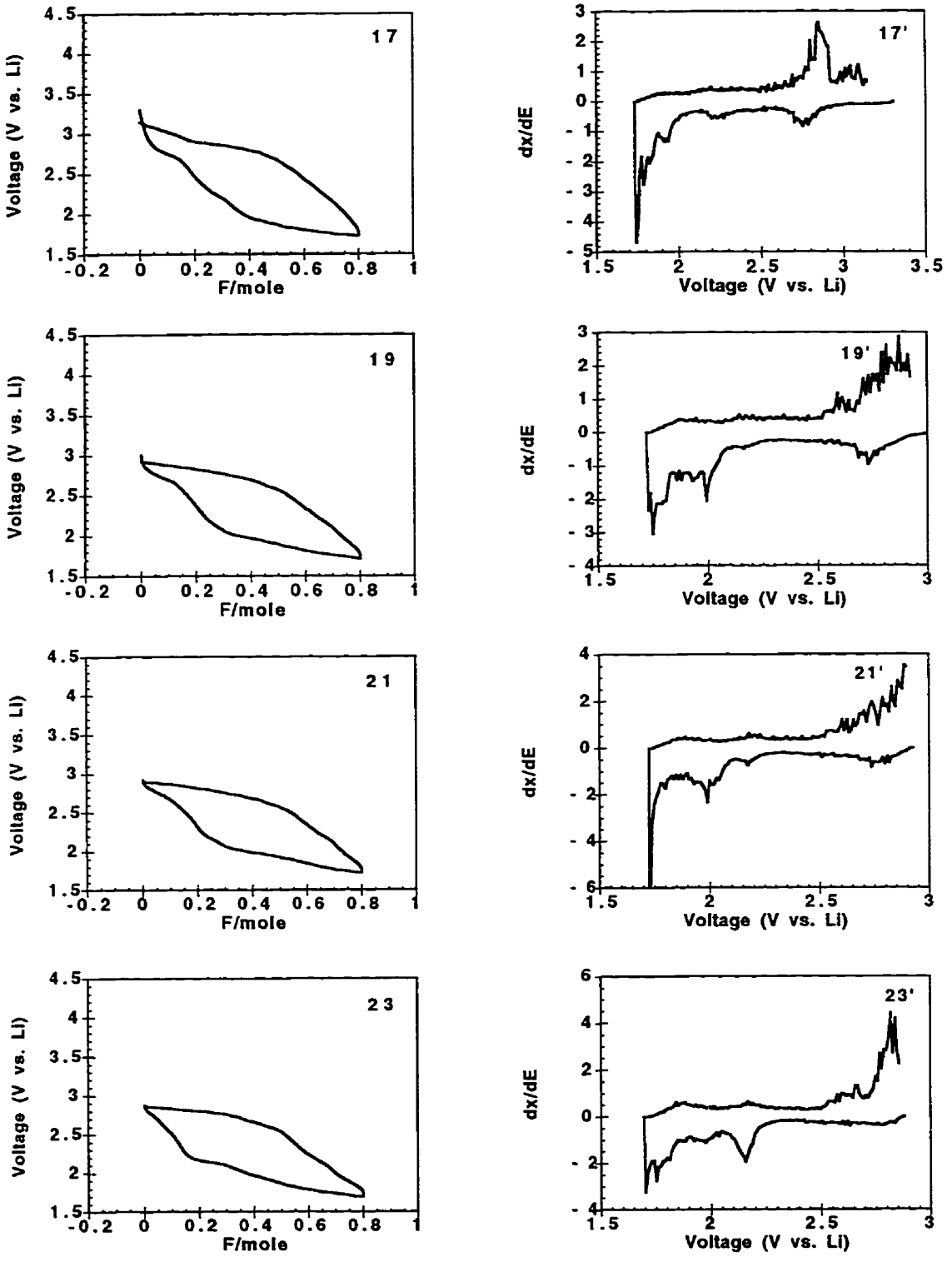

Figure 5.11 (continued) Voltage vs. composition, and differential capacity (dx/dE) vs. voltage for Li insertion into bilayer nanocomposite $(PEO)_{0.9}(Li,Na)MoO_3$. The number indicates the cycling number.

of the peak at 2.8V increases, and that at 2.3V decreases and is almost invisible at the 20th cycle. This suggests that the new phase of 3.0V formed upon further cycling for bilayer $(PEO)_{0.9}(Li,Na)MoO_3$ can be transformed to a new phase under the experimental conditions. It is also noticed that a new peak forms at 2.0V on discharge and the intensity of this peak increases gradually. Beginning at cycle 21, the intensities at 2.8V and 2.0V gradually decrease on discharge. On the other hand, a new peak starts to grow at 2.15V on discharge. Meanwhile there is no significant change during the charging process, except for the formation of a small peak at 2.2 V. This is accompanied by a drop in cell voltage drops from 1.72V to 1.65V . The main charge and discharge at this stage is the process at 2.8 V and 1.68 V, while there is still a process at 2.15 V, indicating a multi-phase system. The lithium intercalation/deintercalation induces the unfavorable phase transition for both the monolayer and bilayer PEO/MoO_3 nanocomposites battery, which is the main cause of the failure of the batteries. The evolution of the potential at the end of the discharge as a function of the number of cycles is plotted in Figure 5.12.

5.3.5 Deeper cycling behavior of the lithium battery with bilayer nanocomposite $(PEO)_{0.9}(Li/Na)MoO_3$ as cathode (x(Li) = 1.5)

Since the bilayer $(PEO)_{0.9}(Li,Na)MoO_3$ nanocomposite battery has better stability than that of the monolayer nanocomposite $(PEO)_{0.4}NaMoO_3$ battery, we performed the cycling of the bilayer nanocomposite $(PEO)_{0.9}(Li,Na)MoO_3$ battery for x(Li) = 1.5. Figure 5.13 shows the cycle curves for bilayer nanocomposites down to a voltage of 1.75V vs. lithium, corresponding to a take of 1.5 lithium per formula weight. Instead of the expected smooth continuous discharge and charge curves for both monolayer and

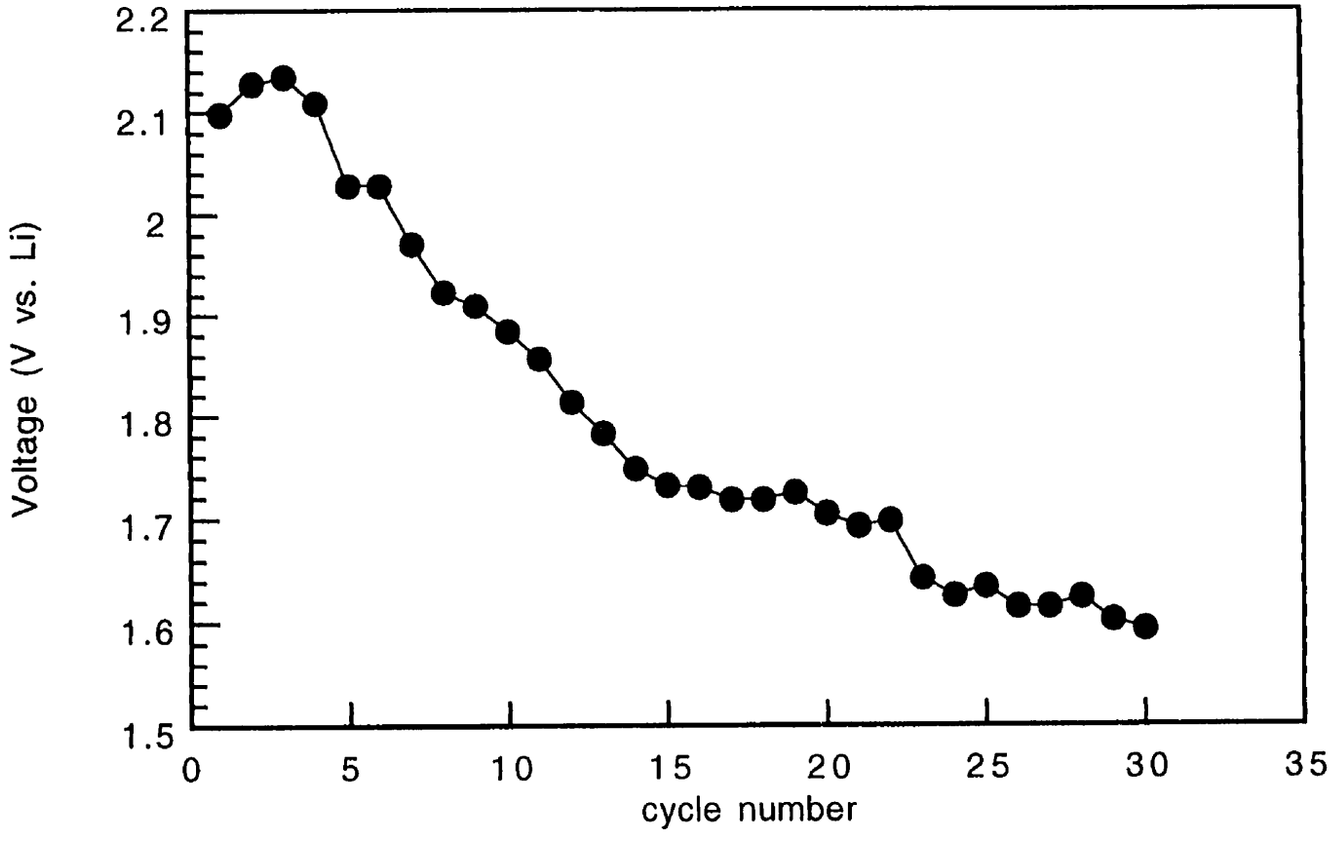

Figure 5.12 **Voltage at x(Li) = 0.8 (end of discharge) vs. cycle number for bilayer nanocomposite $(PEO)_{0.9}(Li/Na)MoO_3$**

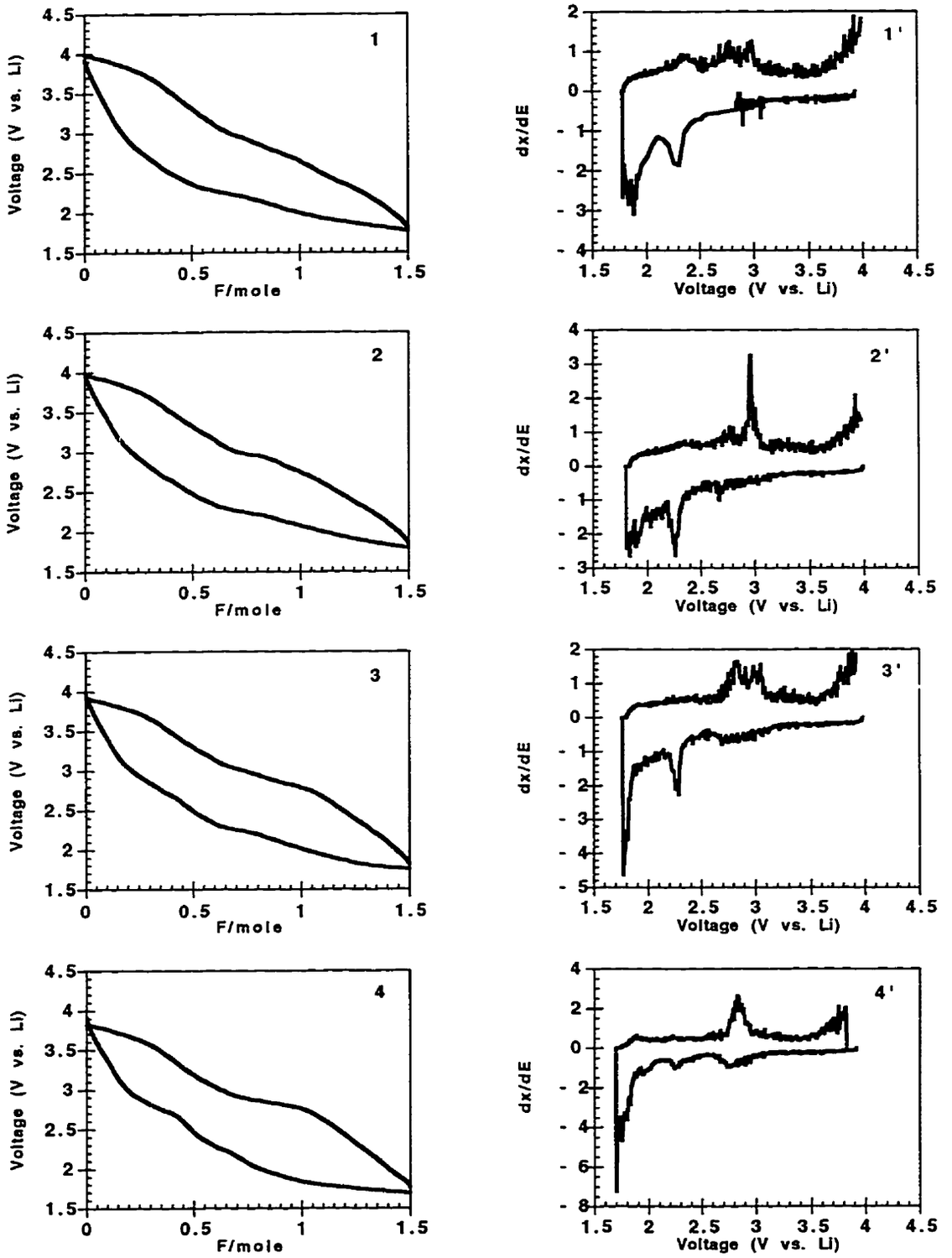

Figure 5.13 Voltage vs. composition, and differential capacity (dx/dE) vs. voltage for Li insertion into bilayer nanocomposite $(PEO)_{0.9}(Li,Na)MoO_3$ (x(Li) = 1.5). The number indicates the cycling number. (continued)

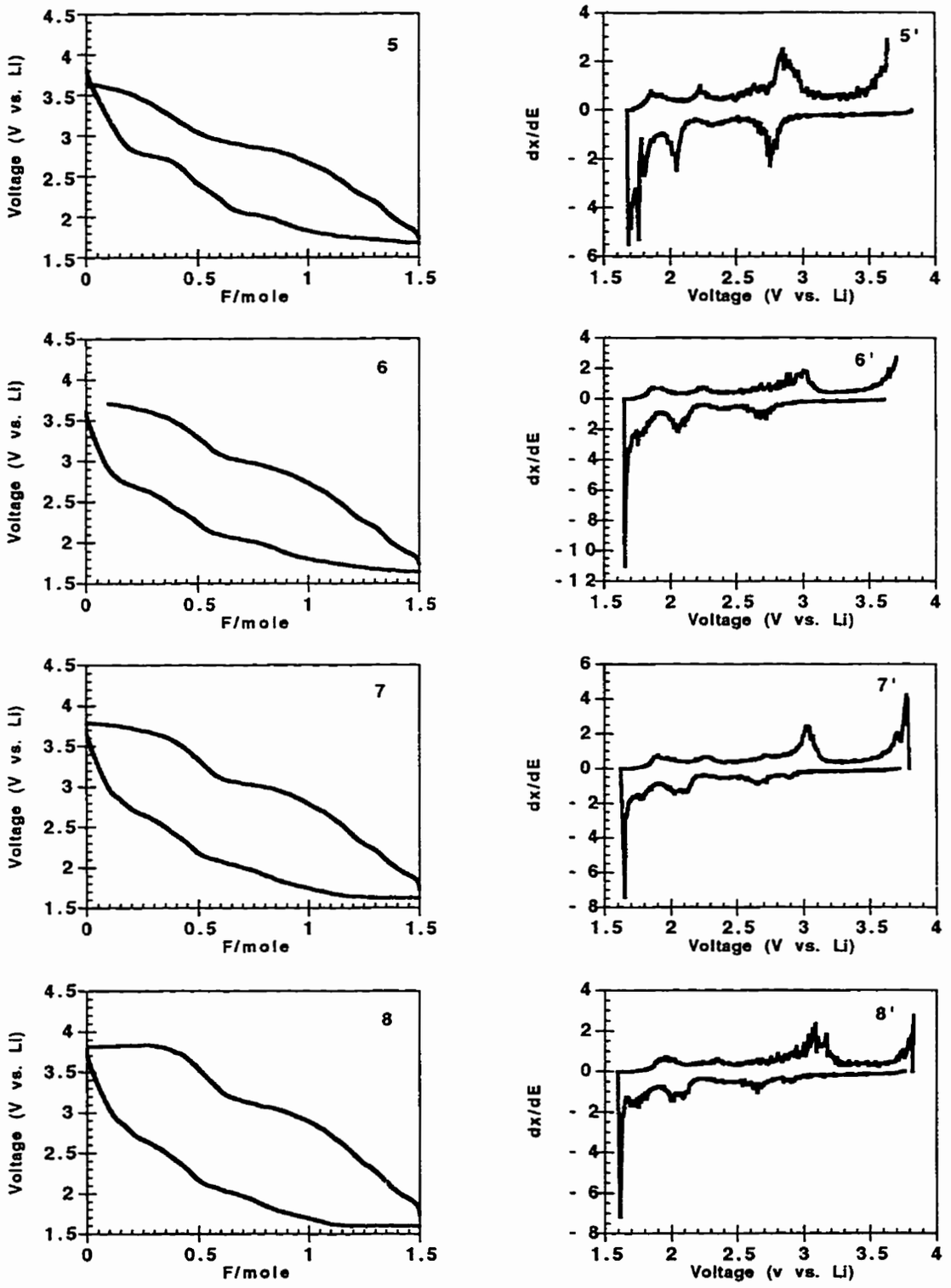

Figure 5.13 (continued) Voltage vs. composition, and differential capacity (dx/dE) vs. voltage for Li insertion into bilayer nanocomposite $(PEO)_{0.9}(Li,Na)MoO_3$ (x(Li) = 1.5). The number indicates the cycling number.

bilayer nanocomposite to the discharge extent of x = 0.8, when the battery was subjected to discharge to x = 1.5, a plateau at 2.3V developed even in the first discharge and recharge process after the initial cycling, suggesting that the deep discharge induced the phase change of the cathode material. In the differential capacity plot for the first cycle, although there is still a peak at 2.3V on discharge corresponding to a one-phase intercalation process for $NaMoO_3$, the main peak was centered at 1.9V. On the recharge cycle, the peak at 2.3 V which was observed both for monolayer and bilayer nanocomposites being charged to x = 0.8, is hardly observed. Peaks at 3.0 V and 2.8 V which only were observed for the bilayer nanocomposite having been charged and discharged several times were observed on the first recharging process. During the second, third and fourth charges (Figure 5.13), the peak at 2.3V gradually disappeared on discharge. Upon recharge, the peak at 3.0V gradually shifted to 2.8V, which is the same as that observed for the bilayer discharged to x = 0.8 between the 15^{th} and 20^{th} cycles. During cycle 5, two new peaks (2.1V and 2.8V) developed. The intensity of these two peaks gradually decreased upon further cycling to the 8^{th} cycle. It should be noted that the differential capacity plot for the 8^{th} cycle is similar to that being discharged to x = 0.8 and cycled more than 30 times, except there is an extra peak at 2.5V on the discharge curve of x = 1.5. Comparing this with those discharged to x = 0.8, we can say that the deep discharge of the battery induced the phase change and destabilized the battery. The transformations of the phases for two batteries are very similar. Therefore the failure of the battery for the bilayer nanocomposite $(PEO)_{0.4}(Li,Na)MoO_3$ battery discharged to x(Li) = 0.8 is due to the accumulation of lithium in the cathode. Lithium inserted during

discharge cannot be completely removed from the cathode material on charging and induces the formation of new phases. This is the main cause for the failure of the battery.

5.4 Discussion

5.4.1 Electrode process

At low temperatures, reactions in the solid state tend to involve minimal structural change. As expected from its layered structure, MoO_3 reacts readily with lithium to form ternary phases at low temperature. This reaction is favored in the electrochemical lithium insertion, since it is a low temperature route. It has been suggested that cell reversibility is optimized when no chemical bonds are broken during discharge. Figures 5.3, 5.7, and 5.9 show the first discharge and charge cycle of $NaMoO_3$, the monolayer nanocomposite $(PEO)_{0.4}NaMoO_3$, and the bilayer nanocomposite $(PEO)_{0.9}(Li,Na)MoO_3$, respectively. They all show smooth continuous potential decreases which, together with the absence of a well-defined plateau region, suggests a classical topotactic single phase Li^+ insertion process. From the point of view of the reversibility, this kind of single phase lithium insertion is favored over multiphase lithium insertion. On the other hand, it has the shortcoming of a continuous drop of potential upon discharge. The electrochemical reaction can be written as a classic lithium intercalation reaction:

$$xLi^+ + e + (Na,Li)_aMoO_3 \rightarrow (Li_{(a+x)},Na_a)MoO_3.$$

$$xLi^+ + e + (Na,Li)_a(P)_yMoO_3 \rightarrow Li_{a+x}MoO_3.\ (P = monolayer\ PEO\ or\ bilayer\ PEO)$$

This type of reaction has been observed for many intercalation cathode reactions. It is also consistent with what has been observed in the MoO_3 film by Julien *et al.*[27]

However it is inconsistent with what has been observed for a bulk MoO_3 cathode. Two plateaus were reported for MoO_3 during discharge to x(Li) = 1.0 with an inflection at about 0.5.[14,24, 25, 29]

Julien *et al.* ascribed the electrochemical behavior of MoO_3 to being largely controlled by the high deficiency of oxygen in MoO_3.[15, 20] In the thin film MoO_3 battery they studied, the molybdenum was partially reduced, since it showed very high electronic conductivity. In this respect, molybdenum bronzes and their PEO intercalated nanocomposites are very similar, as molybdenum is partially reduced in both. Therefore they show different discharge behavior than does bulk MoO_3. The reversibility should be high for a single phase lithium intercalation process. Therefore starting with the prereduced alkaline metal molybdenum bronze is expected to improve the battery performance of molybdenum oxide. In this respect, sodium and lithium molybdenum bronze is expected to be a better candidate for a cathode material than molybdenum oxide in a secondary lithium battery.

Besenhard examined the d-spacing of MoO_3 upon intercalation of lithium.[16] He found that the d-spacing reached a maximum at x(Li) = 0.5. It is not a coincidence that the dispersion of the discharge curves of MoO_3 also occurs at x = 0.5. Therefore, it probably is the continuous increase in d-spacing to a maximum at x = 0.5 that induces the phase transformation to better accommodate lithium. In molybdenum bronze and its PEO intercalated nanocomposites, the d-spacing is already expanded and so little structural rearrangement is required to accommodate a certain amount of lithium. Therefore, a single phase process intercalation/deintercalation of lithium and higher reversibility than that of

bulk molybdenum oxide resulted. The fact that the first two cycle curves are almost superimposable for $NaMoO_3$ (Figure 5.4) supports this idea.

5.4.2 Polarization of battery

Figure 5.10 shows the voltage vs. cycle number at the end of charge (x = 0) for $NaMoO_3$, monolayer nanocomposite $(PEO)_{0.4}NaMoO_3$, and bilayer nanocomposite $(PEO)_{0.9}(Li,Na)MoO_3$. It can be seen that the voltage increases upon further cycling for $NaMoO_3$, while for both monolayer $(PEO)_{0.4}NaMoO_3$ and bilayer $(PEO)_{0.9}(Li,Na)MoO_3$ nanocomposites, the working voltage decreasescontinuously. This different change in working voltage, among other things, reflects the effect of PEO on the mobility of lithium ion. We know that electronic conductivity has the following order: $NaMoO_3$ > monolayer nanocomposite $(PEO)_{0.4}NaMoO_3$ > bilayer nanocomposite $(PEO)_{0.9}(Li,Na)MoO_3$. Therefore, the difference in voltage changes should reflect the changes in ionic conduction due to the intercalation of PEO. For $NaMoO_3$, the strong interaction between MoO_3 sheets and cations makes the deintercalation of lithium on charging more difficult and higher and higher voltage is needed to take away intercalated lithium. Improvement of ionic conductivity in a PEO/MoO_3 nanocomposite can result from both the pillar effect, the shielding effect, and the ionic conduction of PEO. The pillar effect of PEO can be two-fold. While the pillar effect increases the space between MoO_3 sheets by increasing the d-spacing, the bulk polymer itself occupies the major part of the space and can block the ionic conduction. This bulk effect can be manifested by the ionic conduction of PEO. However, from our conductivity and ^7Li, and ^{23}Na NMR spin-lattice relaxation and linewidth studies, the enhancing of the cation motion is only realized at high temperature. Therefore, the most important reason for enhancing cation mobility at room temperature

at which the batteries were cycled is the shielding effect of PEO, reducing the interaction between the MoO_3 sheets and Li^+.

It is also interesting to note that the bilayer nanocomposite has much better ionic conductivity than the monolayer nanocomposite. This can be seen from the comparison of the discharge-charge curves for the two nanocomposites shown in Figure 5.14 (for the reduction /oxidation cycle after the initial cycling). Removal of all the Li ion previously inserted during the discharge is achieved during oxidation for both monolayer and bilayer nanocomposite materials. The voltage difference however, (which is an indirect estimate of cell polarization) between the discharge and charge voltage for the monolayer system is about twice that of the bilayer. We conclude that ionic transport of Li^+ is more enhanced in the bilayer nanocomposite compared to the monolayer nanocomposite. For the bilayer nanocomposite, two layers of PEO isolated cations completely from the MoO_3 sheets, while for the monolayer, the MoO_3 sheets still have close contact at one end with cations. On charge and discharge, lithium is shielded well in the bilayer nanocomposite but not in the monolayer nanocomposite, which accounts for the different polarization of the monolayer and bilayer cells. The above discussion also hints that the lithium ion conduction will be less affected by the phase transformation of MoO_3 sheets for the bilayer nanocomposite compared to that of the monolayer nanocomposite, since there is less direct interaction between MoO_3 sheets and cations in the bilayer phase.

5.4.3 Phase evolution of cathode active materials and the cyclability of batteries

Figures 5.7 and 5.11 show the voltage and differential capacity plots for a monolayer nanocomposite $(PEO)_{0.4}NaMoO_3$ battery and a bilayer nanocomposite $(PEO)_{0.9}(Li,Na)MoO_3$ battery, respectively. At the beginning, a wide single peak centered

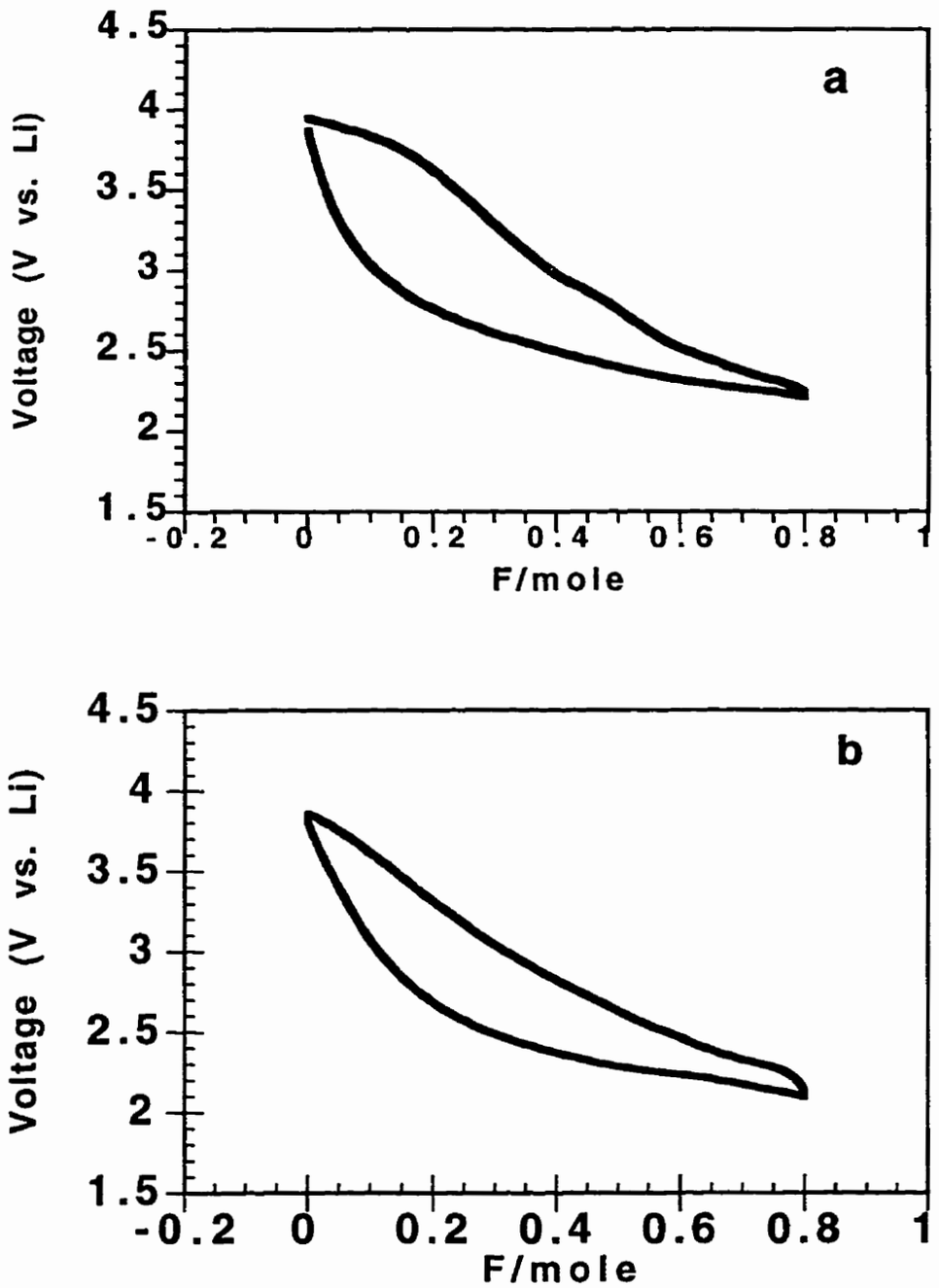

Figure 5.14 Voltage vs. composition for Li insertion into (a) monolayer nanocomposite $(PEO)_{0.4}NaMoO_3$ and (b) bilayer nanocomposite $(PEO)_{0.9}(Li,Na)MoO_3$ after the initial cycling

at 2.3V was observed for both batteries, which should correspond to the single phase Li insertion process, similar to that of $NaMoO_3$ (Figure 5.5). However the cathode is not very stable upon further cycling for both nanocomposite batteries. From the fourth cycle for the monolayer nanocomposite battery and the seventh cycle for the bilayer nanocomposite battery, a small peak starts to grow at 2.95 - 3.0V, suggesting the beginning of a new phase. This phase transition is not quite reversible, as no well-defined peak on discharge can be found to correspond to this peak. We can clearly see that the decay of the battery is accompanied by the formation of the new phase. It is the irreversibility of the new phase which is responsible for the decay of the battery. No corresponding phase transition was observed for the $NaMoO_3$ battery.

The ionic conduction is insensitive to the host change for the bilayer nanocomposite battery, since the Li^+ ion is sandwiched between PEO layers in the bilayer nanocomposite material. The change of the configuration of the MoO_3 sheet to a new phase has a smaller effect on the ionic mobility for the bilayer nanocomposite. On other hand, there is a stronger interaction between Li^+ and one end of the MoO_3 sheet for the monolayer nanocomposite. The transition of the MoO_3 sheet to a new phase may exert a stronger effect on the movement of Li^+. Thus, while the development of the new peak at 3.0V will destroy the monolayer nanocomposite $(PEO)_{0.4}NaMoO_3$ battery after only seven cycles, the bilayer battery will still survive extended cycles, i.e., the bilayer nanocomposite batteries have a higher cyclability.

It is interesting to note that the deep charge (x(Li) = 1.5) induces the same phase transfer for the bilayer nanocomposite battery as was observed for moderate discharge

(x(Li) = 0.80) of the same battery after more cycles (7). A new peak at 2.95V even develops on the first recharge curve. The differential capacity plot for the first cycle (x(Li) = 1.5) after the initial cycling is comparable to those cycled 15 times (x(Li) = 0.80). Further cycling (x(Li) = 1.5, fifth charge) gives a differential capacity plot almost the same as that observed for the moderate cycle (x(Li) = 0.80) for 19 times. It is concluded that the deep charge and discharge induce the same phase transition for the starting material. This also allowed us to draw the conclusion that lithium irreversibly trapped in the lattice is the main cause of failure of the nanocomposite batteries.

Comparing the nanocomposite material batteries with the $NaMoO_3$ battery, it is obvious that both nanocomposite material batteries have much lower polarization than does the $NaMoO_3$ battery upon extended cycling. This suggests that the intercalation of PEO does improve the ionic mobility by shielding the interaction between MoO_3 sheets and cations. However, the stability of nanocomposite materials is much lower than that of $NaMoO_3$ under electrochemical lithium insertion conditions. Actually the discharge voltages of the $NaMoO_3$ battery are very stable; no significant voltage drop was observed after eight cycles (Figure 5.5). However, the high polarization on the charging process limited the performance of the $NaMoO_3$ battery under the present experimental conditions. Therefore change of the charging methods, among others, may improve the performance of the $NaMoO_3$ battery.

It should be pointed out that although we can monitor the phase transformation using differential capacity plots very well, we did not make any attempt to identify the different phases. The phases must be well crystallized in order to be accurately identifiable.

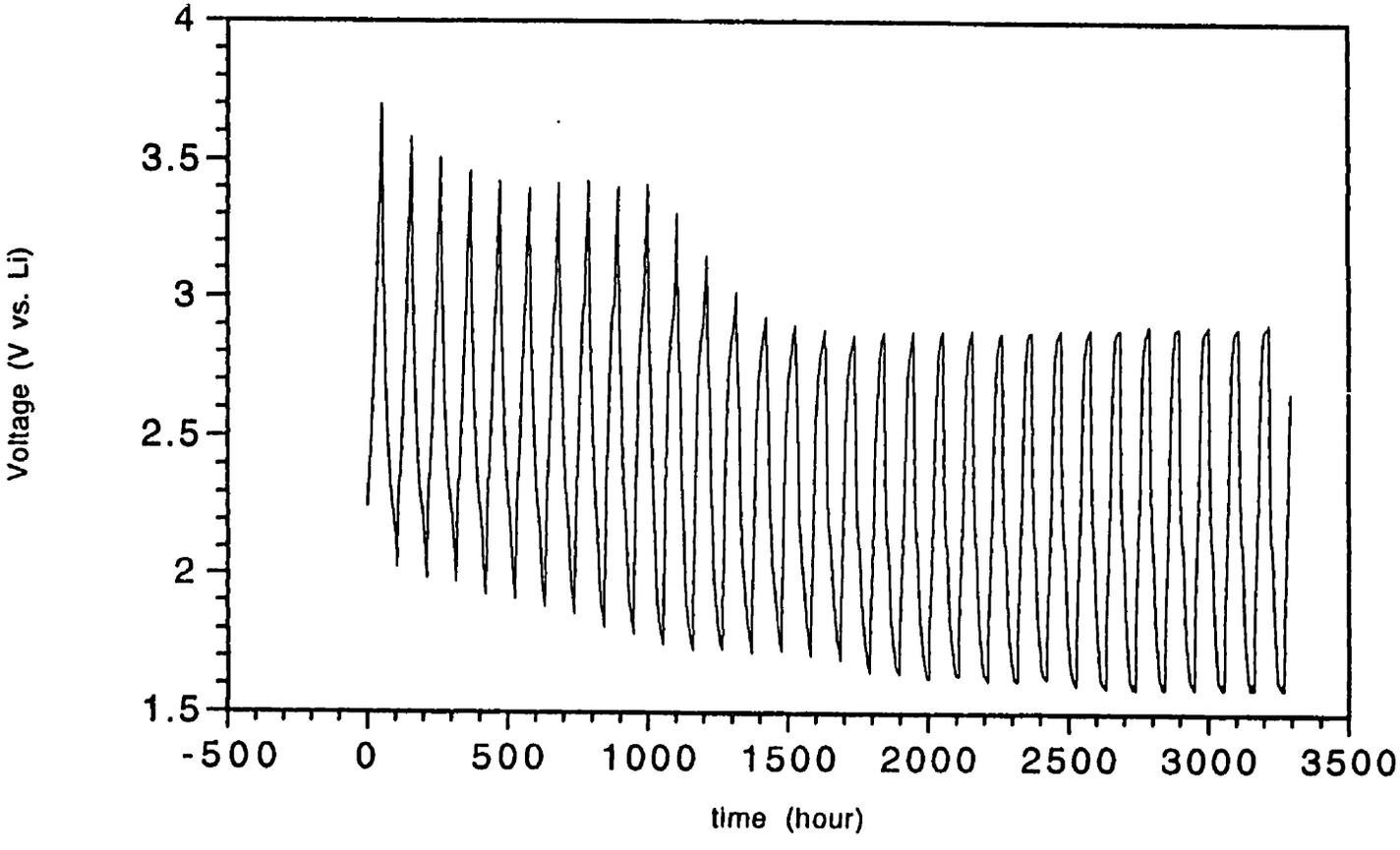

Figure 5.15 **Voltage vs. time for bilayer nanocomposite $(PEO)_{0.9}(Li,Na)MoO_3/Li$ battery**

Identification also requires more sample for each electrode, doubling the experimental time that already takes hundreds of hours for one experiment (Figure 5.15).

5.5 Conclusion

All batteries studied show a single-phase lithium intercalation process. The intercalated lithium can be reversibly deintercalated. Intercalation of PEO into $NaMoO_3$ increases the lithium mobility for electrochemical intercalation/deintercalation. However, it reduces the stability. New materials combining the high stability of $NaMoO_3$ and the high ionic mobility of polymer/$NaMoO_3$ nanocomposite need to be further studied. Also new charging methods, for different compositions of active materials/carbon conductance additive and electrolytes, to overcome the drawback of the low ionic mobility of the $NaMoO_3$ battery and to limit the phase transition of PEO nanocomposite batteries, will be helpful.

5.6 References

1. Jasinski, R. *High-Energy Batteries*, Plenum Press, New York, **1967**.

2. Brandt, K. *Solid State Ionics* **1994**, *69*, 173.

3. Maingot, S.; Baddour, R.; Pereira-Ramos, J.P.; Baffier, N.; Willmann,P. *J. Electrochem. Soc.* **1993**, *140*, L158.

4. Dahn, J. *Better Batteries Through Materials Science (Seminar)*, Hamilton, Ontario,Canada, **1995**.

5. Julien, C. *Mater. Sci. Eng.* **1990**, *B6*, 9.

6. Dahn, J.R.; Stacken, U.V.; Fong, R. *The Electrochemical Society Extended Abstracts*, Vol. *90-2* (Seattle, WA, October 14-19, **1990**) Abstract 42, p. 66.

7. Nishi, T.; Azuma, H.; Omaru, A. *U.S. Patent* , 4959281, **1990**.

8. Chen, L.; Huang, X.; Kelder, E.; Schoonman, J. *Solid State Ionics* **1995**, 76,

9. Chianelli, R.R.; Scanlon, J.C.; Rao, B.M.L. *J. Solid State Chem.* **1979**, *29*, 323.

10. Abraham, K.M. *Solid State Ionics* **1982**, *7*, 199.

11. Desilvestro, J.; Haas, O. *J. Electrochem. Soc.* **1990**, *137*, 5.

12. Besenhard, J.O. *Solid State Ionics*, **1983**, *8*, 61.

13. Kumagai, N. *J. Applied Electrochem.* **1988**, *18*, 857 .

14. Margalit, N. *J. Electrochem. Soc.* **1974**, *121*, 1460.

15. Julien, C. *Solid State Ionics* **1994**, *68*, 111.

16. Besenhard, J.O. *Solid State Ionics* **1982**, *6*, 215.

17. Besenhard, J.O.; Schollhorn, R. *J. Power. Sources* **1976**, *1*, 276.

18. Deb, S.K. *Proc. Roy. Soc. (London) Ser. A* **1968**, *304*, 211.

19. Greenblatt, M. *Chem. Rev.* **1988**, *88*, 31.

20. Campanella, L. Pistoia, G. *J. Electrochem. Soc.*, **1971**, *118*, 1905.

21. BIO-LOGIC, Ave.de l'Europe, F-38640 Claix, France.

22. Campanella, L.; Pistoia, G. *J. Electrochem. Soc.* **1973**, *120*, 383.

23. Dampier, F.W. *J. Electrochem. Soc.* **1974**, *121*, 656.

24. Bonino, F.; Bicelli, L.P.; Rivolta, B.; Lazzari, M.; Festorazzi, F. *Solid State Ionics* **1985**, *17*, 21.

25. Bohnke, O.; Robert, G. *Solid State Ionics* **1982**, *6*, 115.

26. Julien, C.; Hussain, M.; El-Farh, L.; Balkanski, M. *Solid State Ionics* **1992**, *53-56*, 400.

27. Julien, C.; Nazri, G.A.; Guesdon, J.P.; Gorenstein, A.; Khelfa, A.; Hussain, O.M. *Solid State Ionics* **1994**, *73*, 319.

28. Ruiz-Hitzky, E. *Adv. Mater.* **1993**, *5*, 334 and references therein.

29. Nazar, L. F.; Zhang, Z.; Zinkweg, D. *J. Am. Chem. Soc.* **1992**, *114*, 6239.

30. Wu, C.-G.; DeGroot, D. C.; Marcy, H. O.; Schindler, J. L.; Kannewurf, C. R.; Bakas, T.; Papaefthymiou, V.; Hirpo, W.; Yesinowski, J. P.; Liu, Y.-J.; Kanatzidis, M.G.; *J. Am. Chem. Soc.* **1995**, *117*, 9229.

31. Zachau-Christiansen, B.; West, K.; Jacobsen, T.; Skaarup, S. *Solid State Ionics* **1992**, *53-56*, 364.

32. West, K; Zachau-CHristiansen, B.; Jacobsen, T.; Skaarup, S. *Electrochimica Acta.* **1993**, *38*, 1215.

33. Whittingham, M.S. *J. Electrochem. Soc.* **1976**, *123*, 315.

CHAPTER SIX

CONDUCTIVE POLYMER/NONCONDUCTIVE HOST NANOCOMPOSITE (I)

-- INTERCALATION AND POLYMERIZATION OF ANILINE IN LAYERED α-$Sn(HOPO_3)_2 \cdot H_2O$

6.1 Introduction

Layered metal phosphates possess rich intercalation chemistry.[1, 2, 3, 4, 5] The protons in the layers can be exchanged with cations or neutralized with bases. The resulting intercalation compounds, depending on the guest molecules, can have diverse properties. [1, 2, 3, 4, 5, 6, 7] The propensity of layered metal phosphates to intercalate organic molecules has recently been utilized to prepare novel intercalation compounds of conductive polymers.[8, 9, 10] For example, aniline was polymerized in layered uranyl phosphate and zirconium phosphate.[9, 22] These materials consist of interleaved stacks of polymer chains and metal phosphate sheets. The possibility of interactions of organic and inorganic components at the molecular level suggests that new properties may result from their combination. Furthermore, since we can arrange the monomer in a fixed lattice by intercalation before it is polymerized, it can control or affect the conformation of polymers. Here we report the intercalation and polymerization of aniline in layered α-

$Sn(HPO_4)_2 \cdot H_2O$ (α- Tin Phosphate). It was characterized and studied by XRD, FTIR, thermal analysis and solid state ^{13}C and ^{31}P CPMAS NMR.

6.2 Experimental

6.2.1 Synthesis

Materials: The highly crystalline starting material α-$Sn(HOPO_3)_2 \cdot H_2O$ (d_{002} = 7.8) was prepared and stored according to the literature method.[14] $SnCl_4$ and aniline were purchased from Aldrich Company.

Preparation of (Anilinium)$_{1.0}$(α-Sn(OPO$_3$)$_{1.0}$(HOPO$_3$)$_{1.0}$ *a). Reaction of* α-$Sn(HOPO_3)_2 \cdot H_2O$ *with the vapor of aniline*: 2 g of α-$Sn(HOPO_3)_2 \cdot H_2O$ in an open vessel were put into a round bottom flask and 2 mL aniline were added to the flask. The flask was evacuated and left at room temperature for 14 days in order to fully load the aniline. The resulting white product was put over concentrated H_2SO_4 to remove the absorbed aniline.

b). Reaction of α-*$Sn(HOPO_3)_2 \cdot H_2O$ with aniline solution in water*: Various molar ratios of aniline and α-$Sn(HOPO_3)_2 \cdot H_2O$ were used to obtain different loading of aniline. The particular process used is described below for the fully loaded aniline intercalation compound. 500 mg α-$Sn(HOPO_3)_2 \cdot H_2O$ was suspended in 50 mL deionized H_2O. 930 mg aniline in 100 mL water was added to the above suspension. It was stirred at room temperature for three hours. The resulting intercalation compound was isolated by centrifugation, washed thoroughly with H_2O, and dried in air. Chemical and

thermogravimetric analysis indicated an aniline:Sn:P ratio of 1:1:2; i.e. the formulation $(C_6NH_8)_{1.0}Sn(OPO_3)_{1.0}(HOPO_3)_{1.0}$.

Polymerization of aniline in α-$Sn(HOPO_3)_2 \cdot H_2O$ Two portions of $(aniline)_{1.0}$α-$Sn(OPO_3)_{1.0}(HOPO_3)_{1.0}$ were heated at 130 °C in air for 28 days and 45 days to obtain the non-conductive and conductive forms of polyaniline respectively. The color change from white to dark green began to be apparent after heating at 130 °C for one day. The final products were dark green to black. The composition calculated from TGA is $(C_6H_5N)_{0.4}$ $Sn(HOPO_3)_2$.

6.2.2 Instrumentation

Powder x-ray diffraction patterns were carried out on a Siemens D500 diffractometer using CuKα radiation and a step scan of 0.2^{o} 2θ/second. Infrared spectra were recorded on a Nicolet 520 FTIR as KBr pellets. Differential thermal analysis and thermal gravimetric analysis (DTA/TGA) were run in air with a heating rate of 5°C/min and a flow rate of 20 mL/min on a PL Thermal Science STA 1500 thermal analysis system. CPMAS NMR experiments were performed at 125.8 MHz and 202.5 MHz for ^{13}C and ^{31}P respectively on a Bruker AMX-500 spectrometer equipped with a solids accessory rack and a Bruker MAS multinuclear probe. ^{13}C spectra were collected using a cross polarization pulse sequence with a 4.9 μs 90° pulse, a relaxation delay time of four seconds, a contact time of 1 ms, and high power proton decoupling. ^{31}P spectra were collected using a cross polarization pulse sequence with a 3.4 μs 90° pulse, a relaxation delay time of four seconds, a contact time of 1 ms and high power proton decoupling. MAS is on the order of 8--10 kHz.

6.3 Results and Discussion

6.3.1 Description of the structure of α-$Sn(HOPO_3)_2 \cdot H_2O$

Layered hydrogen phosphates of metals in oxidation state IV of composition $M(HOPO_3)_2 \cdot H_2O$ (M = Si, Ge, Sn Pb, Ti, Zr, Hf) constitute an isostructural series. Precise structural data have been derived only for M = Zr.[15, 17, 18] The recent powder XRD data show that crystalline tin(IV) hydrogen phosphate possesses a layered lattice structure similar to that of zirconium(IV) hydrogen phosphate.[22, 20, 17, 21] The structure of α-$M(HOPO_3)_2 \cdot H_2O$ (M = Si, Ge, Sn, Pb, Ti, Zr, Hf) is built up of layers of slightly distorted MO_6 octahedra and alternating (up and down) HPO_4 tetrahedra. The metal atoms nearly lie in a plane; they are bridged by phosphate groups. Three oxygens of each phosphate are linked to three tin atoms. Each metal atom is thus octahedrally coordinated by oxygen. The fourth oxygen of each phosphate group bears a proton. Figure 6.1(a) shows the structure of α-$Zr(HOPO_3)_2 \cdot H_2O$. These layers have a pseudohexagonal symmetry and stack along the c-axis. The water molecules are located in the interlayer space and participate in the hydrogen-bond network. The oxygen of the water acts as donor in one H-bond with the neighboring POH group. The other water hydrogen does not participate in H-bonding. Both acidic POH groups in the same layer form hydrogen bonds with the oxygen of the water molecule. The layers are only bound by van der Waals forces. The polyhedral presentation for the structure of α-$Sn(HOPO_3)_2 \cdot H_2O$ that is isostructural with α-$Zr(HOPO_3)_2 \cdot H_2O$ is shown in Figure 6.1 (b).

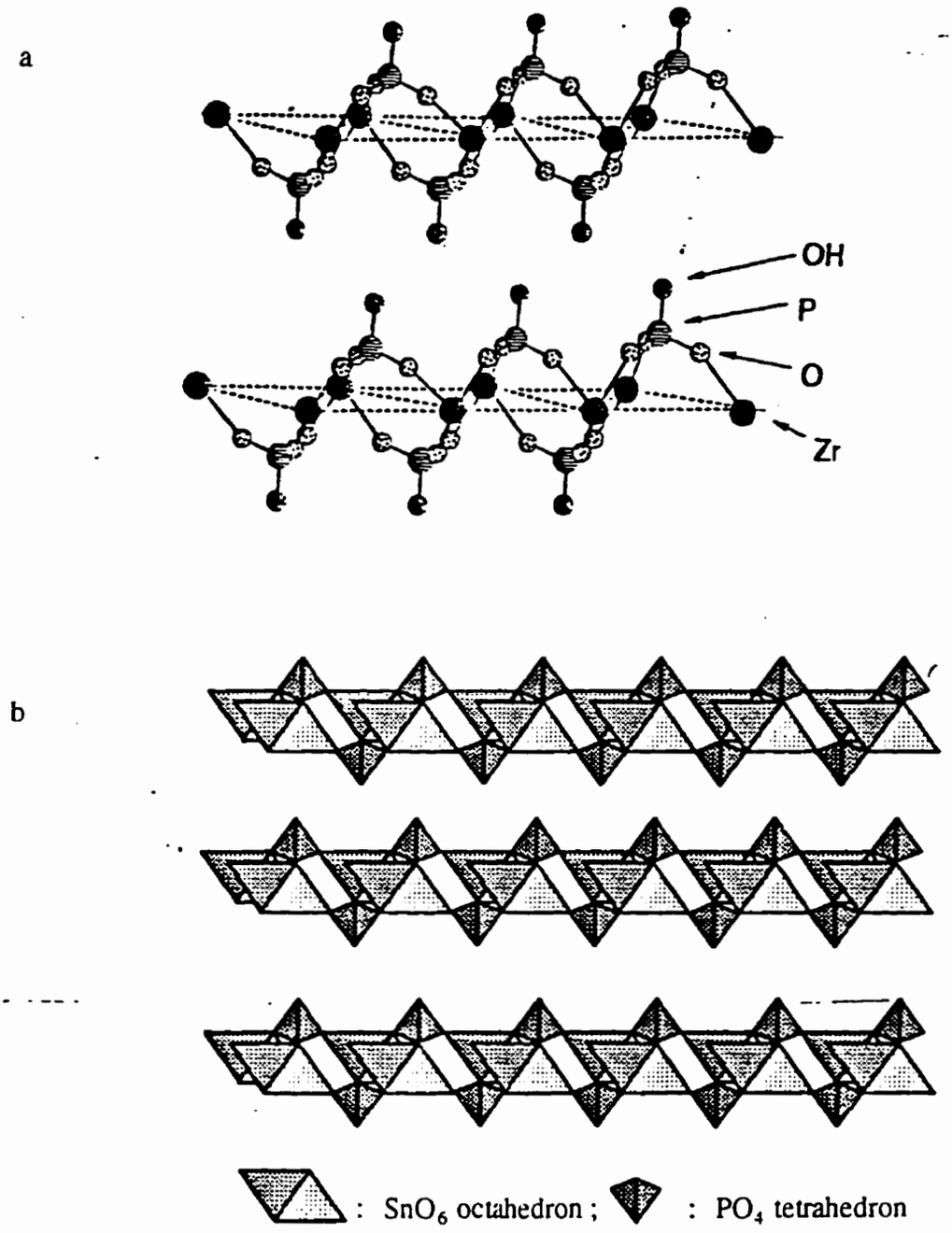

Figure 6.1 Structure of (a) α-$Zr(HOPO_3)_2 \cdot H_2O$ and (b) polyhedral representation isostructural α-$Sn(HOPO_3)_2 \cdot H_2O$

6.3.2 Intercalation of Aniline

Aniline was intercalated into the layered α-$Sn(HOPO_3)_2 \cdot H_2O$ through the reaction of α-$Sn(HOPO_3)_2 \cdot H_2O$ slurries with aniline solution in water or alternatively by contact of α-$Sn(HOPO_3)_2 \cdot H_2O$ with the vapor of aniline (Figure 6.2). By varying the molar ratio of aniline and α-$Sn(HOPO_3)_2 \cdot H_2O$ in water, mixed phases of $(Anilinium)_x$α-$Sn(OPO_3)_x(HOPO_3)_{2-x}$ (x = 0– 1) were obtained. The reaction of layered α-$Sn(HOPO_3)_2 \cdot H_2O$ results in aniline intercalation compounds with well defined sharp XRD diffraction patterns. Figure 6.3 shows the XRD of partially and fully aniline-loaded α-$Sn(HOPO_3)_2 \cdot H_2O$ intercalation compounds. Two phases were identified. One has the d-spacing of 13 Å and the other has the d-spacing of 18 Å. Considering that the α-$Sn(HOPO_3)_2 \cdot H_2O$ has the d-spacing of 7.6 Å, the increase of the d spacing is 5.4 Å and 10.4 Å, respectively, which corresponds well to one layer and two layers of aniline in the gallery of α-$Sn(HOPO_3)_2 \cdot H_2O$, respectively. The models representing monolayer and bilayer aniline in α-$Sn(HOPO_3)_2 \cdot H_2O$ are shown in Figure 6.4.

These different phases are obtained by varying the reactant molar ratio of aniline : α-$Sn(HOPO_3)_2 \cdot H_2O$. If we take the relative intensity of d_{002} of monolayer and bilayer aniline intercalation compounds and α-$Sn(HOPO_3)_2 \cdot H_2O$ as the extent of intercalation, and plot that with the reactant molar ratio of aniline/α-$Sn(HOPO_3)_2 \cdot H_2O$ (Figure 6.5), we can see that at the lowest molar ratio (= 1), only monolayer aniline intercalation compound is formed. When the molar ratio is increased to three, the bilayer aniline intercalation compound starts to form, but the dominant composite is still the monolayer aniline intercalation compound. The intercalation products still contain significant

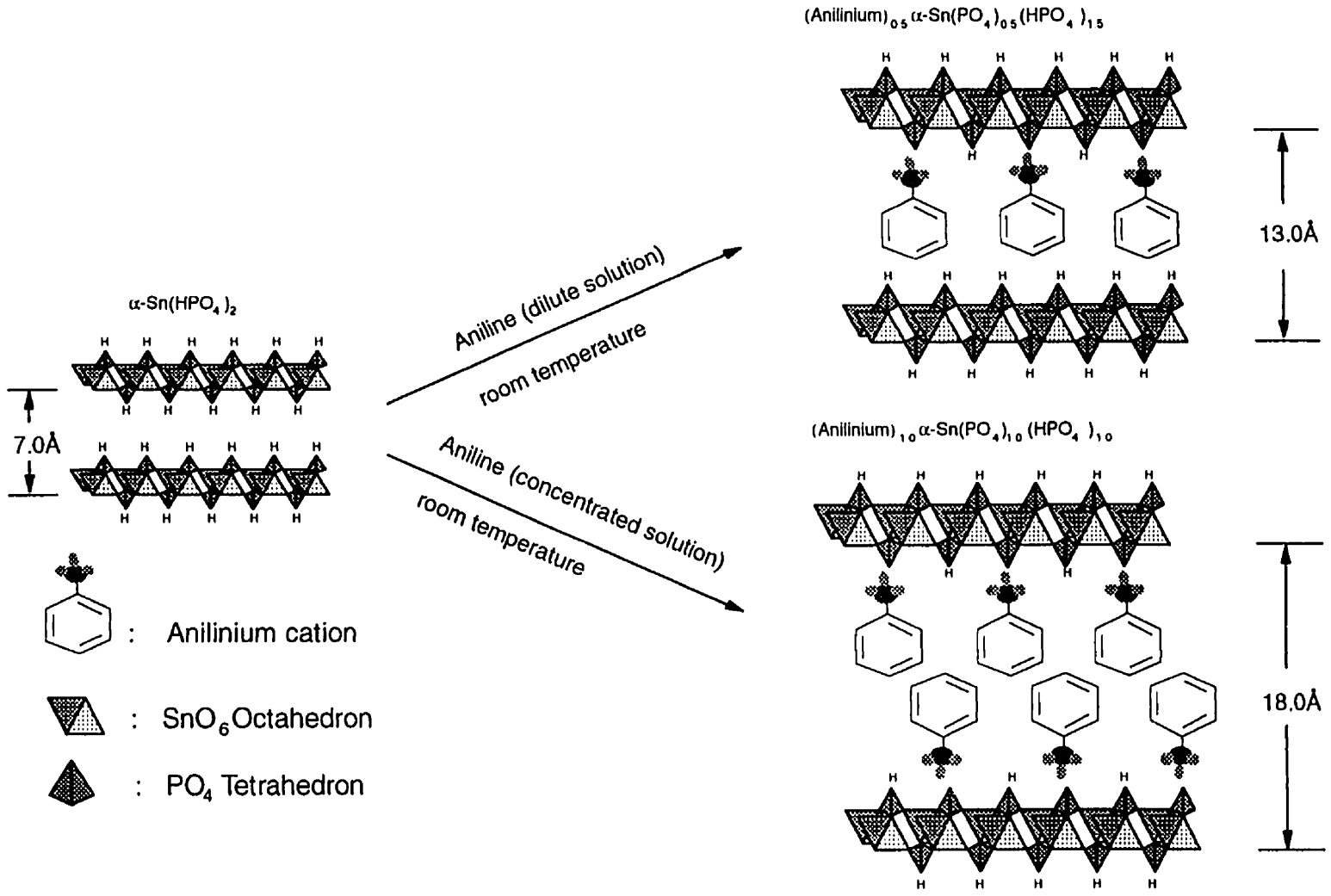

Figure 6.2 **Synthetic scheme for (Anilinium)$_x$α-Sn(OPO$_3$)$_x$(HOPO$_3$)$_{2-x}$ ($0 < x \leq 1$)**

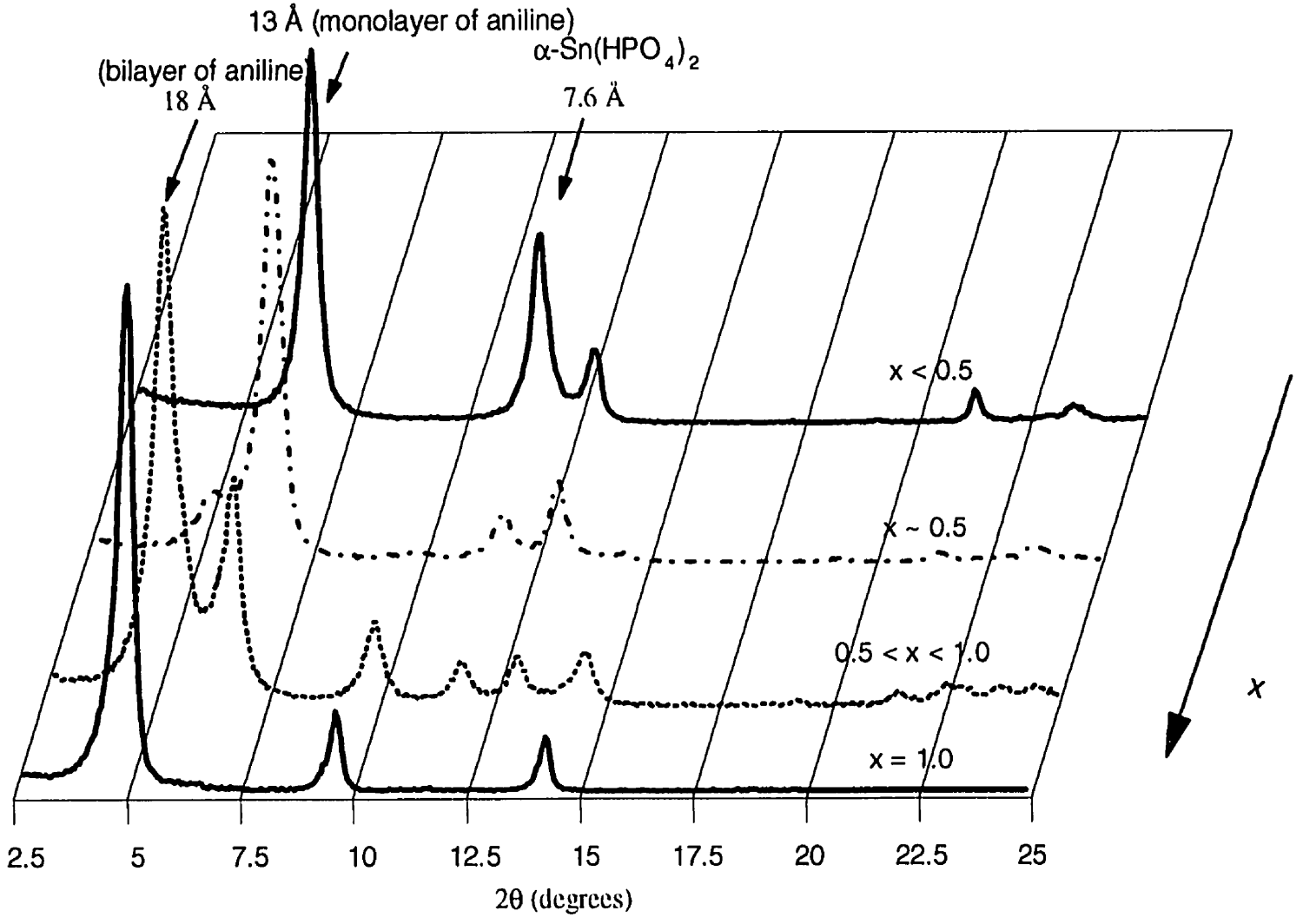

Figure 6.3 **Powder XRD patterns of oriented films of (Anilinium)$_x$α-Sn(OPO$_3$)$_x$(HOPO$_3$)$_{2-x}$ (0 < x ≤ 1)**

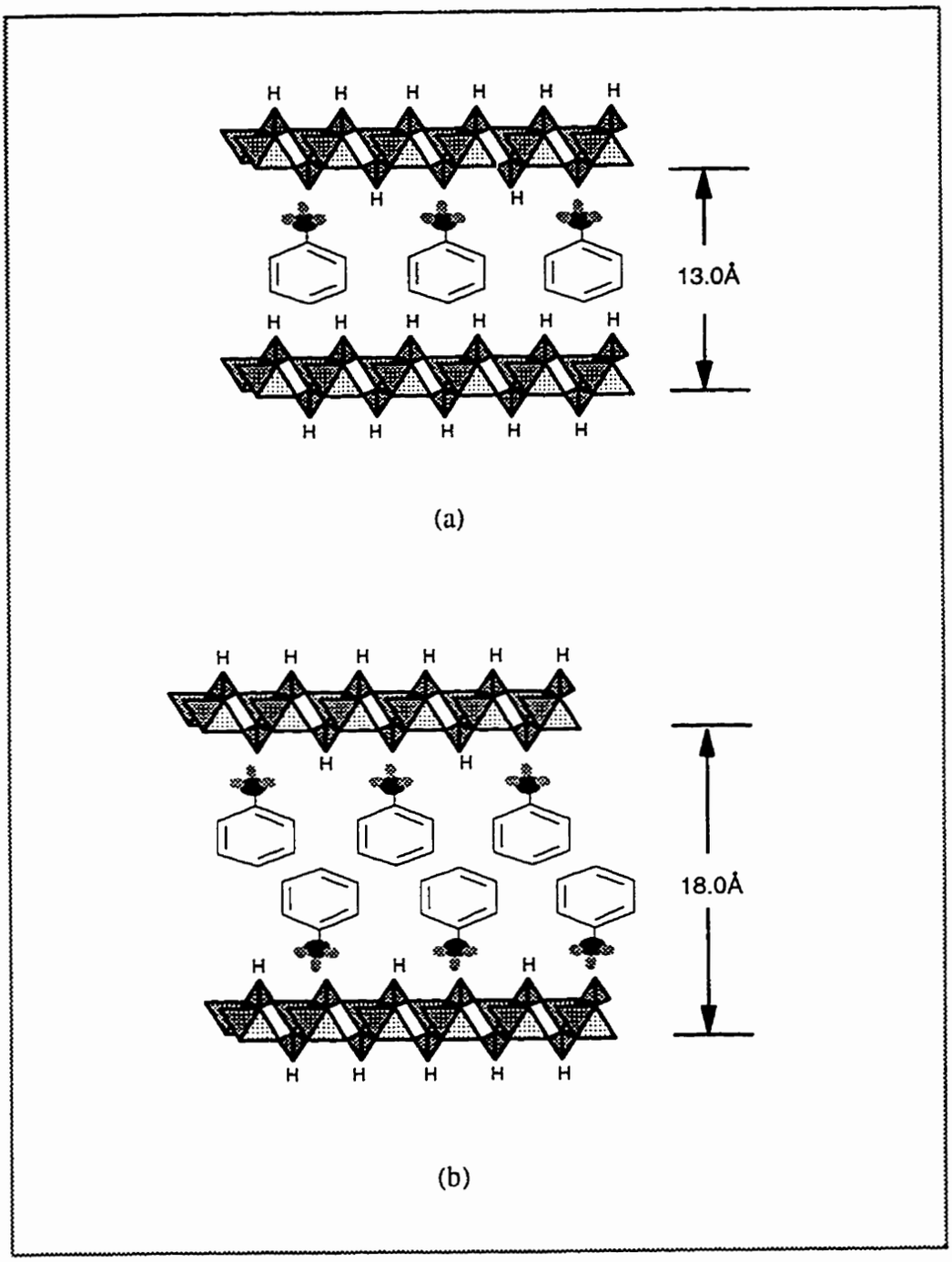

Figure 6.4 Models for (a) monolayer and (b) bilayer aniline intercalated α-$Sn(HOPO_3)_2 \cdot H_2O$

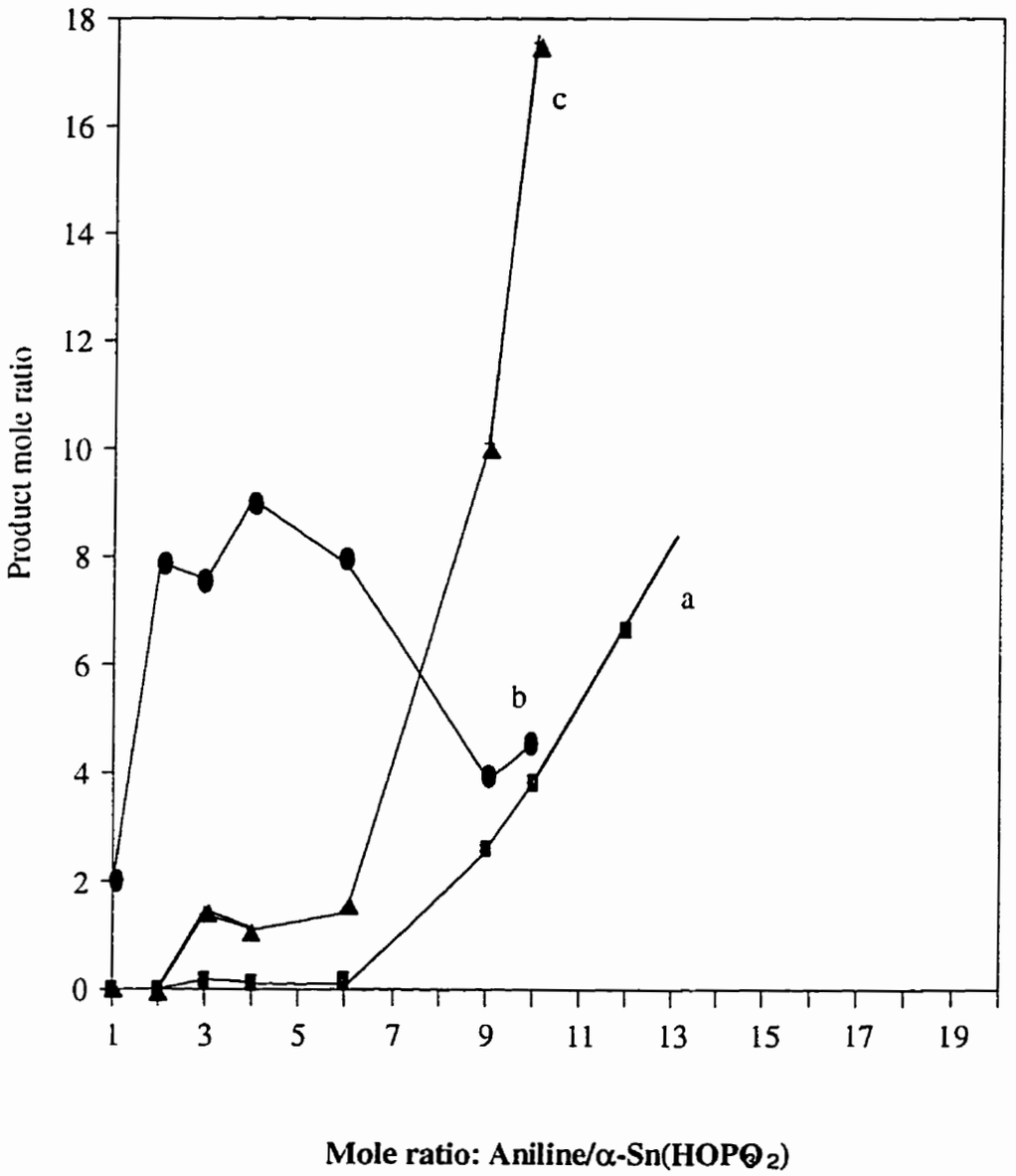

Figure 6.5 **Product mole ratio of (a) bilayer intercalate/monolayer intercalate; (b) monolayer intercalate/α-$Sn(HOPO_3)_2 \cdot H_2O$; and (c) bilayer intercalate/α-$Sn(HOPO_3)_2 \cdot H_2O$ *vs.* reactant mole ratio of aniline/α-$Sn(HOPO_3)_2 \cdot H_2O$ determined by the relative peak intensities in the powder XRD pattern**

amount of monolayer aniline intercated compound until the molar ratio exceeds 12. Beyond that molar ratio, the pure bilayer aniline intercalation compound was formed, which is identical to that prepared by contact of α-$Sn(HOPO_3)_2 \cdot H_2O$ with the vapor of aniline. Therefore this plot shows that the pure monolayer aniline intercalated α-$Sn(HOPO_3)_2 \cdot H_2O$ can not be isolated by this method.

The phase of d = 18 Å is kinetically stable but thermodynamically not very stable. Briefly heating the fully loaded sample at 130°C for 2 hours, the d-spacing decreased to 13 Å with loss of half the amount of aniline; this is an easy way to prepare the pure d = 13 Å phase intercalate. It supports the model for monolayer and bilayer aniline intercalation compounds (Figure 6.4).

Even with a significant excess amount of aniline and a longer reaction time, no more aniline than 1.0 mole aniline per mole α-$Sn(HOPO_3)_2 \cdot H_2O$ could be intercalated. This amount only constitutes half of the hydrogens of the host which are directly involved in the interaction with the aniline. The full use of hydrogens to interact with the aniline must be restricted by spatial availability inside the layer.

6.3.3 Polymerization of Aniline in α-$Sn(HOPO_3)_2 \cdot H_2O$

Polymerization of aniline in α-$Sn(HOPO_3)_2 \cdot H_2O$ with different oxidants such as $FeCl_3$, $(NH_4)_2S_2O_8$, H_2O_2 in water solution were tried, respectively. At the beginning, no colour change could be observed with stirring at room temperature. After about 10 minutes of induction time, a dramatic color change from white to dark green was observed. The reaction was finished in 1 hour. But XRD indicated that the aniline was oxidatively polymerized outside of the layered host. The isolated product had the d-

spacing of 7.6 Å which is the α-$Sn(HOPO_3)_2 \cdot H_2O$ phase itself. This may result from the difficulty for diffusion of the oxidant such as $FeCl_3$ into the galleries to polymerize aniline inside the layers. The factor that restricts the diffusion of these oxidants into the layers is unclear. It is of interest that even no Fe^{3+}- or $(NH_4)^+$- exchanged intercalation compounds were detected by XRD, because the aniline intercalated into the α-$Sn(HOPO_3)_2 \cdot H_2O$ is in the cation form (discussed in later sections), and usually the alkyl amine intercalated α-$Sn(HOPO_3)_2 \cdot H_2O$ is a good ion exchanger (discussed in the next chapter). Instead of the spatial restriction for these ions to diffuse into the gallery (the gallery height is about 11 Å in the bilayer aniline intercalated compounds), it seems that the acidity of the medium plays the major role. Due to the hydrolysis of Fe^{3+} and $(NH_4)^+$, the solution is in the pH range of 4 ~ 5, which is acidic enough for aniline intercalated α-$Sn(HOPO_3)_2 \cdot H_2O$ to attract proton and give up anilinium, or in other words, there is an ion exchange between proton and anilinium cation, but not between Fe^{3+} and $(NH_4)^+$ and anilinium cation. Therefore, avoiding the presence of a large amount of protons, or getting rid of the solvent medium are two ways one can try to polymerize aniline inside the gallery of α-$Sn(HOPO_3)_2 \cdot H_2O$.

We tried the following solid-gas phase reaction to polymerize aniline inside the gallery of α-$Sn(HOPO_3)_2 \cdot H_2O$. The aniline was successfully polymerized in the layer by heating the bilayer aniline intercalation compounds at 130°C in air for 28 days. First, half the amount of aniline was simply driven off by heating at 130°C for 2 hours. This is evident from XRD because only the pure monolayer aniline intercalation compound was detected. After one day, the color changed from colorless to dark green and the

polymerization was finished after 28 days, resulting in a black product which is nonconductive. The conducting polymer was obtained only after heating the bilayer aniline intercalation compounds at 130°C for 45 days.

Figure 6.6 shows the XRD of the fully aniline-loaded intercalation compound, $(Anilinium)_{1.0}\alpha$-$Sn(OPO_3)_{1.0}(HOPO_3)_{1.0}$, and $(PANI)_{0.4}\alpha$-$Sn(HOPO_3)_2$. The d-spacing decreased from 18 Å to 13 Å. There is not much difference in d-spacing between the monolayer aniline intercalation compound and $(PANI)_{0.4}\alpha$-$Sn(HOPO_3)_2$.. The dimension of 5.4 Å for the gallery between tin phosphate layers is consistent with that observed for many polyaniline/inorganic layered host nanocomposites. The line shape of $(PANI)_{0.4}\alpha$-$Sn(HOPO_3)_2$ is much broader than that of aniline intercalation compounds, suggesting that either the dislocation of polyaniline between the host layers, or the much shorter ordering of the host layers due to the accommodation of the polymer, resulting in much smaller crystalline size. Nevertheless, the layered structure remains in $(PANI)_{0.4}\alpha$-$Sn(HOPO_3)_2$.

6.3.4 Thermal Analysis

Thermal analysis is informative for this kind of reaction and these kinds of compounds. Figure 6.7 shows the TGA and DTA of the monolayer aniline intercalation compound and the bilayer aniline intercalation compound, respectively. The monolayer aniline intercalation compound loses aniline mainly at 250°C. Two well-resolved steps were observed for the loss of aniline in the bilayer aniline intercalation compound. One occurs at 130°C and the other at 250°C. The temperature for the second major weight loss is the same as that of monolayer aniline intercalation compounds. Also, the total weight

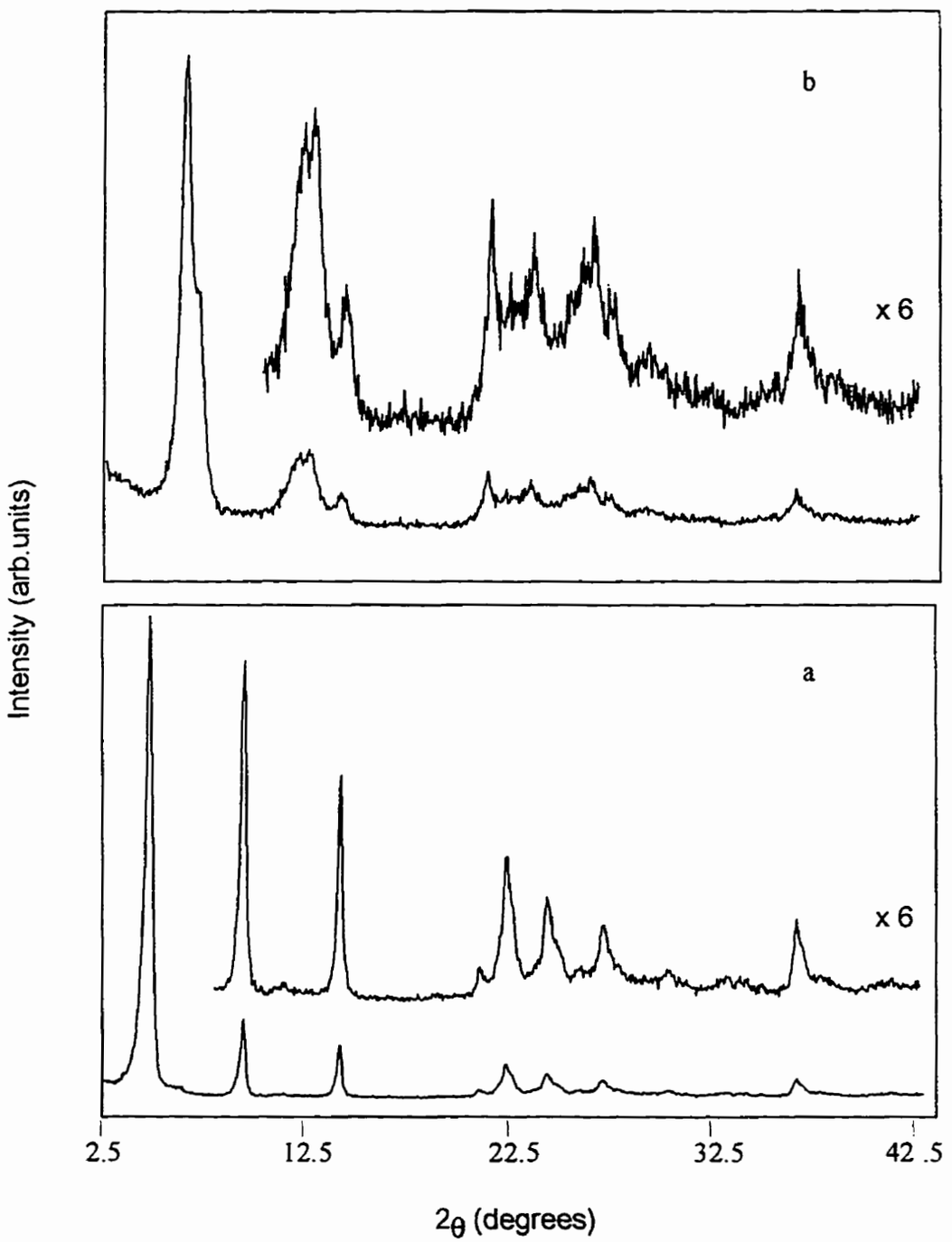

Figure 6.6 **Powder XRD patterns for oriented films of (a) $(Anilinium)_{1.0}\alpha$-$Sn(OPO_3)_{1.0}(HOPO_3)_{1.0}$ and (b) $(PANI)_{0.4}\alpha$-$Sn(HOPO_3)_2$**

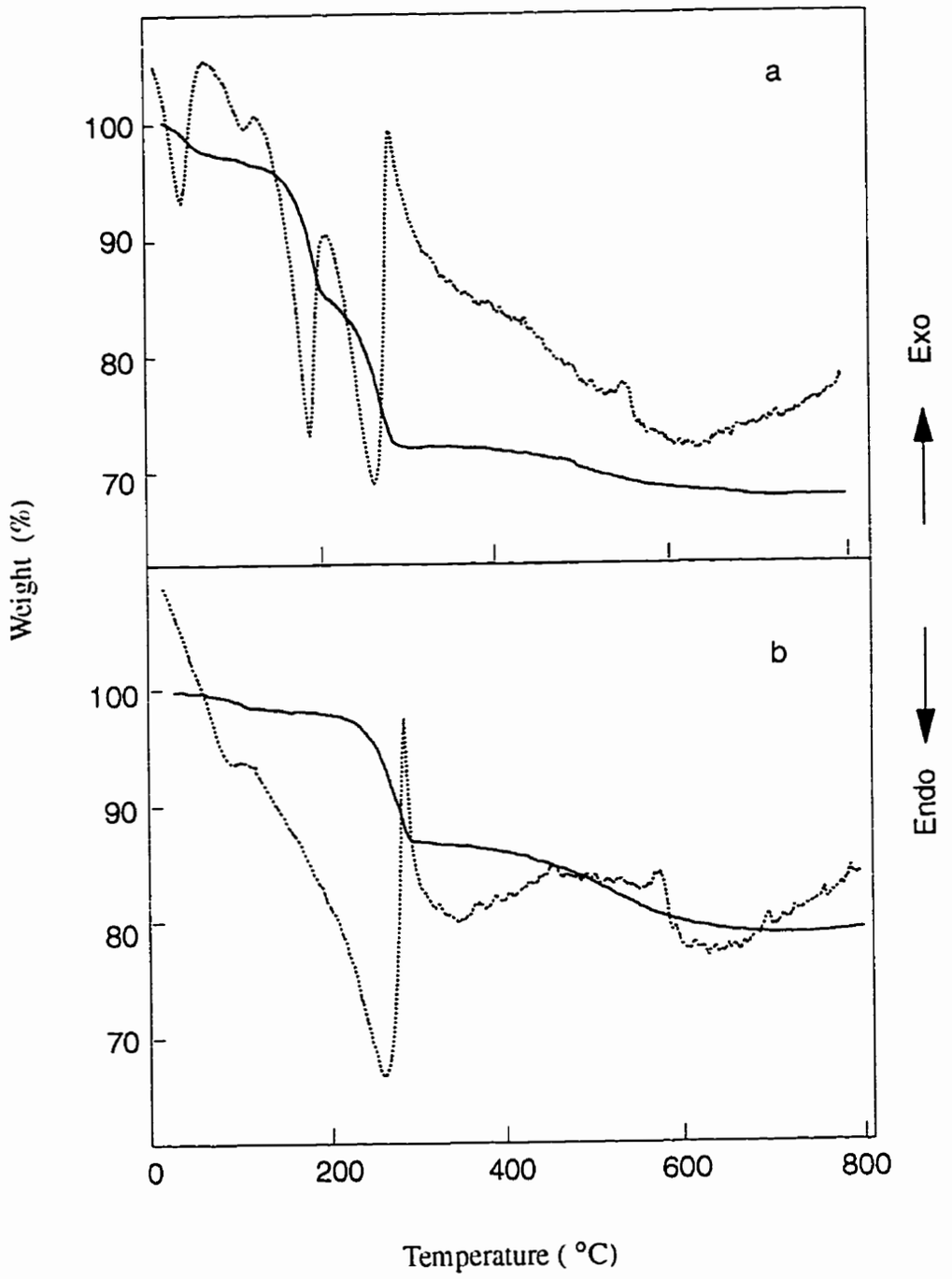

Figure 6.7 Simultaneous TG-DTA traces for (a) $(Anilinium)_{1.0}\alpha$-$Sn(OPO_3)_{1.0}(HOPO_3)_{1.0}$ and (b) $(Anilinium)_{0.5}\alpha$-$Sn(OPO_3)_{0.5}(HOPO_3)_{1.5}$

loss in two steps for the bilayer compound is the same amount, which suggests that the second layer of aniline was lost first at the lower temperature. In the preparation, we tried various reaction conditions such as varying the molar ratio of reactants of aniline/α-$Sn(HOPO_3)_2 \cdot H_2O$, the concentration of reactant, and the medium of the reaction. We were unable to isolate the pure monolayer phase. It is interesting that by heating the bilayer intercalation compound, the pure monolayer phase resulted. That means that the second layer of aniline can enter the gallery of α-$Sn(HOPO_3)_2 \cdot H_2O$ before all monolayer seats are filled by aniline; however, when they are forced to leave by heating, the second layer of aniline leaves first. This, together with the XRD results, is consistent with the monolayer and bilayer aniline models for the intercalation compounds (Figure 6.4).

Figure 6.8 shows the TGA and DTA of $(PANI)_{0.4}$α-$Sn(HOPO_3)_2(PANI)_{0.4}$α-$Sn(HOPO_3)_2$. The nanocomposite starts to lose polyaniline around 400°C which is a much higher temperature than that of aniline in the intercalation compounds and is good evidence of polymerization of aniline in the layered host. The weight loss below 100°C is attributed to water. The weight-loss step starting at 400°C is attributed to the loss of the intercalated polyaniline as it thermally breaks up. Compared to bulk polyaniline (emeraldine salt),[11] the intercalated polyaniline molecules show superior thermal stability. This is due to the spatial confinement and separation of the polymer chains by the metal phosphate layers.

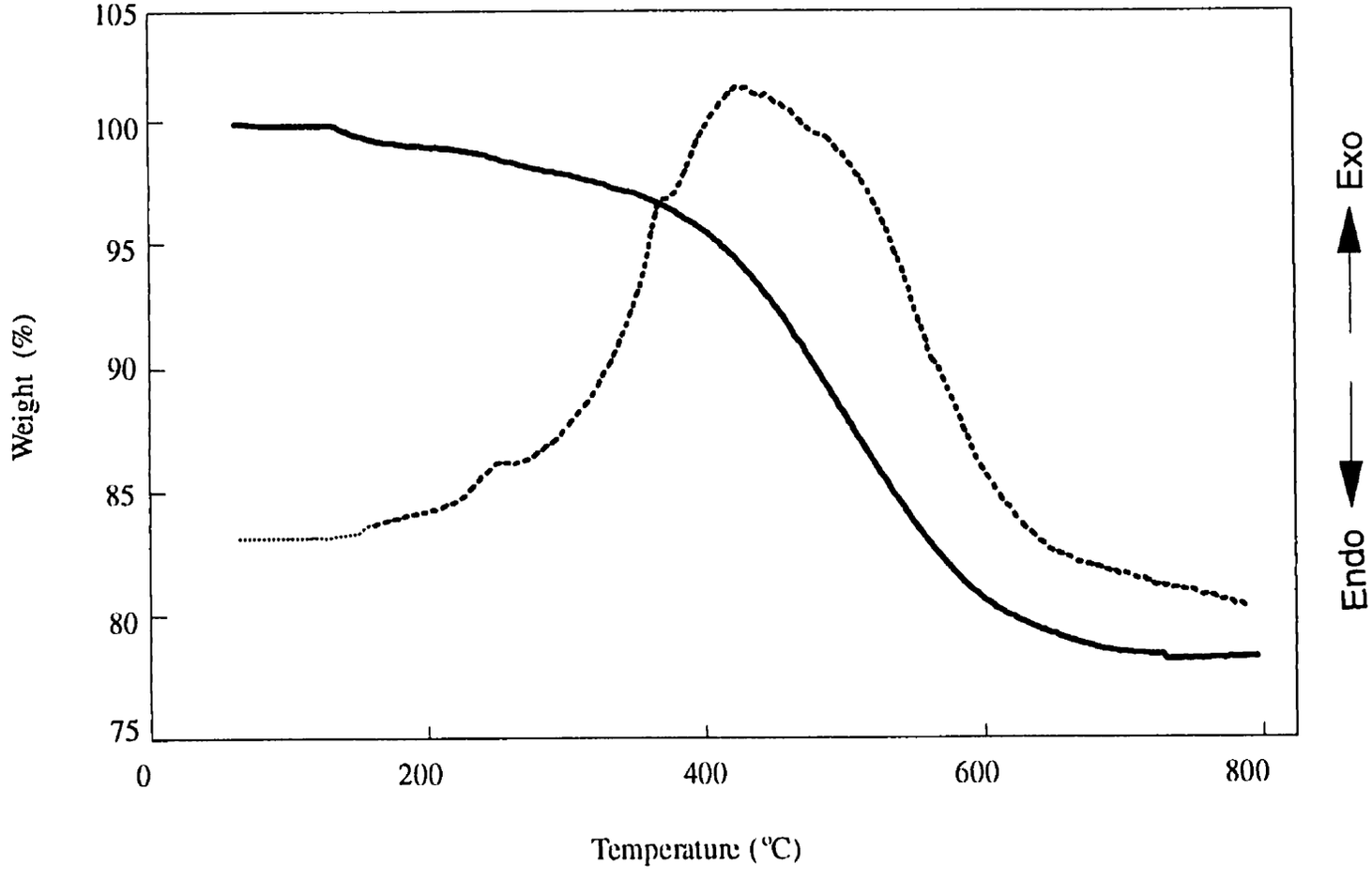

Figure 6.8 **Simultaneous TG-DTA traces for $(PANI)_{0.4}\alpha$-$Sn(HOPO_3)_2$**

6.3.5 FTIR spectra

The FTIR absorption bands observed at 2900 and 743 cm^{-1} for the aniline intercalation compounds suggest that the $PhNH_3^+$ cation is formed upon intercalation[12, 22] (Figure 6.9 (a)). Even in the fully aniline-loaded intercalation compounds, only half the amount of hydrogens of α-$Sn(HOPO_3)_2 \cdot H_2O$ were directly involved in the interactions with aniline to form the anilinium cations. Ideally, we hope to distinguish between two different kinds of hydrogen of H-O-P in the intercalation compounds. But this was blocked by a broad peak at the frequency of 954 cm^{-1} of H-O-P (α-$Sn(HOPO_3)_2 \cdot H_2O$). The broad strong band at 3400- 2900 cm^{-1} of ν_{NH} suggests the strong interaction between aniline and α-$Sn(HOPO_3)_2 \cdot H_2O$.

The polymerization of aniline in α-$Sn(HOPO_3)_2 \cdot H_2O$ is well supported by FTIR spectra (Figure 6.9). Comparing the IR of $(anilinium)_{1.0}\alpha$-$Sn(OPO_3)_{1.0}(HOPO_3)_{1.0}$, and $(anilinium)_{1.0}\alpha$-$Sn(OPO_3)_{1.0}(HOPO_3)_{1.0}$ heated at 130°C for two days and $(PANI)_{0.4}\alpha$-$Sn(HOPO_3)_2$, we see a gradual change of the peaks in the 1600 -- 1400 cm^{-1} region. Two well-resolved peaks at 1591 and 1499 cm^{-1} with similar intensity were observed from $(PANI)_{0.4}\alpha$-$Sn(HOPO_3)_2$. This suggests the formation of polyaniline inside the gallery of α -$Sn(HOPO_3)_2 \cdot H_2O$. These peaks are consistent with the formation of the oxidized form of polyaniline.[23, 24, 25, 26] These two peaks remain in the polyaniline extracted from the nanocomposite by strong base hydrolysis, and are compatible with that of the emeraldine form of polyaniline prepared by a bulk method[27] (Figure 6.10).

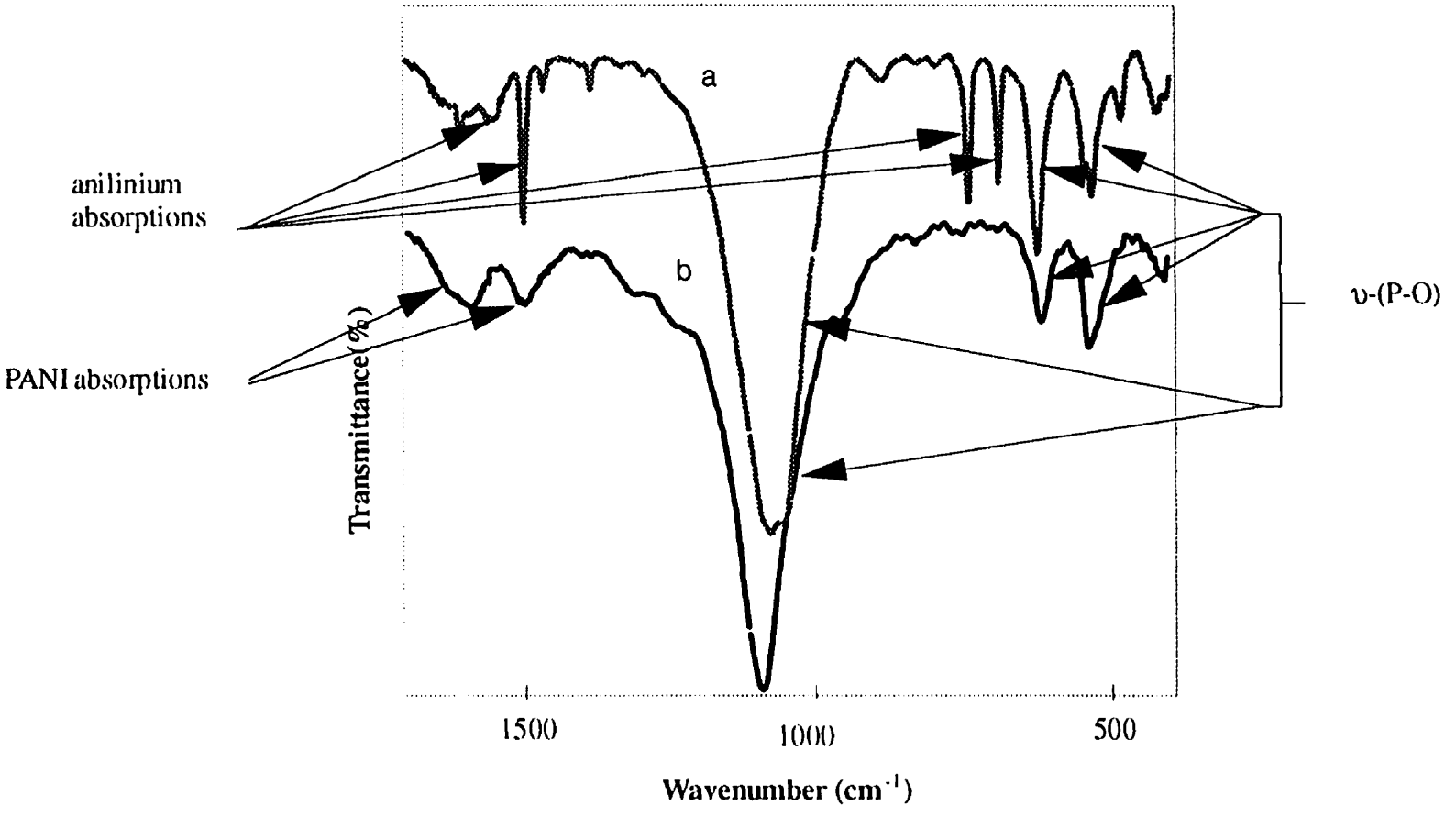

Figure 6.9 FTIR spectra of (a) $(Anilinium)_{1.0}\alpha$-$Sn(OPO_3)_{1.0}(HOPO_3)_{1.0}$ and (b) $(PANI)_{0.4}\alpha$-$(HOPO_3)_2$

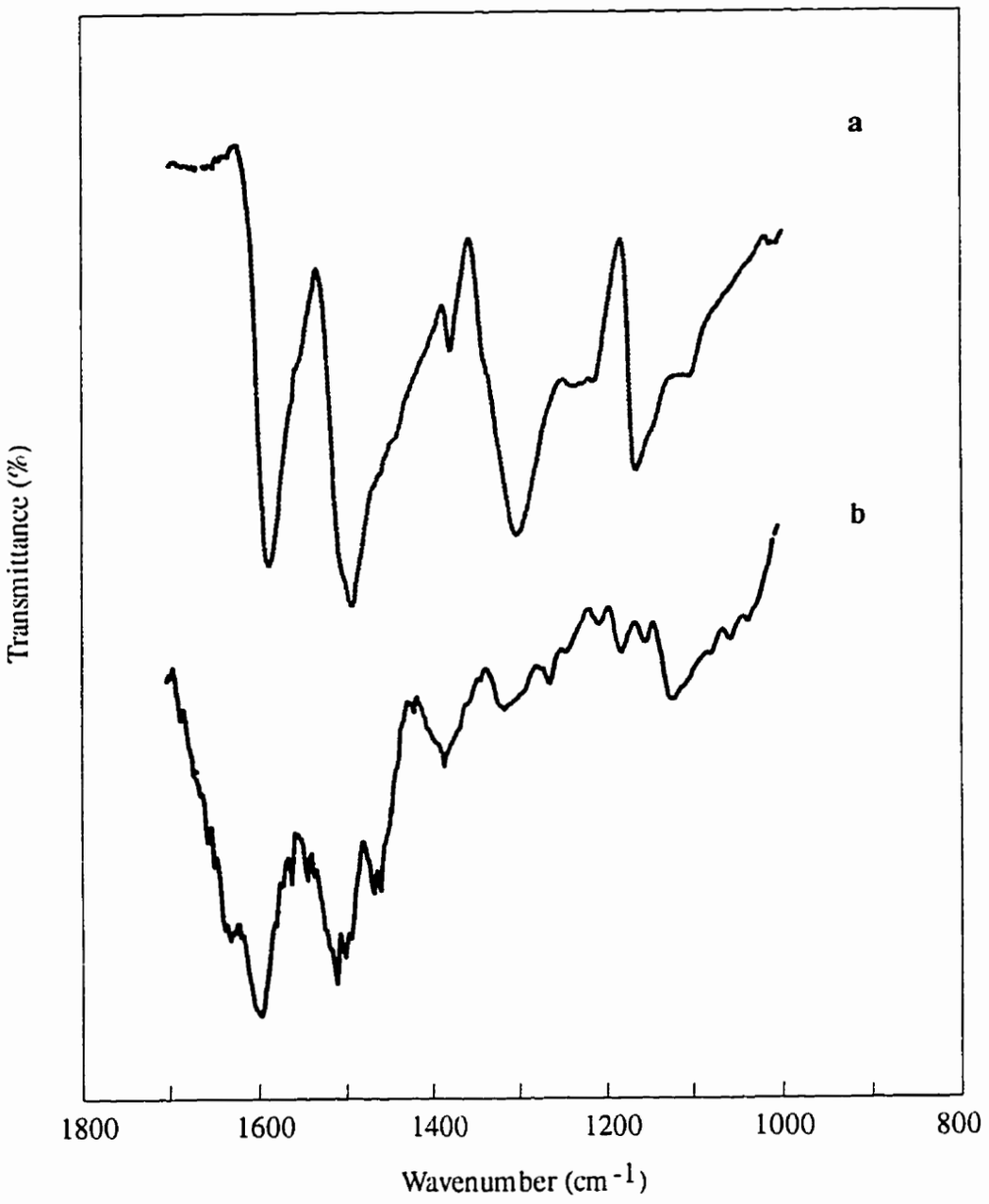

Figure 6.10 FTIR spectra of polyaniline: (a) extracted from $(PANI)_{0.4}\alpha$-$Sn(HOPO_3)_2$ and (b) chemically prepared

6.3.6 Solid State ^{13}C and ^{31}P CPMAS NMR

^{13}C CPMAS NMR spectra were recorded for $(anilinium)_{1.0}\alpha$-$Sn(OPO_3)_{1.0}(HOPO_3)_{1.0}$ and the compounds resulting from heating $(anilinium)_{1.0}\alpha$-$Sn(OPO_3)_{1.0}(HOPO_3)_{1.0}$ at 130°C for different times (Figure 6.11). Two peaks at 129.9 and 124.5 ppm were observed for $(anilinium)_{1.0}\alpha$-$Sn(OPO_3)_{1.0}(HOPO_3)_{1.0}$. The peak at 129.9 ppm results from iso, meta, and para carbons and that at 124.5 ppm results from the ortho carbon of the anilinium cation. It suggests that the aniline is in its salt form in the intercalation compounds, and is consistent with IR data. Upon heating the bilayer aniline intercalation compound at 130°C for two hours, the half height line widths of both peaks become narrower and better resolved (Figure 6.11). From XRD and thermal analysis, we know that the second layer aniline is lost during this heating. The wider linewidth of the bilayer aniline intercalation compound as opposed to that of the monolayer aniline intercalation compound suggests that the second layer of aniline is in a slightly different configuration than that of the first layer aniline due to a steric effect. Otherwise, the broadening of the linewidth may come from the interaction between two layers of aniline. Figure 6.11.c is the spectrum recorded for the sample heated at 130°C for 14 days. The color of the sample is black. Although two peaks become wider, the main features of the two peaks occurred at about the same frequencies as that of the bilayer aniline intercalation compound (Figure 6.11). These wider lines may be the result of the formation of oligomer after heating for 14 days. After heating the sample at 130°C for 28 days, a dramatic change in the ^{13}C CPMAS NMR spectrum was observed. The peak at 129.9ppm became wider and new peaks at high frequencies (around 150 ppm) were observed, which suggests that the non-protonated oxidized form of polyaniline was

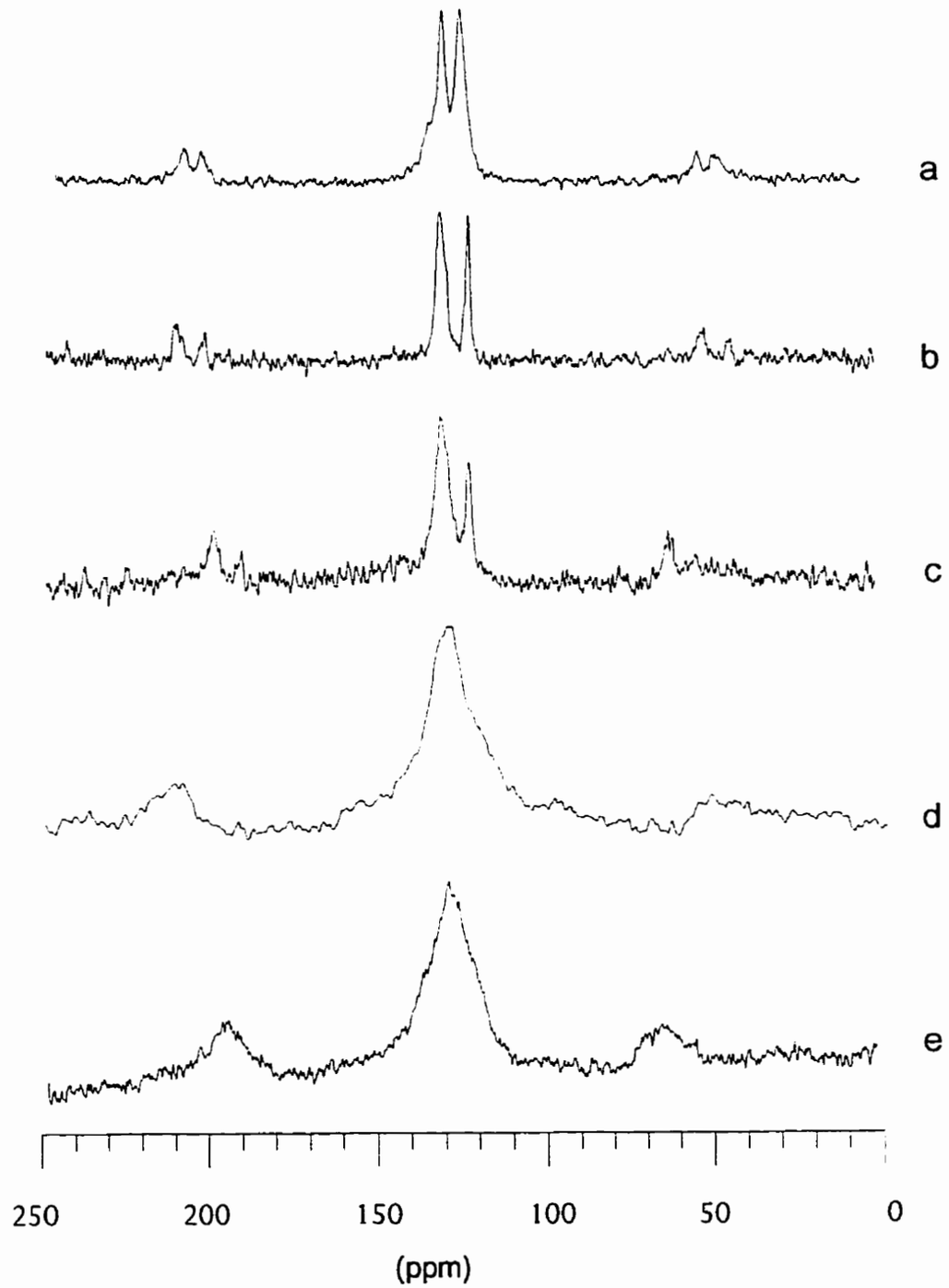

Figure 6.11 **^{13}C MAS NMR spectra of $(Anilinium)_{1.0}\alpha$-$Sn(OPO_3)_{1.0}(HOPO_3)_{1.0}$ heat treated at 130°C in the air for different times (a) 0 hour; (b) 2 hours; (c) 14 days; (d) 28 days; (e) 45 days**

formed.[28, 32] This is consistent with the fact that the sample shows no measurable conductivity (see later discussions). The sample heated at 130°C for 45 days shows a featureless wide peak centered at 130 ppm, strongly suggesting that the polyaniline is in its conducting emeraldine salt form.[28, 32] Indeed, the sample shows measurable conductivity. Combining the thermal analysis, FTIR data, and solid state NMR data, it can be concluded that highly thermally stable polyaniline was formed inside the gallery of α-$Sn(HOPO_3)_2 \cdot H_2O$ after heating the sample in air for 45 days.

α-$Sn(HOPO_3)_2 \cdot H_2O$ has just one type of phosphorous, which resides at -12.5 ppm in its ^{31}P CPMAS NMR. This is assigned to phosphorus with an undissociated P -- O -- H group. [29, 30, 31] Upon intercalation, two peaks at -6.5 and -12.0 ppm were observed (Figure 6.12), which can be assigned to phosphate groups interacting with the aniline and the remaining HOP groups respectively. It is consistent with the formation of $PhNH_3^+$ and only half the amount of hydrogen of H-O-P being directly involved in the interaction with aniline. Thus there are two types with equal amounts of H-O-P and -O-P phosphorus in the aniline intercalation compounds. It has been shown that in ^{31}P MAS NMR the isotropic chemical shift moves to low frequencies as the P--O bond strength increases. There is a large degree of proton transfer from the phosphate group to aniline, the decrease of 6.0 ppm being associated with an increase in negative charge on $P\text{--}O^{x-}$ ($x \leq 1$). However, if the free electron density were to result in an increase in the double-bond character of the phosphate group, an opposite movement in chemical shift would be seen. The movement observed can possibly be explained on the basis of charge localization on

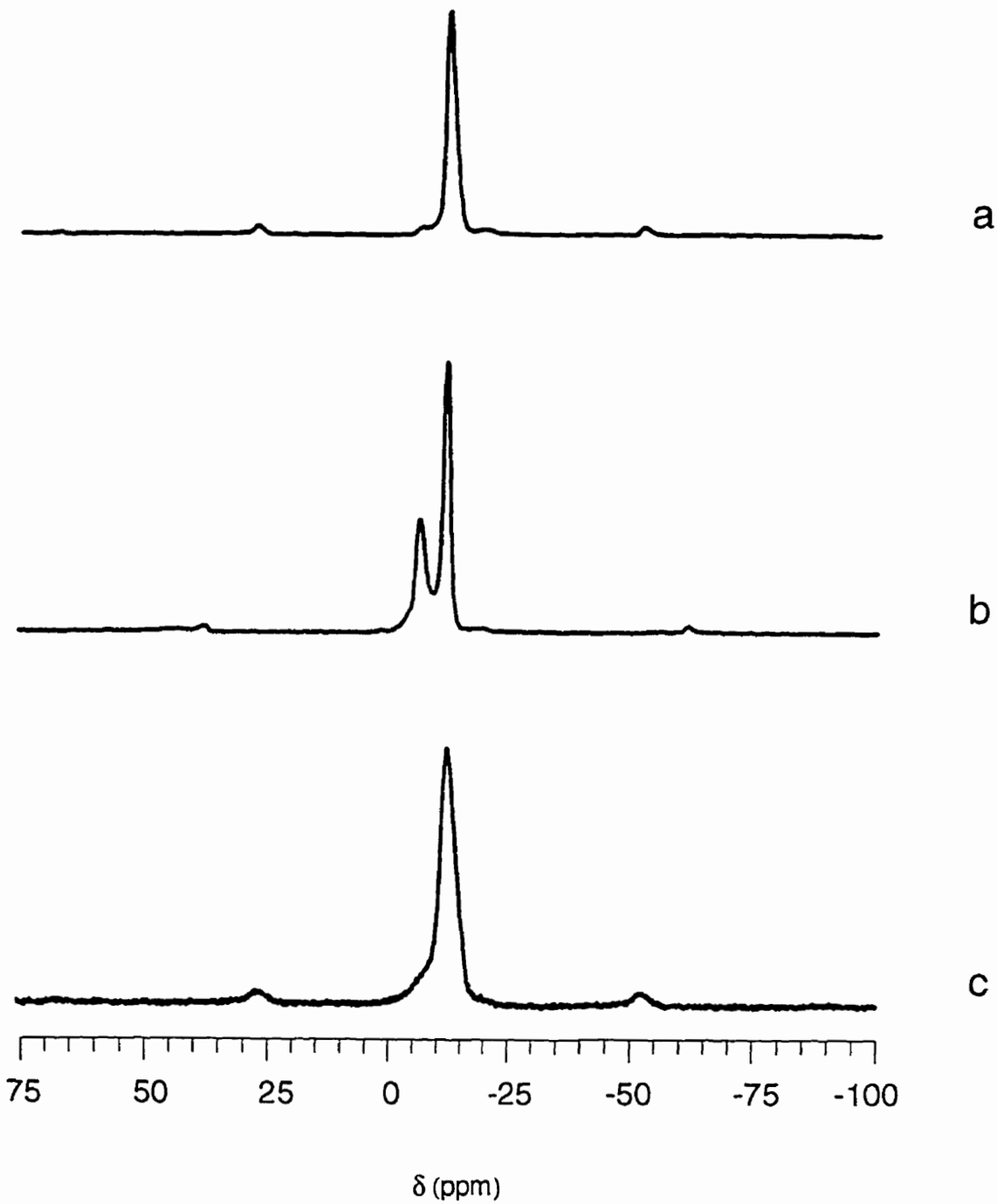

Figure 6.12 ^{31}P CPMAS NMR spectra of (a) α-$Sn(HOPO_3)_2 \cdot H_2O$; (b) $(Anilinium)_{1.0}$α-$Sn(OPO_3)_{1.0}(HOPO_3)_{1.0}$ and (c) $(PANI)_{0.4}$α-$Sn(HOPO_3)_2$

the oxygen, encouraged by hydrogen bonding between the protonated aniline and the layer. The phosphorus is, therefore, more shielded and the peak moves accordingly.

In the $(PANI)_{0.4}\alpha$-$Sn(HOPO_3)_2$, two peaks of phosphorous in the intercalation compound become one peak again at a frequency of phosphorous similar to α-$Sn(HOPO_3)_2 \cdot H_2O$. This suggests that during polymerization, protons were released from the $[PhNH_3]^+$ cation, which were attracted by the dissociated host. This may also facilitate the polymerization process. But after polymerization, the host did not donate protons to the polymer, as only one type of phosphate was observed, which explains why it took 45 days to convert the aniline intercalation compounds to a conducting polyaniline nanocomposite. α-$Sn(HOPO_3)_2 \cdot H_2O$ is not a good doping agent. This is due to its weak acidity, as evident from the discussion in the section on polymerization of aniline in α-$Sn(HOPO_3)_2 \cdot H_2O$. However, the linewidth of ^{31}P NMR for the nanocomposite is much broader than that of α-$Sn(HOPO_3)_2 \cdot H_2O$; this is consistent with that observed for XRD patterns, resulting from either the slight modification of the α-$Sn(HOPO_3)_2 \cdot H_2O$ structure or the random interaction between hydrogen from the HOP group and nitrogen from polyaniline.

6.3.7 Conductivity

The conductivity was measured by the two-probe method for a pressed sample. The sample heated at 130°C for 28 days showed no measurable conductivity. Figure 6.13 shows the conductivity plot of the sample that was heated at 130°C for 45 days. The conductivity at room temperature is about 10^{-7} S/cm. Considering that the polymer is in the lattice of the insulator of α-$Sn(HOPO_3)_2 \cdot H_2O$, the practical conductivity

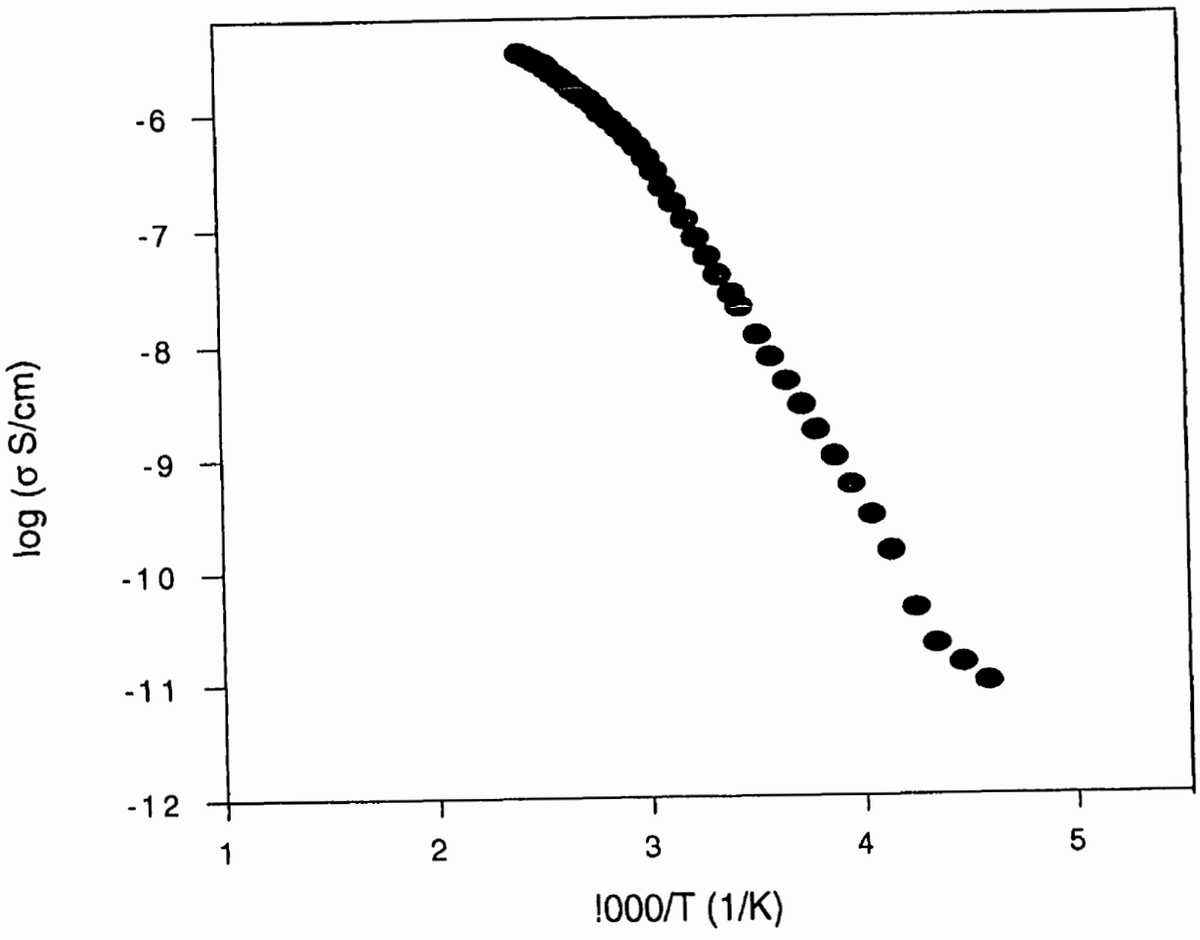

Figure 6.13 **Variable temperature electrical conductivity data for $(PANI)_{0.4}\alpha$-$(HOPO_3)_2$**

of the polyaniline should be several orders higher. Enzel and Bein[22] and Liu and Kanatzidis[16] reported that they could not get the measurable conductivity for the polyaniline formed inside an insulator lattice such as zeolite or $HUO_2HPO_4 \cdot 4H_2O$, even though the polyaniline extracted from the inorganic lattice has a low but measurable conductivity.

6.4 Conclusions

We have successfully intercalated and polymerized aniline in a layered α-$Sn(HOPO_3)_2 \cdot H_2O$. Powder XRD, solid state ^{13}C CPMAS NMR, and thermal analysis data all support the monolayer and bilayer aniline models for aniline-intercalated α-$Sn(HOPO_3)_2 \cdot H_2O$. The intercalated $PhNH_3^+$ cation can be polymerized inside the lattice by a solid-gas phases reaction, but not in an even weakly acidic medium. During different reaction stages, different forms of polyaniline were formed as evidented from ^{13}C CPMAS NMR spectra. After heating the bilayer aniline intercalation compounds at 130°C for 28 days, the nonconductive oxidative form of polyaniline was formed. When heated longer, the nonconductive polyaniline was converted to the conductive polyaniline. α-$Sn(HOPO_3)_2 \cdot H_2O$ is not a good dopant, due to its weak acidity. That explains why it is difficult to convert the polyaniline to a conducting form inside the gallery of α-$Sn(HOPO_3)_2 \cdot H_2O$.

6.5 References

1. Clearfield, A. *Comments Inorg. Chem.* **1990**, *10*, 89.

2. Clearfield, A. *Chem. Rev.* **1988**, *88*, 125.

3. Alberti, G. *Acc. Chem. Res.* **1978**, *11*, 163.

4. Cao, G.; Rabenberg, L. K.; Nunn, C. M.; Mallouk, T. E. *Chem. Mater.* **1991**, *3*, 149.

5. Johnson, J. W.; Jacobson, A. J.; Butler, W. M.; Rosenthal, S. E.; Bordy, J. F.; Lewandowski, J. T. *J. Am. Chem. Soc.* **1989**, *111*, 381.

6. Olken, M. M.; Biagioni, M. M.; Ellis, A. B. *Inorg. Chem.* **1983**, *22*, 4128.

7. Hunsberger, L. R.; Ellis, A. B. *Coord. Chem. Rev.* **1990**, *97*, 209.

8. Wu, H.; Nazar, L. F. "Entrapment of Conjugated Polymers in Layered α-$SnPO_4$", Solid Staet Gordon Conference, 1994.

9. Chao, K.J.; Chang, T.C.; Ho, S.Y. *J. Mater. Chem.* **1993**, *3*, 427.

10. Liu, Y.-J.; Kanatzidis, M. G. *Chem. Mater.* **1995**, *7*, 1525.

11. Yue, J.; Epstein, A. J.; Zhong, Z.; Gallagher, P. K.; MacDiarmid, A. G. *Synth. Met.* **1991**, *41-43*, 765.

12. Nakajima, H.; Matsubayashi, G. *Chem. Lett.* **1963**, 423.

13. Liu, Y.; Kanatzidis, M.G. *Inorg. Chem.* **1993**. *32*, 2989.

14. Costantino, U.; Gasparoni, *A. J. Chromatogr.* **1970**, *51*, 289.

15. Clearfield, A.; Smith, G. D. *Inorg. Chem.* **1969**, *8*, 341.

16. Enzel, P.; Bein, T. *J. Phys. Chem.* **1989**, *93*, 6270.

17. Troup, J. M.; Clearfield, A. *Inorg. Chem.* **1977**, *16*, 331.

18. Albertsson, J.; Oskarsson, A.; Tellgren, R.; Thomas, J. O. *J. Phys. Chem.* **1977**, *81*, 1774.

19. Bruque, S.; Aranda, M.A.G.; Losilla, E.R.; Olivera-Pastor, P.; Maireles-Torres, P. *Inorg. Chem.* **1995**, *34*, 893.

20. Rodriguez-Castellon, E.; Rodriguez-Garcia; Bruque, S. *Inorg. Chem.* **1985**, *24*, 1187.

21. Chernorukow, N. G.; Mochalova, I. R.; Moscuichev, E. P.; Sibrina, G. B. *Zh. Prikl. Khim. (Leningrad)* **1977**, *50*, 1618.

22. Kross, R.D.; Fassel, V.A.; Margoshes, M. *J. Am. Chem. Soc.* **1956**, *78*, 1332.

23. Yasuda, A.; Shimidzu, T. *Polymer. J.* **1993**, *25*, 329.

24. Neugebauer, H.; Neckel, A. Sariciftci, N.S.; Kuzmany, H. *Synth. Met.* **1989**, *29*, E185.

25. Harada, I.; Furukawa, Y.; Ueda, F. *Synth. Met.* **1989**, *29*. E303.

26. Snauwaert, P.; Lazzaroni, R.; Riga, J.; Verbist, J.J. *Synth. Met.* **1987**, *21*, 181.

27. MacDiarmid, A.G.; Chiang, J.; Richter, A.F.; Epstein, A.J. *Synth. Met.* **1987**, *18*, 285.

28. Kaplan, S.; Conwell, E.M.; Richter, A.F.; MacDiarmid, A.G. *J. Am. Chem. Soc.*, **1988**, *110*, 7647.

29. Rodriguez-Castellon, E.; Olivera-Pastor, P.; Maireles-Torres, P.; Jimenez-Lopez, A. Sanz, J.; Fierro, J. L. *J. Phys. Chem.* **1995**, *99*, 1491.

30. Hudson, M. J.; Workman, A. D. *J. Mater. Chem.* **1991**, *1*, 375.

31. Jones, D. J.; Penfold, J.; Tomkinson, J.; Roziere, J. *J. Mol. Structure* **1989**, *197*, 113.

32. Menardo, C.; Nechtschein, M.; Rousseau, A.; Travers, J.P. *Synth. Met.* **1988**, *25*, 311.

33. Troup, J. M.; Clearfield, A. *Inorg. Chem.* **1977**, *16*, 3311.

CHAPTER SEVEN

CONDUCTIVE POLYMER/NONCONDUCTIVE HOST NANOCOMPOSITE (II)

-- *INSERTION OF POLY(P-PHENYLENE VINYLENE) INTO α-$Sn(HOPO_3)_2 \cdot H_2O$*

7.1 Introduction

Poly(*p*-phenylene vinylene), PPV, is an alternating copolymer of p-phenylene and acetylene. PPV belongs to a class of conjugated polymers which becomes electrically conducting upon the addition of electron donors or acceptors. It has been shown that after exposure to oxidizing molecular dopants, the electrical conductivity of free-standing PPV films increases by 12 orders of magnitude into the metallic regime.[1, 2] It was discovered in 1990 that PPV could be used to fabricate a light-emitting diode (LED) [3] which has spawned a considerable amount of interest in PPV. The thermal stability of these polymers coupled with their ability to form flexible devices has fostered an interest in light-emitting polymers for display applications.[4]

It will be of interest to study the effect of the host on the electrical and optical properties of PPV by insertion of PPV into layered materials. It has been shown in this laboratory that PPV can be successfully inserted into MoO_3 by an ion exchange method to

study of optical properties. Here, α-$Sn(HOPO_3)_2 \cdot H_2O$, a colorless layered material, was chosen as host to incorporate PPV, resulted in a yellowish PPV/α-$Sn(HOPO_3)_2$ nanocomposite.

Following the last chapter (the preparation of $(PANI)_{0.4}$α-$Sn(HOPO_3)_2$ by the postintercalative polymerization of aniline), in this chapter, we will describe the preparation of PPV/α-$Sn(HOPO_3)_2$ nanocomposite by the ion exchange method. Powder XRD, solid state NMR, and thermal analysis were used to characterize the nanocomposite.

7.2 Experimental

7.2.1 Synthesis

Materials: The highly crystalline starting material α-$Sn(HOPO_3)_2 \cdot H_2O$ (d_{002} = 7.8Δ) was prepared and stored according to the literature method.[10] The ionomer that is the precursor to PPV, poly(*p*-xylylene-α-dimethylsulphonium chloride), was synthesized as described by Karasz,[1] resulting in a polymer with an estimated molecular weight of 10^5 Da. $[N(CH_3)_4]Cl$ and propylamine were purchased from Aldrich and were used as received.

Preparation of $[(PPV)_{1.0}]^+$α-$Sn(OPO_3)_{1.0}(HOPO_3)_{1.0} \cdot H_2O$: The phosphate α-$Sn(HOPO_3)_2 \cdot H_2O$ was dispersed in a 0.1 M aqueous solution of propylamine with a molar ratio of amine/phosphate 1:1 and then ion exchanged with $[N(CH_3)_4]^+$ cation. The resulting intercalated precursor has the formula α-$Sn[N(CH_3)_4]_{1.0}(OPO_3)_{1.0}(HOPO_3)_{1.0} \cdot 4H_2O$. This colloid suspension was centrifuged, and the solid was washed well with water and air dried.

The dried solid was re-dispersed into a small amount of water. A water solution of PPV^+ was added. The suspension was stirred at room temperature for 24 hours. The ion-exchange of $[N(CH_3)_4]^+$ with PPV^+ was incomplete under these conditions and remained incomplete when subjected to these conditions for an even longer time. Therefore, the above suspension was dialysed against deionized water for two days to completely ion exchange $[N(CH_3)_4]^+$. The product was isolated by centrifugation, washed well with water, cast as a thin film on glass and dried in air. The formula calculated from chemical and thermogravimetric analyses was: $(C_{10}H_{13}S)_{1.0}Sn(OPO_3)_{1.0}(HOPO_3)_{1.0}\cdot H_2O$ (Chemical analysis: Found (%), C, 21.1; H, 3.7; S, 4.2; Sn, 23.0; P, 10.4. Calculated (%), C, 24.3; H, 3.3; S, 6.5; Sn, 24.1; P, 12.6).

Converting PPV^+ to PPV inside the layer of α-$Sn(HOPO_3)_2$: The conversion of $[(PPV)_{1.0}]^+\alpha$-$Sn(OPO_3)_{1.0}(HOPO_3)_{1.0}\cdot H_2O$ to $(PPV)_{1.0}\alpha$-$Sn(HOPO_3)_2$ was realised by heating the film sample at 130°C under vacuum for one hour. The product was yellow in colour. The formula calculated from chemical and thermogravimetric analysis is $(PPV)_{1.0}Sn(HOPO_3)_2\cdot$

7.2.2 Instrumentation

Powder x-ray diffraction patterns were carried out on a Siemens D500 diffractometer using CuKa radiation. Infrared spectra were recorded on a Nicolet 520 Fourier transform infrared spectrometer from KBr pellets. Differential thermal analysis (DTA) and thermal gravimetric analysis (TGA) were run in a flowing atmosphere of air with a heating rate of 5°C/min on a PL Thermal Science STA 1500 thermal analysis system. CPMAS NMR were performed at 125.8 MHz and 202.5 MHz for ^{13}C and ^{31}P respectively on a Bruker AMX-500 spectrometer equipped with a solids accessory rack and a Doty Scientific MAS multinuclear

probe. ^{13}C spectra was collected using a cross polarisation pulse sequence with a 3.1 μs 90° pulse, relaxation delay time of four seconds, various contact times between 50 μs to 10 ms, and high power proton decoupling. MAS is in the order of 8 -- 10 kHz.

7.3 Results and Discussion

7.3.1 Synthesis

The direct insertion of polymer electrolyte into the layered host by the ion exchange method has been demonstrated in this laboratory,[5] where PPV^+, a precursor polymer of PPV, was inserted into MoO_3 by the full swelling of MoO_3 sheets. Although α -$Sn(HOPO_3)_2 \cdot H_2O$ is a good host for intercalation chemistry by an acid-base reaction (for example, see Chapter 6), the acidity of H-OP is not strong enough to merit an ion exchange reaction with cations. Moreover, it is known that it is difficult for α-$Sn(HOPO_3)_2 \cdot H_2O$ to swell in water. Therefore, it will be very difficult to insert a polymer into α-$Sn(HOPO_3)_2 \cdot H_2O$. Maireles-Torres *et al.* have recently employed an intercalate precursor method to prepare Al_{13}α-$Sn(HOPO_3)_2 \cdot nH_2O$ pillar material.[7] We extended this method to prepare the first polymer directly-inserted nanocomposite of phosphate. Figure 7.1 shows the scheme for preparation of $(PPV)_{1.0}$α-$Sn(HOPO_3)_2$. Basically, it involves the preparation of intercalate precursor α-$Sn[N(CH_3)_4]_{1.0}(OPO_3)_{1.0}(HPO_3)_{1.0} \cdot 4H_2O$, ion exchange of $[N(CH_3)_4]^+$ with a PPV precursor (PPV^+), and conversion of PPV^+ into PPV inside the α-$Sn(HOPO_3)_2 \cdot H_2O$ layer. The introduction of $[N(CH_3)_4]^+$ into α-

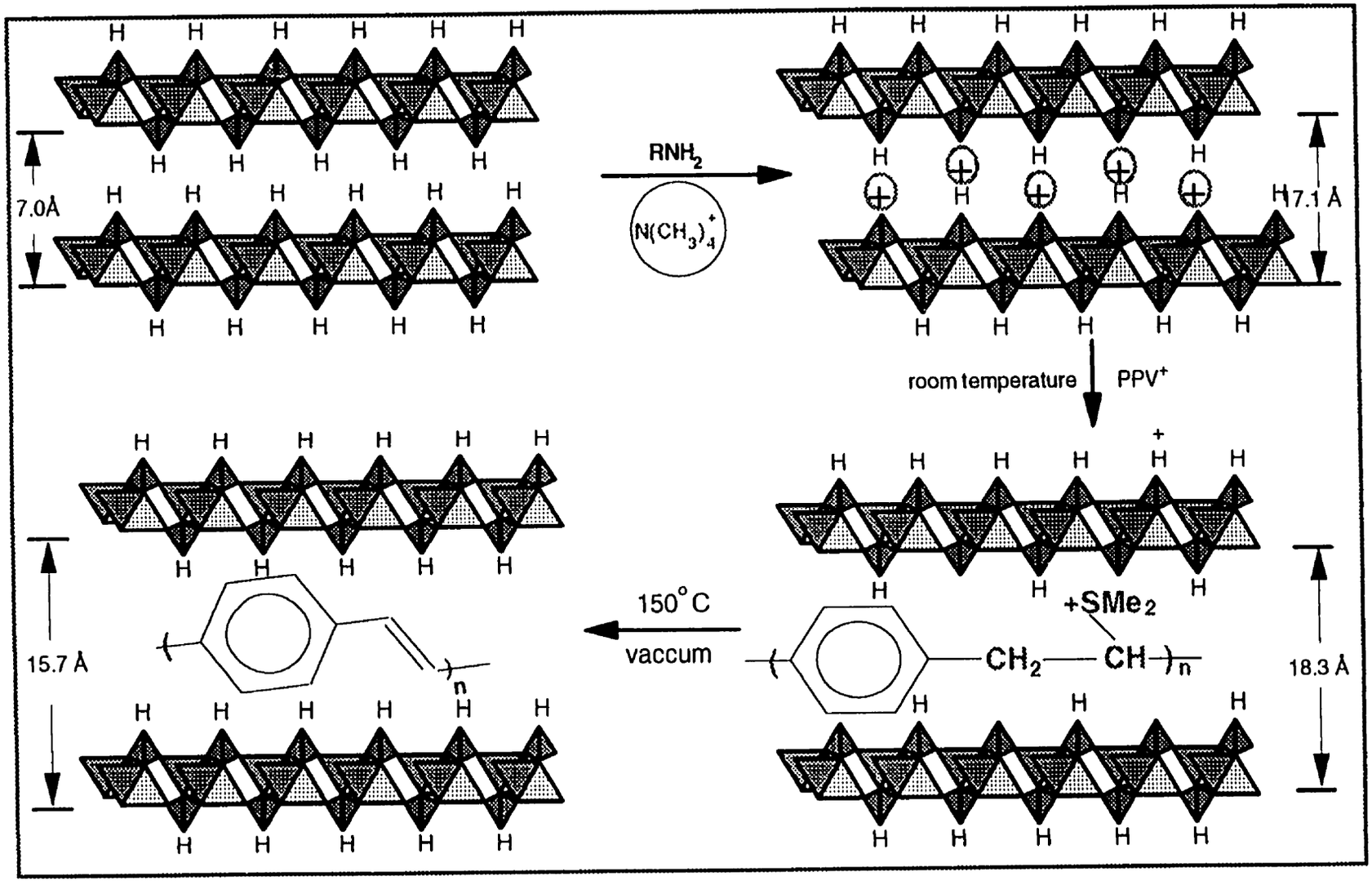

Figure 7.1 Synthetic scheme for $(PPV)_{1.0}\alpha$-$Sn(HOPO_3)_2$

$Sn(HOPO_3)_2 \cdot H_2O$ expanded the d-spacing of α-$Sn(HOPO_3)_2 \cdot H_2O$ to 18 Δ. This expanded α-$Sn(HOPO_3)_2 \cdot H_2O$ was used to exchange with PPV^+, a polyelectrolyte. When α-$Sn[N(CH_3)_4]_{1.0}(OPO_3)_{1.0}(HPO_3)_{1.0} \cdot 4H_2O$ was contacted with PPV^+ at room temperature, $[N(CH_3)_4]^+$ was gradually replaced by PPV^+ by an ion exchange reaction. A new peak at 18.9 Δ was seen from XRD. However $[N(CH_3)_4]^+$ cannot be completely replaced with PPV^+. The equilibrium between $[N(CH_3)_4]^+$ and PPV^+ was reached after 24 hours. The $[N(CH_3)_4]^+$ cation was completely removed from the host by dialyzing the partly exchanged products suspended in PPV^+ water solution against deionized water for two days. XRD and IR showed the complete exchange of $[N(CH_3)_4]^+$ cation by PPV^+ precursor polymer after dialyzing.

The conversion of PPV^+ into PPV can be completed either by base-induced or thermal elimination of dimethylsulfide $S(CH_3)_2$[15, 16] The thermal conversion of $[(PPV)_{1.0}]^+$ α-$Sn(OPO_3)_{1.0}(HOPO_3)_{1.0} \cdot H_2O$ to $(PPV)_{1.0}\alpha$-$Sn(HOPO_3)_2$ is a facile route. This can be done either by heating $[(PPV)_{1.0}]^+\alpha$-$Sn(OPO_3)_{1.0}(HOPO_3)_{1.0} \cdot H_2O$ in air at 220°C for three hours or under vacuum at 130°C for one hour. The latter method is preferred due to the thermal instability of the layered host at high temperature.

7.3.2 XRD

The powder XRD data for α-$Sn[N(CH_3)_4]_{1.0}(OPO_3)_{1.0}(HPO_3)_{1.0} \cdot 4H_2O$, $[(PPV)_{1.0}]^+\alpha$-$Sn(OPO_3)_{1.0}(HOPO_3)_{1.0} \cdot H_2O$ and $(PPV)_{1.0}\alpha$-$Sn(HOPO_3)_2$ are shown in Figure 7.2. α-$Sn(HOPO_3)_2 \cdot H_2O$ has the d-spacing of 7.8 Δ (d_{002}). Taking into account that the d-

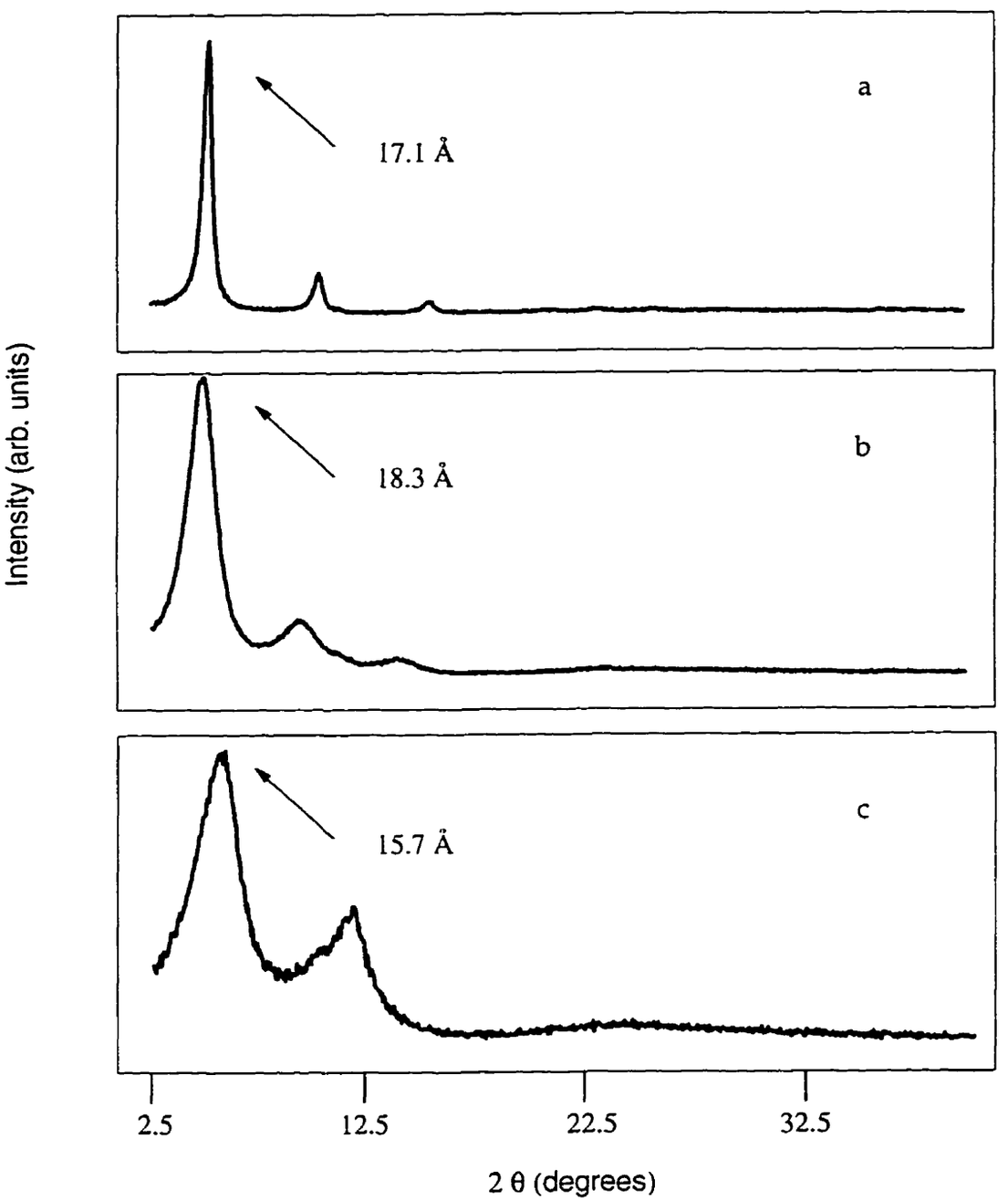

Figure 7.2 Powder XRD patterns of
(a) $[N(CH_3)_4]_{1.0}\alpha$-$Sn(OPO_3)_{1.0}(HOPO_3)_{1.0}\cdot 4H_2O$;
(b) $(PPV^+)_{1.0}\alpha$- $Sn(OPO_3)_{1.0}(HOPO_3)_{1.0}\cdot H_2O$; and
(c) $(PPV)_{1.0}\alpha$- $Sn(HOPO_3)_2$

spacing is the summation of the diameter of water and the thickness of the tin phosphate layer, the layer thickness is about 6.5 Δ. $[N(CH_3)_4]^+$ intercalated precursor has the d-spacing of 17.1 Δ (Figure 7. 2). The 10.6 Δ expansion of interlayer distance is much larger than expected on the basis of the diameter of $[N(CH_3)_4]^+$ (5.3 Δ) alone.[7] It is suggested that there is ordering of water molecules between $[N(CH_3)_4]^+$ and the layer of P-OH groups, as demonstrated for α-$VO(PO_4).5H_2O$.[20]

Upon ion exchange of $[N(CH_3)_4]^+$ with PPV^+, the d-spacing between tin phosphate layers is further expanded to 18.3 Δ (Figure 7.2). The contribution to the d-spacing from PPV^+ is 18.3 Δ-6.5 Δ= 11.8 Δ, corresponding to the formation of bilayer PPV^+ inside the layer. For the only other studied PPV nanocomposite, PPV/MoO_3, a single layer of PPV^+ was inserted between MoO_3 sheets.[5] The d-spacing increased due to the insertion of PPV^+ by 6.4 Δ over that of pristine MoO_3, which is in good agreement with the estimated dimensions of the phenyl ring of the polymer, suggesting that the polymer chains are oriented with the aromatic ring plane perpendicular to the oxide sheets. The d-spacing increase of 11.8 Δ in $[(PPV)_{1.0}]^+$α-$Sn(OPO_3)_{1.0}(HOPO_3)_{1.0}\cdot H_2O$ is approximately twice that of that of PPV^+/MoO_3. Therefore, the polymer chains are oriented with the aromatic ring plane perpendicular to the host sheets.

Upon heating the $[(PPV)_{1.0}]^+$α-$Sn(OPO_3)_{1.0}(HOPO_3)_{1.0}\cdot H_2O$ nanocomposite at 130°C under vacuum, the d-spacing decreased to 15.7 Δ, which is consistent with the elimination of $S(CH_3)_2$ from the ionomer and interlayer H_2O, and is consistent with that observed for PPV^+/MoO_3, where thermal treatment of a thin film of PPV^+/MoO_3 at 260-

280°C (air or N_2) decreased the interlayer spacing from 13.3 Δ to 12.5 Δ, resulting in the formation of PPV inside the inorganic sheets. The larger decrease in d-spacing compared to that of PPV^+ /MoO_3, is consistent in that there is a bilayer of PPV^+ inside the layer while only one layer of PPV exists between MoO_3 layers. The d-spacing of 15.7 Δ - 6.5 Δ= 9.2 Δ for $(PPV)_{1.0}$α-$Sn(HOPO_3)_2$ is smaller than the twice the dimension of the phenyl ring. However, the two chains of polymer, one pointing up, and one pointing down, need not line up vertically. In that way, the host accommodates two layers of PPV with the phenyl ring perpendicular to the tin phosphate sheets using only 9.2 Δ.

7.3.3 FTIR spectra

FTIR spectra have been used to monitor the ion exchange process of $[N(CH_3)_4]^+$ with PPV^+ (Figure 7.3). There is a characteristic C-N stretch band of $[N(CH_3)_4]^+$ α-$Sn[N(CH_3)_4]_{1.0}(OPO_3)_{1.0}(HPO_3)_{1.0}\cdot 4H_2O$ at 1488 cm^{-1}. The peak did not disappear completely after contacting α-$Sn[N(CH_3)_4]_{1.0}(OPO_3)_{1.0}(HPO_3)_{1.0}\cdot 4H_2O$ with PPV^+ at room temperature for 24 hours or longer. The complete ion exchange of $[N(CH_3)_4]^+$ with PPV^+ however, can be realized by dialysis of the partially exchanged α-$Sn[N(CH_3)_4]_{1.0}(OPO_3)_{1.0}(HPO_3)_{1.0}\cdot 4H_2O$ together with PPV^+ against distilled water. Figure 7. 3 shows that the peak at 1448 cm^{-1} of $[N(CH_3)_4]^+$ disappeared completely, suggesting the complete replacement of $[N(CH_3)_4]^+$ with PPV^+ ions.

FTIR data for α-$Sn(HOPO_3)_2\cdot H_2O$, α-$Sn[N(CH_3)_4]_{1.0}(OPO_3)_{1.0}(HPO_3)_{1.0}\cdot 4H_2O$, $[(PPV)_{1.0}]^+$α-$Sn(OPO_3)_{1.0}(HOPO_3)_{1.0}\cdot H_2O$ and $(PPV)_{1.0}$α-$Sn(HOPO_3)_2$ are listed in Table 7.1. Bands characteristic of PPV^+ at 2924, and 2855 cm^{-1} were observed for $[(PPV)_{1.0}]^+$α-

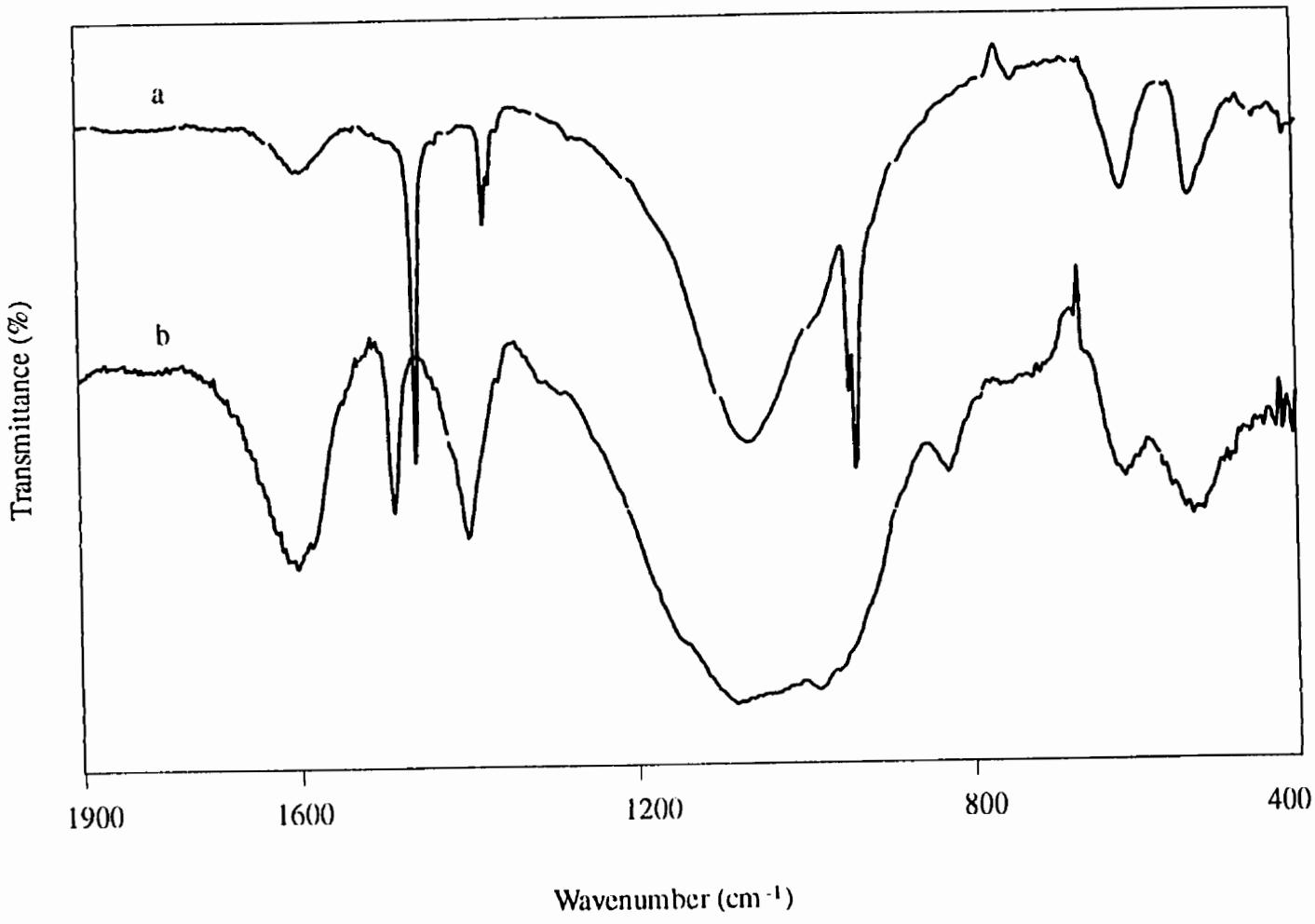

Figure 7.3 **FTIR spectra of (a) $[N(CH_3)_4]_{1.0}\alpha$-$Sn(OPO_3)_{1.0}(HOPO_3)_{1.0}\cdot 4H_2O$ and (b) $(PPV^+)_{1.0}\alpha$-$Sn(OPO_3)_{1.0}(HOPO_3)_{1.0}\cdot H_2O$**

Table 7.1 FTIR data for α-$Sn(HOPO_3)_2 \cdot H_2O$ (A), α-$Sn[N(CH_3)_4]_{1.0}(OPO_3)_{1.0}(HPO_3)_{1.0} \cdot 4H_2O$ (B), $[(PPV)_{1.0}]^+$α-$Sn(OPO_3)_{1.0}(HOPO_3)_{1.0} \cdot H_2O$ (C) and $(PPV)_{1.0}$α-$Sn(HOPO_3)_2$ (D)

A[a]	B	C	D	Assignments
3558 (s)				H_2O
3484 (s)				H_2O
	3400-2800 (b, s)			H_2O, CH_3
		3010	3022 (s, b)	trans-vinylene C-H
		2922		C-H stretch
		2855		C-H stretch
1625 (s)	1635 (s)	1644 (s)	1628 (s)	α-$Sn(HOPO_3)_2 \cdot H_2O$
		1514 (s)	1512 (s)	C-C phenyl ring stretch
	1488 (s)			C-N stretch
	1397			$[N(CH_3)_4]^+$
1095 (vs)	1100 (s, b)	1047 (s)	1058 (s)	α-$Sn(HOPO_3)_2 \cdot H_2O$
965 (s)	957 (sh)		953 (s)	P-O-H
954 (sh)	947 (sh)			P-O-H
		838 (m)	832 (s)	phenylene ring C-H out of plane bend
717 (s)	620 (s)	622 (s)	612 (s)	α-$Sn(HOPO_3)_2 \cdot H_2O$
530 (s)	535 (s)	535 (s)	529 (s)	α-$Sn(HOPO_3)_2 \cdot H_2O$

[a] All frequency values are expressed in cm^{-1}: vs = very strong, s = strong, m = medium, sh = shoulder, b = broad.

$Sn(OPO_3)_{1.0}(HOPO_3)_{1.0}\cdot H_2O$.[5] A peak at 3010 cm^{-1} is also seen which indicates the presence of PPV in the nanocomposite.[5, 28] It suggests that partial elimination of dimethyl sulfide has occurred during the ion exchange process, which is the same as that observed for the PPV^+/MoO_3 nanocomposite material.[5]

Upon heating $[(PPV)_{1.0}]^+\alpha$-$Sn(OPO_3)_{1.0}(HOPO_3)_{1.0}\cdot H_2O$, there is a strong and broad peak in the IR, in the C-H stretch region, at 3000 cm^{-1}. The peak at 3022 cm^{-1}, characteristic of C=H of PPV, was clearly observed. This is strong evidence for the formation of PPV. Otherwise, the IR spectrum of heated $[(PPV)_{1.0}]^+\alpha$-$Sn(OPO_3)_{1.0}(HOPO_3)_{1.0}\cdot H_2O$ does not differ very much from that of unheated $[(PPV)_{1.0}]^+\alpha$ -$Sn(OPO_3)_{1.0}(HOPO_3)_{1.0}\cdot H_2O$ (Table 7.1). Some other characteristic bands at 1433, 1318, 1047, and 632cm^{-1} of PPV^+ overlap with those of the host α-Sn $(HOPO_3)_{2.0}\cdot H_2O$.

7.3.4 Thermal analysis

The TGA curves of α-$Sn[N(CH_3)_4]_{1.0}(OPO_3)_{1.0}(HPO_3)_{1.0}\cdot 4H_2O$, $[(PPV)_{1.0}]^+\alpha$-$Sn(OPO_3)_{1.0}(HOPO_3)_{1.0}\cdot H_2O$, and $(PPV)_{1.0}\alpha$-$Sn(HOPO_3)_2$ are shown in Figure 7.4. α-$Sn[N(CH_3)_4]_{1.0}(OPO_3)_{1.0}(HPO_3)_{1.0}\cdot 4H_2O$ is a compound which easily absorbs water. Its water content usually varies over a large range. There are three major weight losses for $[(PPV)_{1.0}]^+\alpha$-$Sn(OPO_3)_{1.0}(HOPO_3)_{1.0}\cdot H_2O$ up to 600°C. At low temperature, the weight loss is mainly due to the loss of water. Overlapped with this water loss until 250°C is the weight loss of the $S(CH_3)_2$ group. Above this temperature, the host material tin phosphate is not stable; it starts to decompose. The major weight loss, occurring between 400°C and 600°C, is the degradation of PPV inside the layered host.

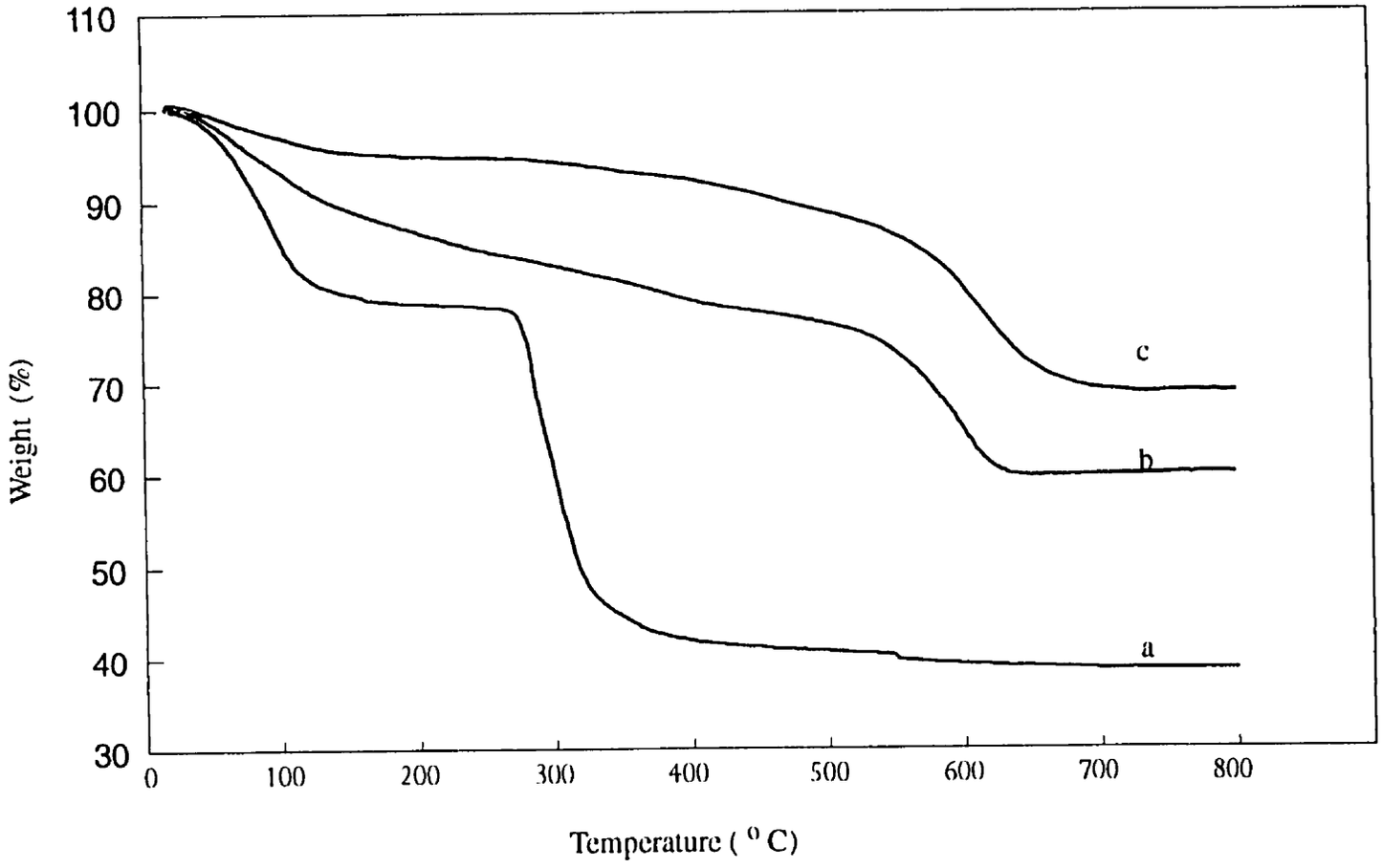

Figure 7.4 TGA traces of (a) $[N(CH_3)_4]_{1.0}\alpha$-$Sn(OPO_3)_{1.0}(HOPO_3)_{1.0}\cdot 4H_2O$ and (b) $(PPV^+)_{1.0}\alpha$-$Sn(OPO_3)_{1.0}(HOPO_3)_{1.0}\cdot H_2O$ and (c) $(PPV)_{1.0}\alpha$-$Sn(HOPO_3)_{2.0}$

The TGA curve for $(PPV)_{1.0}\alpha$-$Sn(HOPO_3)_2$ is similar to that of $[(PPV)_{1.0}]^+\alpha$-$Sn(OPO_3)_{1.0}(HOPO_3)_{1.0}\cdot H_2O$ except that there is no major loss between temperatures of 120°C and 250°C, as there is no $S(CH_3)_2$ to lose for this material. TGA curves of $(PPV)_{1.0}$ α-$Sn(HOPO_3)_2$ and $[(PPV)_{1.0}]^+\alpha$-$Sn(OPO_3)_{1.0}(HOPO_3)_{1.0}\cdot H_2O$ are almost parallel after 220°C, suggesting that conversion of PPV^+ into PPV inside the tin phosphate was completed around 220°C in the air.

It should be noted that the decomposition temperature of PPV inside the layer is about 100°C higher than that of free PPV, i.e., the thermal stability of the polymer was enhanced by intercalation of PPV into the phosphate layer. This is also observed for polyaniline intercalated in α-$Sn(HOPO_3)_2\cdot H_2O$.

It may be appropriate here to compare the different thermal stabilities of polymers inside the inorganic layer and free polymers. For $(PPV)_{1.0}\alpha$-$Sn(HOPO_3)_2\cdot H_2O$, and $(PANI)_{0.4}\alpha$-$Sn(HOPO_3)_2$, the polymers decomposed at a higher temperature than that of the free polymers. The inorganic host increases the thermal stability of polymers. However, for PPY/MoO_3, PANI/MoO_3, and PEO/MoO_3 nanocomposites, the polymers all decomposed at lower temperature than that of the free polymers. This is mainly due to the catalytic properties of MoO_3; it is known to be a versatile catalyst for many reactions. The catalytic property of MoO_3 surpassed the thermal stability enhanced by the inorganic component. Therefore, the chemical properties of the inorganic host are very important factors affecting the thermal stability of polymers.

7.3.5 Solid state NMR

^{13}C CPMAS NMR: Solid state ^{13}C NMR has been employed to study the crystallinity and morphology of PPV films. The NMR spectral line shape of PPV depends upon the conditions employed for film processing. NMR spectra have been used to monitor the quality of films produced by different processing procedures.[21] Likewise, NMR spectra may provide the evidence needed to describe the conformation of PPV inside and outside the layers. Figure 7.5 shows the numbered structure of PPV^+. The ^{13}C CPMAS NMR spectrum of $[(PPV)_{1.0}]^+\alpha$- $Sn(OPO_3)_{1.0}(HOPO_3)_{1.0}\cdot H_2O$ is shown in Figure 7.6. The two higher frequencies of 136.7 and 131.5 ppm were identified as lines due to the nonprotonated (C2 and C2') and protonated aromatic carbons (C1 and C1') respectively with the aid of ^{13}C CPMAS NMR spectra with various contact times (Figure 7.7). ^{13}C CPMAS NMR is a very powerful tool to distinguish between nonprotonated carbons and protonated carbons. In CPMAS NMR, the effectiveness of cross polarization is directly related to the dipolar interaction. Usually nonprotonated carbons have a much smaller dipolar interaction associated with them compared to those protonated carbons. The cross-polarization of nonprotonated carbons is much more ineffective than those of protonated carbons. Much longer contact times needed for nonprotonated carbons. Therefore, by varying the contact times, the relative intensity of nonprotonated carbons and protonated carbons vary, and from that they can be distinguished. From Figure 7.7, the peak at 136.7 ppm is hardly visible until the contact time of 2 ms. At a longer time, the intensity of the peak at 136.7 ppm grows. Therefore, this peak can be assigned to the nonprotonated carbons. The peak at 131.5 ppm is assigned to the protonated carbons.

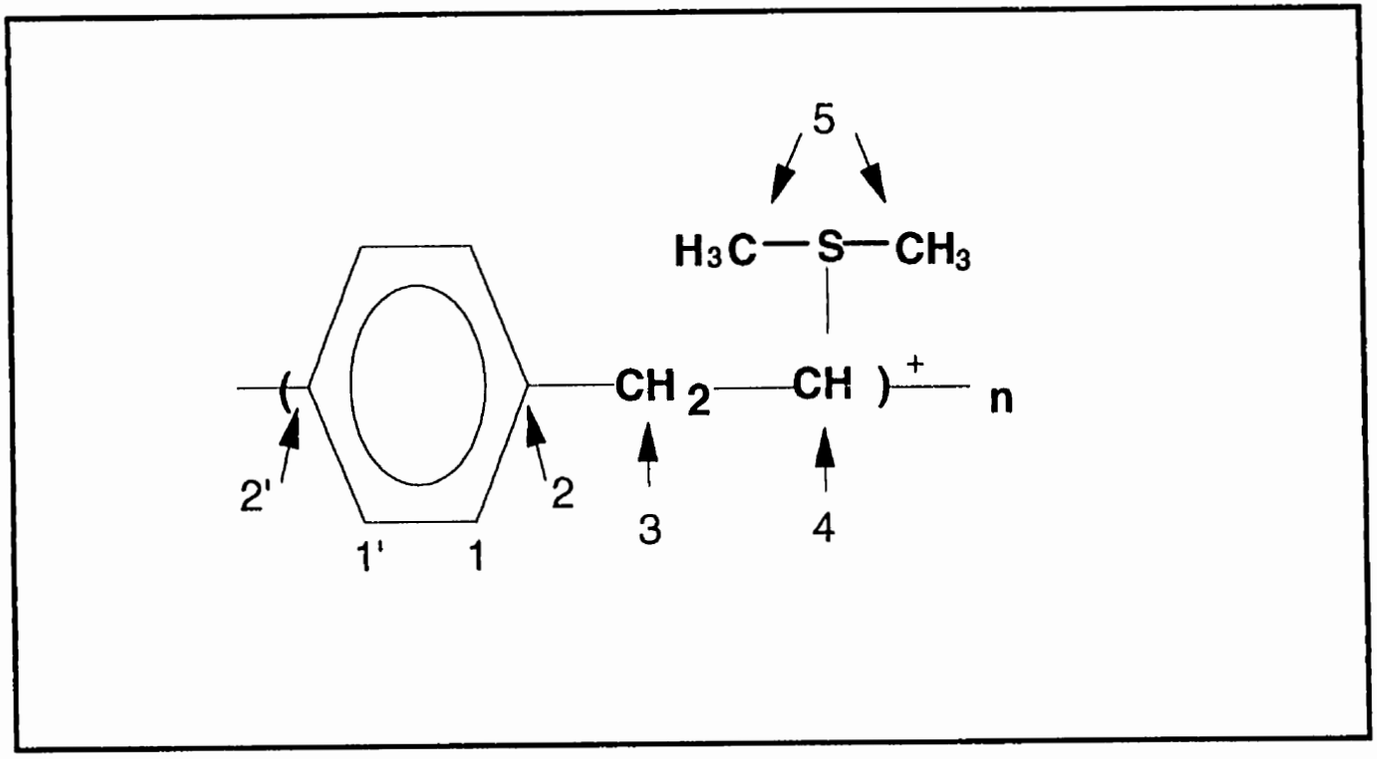

Figure 7.5 Schematic structure of PPV^+

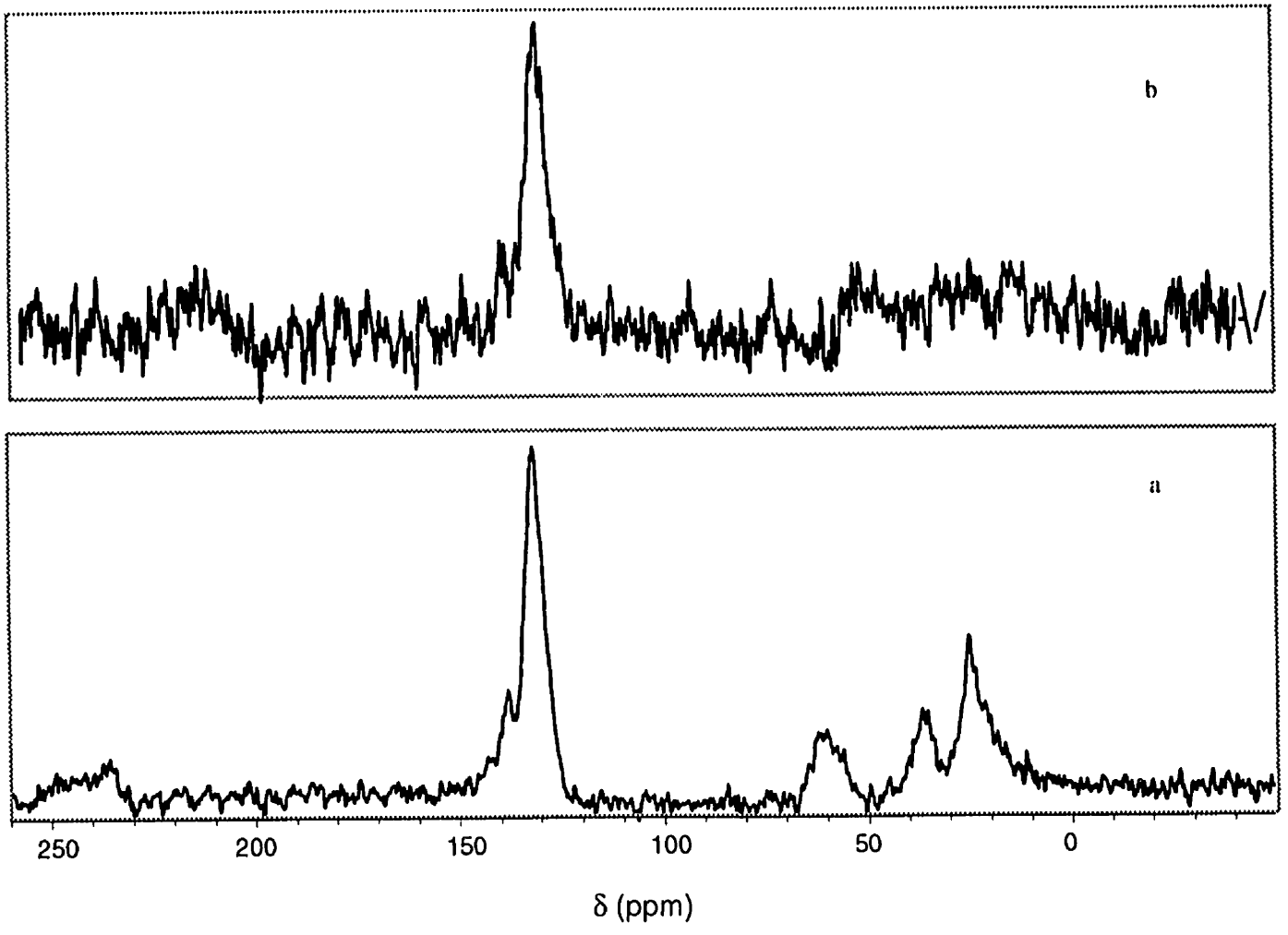

Figure 7.6 ^{13}C CPMAS NMR spectra of (a) $(PPV^{+})_{1.0}\alpha$-$Sn(OPO_3)_{1.0}(HOPO_3)_{1.0}\cdot H_2O$ and (b) $(PPV)_{1.0}\alpha$-$Sn(HOPO_3)_{2.0}$

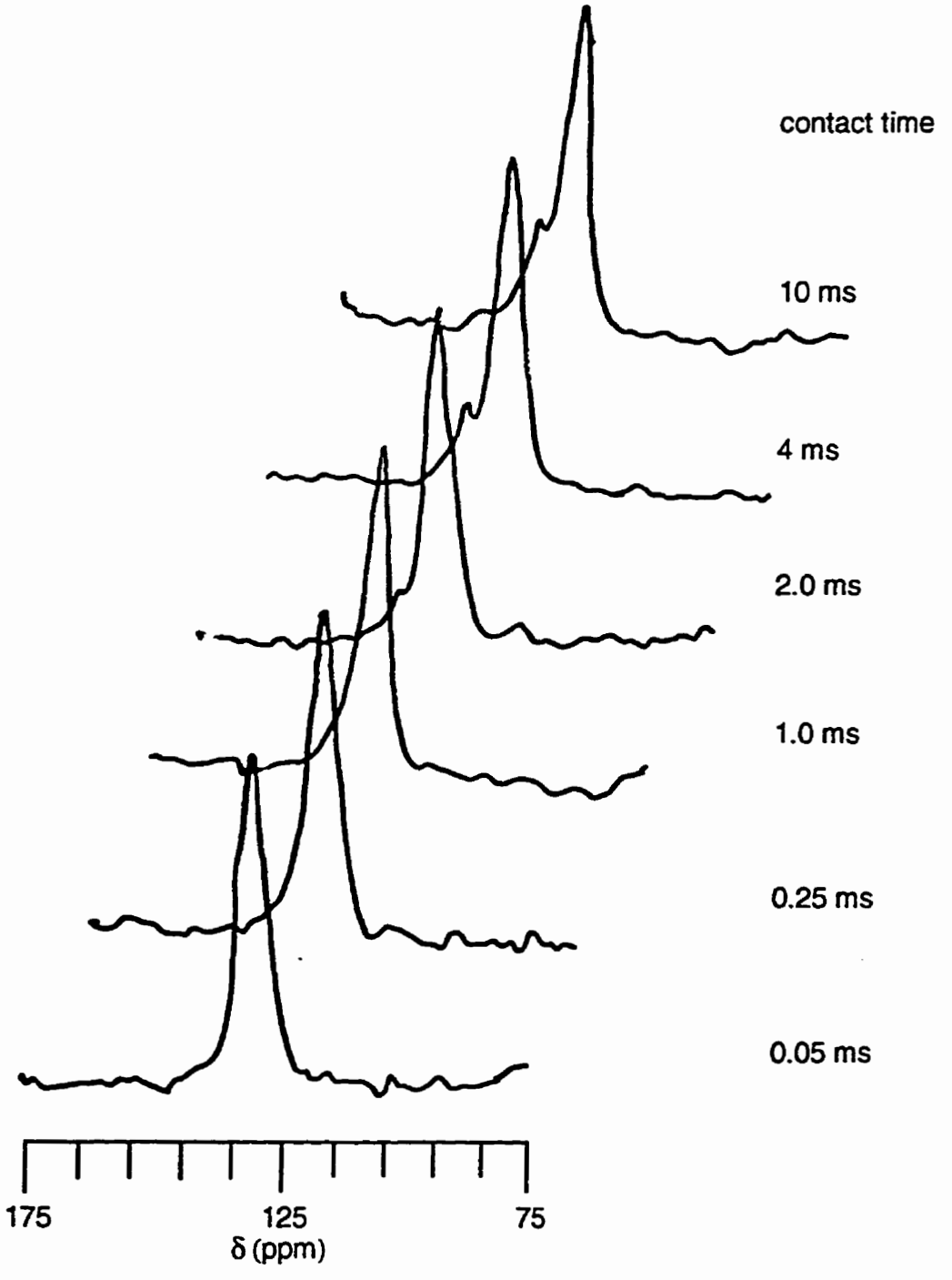

Figure 7.7 ^{13}C CPMAS NMR spectra of $(PPV^{+})_{1.0}\alpha$-$Sn(OPO_3)_{1.0}(HOPO_3)_{1.0}\cdot H_2O$ taken at various contact times

The methine carbon (C4) peak is at ~63 ppm, which is well separated from the remaining peaks. A peak at 37 ppm was assigned to the carbons of the main chain methylene groups (C3). The methyl of dimethyl sulfide carbons (C5) gave rise to a line at ~25.6 ppm. The assignments of the peaks at 37 ppm and 25.6 ppm to the carbons of the main chain methylene groups (C3) and to the dimethyl sulfide carbons (C5) can be controversial. However while we observed that only the line assigned to the nonprotonated aromatic carbons disappear in the spectrum obtained by a very short contact time, it is noteworthy that the intensity of the resonance at ~26 ppm is somewhat suppressed relative to the line at 37 ppm, indicating a substantial averaging of the dipolar interaction between methyl carbons and their bound protons. Such behavior points out that with variable contact time there is evidence of very fast rotation of the methyl group reducing the static carbon-proton dipolar interactions. It also should be pointed out that even at a very short contact time of 50 μs, there was still significant intensity, suggesting that the rotation of methyl is hindered to some extent by incorporation of PPV^+ into the layered host.

Figure 7.6 (b) shows the ^{13}C CPMAS NMR spectrum of $[(PPV)_{1.0}]^+\alpha$-$Sn(OPO_3)_{1.0}(HOPO_3)_{1.0}\cdot H_2O$ heated at 130°C under vacuum for one hour. ^{13}C solid-state NMR provides a sensitive probe for determining the presence of sp^3 hybridized carbons, which disturb the conjugated systems in conducting polymers and account for low conductivity. Upon converting the PPV^+ to PPV inside the host galleries, carbons 3 and 4 were connected by a double bond. The peaks of these carbons will be in the same region as those of the phenyl rings. The resulting spectrum is a peak at ~137 ppm, corresponding to the nonprotonated carbon and a poorly resolved line centered at 128 ppm corresponding to protonated aromatic and olefinic carbons of PPV. From Figure 7.6 we

see that the peaks corresponding to sp^3 carbons of PPV^+ (Figure 7.6) disappeared Therefore, consistent with FTIR and thermal analysis data, NMR data suggest that PPV^+ inside α-$Sn(HOPO_3)_{2.0}\cdot H_2O$ can be easily converted to PPV. The attraction of proton with P--O group may facilitate the conversion process, as we know that deprotonated α-$Sn(HOPO_3)_{2.0}\cdot H_2O$ is a strong base.

Simpson *et al.*[21] have been able to determine the crystallinity of PPV by observation of the line shape of ^{13}C solid state NMR. They show that highly crystalline PPV can be obtained by annealing at a temperature at 300°C, as three lines can be resolved at 128 ppm region for PPV annealed at 300°C. Our NMR data suggest that good crystallinity of PPV has not been realized in $(PPV)_{1.0}\alpha$-$Sn(HOPO_3)_2$ nanocomposite. This may be due to the fact that we only heated the sample to 130°C, since the layered host is unstable in temperatures higher than 200°C. Otherwise, PPV inside the layer is expected to be more ordered or better crystallized than free polymer. Therefore, hosts that are more thermally stable than tin phosphate should be employed to better study the conformation of PPV by ^{13}C NMR methods.

^{31}P CPMAS NMR: It is known that the phosphate group chemical shift in the solid state is remarkably sensitive to its local environment.[22, 23, 24] Solid state ^{31}P NMR is a powerful tool to study the structure,[25] the ion exchange reaction,[22] and intercalation chemistry [26, 27] of transition metal phosphates. It has been found that, as for condensed silicates, there is a linear relationship between the connectivity of the phosphorous and the isotropic chemical shift for transition metal hydrogen phosphates. The isotropic chemical shift of ^{31}P moves to low frequency as the connectivity (Q^n) increases. Figure 7. 8 shows

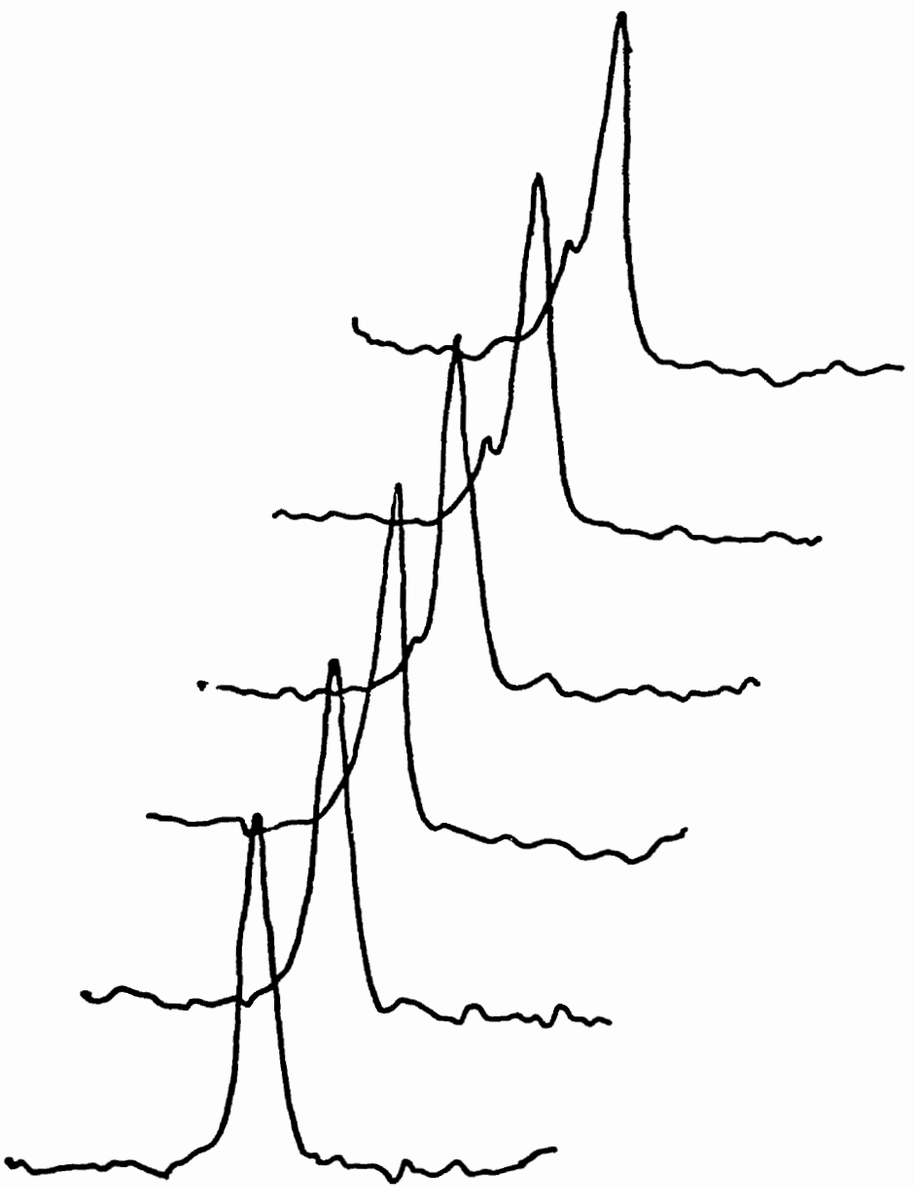

Figure 7.8 ^{31}P CPMAS NMR of
(a) $(PPV)_{1.0}\alpha$- $Sn(HOPO_3)_2$ and
(b) $(PPV^{+})_{1.0}\alpha$- $Sn(OPO_3)_{1.0}(HOPO_3)_{1.0}\cdot H_2O$

the ^{31}P CPMAS NMR spectra of $[(PPV)_{1.0}]^{+}\alpha$-$Sn(OPO_3)_{1.0}(HOPO_3)_{1.0}\cdot H_2O$ and $(PPV)_{1.0}\alpha$-$Sn(HOPO_3)_2$. From the discussion of the last chapter, we know that there is one peak of phosphorous at -13.6 ppm for α-$Sn(HOPO_3)_2\cdot H_2O$, consistent with that of only one type of phosphate (Q^3) in α-$Sn(HOPO_3)_2\cdot H_2O$. For $[(PPV)_{1.0}]^{+}\alpha$-$Sn(OPO_3)_{1.0}(HOPO_3)_{1.0}\cdot H_2O$, two peaks at -7.7 ppm and -13.5 ppm were observed. These are consistent with the fact that only half of the protons were ion exchanged with PPV^{+}. There are two types of Q^3 phosphorous in $[(PPV)_{1.0}]^{+}\alpha$-$Sn(OPO_3)_{1.0}(HOPO_3)_{1.0}\cdot H_2O$. One has undissociated protons (P-O-H) (-13.6 ppm) and the other has no protons ($P\text{-}O^{x-}$) ($x \leq 1$)(-7.7 ppm). The -7.7 ppm for dissociated protons of phosphorous is comparable with -7.3 ppm of aniline intercalated α-$Sn(HOPO_3)_2\cdot H_2O$ compounds.[26, 27] The decrease of 6.5 ppm is associated with an increase in negative charge on $P\text{-}O^{x-}$ ($x \leq 1$). The explanation for aniline intercalated α-$Sn(HOPO_3)_2\cdot H_2O$ discussed in Chapter 6 is valid here, too. The movement of chemical shift observed can possibly be explained on the basis of charge localized on the oxygen. In the undissociated phosphate group there is an amount of double bond character in the P-O-H system. With the formation of negative charge on the oxygen the lone pair in which the charge resides has a greater repulsive effect on the electrons that are already present. Interaction between multi cations PPV^{+} and the oxygen could encourage localization of charge in the oxygen. The phosphorus is therefore more deshielded by the increase in localization of the electrons and the peaks move accordingly.

The ^{31}P CPMAS NMR of $(PPV)_{1.0}\alpha$-$Sn(HOPO_3)_2$ is shown in Figure 7. 8 (b). Upon conversion of PPV^{+} into PPV, two phosphorus peaks become one peak again.

During conversion of PPV^+ to PPV, in addition to the elimination of $S(CH_3)_2$, there is release of one hydrogen from the methine carbon for each aromatic unit. The hydrogen atom can form hydrogen gas and be released or can interact with phosphate. In this case, the released hydrogen is captured by the deprotonated layered host to form the neutral phosphate. Thus, there is only one type of phosphorus in $(PPV)_{1.0}\alpha$-$Sn(HOPO_3)_2$. (However, the line is broad which suggests that there is some degree of interaction between PPV and phosphate OH group.) This is also consistent with the fact that the insertion of PPV^+ into α-$Sn(HOPO_3)_2 \cdot H_2O$ facilitates the conversion of PPV^+ to PPV. There is no measurable conductivity for this nanocomposite, because the weak acid α-$Sn(HOPO_3)_2 \cdot H_2O$ is a poor dopant to PPV. The lines of the ^{31}P CPMAS NMR spectra $(PPV)_{1.0}\alpha$-$Sn(HOPO_3)_2$ are much broader than those of α-$Sn(HOPO_3)_2 \cdot H_2O$, suggesting decreased crystallinity of α-$Sn(HOPO_3)_2 \cdot H_2O$ upon insertion of PPV and some degree of interaction between PPV and phosphate OH group.

The ^{31}P CPMAS NMR spectra observed for PPV intercalated α-$Sn(HOPO_3)_2 \cdot H_2O$ compounds are very similar to those of aniline and polyaniline intercalated α-$Sn(HOPO_3)_2 \cdot H_2O$. This is due to the fact that phosphorous in these compounds is only sensitive to the charge of oxygens.

7.4 Conclusions

Using the intercalated precursor, α-$Sn[N(CH_3)_4]_{1.0}(OPO_3)_{1.0}(HPO_3)_{1.0} \cdot 4H_2O$, we are able to introduce PPV^+ ionomer into the layered tin phosphates. This is the first example

of direct insertion of an organic polymer into the very much studied layered metal phosphate host. The PPV^+ ionomer is converted into PPV inside the layers by thermal treatment under vacuum. There is no measurable conductivity for the nanocomposite, consistent with the fact that the weak acid α-$Sn(HOPO_3)_2 \cdot H_2O$ is a poor dopant to PPV. FTIR data suggest that the ion exchange of $[N(CH_3)_4]^+$ with PPV^+ becomes complete by using the dialysis method. XRD data suggest that two layers of PPV are inserted between tin phosphate layers. Solid state ^{13}C CPMAS NMR data indicated the complete conversion of PPV^+ into PPV inside layer.

7.5 References

1. Gagnon, D. R.; Capistran, J. D.; Karasz, F. E.; Lena, R. W.; Antoun, S. *Polymer*, **1987**, 28, 567.

2. Murase, I.; Ohnishi, T.; Noguchi, T.; Hirooka, M.; Murakami, S. *Mol. Cryst. Liq. Cryst.* **1985,** 118, 333.

3. Burroughes, J. H.; Bradley, D. D. C.; Brown, A. R.; Marks, R.N.; Mackay, K.; Friend, R. H.; Burn, P. L.; Holmes, A. B. *Nature*, **1990**, *347*, 539.

4. Papadimitrakopoulos, F.; Konstadinidis, K.; Miller, T. M.; Opila, R.; Chandross, E. A.; Galvin, M. E. *Chem. Mater.* **1994,** *6*, 1563.

5. Nazar, L. F.; Zhang, Z.; Zinkweg, D. *J. Am. Chem. Soc.* **1992**, *114*, 6239.

6. Bruque, S.; Aranda, M.A.G.; Losilla, E.R.; Olivera-Pastor, P.; Maireles-Torres, P. *Inorg. Chem.* **1995**, *34*, 893.

7. Maireles-Torres, P.; Olivera-Pastor, P.; Rodriguez-Castellon, E.; Jimenez-Lopez, A.; Alagna, L.; Tomlinson, A. A. G. *J. Mater. Chem.* **1991**, *1*, 319.

8. Maireles-Torres, P.; Olivera-Pastor, P.; Rodriguez-Castellon, E.; Jimenez-Lopez, A. *J. Solid State Chem.* **1991**, *94*, 368.

9. Alagna, L.; Tomlinson, A. A. G.; Rodriguez-Castellon, E.; Olivera-Pastor, P.; Bruque, S. J. *Chem. Soc. Dalton Trans.*, **1990**, 1183.

10. Rodriguez-Castellon, E.; Rodriguez-Garcia, A.; Bruque, S. *Mat. Res. Bull.* **1985**, 20, 115.

11. Rodriguez-Castellon, E.; Bruque, S; Rodriguez-Garcia, A. *J. Chem. Soc. Dalton Trans.* **1985**, 213.

12. Criado, C.; Barrado, J. R. R.; Maireles-Torres, P.; Olivera-Pastor, P.; Rodriguez-Castellon, E.; Jimenez-Lopez, A. *Solid State Ionics*, **1993**, *61*, 139.

13. Jones, D. J.; Leloup, J-M.; Ding, Y.; Roziere, J. *Solid State Ionics* **1993**, *61*, 117.

14. Liu, Y.-J.; Kanatzidis, M. G. *Chem. Mater.* **1995**, *7*, 1525.

15. Wessling, R.A.; Zimmermann, R.G. *U.S.Pat.* No. 3.401,152 and 3,706,677.

16. Capistran, J.D.; Gagnon, D.R.; Lenz, R. W.; Karasz, F. E.; George, A. ACS Polymer Prep. 1984, 25, 284.

17. Rodriguez-Castellon, E.; Rodriguez-Garcia; Bruque, S. *Inorg. Chem.* **1985**, *24*, 1187.

18. Troup, J. M.; Clearfield, A. *Inorg. Chem.* **1977**, *16*, 331.

19. Chernorukow, N. G.; Mochalova, I. R.; Moscuichev, E. P.; Sibrina, G. B. *Zh. Prikl. Khim. (Leningrad)* **1977**, *50*, 1618.

20. Alagna, L.; Attanasio, D.; Prosperi, T.; Tomlinson, A. A. G. *J. Chem. Soc. Faraday Trans* **1989**, *85*, 689.

21. Simpson, J. H.; Egger, N.; Masse, M. A.; Rice, D. M.; Karasz, F.E. *J. Polymer Scic. part B: Polymer Physics* **1990**, 28, 1859.

22. Clayden, N. *J. Chem. Soc. Dalton trans* **1987**, 1877.

23. Cheetham, A. K.; Clayden, N. J.; Dobson, C. M.; Jakeman, R. J. B. *J. Am. Chem. Soc.* **1985**, *107*, 6249.

24. Jakeman, R. J. B.; Cheetham, A. K.; Clayden, N. J.; Dobson, C. M. *J. Chem. Soc. Chem. Commun.* **1986**, 195.

25. Clayden, N.J. *Solid State Ionics* **1987**, *24*, 117.

26. Hudson, M. J.; Workman, A. D. *J. Mater. Chem.* **1991**, *1*, 375.

27. Hudson, M. J.; Workman, A. D.; Adams, R. J. W. *Solid State Ionics*, **1991**, *46*, 159.

28. Bradley, D. D. C.; Friend, R. H.; Linderberger, H.; Roth, S. *Polymer* **1986**, *27*, 1709.

CHAPTER EIGHT

SUMMARY AND FUTURE WORK

8.1 Summary

A variety of polymer/inorganic layered host nanocomposite materials have been prepared with a variety of preparation methods. The polymers include doped polypyrrole, polyaniline, undoped poly(*p*-phenyl vinylene), and ionic conducting polyethylene oxide. The inorganic layered hosts include electronically conducting MoO_3^{x-} and nonconducting α-$Sn(HOPO_3)_2 \cdot H_2O$.

$(PPY)_{0.5}MoO_3$ was prepared by a novel method, namely, an oxidative polymerization/ion exchange method. This method extends the possible useful host materials to those having poor oxidizing power. The reaction mechanism involves (i) the oxidative polymerization of pyrrole with Fe^{3+}; and (ii) the ion exchange of alkali molybdenum bronzes with the instantly formed doped PPY. FTIR and conductivity data suggested the conductive form of PPY in $(PPY)_{0.5}MoO_3$. The gallery dimension of PPY of 7.0 Å, determined from XRD, is larger than that observed for most reported PPY nanocomposites such as PPY/V_2O_5. This was explained by a hydrogen bonding model, in which each H--N of the pyrrole units forms a hydrogen bond with the terminal oxygens of the molybdenum oxide double layer. It is of interest to note that the conductivity of $(PPY)_{0.5}MoO_3$ is more than doubled after heating at 200°C under nitrogen; this was

explained as either the further polymerization of oligomer inside the MoO_3 gallery or the self-doping process of the nanocomposite at high temperature.

By controlling the degree of swelling of MoO_3^{x-} sheets with various ratios of Li/Na of molybdenum bronze and mixed solvents, both the monolayer $(PEO)_{0.4}NaMoO_3$ and bilayer $(PEO)_{0.9}(Li,Na)MoO_3$ nanocomposites were isolated. A model based on XRD, $^{13}C/^{23}Na$ solid state NMR, and FTIR data was proposed for the structure of the PEO/MoO_3 nanocomposites.

$^{7}Li/^{23}Na$ solid state NMR spin-lattice relaxation and linewidth studies of bilayer $(PEO)_{0.9}(Li,Na)MoO_3$ nanocomposite show different relaxation mechanisms in different temperature regions; these were explained by mode coupling theory with extension. It states that, in the low temperature region, only the cation hopping in a frozen polymer matrix contributes to the spin-lattice relaxation; in the medium temperature region, the restricted motion of PEO contributes to the spin-lattice relaxation; in the high temperature region, the cations can move freely within the gallery between MoO_3 layers, thus contributing to the effective spin-lattice relaxation. The extended mode coupling theory, the author believes, can be extended to any system containing a submotional phase that may correspond to different relaxation mechanisms.

A comparative study of the electrochemical insertion of lithium into the two polymer nanocomposites and $NaMoO_3$ by using the materials as the cathode in rechargeable lithium batteries, indicates that while the kinetics of the electrochemical Li intercalation/deintercalation process is improved by incorporation of polymer, thermodynamically the PEO/MoO_3 nanocomposites are not very stable under these

conditions. The data suggested that molybdenum bronzes, which have better reversibility than the pristine MoO_3, are promising candidates for cathode materials in secondary lithium batteries.

$(PANI)_{0.4}\alpha$-$Sn(HOPO_3)_2$ was prepared by first intercalating aniline into α-$Sn(HOPO_3)_2 \cdot H_2O$ and then polymerizing aniline within the α-$Sn(HOPO_3)_2 \cdot H_2O$ by heating at 130°C. The two step preparation of PANI should provide the means of controlling the conformation of PANI, because the monomer aniline was organized by the inorganic host. On the other hand, the host must hold aniline molecules at appropriate distances for them to be successfully polymerized. It seems that α-$Sn(HOPO_3)_2 \cdot H_2O$ is not the best host to hold aniline in the optimized position for polymerization, as is evident from the 28 days required to convert aniline into polyaniline inside α-$Sn(HOPO_3)_2 \cdot H_2O$.

$(PPV)_{1.0}\alpha$-$Sn(HOPO_3)_2$ was prepared via an ion exchange reaction. $(PPV)_{1.0}\alpha$-$Sn(HOPO_3)_2$ is, so far, the only example of a polymer that was directly inserted into a metal phosphate. In contrast to the PPV/MoO_3 nanocomposite where PPV is in the doped form, PPV in α-$Sn(HOPO_3)_2 \cdot H_2O$ is in the non-doped form, which is consistent with the fact that α-$Sn(HOPO_3)_2 \cdot H_2O$ is a very weak acid and thus a poor dopant. The XRD data suggested that two layers of PPV lie between layers of α-$Sn(HOPO_3)_2 \cdot H_2O$.

The thermal stability of the polymer in the nanocomposite is very much affected by the chemical properties of the inorganic host. Polymers in $(PPY)_{0.5}MoO_3$, $(PEO)_{0.4}NaMoO_3$, and $(PEO)_{0.9}(Li,Na)MoO_3$ nanocomposites decompose at lower temperatures than free polymer, due to the catalytic properties of MoO_3. Polymers

incorporated into α-$Sn(HOPO_3)_2 \cdot H_2O$ decompose at higher temperatures than free polymers, due to the effect of the inorganic filler.

The thesis shows that, according to the different properties of polymer and host materials, various preparation methods are available to prepare polymer/inorganic host nanocomposite materials. The rigid inorganic host and the relatively flexible polymer may provide a unique environment for cations as in the PEO/MoO_3 nanocomposites; the unique environments produce interesting properties as probed by NMR spin-lattice and linewidth studies. These composites may provide other unique useful physical properties. The electronic properties and the application of these kinds of materials in rechargeable batteries should be further explored.

8.2 Future Work

The promise that the specific interactions in hybrid polymer/inorganic host nanocomposite materials may provide the means to control and modify the conformation of the polymer is exciting. It may be possible to better characterize the structure of such polymers, and thus to better understand the relationship between their properties and structures. So far, the goal is still not reached. The interaction between polymer and inorganic host has not been sufficiently powerful for the rigid inorganic host to direct the structure and conformation of the polymers studied.

On the other hand, in recent years, tremendous progress in the use of organic surfactants to organize complex inorganic frameworks, such as those observed in zeolitic

materials, has been made. A mechanism, such as the cooperative formation of inorganic-organic interfaces in the synthesis of silicate mesostructures, has been suggested. The cooperative formation makes the method versatile and suitable for a wide spectrum of inorganic/organic templates and inorganic/organic reactants. The inflexibility of the inorganic host we used to prepare the polymer/nanocomposite materials, in this respect, may restrict the usefulness of the approach. Cooperative interaction between polymer and inorganic framework is needed for the inorganic framework to be able to effectively affect or direct the structure and conformation of polymers. However, so far, there is no report that polymers have been used as templates for the formation of the inorganic framework for the production of polymer/inorganic host nanocomposite materials.

Ways to approach the goal still need to be explored. The rigid inorganic host is still promising as a material for directing the formation of polymer, especially by preparation method II in which the monomer is arranged by the inorganic host first and then polymerized inside the layer, such as in the preparation of $(PANI)_{0.4}\alpha$-$Sn(HOPO_3)_2$. However the dimensions and properties of inorganic hosts need to be suitable for not only bringing monomer together, but also for accommodating the polymer. On the other hand, the chemical properties of the inorganic hosts may need to be modified to allow them to interact more strongly with the polymer and to direct the structure and conformation of the polymers. The inorganic hosts need to be matched either in dimension or chemical properties with the polymers to exert the required strong influence on the structure and conformation of the polymers.

The match is needed not only for the controlling the structure and the conformation of polymers, but also for optimizing the electronic properties. The promising mutually enhanced electronic properties of nanocomposite materials need to match the doping properties of host and guest. The application of this kind of nanocomposite material as a cathode material in a secondary lithium battery requires the match of the redox properties of the inorganic host and polymers.

The introduction of the rigid inorganic host around the polymer may produce the properties of interest. The incorporation of polymer such as PPV into inorganic host materials may also provide a way to modify the optical properties of the polymer. These properties have a number of applications and deserve further study.